ENHANCEMENT OF TITANIUM ALLOY BIOACTIVITY VIA PEPTIDE AND

HYDROXYAPATITE COATINGS

by

GABRIELA MELO RODRÍGUEZ

A thesis submitted to the University of Birmingham for the degree of DOCTOR OF

PHILOSOPHY

School of Metallurgy and Materials

College of Physical Science and Engineering

University of Birmingham

September 2017

UNIVERSITY OF BIRMINGHAM

Abstract

A metal/peptide interface was developed to nucleate hydroxyapatite from aqueous solution. To achieve this, three different modifications were performed on polished Ti-6Al-4V (MPT): 1) thermal oxidation (TO) at 500, 600, 700, 800 °C, 2) chemical treatment with H_2O_2/HCl and 3) chemical treatment with H_2O_2/HCl followed by TO at 500, 600, 700, 800 °C. It was found that with the increase of the TO temperature the topography increased and the composition of the surfaces changed, forming TiO_2 crystals and increasing the Al_2O_3 content on the surface.

These changes affected locally the surfaces charge behaviour in acidic and alkaline aqueous environments that were clue to the electrostatic interaction between the peptide, which presented positive and negative charged amino acids, and the surface. The peptide adsorption was highest on the surfaces that was chemically treated and thermal oxidised at 500 °C.

The peptide coating was confirmed on the surface by the change of the charge behaviour in acidic and alkaline aqueous environments and its chemical composition. In addition, the growth of hydroxyapatite (HA) was obtained on the peptide coated surfaces confirming its bioactivity. Finally, it was shown that the surfaces with HA presented a better cell adhesion than the other modified surfaces.

I

Dedico esta tesis a: Luz Amparo, Gonzalo, Alvaro, Camilo, Jose, Juan Manuel y Juan Carlos. Cada uno hizo uno aporte importante para la realización de este proyecto.

Acknowledgement

I would like to thank my supervisors, Dr. Artemis Stamboulis for her guidance and support during the process and Dr. James Bowen for his always supporting and novel ideas, long work hours shared in the laboratory and guidance during this long process in the write-up.

I would like to thank Camilo, Jose, Juan Manuel, Juan Carlos and my parents Luz Amparo and Gonzalo for all their support in every stage of this project.

I would like to have a special thanks to my partner Alvaro Guerrero who guided, helped and supported me in the most difficult times during my thesis write-up.

I would also like to thank all the students, academics and researchers who collaborated during this project helping, supporting and providing technical and life advices. These people are Dr. Aleksey Molokanov, Dr. Zuzanna Trizcinska, Dr. Francisco Nieves, Dr. Santiago Corujeira, Dr. Michelle Casarin, Professor Hanshang Dong, Dr. Elizabeth Blackburn, Erik Jellyman, Dr. Nik Hodges, Dr. Mark Webber, Dr. William Griffins, Dr. Jaimes Davies, Dr. Elizabeth Hinton, Dr. Daniel Reed, Simone Basile.

I would like to thank Science City Advanced Materials lab, NEXUS lab, CIRIMAT-ENSIACET, University of Technology, Sydney Faculty of Science and all the members of these institutions that supported my project.

I would like to thank other researchers, collaborators and friends from different institutions who supported my research from different points of view. These include Dr.

Mischa Zelzer, Dr. David Grossin, MD. Gérard Giordano, Professor Besim Ben-Nissa, Dr. Felicity Williams.

Content listing

XII

List of figures

XIX

XXV

List of tables

List of equations

List of abbreviations and acronyms

aa   Amino acids

AE   Auger electron

AFM   Atomic force microscope

aq   Aqueous solution

ASTM   American society for testing and materials

BSE   Back scattering electron

CAS   Chemical abstracts service

CpTi   Commercially pure titanium

DCA   Dynamic contact angle

dH$_2$O   Deionised water

DMEM   Dulbecco's modified eagle's medium

ELI   Extra low interstitial

Eq.   Equation

EZ-PCR   Polymerase chain reaction

HA   Hydroxyapatite

HOS	Human osteosarcoma cells
IEP	Isoelectric point
JCPDS	Joint committee on powder diffraction standards
MPT	smooth polished Ti-6Al-4V
$nTiO_x$	Native titanium oxide
PBS	Phosphate buffer saline
SBF	Simulated body fluid
SE	Secondary electron
SEM	Scanning electron microscope
TGL	Titania gel layer
TGL-TO	Titania gel layer -Thermal oxidation
Ti-HA-pep	Titanium – hydroxyapatite peptide sequence
TiO_x	Titanium oxide
TO	Thermal oxidation
XPS	X-ray photo electron scanning
XRD	X-ray diffraction

Chapter 1

1.1. Introduction

Ti and its alloys are commonly used in the human body to replace and repair hard tissue [1–3] for example in knees, hips [1,2], bone plates [3] and in the dental field for dental roots [1], crowns and bridges [3]. They are used because of their desirable mechanical properties such as lower Young's modulus compared with other implant materials, low density and good corrosion resistance [1–3]. However, Ti and its alloys present some drawbacks such as poor tribological properties which induce high unstable friction coefficients and low wear resistance [1,4,5]. In addition, these metals present lower bioactivity compared with other materials such as bio-glasses or Ca/P [6]. Nowadays these drawbacks are mitigated modifying the Ti surface [7–9] ,which is mainly formed by titanium oxide (TiO_x) [10–12], and/or implementing coatings on the surface [6,13,14] with materials such as Ca/P [15], polymers [16], metal oxides (Al_2O_3 [17], TiO_2 [18], ZrO_2 [19]) and biomolecules [20]. Hydroxyapatite (HA) bioactive coatings can be deposited using plasma spray [21], sputter [22], electrophoretic deposition, sol-gel deposition and biomimetic deposition [23]. Industrially, the most used technique to obtain the HA coating is plasma spray [21,24] but some drawbacks such as crystal phase change [25] , and weak bond strength between the coating and the metal interface [26] , which can lead to delamination [27] and detachment of the coating [23] , can decrease the bioactivity of the implant and in some occasions induce implant failure [21].Ongoing research focuses on how to mitigate these drawbacks via biomimetic procedures such as precipitation processes using simulated body fluid (SBF), a solution that simulates the salt concentration of the blood plasma. SBF is a potential alternative due to that the process is performed at physiological temperature (37 °C) [28,29] without crystal phase changes,

with a strong bonding between the metal and coating, and without delamination or detachment of the HA coating over extended periods of time [30].

The objective in this project is the use of peptides on the surface that can work as an interface to nucleate HA. The novelty of the approach required brings new challenges such as the quantification of peptide coating, the selection of amino acid (aa) to be used in the sequences, the peptide adsorption on the surface, the identification of surface treatments prior peptide adsorption, the mechanism of interaction between materials (peptide-Ti surface, peptide-HA formation) in aqueous environments, the activity of the peptide after adsorption and the stability of the peptide coating.

In the literature many surfaces are functionalised with peptides covalently binding by silanization [31–33] and grafted [34–36] techniques but there is a significant information gap in the literature because there are few studies available detailing electrostatic peptide binding on surfaces. Groups that work with electrostatic peptides have different focuses including tracking of metal oxide nanoparticles [37], binding sites to hydroxyapatite crystals [38] and development of biocompatible surfaces [39] however none of these works make reference to the mechanism of interaction between the peptide and the surface. In the literature there is only one leading study performed by Sano and Shiba that suggests that the peptide segment RKLPDA adsorbed to TiO_2 surfaces could be due to electrostatic interactions produced between the positively and negatively charged amino acids of the peptide sequence and the amphoteric TiO_2 surface. [40].

The primary contribution of this thesis is to show the peptide coating adsorption on TiO$_2$ surface, derived from Ti-6Al-4V, while the peptide maintains the bioactive nucleating hydroxyapatite capability.

1.2. Objective

The aim of this thesis was to present an innovative metal-peptide system that can be used on the surface of Ti-6Al-4V for biomedical purposes such as bioactivity, defined as the response of the biological species to the surface inducing the generation of a binding between the living tissue and the implant material [19]. The approach followed to develop the metal-peptide system is based on the use of peptides with ionic regions which can interact electrostatically with the TiO$_x$ surface [40] in an aqueous environment.

1.3. Background

The interaction between the metal and the peptide has been demonstrated in the literature to improve with the modification of the native TiO$_x$ surface via H$_2$O$_2$ chemical treatments [40]. It is also extensively shown in the literature that in presence of TiO$_2$ crystals (anatase and rutile) improves the adsorption of biomolecules [41–45]. Thus, these chemical treatments and the necessary thermal treatments required to develop TiO$_2$ crystals have been included as part of the work to build the metal-peptide system and to enhance the adsorption of the ionic peptide on the modified surfaces.

1.4. Overview

Throughout the work, surfaces were analysed to understand which factors such as composition, topography and electrostatic behaviour in aqueous solution was critical to produce the optimal interaction between the surface and the peptide coating. In addition, the stability of the peptide coating from the modified surfaces were evaluated to understand under which conditions of pH, temperature and ionic strength the metal-

peptide system remains stable. On top of that, the peptide coated surfaces were exposed to SBF to assess the formation of the biomimetic HA which at the same time was an *in vitro* experiment to evaluate the bioactivity of the surface. Finally, because modified surfaces were developed to interact with cellular bones, the biocompatibility which is defined as: "*the ability of the material to perform with and appropriate host response in a specific situation*" [46], was evaluated for all modified surfaces using a cellular culture of human osteosarcoma cells (HOS).

1.5.   Structure of the thesis

This research which this thesis reports is divided in 5 chapters, where each issue is introduced, results are presented and discussed, and conclusions are drawn.

1.5.1. Chapter 3

Surface characterization to understand how the composition and topography of the metal surface influences the adsorption of ionic peptides.

According with the literature the modification of the native TiO_x by H_2O_2 solutions present the formation of titania gel layer (TGL) that shows porous structure [47–49]. On the other hand, the thermal oxidation (TO) in air forms TiO_2 crystals (anatase or rutile) which also changes the surface topography [50,51]. These compositional and topographical changes on the TiO_x surface can interfere in the interaction of the peptide with the surface. Surfaces modified by TO, TGL, and a combination of both (TGL-TO) were characterised to assess under which condition the surface adsorbs the ionic peptide. In this chapter, the characterization and differences of the modified Ti-6Al-4V surfaces by TO, TGL, and TGL-TO are shown.

1.5.2. Chapter 4

Surface characterization of the modified metals in the presence of acidic and alkaline unbuffered aqueous solution (aq) to understand the charge properties and consequences for adsorption of the peptides.

The adsorption of biomolecules such as peptides, proteins, ions and cells on the implant surface is always performed in aqueous environments [41,52–54] under certain conditions of temperature, pH and ionic strength. The pH plays an important role on the surface properties, because depending on the pH value the metal oxide can present positive, neutral or negative charges [55] due to protonation or deprotonation of surface moieties. This determines under which condition the peptide will bind to the surface. For TiO_x the zero charge or isoelectric point (IEP) can be between pH 4 and 6 [56,57] . At pH < IEP the surface presents positive charges, whereas at pH > IEP the surface presents negative charges. The TO, TGL, and TGL-TO modified surfaces are studied with different pH solutions in this chapter to evaluate how the pH response of the surface is altered following the modifications.

1.5.3. Chapter 5

Adsorption of peptides onto modified metal surfaces to evaluate which surface treatments promote adsorption of the ionic peptides.

The peptide that will be used in this study presents charged and uncharged amino acids (aa), the charged aa are expected to bind electrostatically to the TiO_2 surfaces and nucleates HA. The peptide sequence (Ti-HA-pep) is shown in Figure 1.
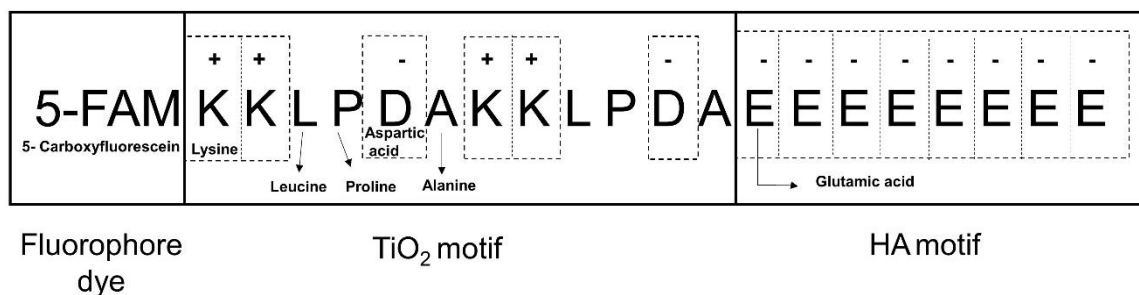
Figure 1: Peptide sequence presenting the amino acids and their charge at pH 7.4, together with their motif functionality.

The TiO$_2$ motif present on the Ti-HA-pep is designed based on the peptide sequences RKLPDA (minTBP-1) (where R is arginine) studied by Sano and Shiba [40] which presented an electrostatic interaction with TiO$_2$ surfaces. This peptide aptamer presents an electrostatic interaction mechanism with the TiO$_2$ at pH 7.5 that interact simultaneously on the amphoteric TiO$_2$ surface in two points, one with the positively charged aa R and the other with the negatively charged aa D [40].

The HA motif present on the Ti-HA-pep sequence contains multiple glutamic acid (E) which presents negative charges due to the COOH moiety that induces the formation of HA via simulated body fluid (SBF) [58–61].

The purpose of this chapter is to evaluate which surface modification performed by TO, TGL and TGL-TO presents an optimal interaction with the Ti-HA-pep.

1.5.4. Chapter 6

Characterization of the metal surface post-adsorption of peptide, as obtained in Chapter 5, to evaluate the presence of the ionic peptides.

The Ti-HA-pep adsorbed on the TiO_2 under the mechanism described previously is expected to have the HA-binding motif rich of glutamic acids on the surface. This motif could influence the pH response of the surface due to the protonation and deprotonation of the COOH moieties of the glutamic acid [62]. In this chapter, the presence of peptides on the surfaces is evaluated with the changes of the surface charge in acidic and alkaline environments.

1.5.5. Chapter 7

Surface characterization to evaluate the stability of the adsorbed peptide on Ti modified surfaces and the bioactivity of peptide coated surface.

Adsorption of peptides and proteins in solid surfaces is presented under certain conditions of pH, temperature and ionic strength [53]. However, these conditions can be modified presenting changes of adsorbed peptides [64] that leads to a different configuration of the peptide on the surface or even to the desorption of the peptide [53]. In this chapter, the Ti-HA-pep coating of the optimally coated sample is analysed at different pH, temperatures and ionic strengths to evaluate how these factors can affect the adsorption of the peptides on the surface.

The HA formation via SBF on surfaces is a signal of bioactivity [30,61,65–68] and therefore the formation of HA on the optimal peptide coated and uncoated Ti-6Al-4V modified surface is assessed in this chapter.

The adhesion of mammalian cells on surfaces is a process that involves the formation of a whole system of proteins that include extracellular proteins, cytoskeletal proteins, integrins, and cadherins [69]. According to the literature to promote the adhesion process it is necessary that the surface presents a topography [70], chemistry and surface

charges [71] that could lead to the cellular proliferation and differentiation [72] that induces bone healing and regeneration [73]. Evaluation of the cellular adhesion was performed for all modified surfaces to assess how the topography and composition alter the cells adhesion, and these studies can be found in Chapters 3 and 7.

Chapter 2

Materials and methods

2.1. Introduction

The techniques used in this study for the characterization of surfaces in each stage are shown in Figure 2. The reason for them to be used are explained below.
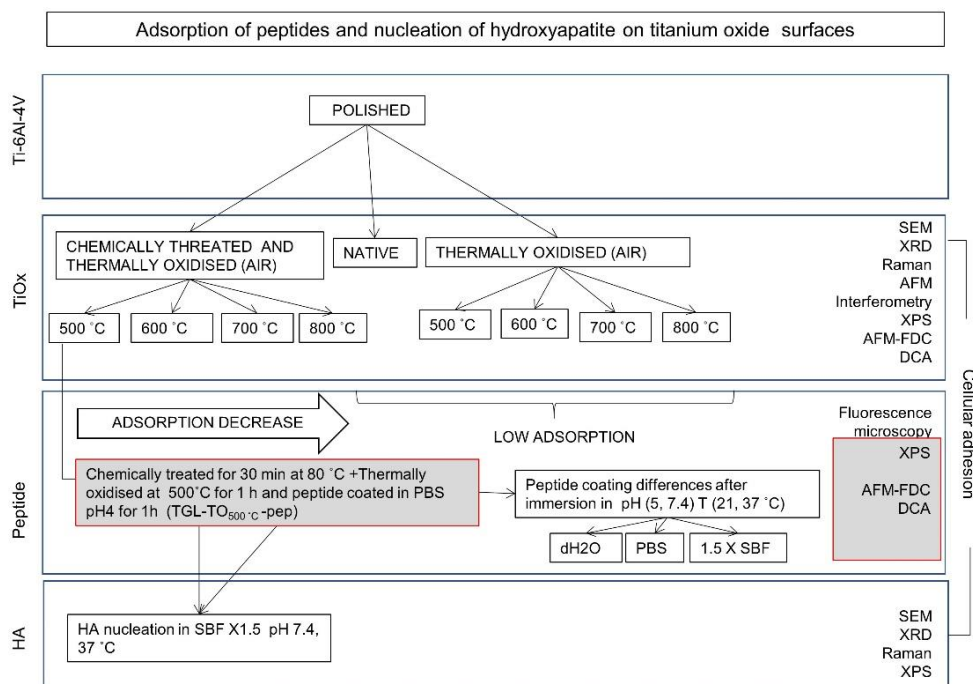
Figure 2: Ti-6Al-4V surfaces modifications and characterisations performed for each modification.

Scanning electron microscopy (SEM), atomic force microscopy (AFM) and interferometry were used in this study to characterise the topographical changes on the surfaces after the mechanical, thermal and chemical treatments. With this set of techniques is possible to identify micro and nano scale differences on the surface. The limitation of interferometry is that when the surfaces present heterogenous composition the measurement change due to the differences on the reflective index. The limitation

of AFM is that when the surface presents larger topographical alterations than the probe size is not possible to measure all the areas expose on the surface. The limitation of the SEM is that to measure the topography changes requires extensive running time and sampling that can be performed by other techniques e.g. profilometry, AFM.

To identify the structures of the hydroxyapatite (HA) and the structure of the cells adhered on the surface the SEM was used due to the need to observe the cellular extension spread on the surface at the submicron level.

Raman spectroscopy and X-ray diffraction (XRD) were used in this study to identify the formation of TiO_2 crystals on the surface after the thermal treatment and calcium phosphates crystals after the surface immersion in simulated body fluid (SBF). Both techniques should be used in a complementary way because of their limitations. The XRD setup even at small angles present the limitation to measure crystals at the surface level. To complement the measurement and to determine the presence of the crystals in the surface, Raman spectroscopy was used to identify the vibration modes of the atoms in the given arrangement. Nonetheless, the use of both techniques presents a limitation when the thickness of the layer is less than 100 nm.

X-ray photoelectron spectroscopy (XPS) was used in this study to identify the chemical changes on the surfaces for Ti, Al, V, O, C, N, Ca and P after the thermal treatments, peptide adsorption and hydroxyapatite (HA) growth. The limitation on this technique is that any contamination on the surface sample can alter highly the results.

Dynamic contact angle (DCA) and AFM-force distance curves (AFM-FDC) were used in this study to identify the charge behaviour under aqueous environments of surfaces that were mechanically, thermally and chemically treated. Surfaces with peptide coating were also analysed under these techniques to identify the charge changes due to the coating. The limitation is that both techniques require smooth and homogenous surfaces.

Fluorescence microscopy was used in this study to identify the adsorbed peptides on the surface because the peptide sequence presents a fluorophore dye that helps to track them on the surface. The limitation of this technique is that it is only possible to determine the presence of peptides and not their quantity because intensity measurement changes generated by a possible decay or protonation of the fluorophore.

2.2. Ti-6Al-4V surface modifications by chemical and thermal treatments

Titanium alloy medical grade plate with 1.6 mm thickness, Ti-6Al-4V ELI ASTM F136-2002a (Titanium Industries UK Ltd, UK) was used in this project. The chemical composition of the plate according with the mill test certificate (attached in Appendix 1) is shown in Table 1.

Table 1: Chemical composition of Ti-6Al-4V ELI ASTM F136-2002a.

	Chemical composition (% w/w)									
									Residual element	
	Ti	Al	V	Fe	C	N	O	H	Each	Total
Top	> 88.854	6.42	4.12	0.03	0.02	0.02	0.13	0.006	< 0.1	< 0.4
Bottom	> 88.864	6.38	4.14	0.04	0.02	0.02	0.13	0.006	< 0.1	< 0.4

The Ti-6Al-4V plates were processed to obtain the modified surfaces and the procedure is summarised in Figure 3. The detail of the procedure is explained below.
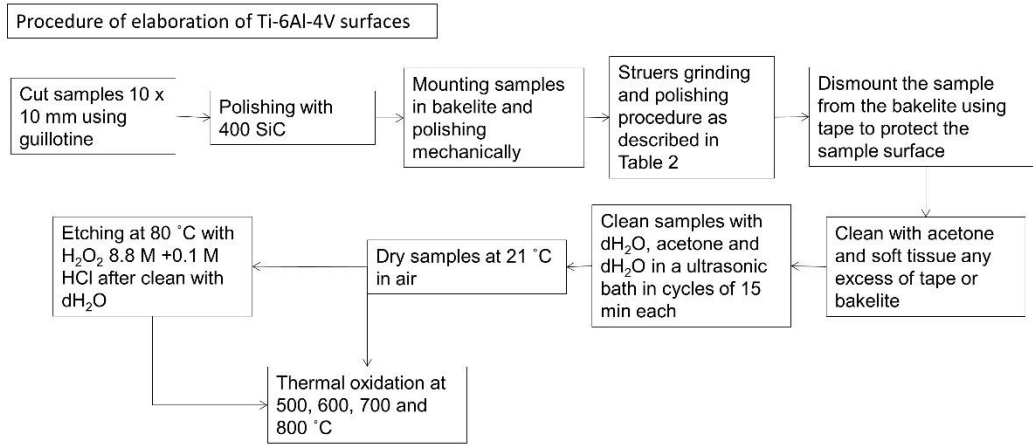
Figure 3: Schematic flow diagram to elaborate of Ti-6Al-4V surface modification.

- Ti-6Al-4V were cut in 10 X 10 mm by guillotine.

- Polished with 400 SiC paper until the surface is planar.

- Samples were mounted in bakelite (CAS No. 9003-35-4) for grinding and polishing (Struers, USA) following Struers protocol shown in Table 2.

Table 2: Struers protocol for Ti-6Al-4V mechanical polishing.

Struer's disks	MD-Piano	MD-Largo	MD-Chem
Suspension/lubricant	Water	DIaPro (Diamond 9 μm)	OP-S (colloidal silica 0.04 μm + 10 % v/v H_2O_2 (30 %)
rpm	300	150	150
Force (N)/ specimen	15	20	20
Time (min)	Until plane	5	15

- After the smooth polishing, the Ti-6Al-4V surfaces were protected with insulating tape (3M, USA) and dismounted from bakelite using a hammer until the bakelite was broken. Large residuals of bakelite on the plate were taken out by polishing them until the plates were free of bakelite.

- All surfaces were acetone (CAS No. 67-64-1, analytical grade EMSURE) cleaned and dried with a soft cellulose tissue paper (Tork, Sweden) until visible bakelite and residual tape were taken out from the plate in both surfaces. Surfaces that presented visible scratches or deformations at this point were discarded.

- Once the surfaces were visibly cleaned, a deeper cleaning procedure with ultrasonic and cycles of 15 min with deionised water (dH$_2$O), acetone and dH$_2$O were performed in individual glass vessels for each sample. When the cycle was completed, samples were air dried at room temperature 21±2 °C.

- Chemical modification and thermal oxidation on polished obtained surfaces are explained below.

2.2.1. Chemical treatment

The chemical solution was prepared with H$_2$O$_2$ 30 w/w % (CAS No. 7722-84-1) (≈9,53 M) and 1M HCl, prepared from HCl 32 w/w % (product No. 100319, Merck Millipore, USA), in a clean glass flask. The final concentration of H$_2$O$_2$ was 8.8 M and for HCl was 0.1 M (colour less). Cleaned and dried Ti-6Al-4V samples in individual glass covered vessels of 20 mL were reacted with 10 mL of the previous mix H$_2$O$_2$/ HCl at 80 °C in an oven (Pickstone, UK) for 30 min. After the 30 min of reaction the reagent was discarded and the Ti-6Al-4V plate was rinsed with dH$_2$O. Surfaces were allowed

13

to air dry at 21±2 °C and were kept in the desiccator (Thermo Fisher scientific, UK) for further procedures.

2.2.2. Thermal oxidation in air

Ti-6Al-4V plates with and without chemical treatment were placed into alumina boats and thermally oxidised in an air furnace (Lenton, UK) at different temperatures: 500±5, 600±5, 700±5 and 800±5 °C. When the oven reached the setpoint temperature, the samples were introduced in the oven for 1 h, as is shown in Figure 4 (that was counted when the oven reach the target temperature after been opened to introduce samples). Samples were taken out from the oven after 1 h and left at 21±2 °C to cool to room temperature. Ti-6Al-4V plates were kept in sterile 24-well polystyrene plates (product No. 353226, Corning, Inc., USA) from in the desiccator for further procedures.
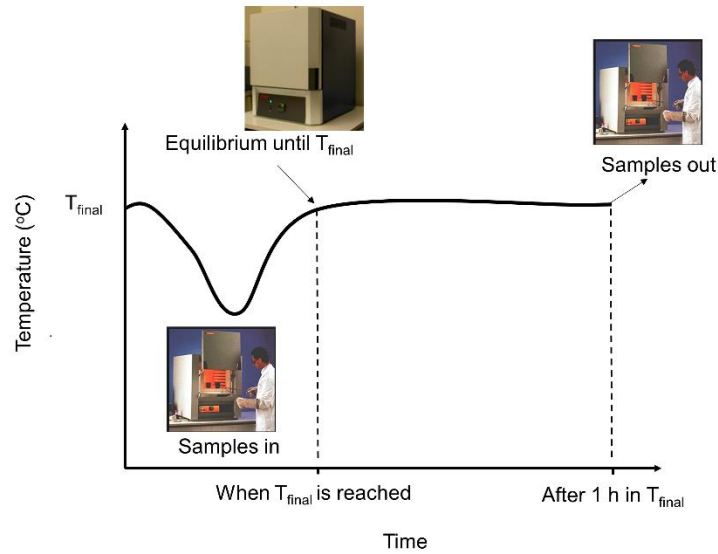
Figure 4: Schema of samples' introduction and removal from the oven, and time of oxidation.

2.3. Peptides

Peptide sequences (5-FAM)-KKLPDAKKLPDAEEEEEEEE (Ti-HA-pep), abbreviations and named as shown in Table 3, were synthesised by ProteoGenix (France) with 95.34 purity (preparation, HPLC and MS are shown in Appendix 2). A fluorescence dye was used to quantify and monitor the peptides in the liquid and on the surfaces. Peptides were used no light condition to prevent the damage of the fluorophore.

Table 3: Peptide sequences one letter code and fluorescence dye name.

Abbreviation	Name
5-FAM	5-Carboxyfluorescein
K	Lysine
L	Leucine
P	Proline
D	Aspartic acid
A	Alanine
E	Glutamic acid

2.3.1. Quantification of peptide in solution

An absorbance curve of the fluorescence dye 5- FAM (CAS No. 72088-94-9, 99 % purity), was performed to find the molar absorption coefficient from the Beer-Lambert law, shown in Eq. 1.

$$A = \varepsilon l C \qquad \text{Eq. 1}$$

Where: A = absorbance

  ε = molar adsorption coefficient (L/mol * cm)

  l = path length (cm)

15

C = concentration (mol/L)

5-FAM was dissolved in phosphate buffer saline (PBS), prepared from tablets (product No. P4417, Sigma-Aldrich, USA) dissolved in dH_2O and adjusted the pH 7.4, using acidic solution of HCL 0.01 M previously prepared with HCL 32 % w/w and/or alkaline solution of NaOH 0.01 M previously prepared with pure pellets of NaOH (CAS No. 1310-73-2, pure), measured with a pH meter (Hanna, Italy). The absorbance curve was performed in a Helios -γ UV-visible light spectrophotometer (Thermo Fisher Scientific, UK) at a wavelength of 492 nm, that was the maximum emission peak of 5-FAM when it was exposed to UV-Vis wavelengths (190 – 700 nm), shown in Figure 5.
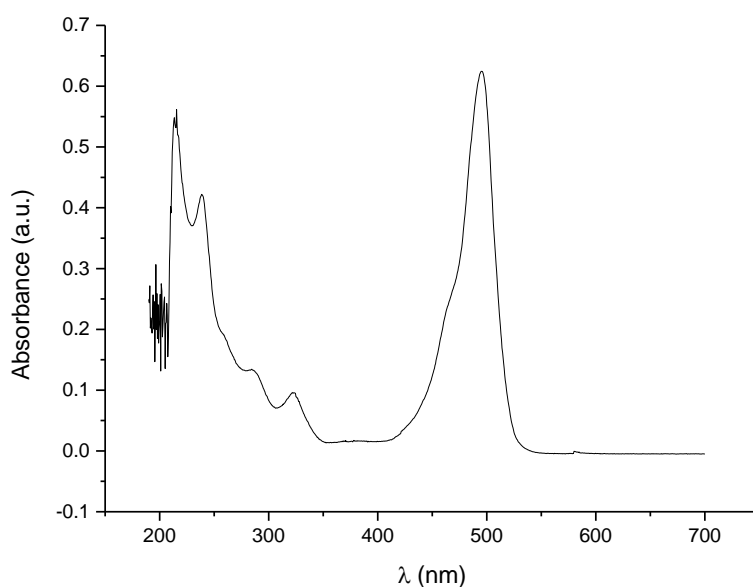
Figure 5: Absorbance spectrum for 5-FAM in PBS at pH 7.4, measured using UV-Vis spectrometry.

The absorbance curve was run for 6 concentrations of 5-FAM, shown in Table 4 .

Table 4: Concentration and absorbance of 5- FAM at 492 nm.

5-FAM (μM)	Abs 492 nm (a.u.)
2.0	0.130
4.0	0.265
8.0	0.502
12.5	0.780
25.0	1.430
40.0	2.138

A graph where concentration is on the x-axis and absorbance on the y-axis was sketched, and a linear fitting was obtained, shown in Figure 6, using a first order polynomial $y = a + bx$. The y-axis intersection point (a) is 0 and the slope (b) is 53.42 mM. Solving for Eq. 1 $b = \varepsilon l$ and knowing the path length (1 cm) the peptide concentration can be obtained when the absorbance is measured.

Equation	y = a + b*x	
Pearson's r	0.99834	
Adj. R-Square	0.99602	
		Value
	Slope	0.05342
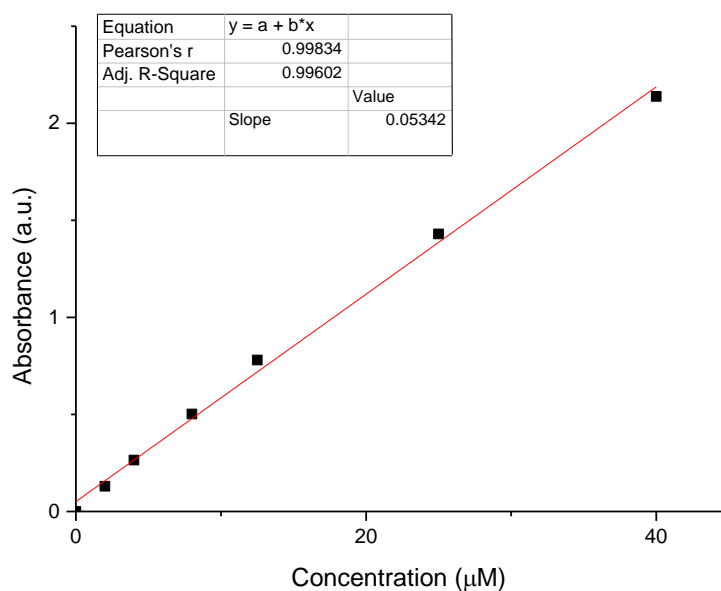
Figure 6: Data and linear fitting from the 5-FAM concentration and absorbance measured at 492 nm.

Peptides were dissolved in PBS at pH 7.4 until it was possible to measure the absorbance at 492 nm (between 0.2 and 2). The dilution involved a dilution factor which was included in the calculation of the peptide concentration.

2.3.2. Ti-6Al-4V dip coating with peptides

Ti-6Al-4V treated surfaces were dip coated with Ti-HA-pep 10 µM in PBS at pH 4. Each treated Ti-6Al-4V plate was introduced in a well of sterile 24-well plates with 1 mL of the Ti-HA-pep solution for 1 h at 21±2 °C. After 1 h the liquid was discarded from the wells. The Ti-6Al-4V plates were rinsed with dH_2O and left at 21±2 °C in air until dried for further characterisation.

2.3.3. Immersion of peptide treated surfaces in unbuffered aqueous solution, phosphate buffer saline and saturated simulated body fluid

Ti-6Al-4V chemically treated, then thermally oxidised at 500 °C (TGL-TO$_{500\ °C}$) and dip coated with Ti-HA-pep (TGL-TO$_{500\ °C}$-pep) were immersed in unbuffered aqueous soluition (aq), PBS and saturated simulated body fluid (SBF X 1.5).

The unbuffered (aq) solution was prepared with dH_2O and adjusted to pH 5 and pH 7.4 using NaOH 0.01 M, and/or HCL 0.01 M. PBS was prepared from tablets before mentioned (Section 2.2.1) and pH adjusted to pH 5 and pH 7.4. with NaOH 0.01 M and/or HCl 0.01 M. SBF X 1.5 was prepared using two solutions (cationic and anionic) reported by Demnati et al. [74], shown in Table 5.

Table 5: Salt content for SBF X 1.5.

SBF X 1.5					
Cationic solution (500 mL)			**Anionic solution (500 mL)**		
Reagents	**Amount**	**CAS No.**	**Reagent**	**Amount**	**CAS No.**
NaCl	4.01 g	7647-14-5	NaCl	4.01 g	
KCl	0.23 g	7447-40-7	Na_2SO_4	0.07 g	7757-82-6
$CaCl_2$	0.44 g	10043-52-4	K_2HPO_4 $3H_2O$	0.35 g	16788-57-1
$MgCl_2$ $6H_2O$	0.31 g	7791-18-6	HCL (1M)	19.5 mL	--
HCl (1M)	19.5 mL	--	TRIS	until pH 7.4	
Tris[*]	until pH 7.4	77-86-1	$NaHCO_3$[a]	0.35 g	144-55-8

[*]Tris: tris(hydroxymetyl)aminomethane.

[a] $NaHCO_3$: added when both solutions were mixed.

The SBF X 1.5 solution was prepared in clean glass beaker of 1,000 mL where 250 mL of dH_2O was poured, heated to 37 °C on a magnetic hot plate stirrer (IKA, Germany). Salts were introduced individually, in turn, until dissolved. Each solution (cationic and anionic) was adjusted at pH 7.4 and kept at 5 °C until used. When the two solutions were mixed, $NaHCO_3$ was added and the pH was adjusted to pH 5 and pH 7.4.

TGL-TO$_{500 °C}$ -pep samples were deposited individually in 24-well plates with 1.5 mL of the solution at each pH and it was incubated at room temperature 21±2 °C and at 37 °C in an oven (Gallenkamp, UK) for 1, 3, 6, 24, 48 and 72 h. In total 72 plates were characterized before and after the immersion.

2.4. Apatite formed via saturated simulated body fluid

TGL-TO$_{500\,°C}$ and TGL-TO$_{500\,°C}$-pep samples were immersed in SBF X 1.5 (preparation

before mentioned in Section 2.2.3) using polypropylene sterile conical base centrifugal

tubes of 50 mL volume (BD falcon^{TM}, USA). The volume of SBF X 1.5 was calculated

according Eq. 2 reported by Kokubo and Takadama [65].

$$V_s = S_a / C \qquad \text{Eq. 2}$$

Where: V_s = volume of SBF (mL)

S_a = apparent area of the immersed surface (mm^2)

C = constant of value 10 (mL / mm^2)

Samples were immersed for 1, 2, 3, 4, 5, 8 and 15 days in 10 mL of SBF X 1.5 at pH

7.4. The SBF X 1.5 solution was replaced every 2 days in the remaining samples.

Samples were taken out from the centrifugal tube and were rinsed with dH$_2$O and left

at 21±2 °C until dried. When samples were dried, they were stored in 24-well plates in

a desiccator until further analysis.

2.5. Cell adhesion test

Human osteosarcoma cell (HOS) line was obtained from the European Cell Culture

Collection (catalogue No. 87070202). Cells were maintained at 37 °C in air containing

5 % v/v CO$_2$. The liquid medium was in Dulbecco's modified eagle's medium (DMEM)

supplemented with 10 % (v/v) fetal bovine serum, 2 mM L-glutamine, 100 U/mL

penicillin, 100 µg/mL streptomycin and 1 % (v/v) non-essential amino acids. Cell cultures were confirmed free from Mycoplasma sp. contamination using the EZ-PCR mycoplasma detection kit according to the manufacturer's instructions.

Cells were sub-cultured into 24-well plates at a cell density of $2x10^4$ cells/cm^2 and left for 24 hours to attach to the test surfaces. The following day the medium was removed and the cells washed with PBS (2 mL). Cells were fixed with neutral buffered formalin pH 7.0 at room temperature (21±2 °C) for 15 min, washed with PBS (2 mL) and then finally washed with 100 % ethanol and allowed to air dry at room temperature. All samples with the immobilised cells were kept for further characterization.

2.6. *Surface characterisation*

Surface characterisation techniques used for modified surfaces are summarised in Figure 2. Metal surfaces after polishing, chemical treatment and/or thermal oxidation were characterised in dry environment by: scanning electron microscopy (SEM), X-ray diffraction (XRD), Raman spectroscopy, atomic force microscope (AFM), interferometry and X-ray photoelectron spectroscopy (XPS), and involving an aqueous media environment by: AFM - force distance curves and dynamic contact angle (DCA).

After the addition of the peptide coating the surfaces were characterised by: fluorescence microscopy, XPS, AFM-force and distance curves and DCA.

The apatite layer was characterised in dry environment by SEM, XRD, Raman and XPS. The method principles and conditions for all characterisation techniques are described below in this section.

2.6.1. Scanning electron microscopy (SEM)
Method Principle

The scanning electron microscope (SEM) is a microscope that uses electrons to produce an image. Electrons are generated, accelerated and conducted to the specimen through an arrangement of anodes, micro-scale holes and magnets that generate a focused electron beam that hits the specimen, a SEM equipment diagram is shown in Figure 7. As a result, signals from the specimen such as Auger electrons (AE), secondary electrons (SE), back scattered electrons (BSE) among others are produced. The images in SEM are formed by the detection of SE which are converted to an image in the screen. The scanning is performed from left to right and top to bottom until the area is covered producing a micrograph.
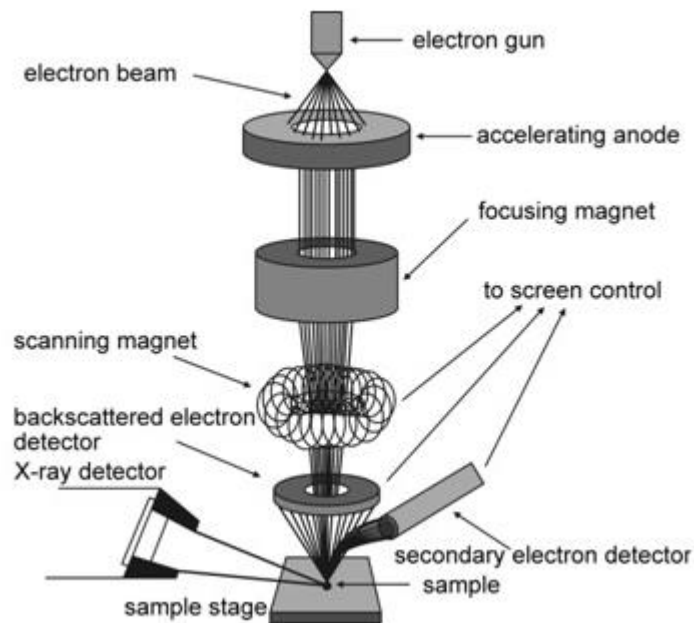
Figure 7: SEM schematic [75].

Experimental

SEM micrographs were obtained using JSM-7000F SEM (JEOL, Japan) using an electron voltage of 20 kV. Micrographs were imaged at different magnitudes. Analysed samples were immobilised in aluminium stubs with carbon conductive adhesive tabs. Samples which presented non-metallic surfaces, such as the apatite coating and surfaces with immobilised cells, were gold coated using a SC7640 sputter coater (Polaron, UK).

2.6.2. X-ray diffraction (XRD)
Method principle

The crystalline structure of solids can diffract X-rays due to the similar size of the wavelength and the spacing between atoms in a crystal (≈ 1 Å). When X-rays reflect on the material at certain angle (θ) some of the X-rays scatter from atoms close to the surface and others scatter from atoms deeper than the surface atoms in a solid arrangement of atoms. This diffracted X-rays produce a constructive interference that satisfies Bragg's law, shown in Figure 8. This law relates the wave length (λ) to the incident angle and the spacing lattice of the crystal sample.
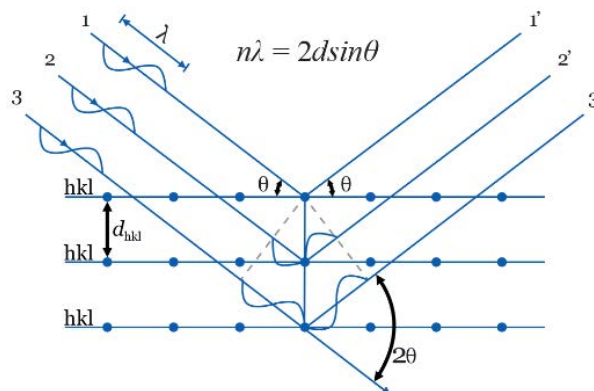
Figure 8: Diagram depicting Bragg's law for X-ray diffraction in solids. "Adapted from reference [76]".

23

Incident X-rays are generated by a cathode X-ray that hit the sample at certain angle (θ) producing the reflected X-rays which are detected and processed, a XRD diagram is shown in Figure 9. The scan is perfomed for various 2θ generating a pattern (difractogram). The diffraction peaks are then typically identified by referencing a pre-existing database.
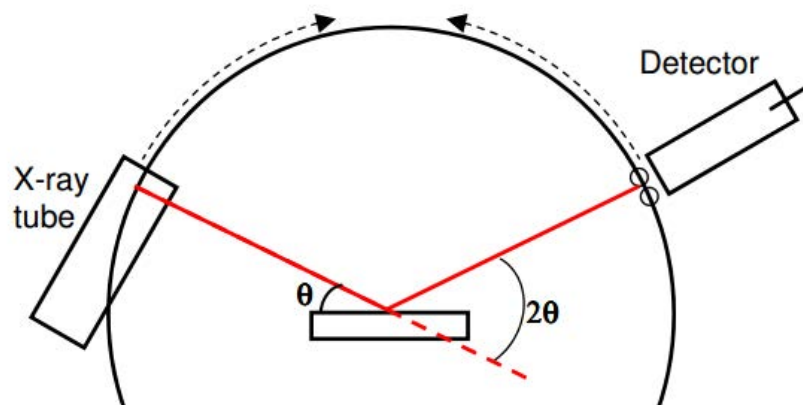
Figure 9: XRD schematic. "Adapted from reference [77] ".

Experimental

XRD diffractograms were obtained using a D8 Advance XRD (Bruker, Germany) with Bragg Brentano mode at 2θ between 20-60 ° analysed using a step size of 0.02 ° (integration time, 10 s/step). The X-rays were generated by a copper tube ($λ = 0.15418$ nm). The obtained data were analysed using Match software (Crystal Impact, Germany).

2.6.3. *Raman spectroscopy*
Method principle

Raman spectroscopy is a technique used to identify molecules through the inelastic scattering of photons. After the photon interaction with the molecule, a rotational or vibrational state of the molecule can be detected by the change of the energy between the scattered photon and the incoming photon. This photon energy difference is known as inelastic or Raman scattering. Photons that present the same incoming energy, which are the great majority after the scattering, are known as elastic or Rayleigh scattering. Both Raman and Rayleigh scattering are shown in Figure 10.
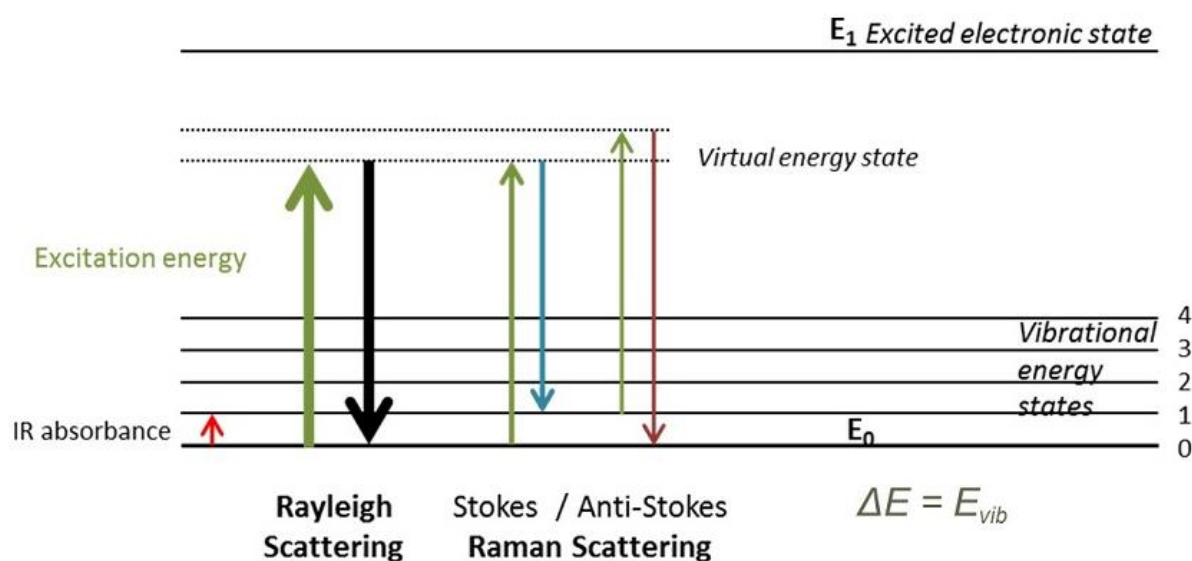
Figure 10: Rayleigh and Raman photon scattering [78].

The photon source for Raman spectroscopy is commonly a monochromatic laser that illuminates the sample. The electromagnetic radiation from the illuminated spot is collected and filtered from the elastic scattering photons. The remaining collected

radiation is dispersed in a detector and recorder for analysis, a diagram of Raman spectroscopy is shown in Figure 11. The obtained spectrum is processed using a database or compared against a spectrum obtained using a high purity sample.
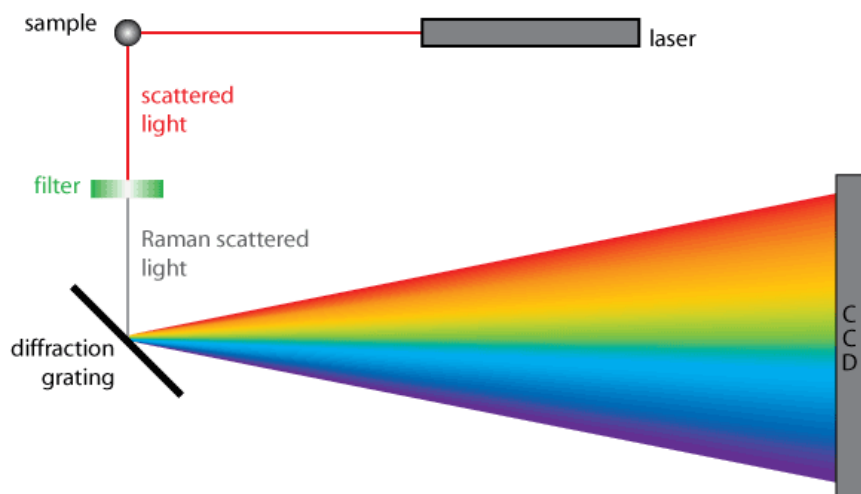
Figure 11: Raman spectroscopy schematic [78].

Experimental

Raman spectra were obtained using a LabRAM HR 800 Raman microscope (Horiba Jobin Yvon, Japan) using a laser source of wavelength 532 nm (green). The analysed areas were 60 μm X 70 μm and the data was acquired for 45 s (in 3 different areas). The data was analysed by LabSpec 5 software (Horiba, Japan).

2.6.4. Atomic force microscope (AFM)

AFM is a technique used to measure surface structures (imaging) at the nano- and microscale, and intramolecular forces (force-distance curves). Both modes of analysis were used in this study and are explained below:

26

2.6.4.1.   *Imaging*

Method principle

The AFM image is obtained by the measurement of small forces between the atoms or molecules of the measurement material (cantilever) and the interested surface material when are close enough to detected them. A cantilever is fixed at one end, and remains free in the other to interact with the surface. When the flexible cantilever is close enough to the surface of interest, repulsion and attraction forces can be measured by the deflection of the cantilever, shown in Figure 12.
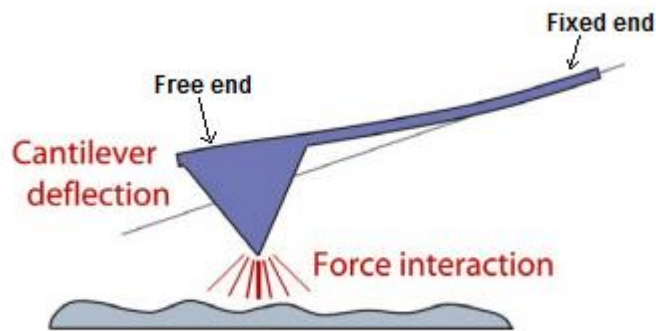
Figure 12: Deflection of the cantilever due to a force detection. " Adapted from reference [79] ".

The deflection of the cantilever is detected by a laser beam that reflects from the cantilever onto a position-sensitive photodetector. Thus, when the cantilever deflection changes from the initial position, the angle of the reflected laser beam changes, and the reflected spot on the photodetector moves from the initial position; the effect is represented in Figure 13. The cantilever typically scans a sample 'book-wise', from left to right, line-by-line, and gradually moving from the top to the bottom of a scan window.

An image from the deflection of the cantilever as a function of position across the sample.
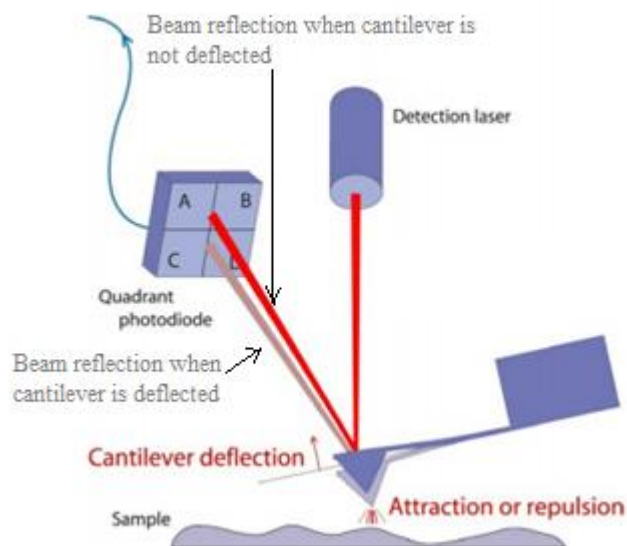
Figure 13: Diagram of the detection of the cantilever deflection in AFM. "Adapted from reference [79] ".

Experimental

Images were obtained using a NanoWizard II AFM (JPK instruments, UK) operating in intermittent contact mode at 18 °C and a relative humidity of < 40 %. Rectangular pyramidal-tipped Si cantilevers (PPP-NCL, Windsor Scientific, UK) were employed (nominal length and width were 225 μm and 38 μm respectively; their nominal tip diameter was <10 nm). The nominal frequency of the first resonant mode was 190 kHz. A tip velocity of 10 μm/s was employed when scanning across the sample surface. Each image was composed of 512 x 512 pixels, and took approximately 20 min to acquire. Images were analysed using JPK Data Processing software (JPK Instruments, UK) and Scanning Probe Image Processor software (Image Metrology, Denmark).

2.6.4.2.   Force- distance curve
Method principle

The AFM force -distance curves are obtained by the deflection of the cantilever and in

this mode the cantilever is used as a spring. From Hooke's law in Eq. 3.

$$F = -kx \qquad \text{Eq. 3}$$

Where: F = force (N)

   k = spring constant (N/m)

   x = length of extension/compression (m)

The restoring force of a spring is proportional to the deforming distance of the spring,

effect shown in a spring and in a cantilever in Figure 14.
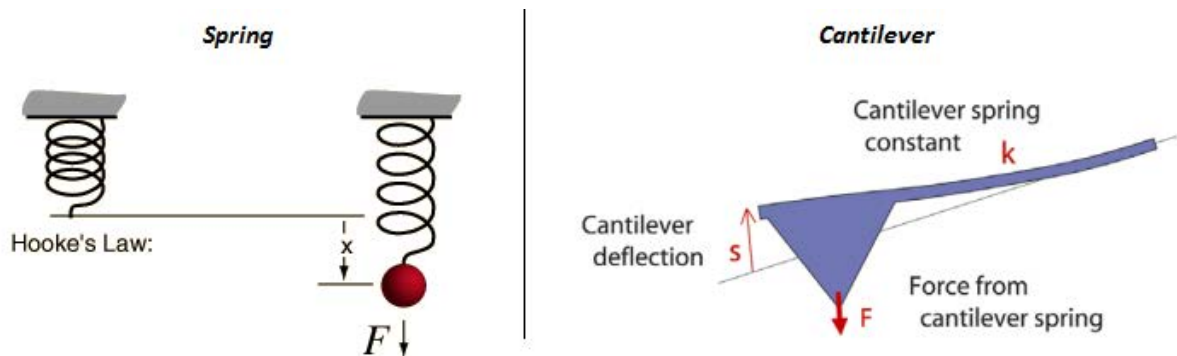
Figure 14: Hooke's law applied to a spring and a cantilever. "Adapted from references [80] and [81] ".

The AFM force - distance curves from the cantilever deformation are recorded when the cantilever is approaching and retracting from the surface of interest. The curves and the sequence steps of the deflection are shown in the Figure 15.

1. Approach of the cantilever to the surface (non-contact)

2. Jump to force when the cantilever starts the contact with the surface

3. Contact of the cantilever with the surface in the approach and retract curve

4. Cantilever maintains in contact with the surface due to the adhesive forces between the cantilever and the surface

5. The cantilever is pulled away from the surface.
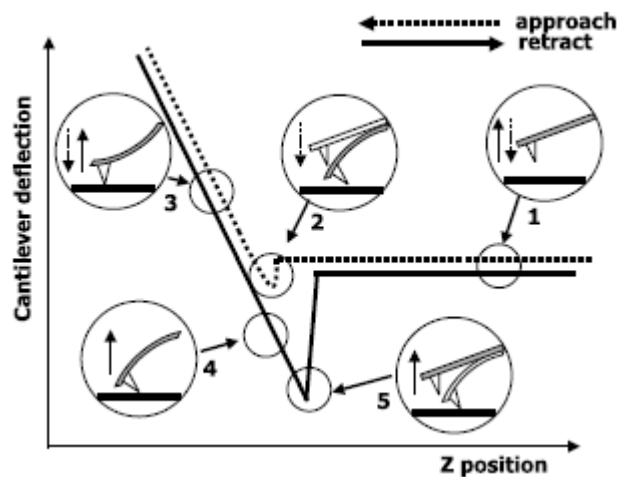
Figure 15: Diagram of the force distance curves in the AFM [82].

Measured forces are shown in Figure 16. Out-of-contact repulsion force (F_{rep}) is measured in the first peak from right to left of the approaching curve, the height of the triangle that is formed in the peak from the origin to the highest part of the peak until the signal is stable in the approach curve is measured as the force. The jump to force

(F_{JT}) is measured in the minimum point of the approach curve and the pull-off force (F_{PO}) is measured in the minimum point of the retract curve. The pull-off energy (W_{PO}) is calculated from the area under the retract curve.
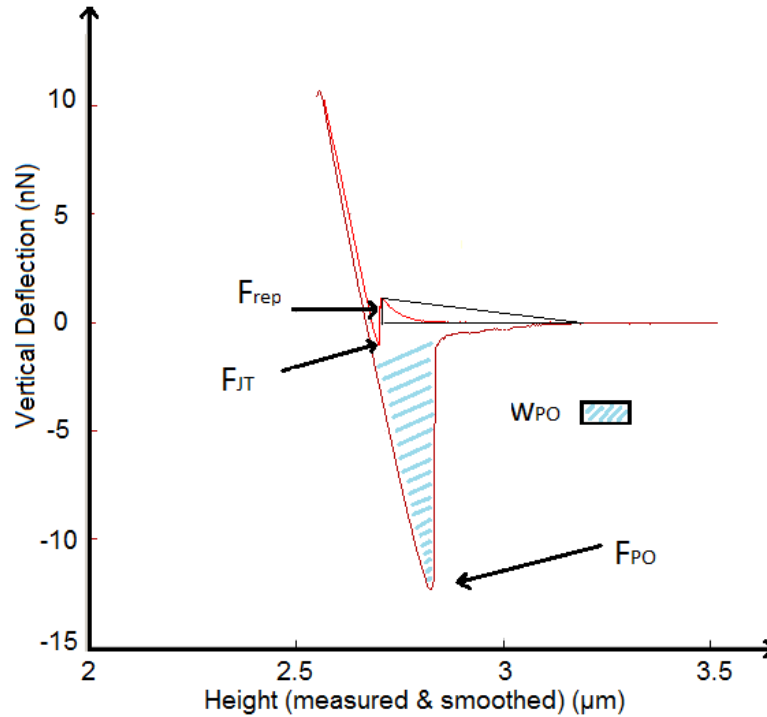
Figure 16: Measured forces in the force distance curves obtained by AFM.

Experimental

Acquisition of adhesion data was performed using a NanoWizard II AFM (JPK Instruments, UK) employing a CellHesion module (JPK Instruments, UK), operating in force spectroscopy mode at 18 °C. The sample and cantilever were immersed in acidic and alkaline, using dH_2O and pH adjusted with NaOH 0.01 M and HCl 0.01 M at pH 3, 5, 7 and 9, contained within a clean glass Petri dish. Samples were immobilised using double-sided Shintron adhesive tape (Agar Scientific, UK).

Rectangular Si cantilevers with hemispherical-tips (SD-Sphere-CONT-M-10, NanoWorld, Switzerland) were employed (nominal length and width were 450 µm and 50 µm respectively; nominal tip diameter was 2 µm). Their nominal spring constants were 0.2 N/m, and were calibrated according to the method reported by Bowen *et al.*[83]

The laser beam was positioned onto the cantilever, followed by thermal equilibration, typicallyfor around 10-15 min, until the vertical deflection signal was constant. Data were acquired by driving the fixed end of the cantilever at a velocity of 3 µm/s towards the sample surface, whilst monitoring the deflection of the free end of the cantilever. A maximum compressive load of 20 nN was applied to the surface during data acquisition. Vertical deflection and z-axis displacement data were recorded at a frequency of 10 kHz. A grid of 100 force-displacement curves were acquired for each sample/liquid combination, equally spaced over an area of 100 µm x 100 µm. Force-displacement data were analysed using JPK Data Processing software (JPK Instruments, UK).

2.6.5. *White Light Interferometer*
Method principle
The white light interferometer measures the difference of surface structure between the reference surface and the test surface. The interferometry components are the light source, the beamsplitter, the reference and the test surface. The beam light is split in two beams of the same frequency and travel in different paths, one interacts with the reference surface and the other with the test surface. When both beams recombine, a constructive or destructive interference takes place creating a fringe patter (bright fringe is constructive and dark fringe is destructive), shown in Figure 17. Pattern differences are associated with the difference in the path length which are associated

with the differences of the surface morphology (tilt and shape) between the reference and the test surface.
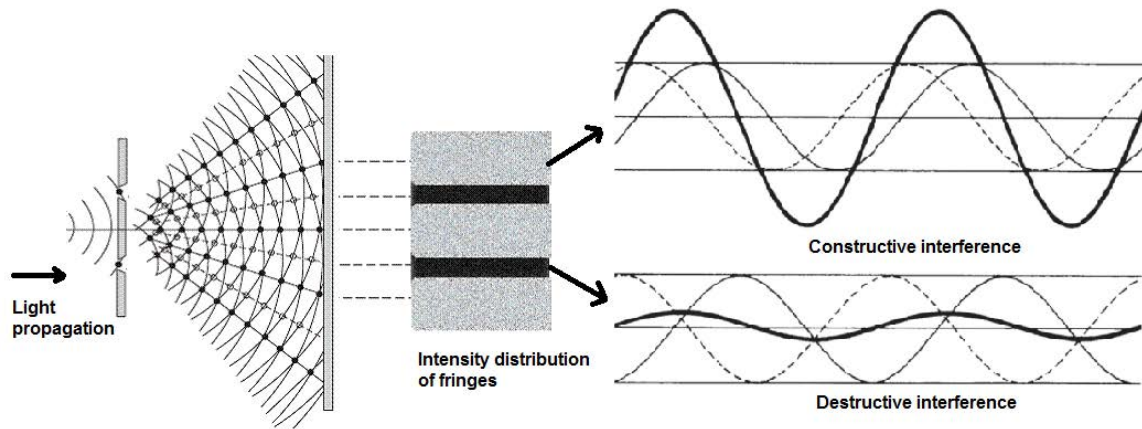
Figure 17: Fringe pattern from constructive and destructive interference. "Adapted from references [84] and [85] ".

The combined techniques of the microscope together with the interferometry, shown in Figure 18, provide detailed information about the areal topography with different textures on the surface.
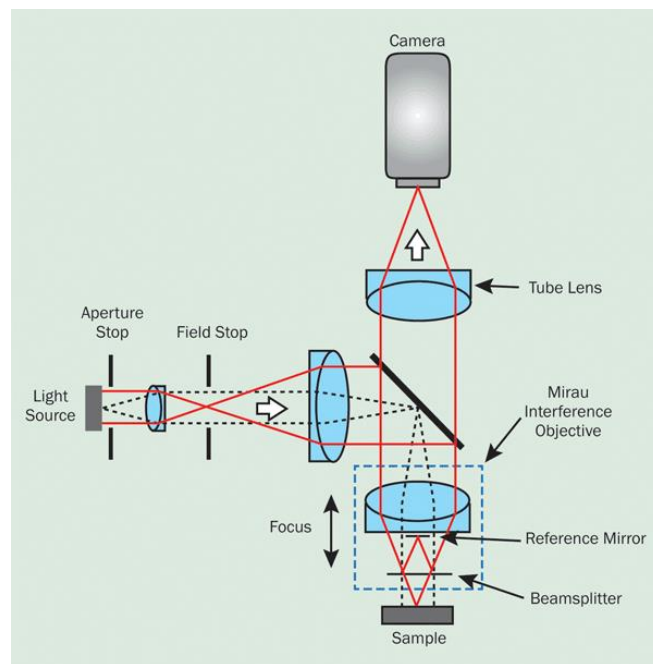
Figure 18: Interferometry microscope schematic [86].

Experimental

Images were obtained using a MicroXAM interferometer (Omniscan, UK) and white optical light was used. Regions of dimensions 432 x 321 µm were analysed. Six regions were recorded per sample in non-overlapping areas. Scanning Probe Image Processor software (Image Metrology, Denmark) was employed for image analysis, providing 3D rendering of the surface topography of the surface, and statistical analysis of surface roughness

2.6.6. X-ray photoelectron spectroscopy (XPS)
Method principle

X-ray photoelectron spectroscopy (XPS) is a technique used to identify the elements and the chemical state of the elements on the surface. The ejection of the core electrons from the surface is performed when photons of large energy (X-rays) are

absorbed by the system (under high vacuum or ultra-high vacuum), shown in Figure

19 .
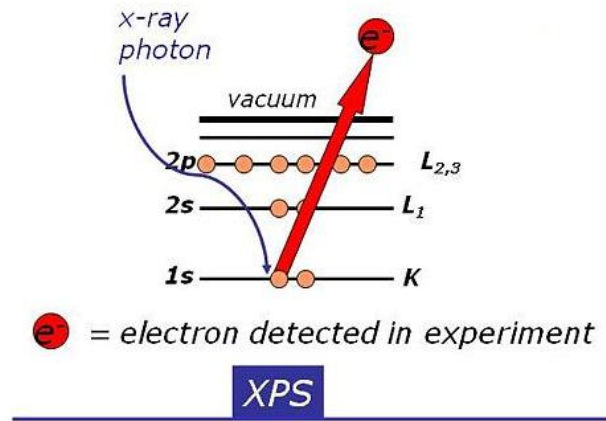
Figure 19: XPS diagram of the core ejection electron by X-ray photon. "Adapted from reference [87] ".

In XPS the kinetic energy of the ejected electron ($E_{kinetic}$) is obtained and the binding

energy of the ejected electron ($E_{binding}$) can be calculated from Eq. 4.

$$E_{binding} = E_{photon} - (E_{kinetic} + \emptyset) \qquad \text{Eq. 4}$$

Where: $E_{binding}$= binding energy of the ejected electron (eV)

E_{photon} = binding energy of the X-ray photon

$E_{kinetic}$= kinetic energy of the ejected electron

$\emptyset$= workfunction is a value that dependence of the material and the spectrophotometer.

The binding energies of the ejected core electrons are related to the elements and therefore it is possible to obtain information about the surface chemistry.

The XPS principal components are shown in Figure 20. Mainly composed by the photon source, electron lenses, analyser for the kinetics energies and the detector that count the electrons. The obtained information is in the form of a spectrum.
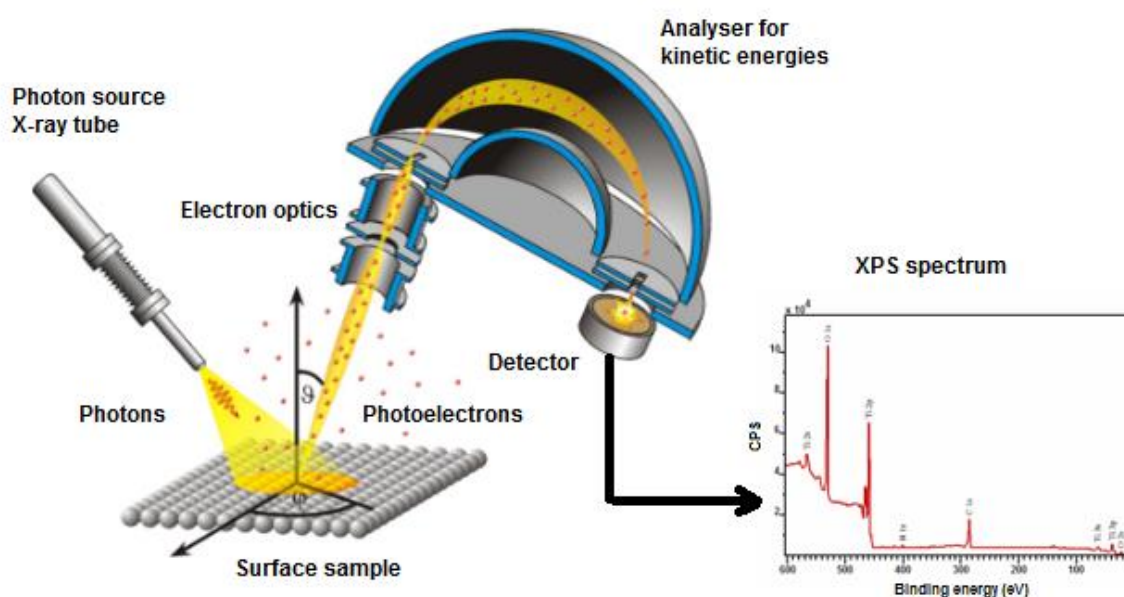
Figure 20: XPS schematic. " Adapted from reference [88]".

Experimental

The composition and titanium oxidation states of the surface was investigated using X-ray photoelectron spectroscopy (XPS). Analysis was performed using a κ-alpha X-ray Photoelectron Spectrometer (Thermo Fisher Scientific, UK), operating a microfused, monochromated Al κα X-ray source with a spot size of 400 μm and a power of 36 W. The step size in order to obtain individual peaks was 0.1 eV, whereas 0.4 eV was used for the acquisition of a full spectrum between 1349.2 eV and -10.8 eV binding energies

(BEs). The vacuum pressure in the analysis chamber was < 10^{-9} mbar. Three non-overlapping regions were measured for each sample. Data were fitted using the Gauss-Lorentz function method was used for background subtraction. CasaXPS software was used for data processing.

2.6.7. Fluorescence microscope
Method principle

The fluorescence microscope is used to produce images that contain fluorophores. A fluorophore can emit light after an excitation with a different wave length, 5-FAM excitation and emission wavelengths are shown in Figure 21.
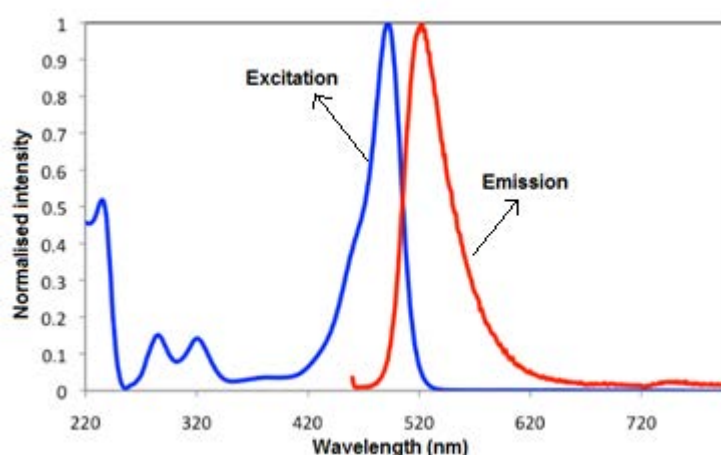
Figure 21: Excitation and emission of 5-FAM fluorophore [89].

The fluorescence microscope has a light source that is filtered according to the excitation wavelength and it is directed to the sample that excites and emits with a different wavelength. A combination of the emitted and the illuminated light is obtained from the sample but the illuminated light is filtered before reaching the detector allowing only the detection of the emitted light. A schematic of a fluorescence microscope is

shown in Figure 22. The emitted light from the sample is processed and a fluorescence image is obtained.
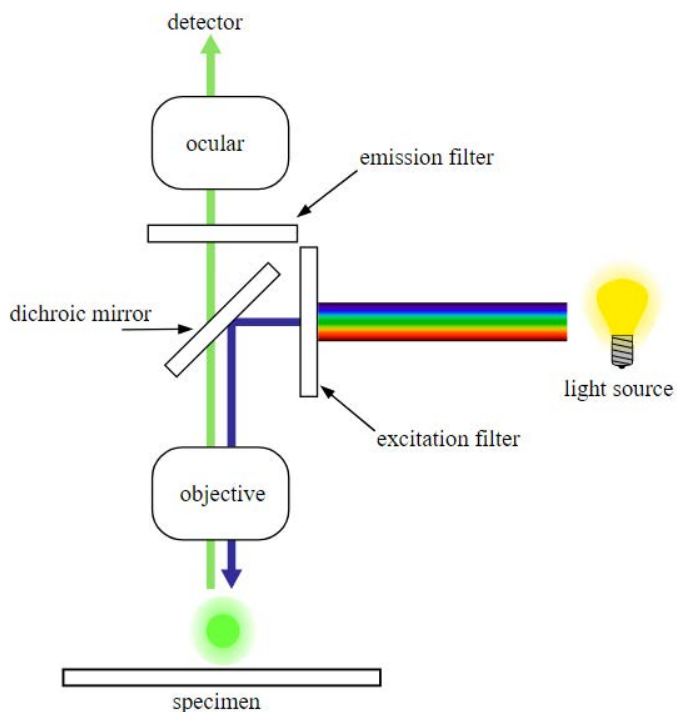
Figure 22: Fluorescence microscope schematic [90].

Experimental

Images were obtained using a DM6000 Leica microscope (Leica, Germany). A blue filter (excitation range 450-495 nm) was used due to the fact that the maximum excitation of 5-FAM is at 495 nm. The emission of 5–FAM is at 519 nm. Imaged areas were of 1280 μm X 957 μm and the exposure time was 1 s. Three non-overlapping areas of each sample were acquired. Images fluorescence intensity were measured by ImageJ software (NIH, USA).

2.6.8. Dynamic contact angle titration
Method principle

The contact angle technique gives information about the wettability of a solid when a liquid drop is in contact with the surface. A liquid vapour interface is found when a drop is deposited on a solid, the schema of the liquid droplet and the interfaces with the vapour (V), solid (S) and liquid (L) phases are shown in Figure 23.
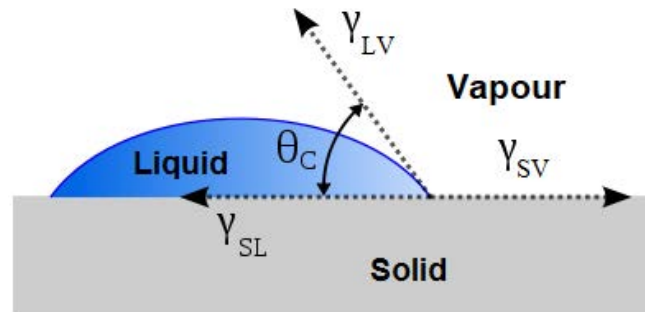
Figure 23: Schematic of a liquid drop on a solid surface." Adapted from reference [91]".

The equation that relates the interfaces of the three phases when a liquid drop is on a surface is Young's equation (Eq. 5)

$$\gamma_{SV} - \gamma_{SL} = \gamma_{LV} \, \cos \theta_C \qquad \text{Eq. 5}$$

The dynamic contact angle (DCA) is a measurement where the boundaries of the three phases are moving, that can be obtained by the change of drop volume, method shown in Figure 24. Advancing contact angle (maximum value in the static contact angle) and receding contact angle (minimum value in the static contact angle) can be measured using the dynamic contact angle. The difference between the advancing and receding contact angle results in the contact angle hysteresis that is related to the topography and chemical differences of the surface.
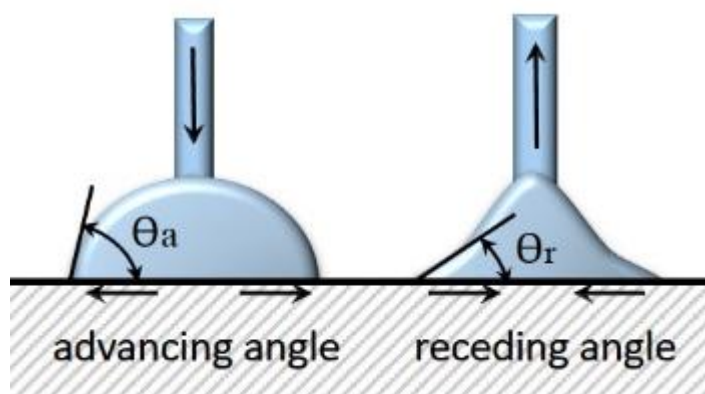
Figure 24: Dynamic contact angle by drop volume changes (advancing and receding angles). " Adapted from reference [92]".

The contact angle titration at different pH according with the literature suggests that γ_{SV} and γ_{LV} present small variation [93] and therefore the information obtained by the titration can be attributed by the γ_{SL} predominant by the ionization of flat solid surfaces.

Experimental

DCA data was obtained using a Theta OneAttension optical tensiometer (Biolin Scientific, Sweden). Contact angle data was measured in triplicate (3 different samples) with acidic and alkaline solutions, using dH_2O and pH adjusted with NaOH 0.01 M and HCl 0.01 M at pH 3, 5, 7 and 9. The drop size was 2 µL and the rate of volume change was 0.5 µL/s. Data was analysed with a curve Young-Laplace fitting, using OneAttension software (Biolin Scientific, Sweden).

Chapter 3

Titanium oxide formed by thermal oxidation of polished Ti-6Al-4V and H_2O_2 /HCl chemically treated followed by thermal oxidation of polished Ti-6Al-4V to induce bioactivity

3.1. Introduction

Ti-6Al-4V is widely used in orthopaedics and dental fields because its desirable properties such as good strength, toughness, low density, good corrosion resistance and Young's modulus closer to bone compared with other metal alloys [94–96]. In addition, TiO_x forms on the surface confer bioactive to Ti-6Al-4V [97,98]. This bioactive property is attributed to the amphoteric behaviour of TiO_2 in aqueous solution that leads to the surface adsorption of ions present in physiological media, such as Ca^{2+} and PO_4^{3-} [99–101], promoting bonelike apatite formation [102], inducing cell adhesion, proliferation and maturation [101,103].

3.1.1. Titanium surface modifications

Mechanical, chemical, physical and biochemical methods are widely used to increase bioactivity in TiO_x surfaces [72,99,104,105]. These modifications change the initial surface properties of TiO_x layer including composition, topography and roughness [1]. Both chemical treatment with H_2O_2 /HCl [42,49,106,107] and thermal oxidation (TO) [41–45] are widely used to increase the bioactivity of Ti implant surfaces.

The composition of the native TiO_x surface is primarily TiO_2 in amorphous phase [108,109] but it has been shown that crystal phases (anatase and rutile) on the surface present more bioactivity than only amorphous phase [44,68,110] and therefore these phases are more desirable. A method commonly used for the crystallisation of amorphous TiO_2 is thermal oxidation. During this method, the crystal phase formation is highly dependent on the temperature, and in Figure 25 the phase diagram of TiO_2 [111] is shown. In

addition, according with the literature the TiO_2 layer formed below 500 °C presents amorphous and anatase phases [49,112], at 550 °C presents rutile and anatase phases [51,112,113] and above 800 °C presents rutile phase [4,51]. Therefore, both anatase and rutile TiO_2 phases can be obtained by thermal oxidation.
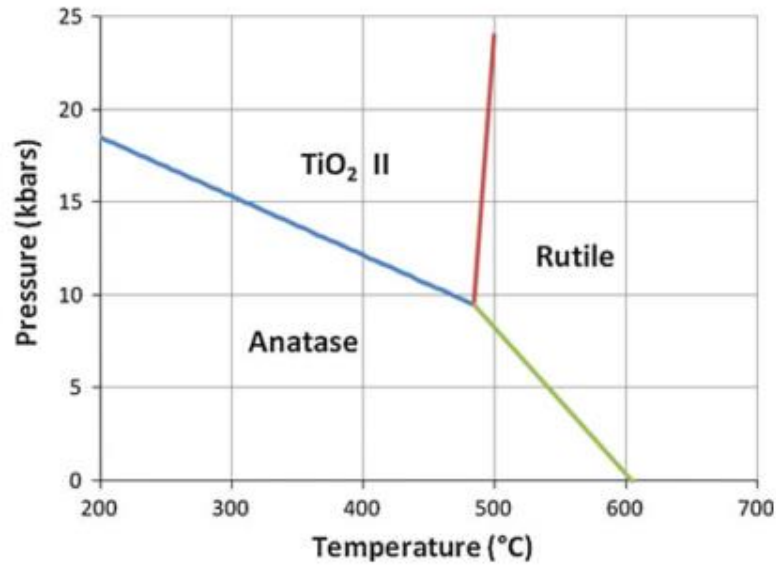
Figure 25: Phase transformation of TiO_2 crystals [111].

Chemical surface modifications are performed on Ti alloy surfaces to change their topography, composition, and charge density [13,112,114,115]. One approach to modify these surfaces chemically is to use H_2O_2 in aqueous solution. This modification produces a titania gel layer (TGL) rich in OH^- with nano and micro porosity [1,49] desirable for the adsorption of ions, peptides, and proteins, and the promotion of cell adhesion [54,103,116]. The bioactivity of TGL formed on Ti surfaces was shown by Wang *et al.* [49] and by Lee *et al.* [117].

The nano- and micro-topography of a surface can generally influence and enable cell adhesion and proliferation, synthesis of proteins, formation of the extracellular matrix (ECM), mineralization of ECM, cell maturation and bone formation [118]. It has been reported, that TiO_x surface modifications with granular and/or porous textures below cell size, can positively influence cell adhesion [14,119,120]. In addition, rough surfaces lead to the formation and deposition of hydroxyapatite that intervene as anchorage for collagenous fibres produced by bone cells or osteoblasts [101]. Deligianni *et al.* [121] studied the interaction between human bone marrow cells and Ti-6Al-4V surfaces of different roughness and noticed that rougher surfaces present better interaction with the serum protein and fibronectin which are responsible for the binding of ECM components such as collagen, compared with smoother surfaces.

3.1.2. Adsorption of biomolecules on titanium oxide

As mentioned above, TiO_2 exhibits amphoteric behaviour in aqueous solutions leading to ion adsorption as well as adsorption of proteins and peptides in aqueous solution [122,123]. Specifically, adsorption of small peptides on TiO_2 surfaces is very useful for applications such as biocompatibility [124], drug delivery, biosensing and diagnostics [125] which are desirable for dental and orthopaedic fields. Recent studies on how phage interact with TiO_2 surfaces showed that a hexapeptide sequence RKLPDA has high electrostatic affinity with TiO_2 [40,126–128].

Biomolecules can interact in the nucleation, crystallization and composition of inorganic crystals [129] found in biological systems such as bone, teeth and shell [130]. Some small domains of proteins present the repetition of amino acids which are associated with the nucleation of these inorganic crystals [129]. For example, in bone sialoprotein (BSP) continuous small domains of polyglutamic acid are found to be

involved in the nucleation of hydroxyapatite (HA) [131]. Considering the behaviour of the polyglutamic acid domain for the nucleation of HA and the electrostatic interaction of Ti binders with TiOx surfaces, a peptide sequence that includes both active motifs was designed to be used in this study.

3.2. Objective

The aim of this part of the project was to develop different surfaces in composition, roughness and topography to understand how these factors can influence the adsorption of ionic peptides on Ti-6Al-4V surfaces. Two main modifications were performed on polished Ti-6Al-4V. Thermal oxidation (TO) at 500, 600, 700, and 800 °C and chemical modification by H_2O_2 /HCl followed by thermal oxidation (TGL-TO) at 500, 600, 700 and 800 °C. Both techniques were shown by literature to increase the adsorption of biological material such as proteins and peptides on TiOx surfaces. However it is not yet reported how the surface variations can affect the adsorption of ionic peptides and therefore the characterization of the surfaces will help to understand which factors have more influence in the peptide adsorption.

3.3. Topography and composition of native titanium oxide from polished Ti-6Al-4V and titanium oxides formed by thermal oxidation on polished Ti-6Al-4V

3.3.1. Specific objective

The objective of this section was to evaluate the topography and composition of the native Ti-6Al-4V and the modified Ti-6Al-4V surfaces by TO at different temperatures to understand how the changes can influence the ionic peptide adsorption. In addition, the biocompatibility of the above mentioned surfaces was assessed to show how the modifications affect the cellular adhesion on the surfaces.

3.3.2. Results

TiO$_x$ obtained after polishing and thermal treatment were characterized to identify and, where possible, quantify surface topography and roughness, surface crystal phases, and surface chemical composition. The TiO$_x$ analysed was:

1) Native TiO$_x$ on polished Ti-6Al-4V (MPT).

2) Polished Ti-6Al-4V thermally oxidised for 1 h in air at 500, 600, 700 and 800 °C (TO$_{500-800\,°C}$).

Adhesion cell test was performed on all surfaces with osteoblast- like cells human osteosarcoma (HOS) to evaluate biocompatibility.

3.3.2.1. Topography and composition of native titanium oxide from polished Ti-6Al-4V

3.3.2.1.1. Surface Topography of native titanium oxide from polished Ti-6Al-4V

Ti-6Al-4V plates were mechanically polished on one face until a mirror-like finish was achieved. Scanning electron microscopy (SEM) and force microscopy (AFM) were used to characterize the surface topography.

A SEM micrograph of MPT surface is shown in Figure 26a. The micrograph shows two colour contrasts suggesting differences in electron reflectivity, and hence composition of the surface. To further visualize any difference in topography AFM analysis was performed. Figure 26b shows the AFM image with distinct heights. The measurement of the surface average roughness (R$_a$) is 0.7 nm and the root mean square (R$_q$) is 2.1 nm.
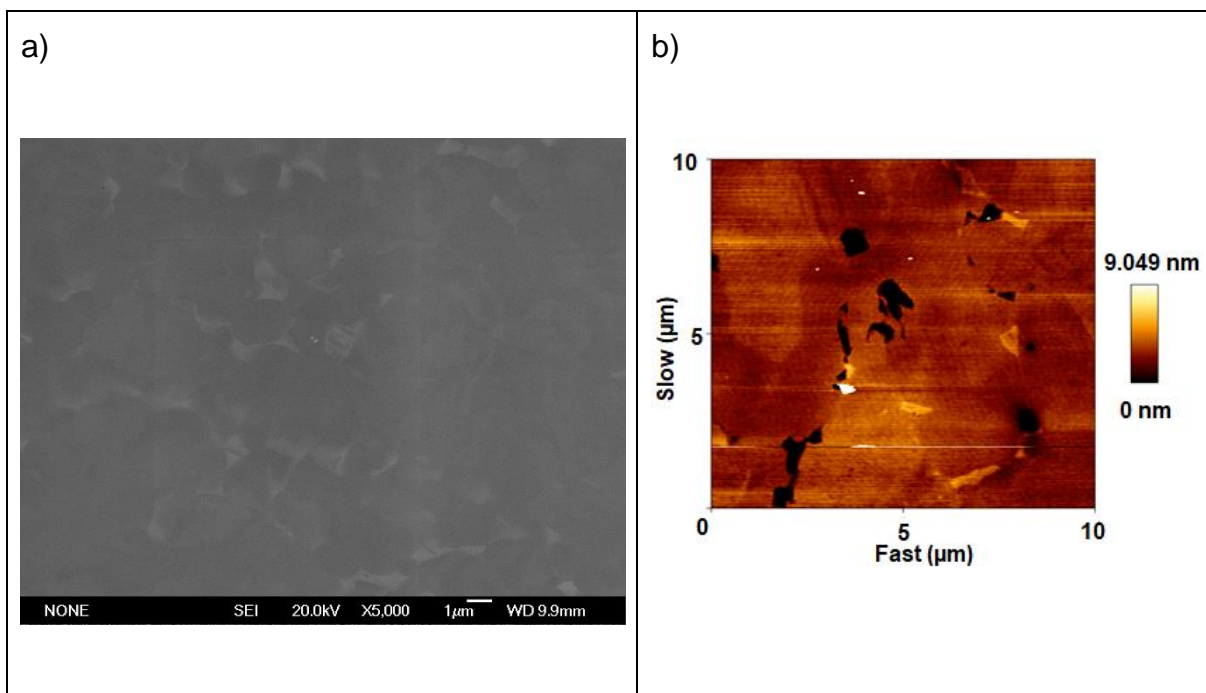
Figure 26: Topography of MPT surfaces by a) SEM micrograph and b) AFM image (10 x 10 μm).

3.3.2.1.2. Surface crystal phases and chemistry composition of native titanium oxide from polished Ti-6Al-4V

X-ray diffraction (XRD) was used to analyse the surface crystal phase composition, and X-ray photoelectron spectroscopy (XPS) was used to analyse the chemical composition of the surface.

The XRD diffractograms of MPT surface is shown in Figure 27. The α Ti (JCPDS No. 44-1294) and β Ti (JCPDS No. 44-1288) patterns are also shown in Figure 27. The diffractogram exhibits four peaks at 35.42, 38.54, 40.44 and 53.26° matched with α Ti. β Ti pattern is showed for comparison.
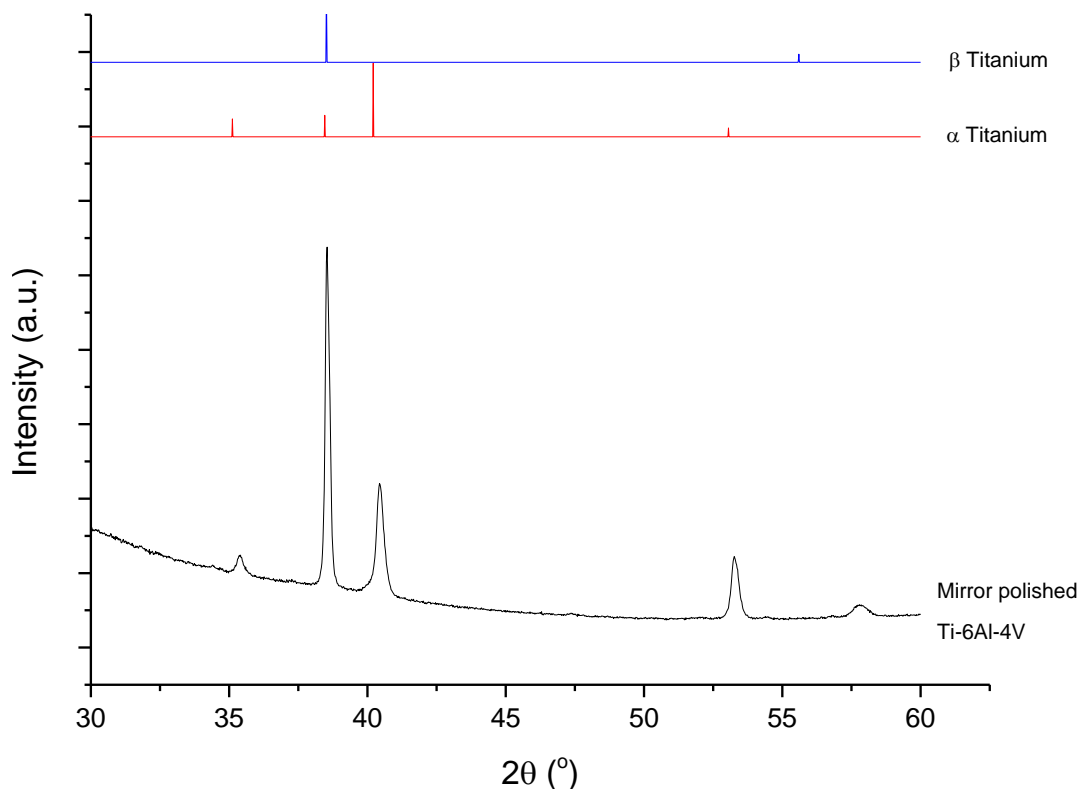
Figure 27: XRD diffractogram of MPT, α Ti (JCPDS No. 44-1294) and β Ti (JCPDS No. 44-1288).

Chemical elements quantified by XPS are shown in Figure 28 and the percentage composition is presented in Table 6. The main sharp intensity peaks indicate the presence of O at 530 eV, C at 284 eV and Ti at 458 eV. Other peaks also present are associated to V at 515 eV and Al at 118 eV as would be expected from the alloy. On top of this, other elements are detected in small amounts such as N at 400 eV, P at 190 eV, and Si 153 eV that can be present in the residual elements unmentioned in the manufacturer's data certificate (Appendix 1).
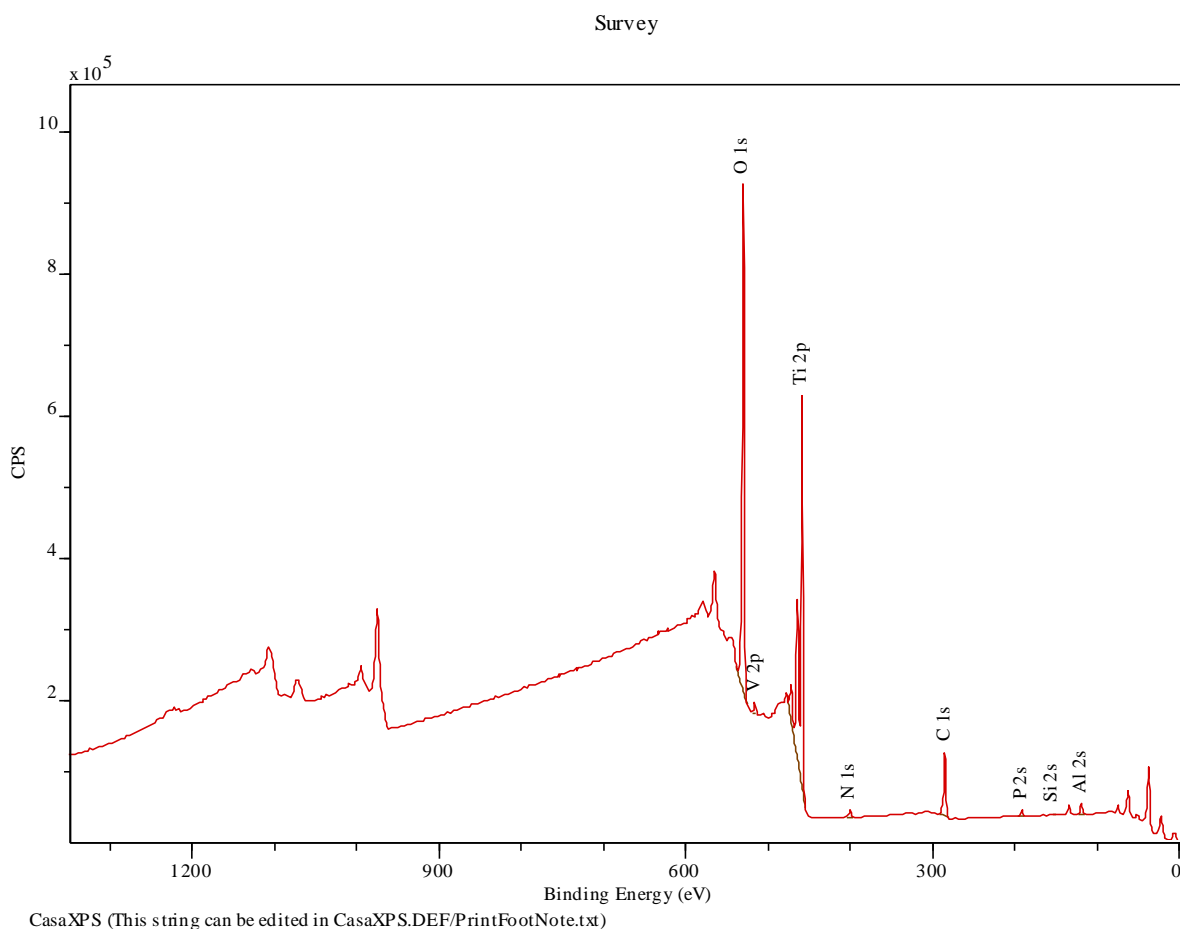
Figure 28: XPS survey of MPT surface with identified chemical elements.

Table 6: Chemical elements percentage of the MPT surface analysed by XPS.

Element	O %	V %	C%	Ti %	N %	Al%	*Other %
	53.5	0.2	19.3	19.2	0.6	4.1	3.1

*Other includes P, Si Na and K

The XPS Ti 2p spectrum of the MPT surface is shown in Figure 29. The presence of three peaks in the Ti 2p spectrum is the contribution of Ti and its oxidation states forming the metal / oxide Ti system on the MPT surface. The binding energy of the 2p orbital is divided in $2p_{1/2}$ and $2p_{3/2}$ for each oxidation state. The Ti 2p spectrum shown after deconvolution in Figure 29 below, exhibits 2p doublets associated with Ti (0), Ti (II), Ti (III) and Ti (IV). The metal/oxide systems for Al and V were not detected.

48
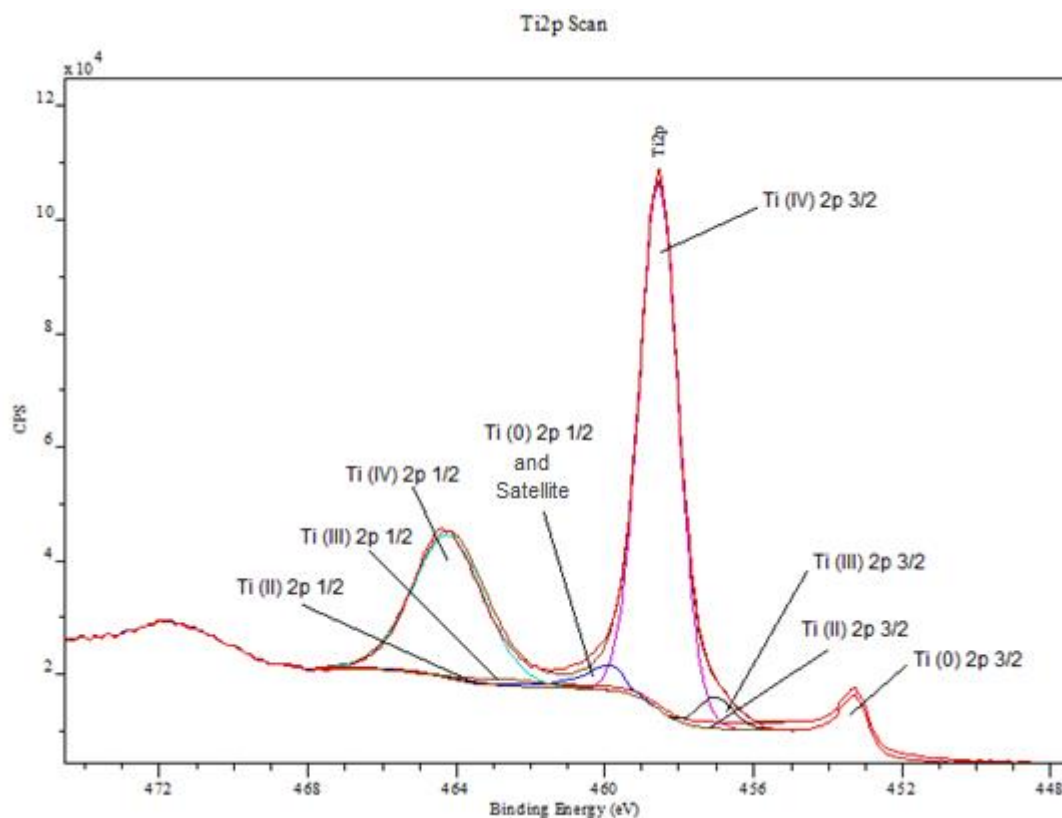
Figure 29: XPS spectrum of Ti 2p for MPT surface.

The dominant oxidation state of the MPT surface according to the Ti 2p spectrum is Ti (IV). The deconvoluted Ti 2p shows Ti (IV) $2p_{1/2}$ and Ti (IV) $2p_{3/2}$ in the binding energies 464.3 eV and 458.6 eV respectively. Ti (0) $2p_{3/2}$ is at the binding energy 453.8 eV and Ti (0) $2p_{1/2}$ is overlapped at 459.9 eV. Ti oxidation states Ti (II) and Ti (III) are present in small proportion. The percentage contribution of each Ti oxidation state of the MPT surface is shown in Table 7 together with the binding energies corresponding to each 2p Ti doublet. In addition, the deconvoluted peak around 460 eV is due to Ti (0) $2p_{1/2}$ and a satellite peak.

Table 7: Ti $2p_{3/2}$ and Ti $2p_{1/2}$ binding energies according to the literature [132] and percentage contribution of each Ti oxidation state for the MPT surface.

Compound	Ti $2p_{3/2}$ (eV)	Ti $2p_{3/2}$(%)*	Ti $2p_{1/2}$ (eV)	Ti $2p_{1/2}$(%)*
Ti	453.86	7.1	459.99	3.5+
Ti (II)	455.34	0.0	461.07	0.0
Ti (III)	457.13	3.4	462.73	1.7
Ti (IV)	458.66	56.2	464.32	28.1

*Ti $2p_{3/2}$ (%) and Ti $2p_{1/2}$ (%) are the percentages of Ti2p deconvoluted peak

+ Percentage of Ti (0) $2p_{1/2}$ and satellite peak.

3.3.2.1.3. Cellular adhesion on native titanium oxide from polished Ti-6Al-4V

SEM micrograph of adhered human osteosarcoma cells (HOS) on MPT surface is shown Figure 30a. The high resolution SEM micrograph is shown in Figure 30b. Cells exhibit round and flatted morphologies indicated by arrows on the MPT surface. The attachment of cells on MPT surfaces are combined, some cells present filopodia attachment represented by finger-like protrusions and other cells present lamellipodium attachment represented by uniform elongation of cell edges on the surface in form of mesh [69], both types of attachment are shown and labelled in Figure 30b.
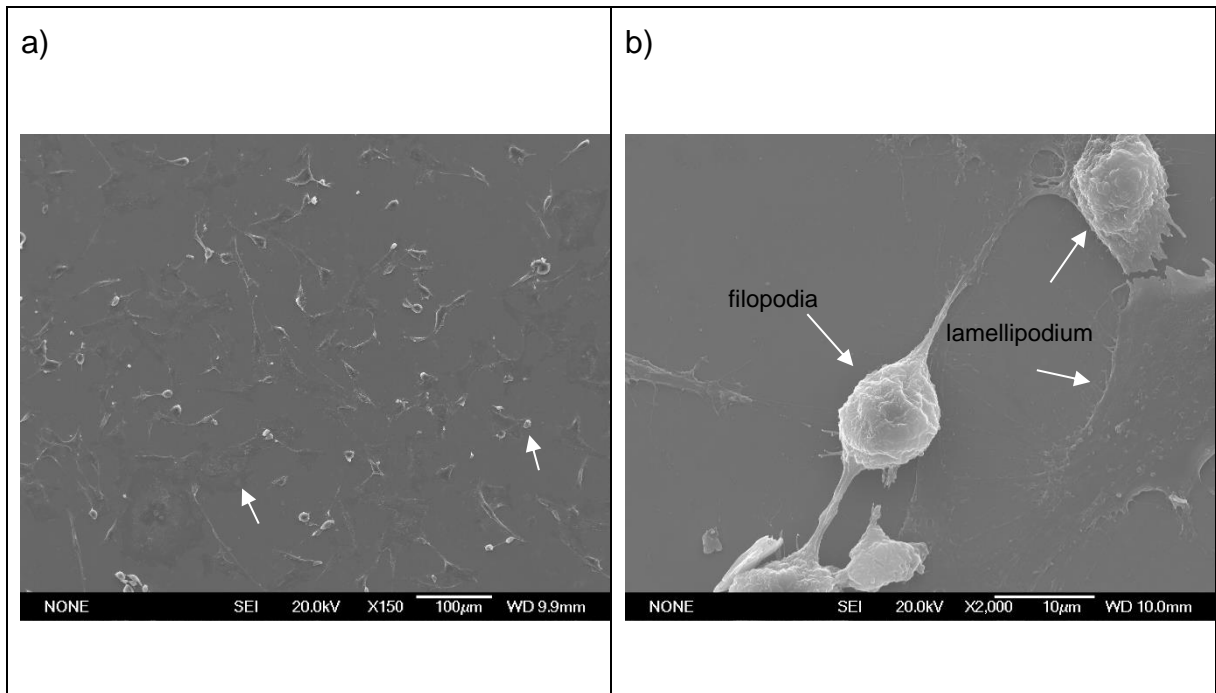
Figure 30: SEM micrograph a) low and b) high magnification of HOS seeded on MPT surfaces.

3.3.2.2. Topography and composition of polished Ti-6Al-4V surfaces thermally oxidised

3.3.2.2.1. Surface topography of polished Ti-6Al-4V surfaces thermally oxidised

SEM, AFM and interferometry were used to analyse the surface topography of $TO_{500-800\,°C}$.

SEM micrographs of samples annealed at each temperature are shown in Figure 31a-d. Distinctive morphologies on TO samples can be observed in the SEM micrographs:

- At 500 °C, the grain boundaries on the surface as well as a combination of small and large grains with different contrasts are observed in Figure 31a.

- At 600 °C, small particles are observed on the grains. Small grains start to protrude from the surface present in Figure 31b.

- At 700 °C, well defined grain boundaries and gaps are observed in Figure 31c.

- At 800 °C, crystals are observed on the surface in Figure 31d.

a)

b)

c)

d)
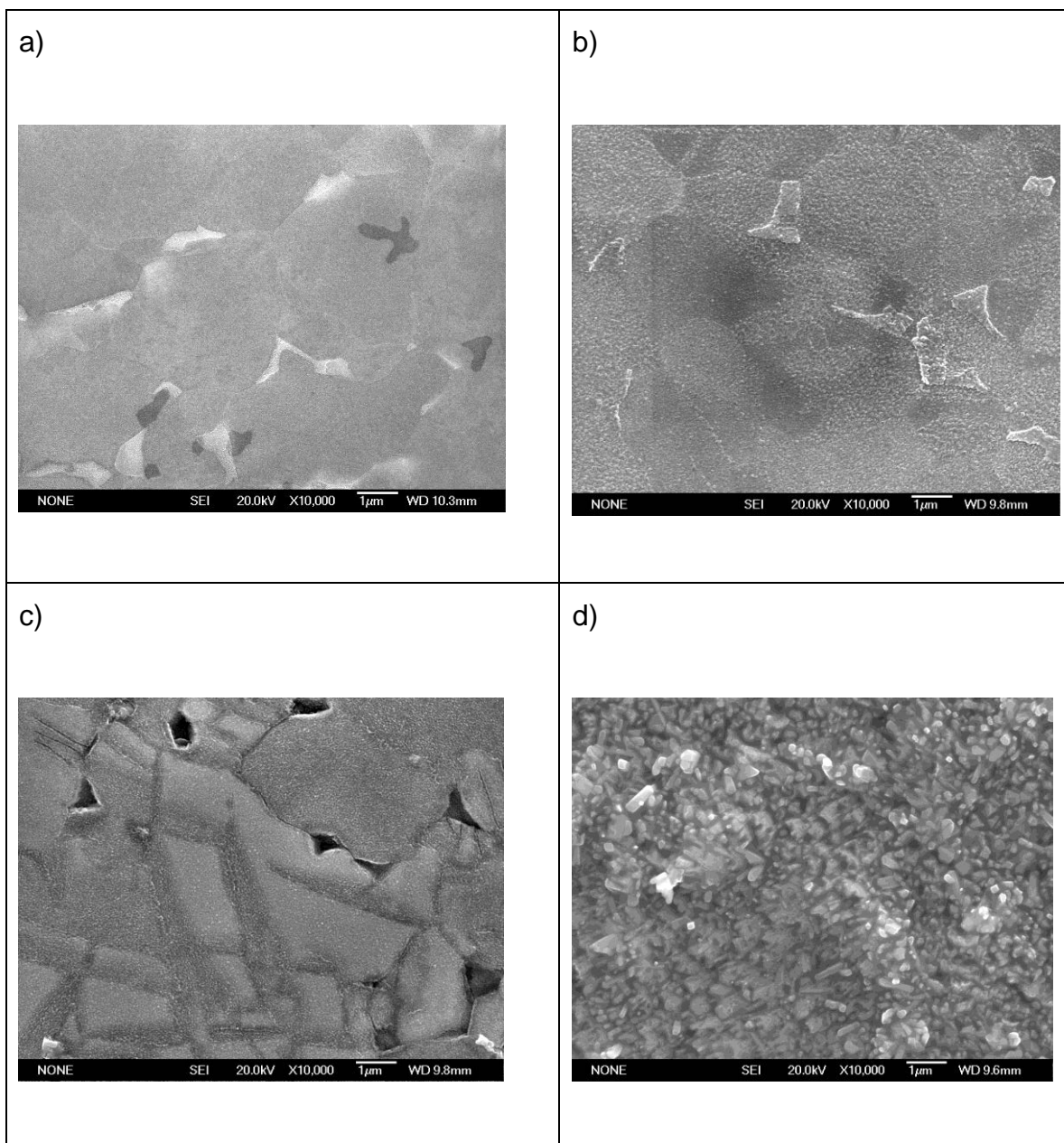
Figure 31: SEM micrographs of a) TO$_{500\,°C}$, b) TO$_{600\,°C}$, c) TO$_{700\,°C}$, d) TO$_{800\,°C}$.

Topography changes on Ti-6Al-4V surfaces after annealing studied by AFM are shown in Figure 32a-d and the following results are observed:

- At 500 °C, the surface presents different heights observed in Figure 32a.

- At 600 °C, small round particles with medium height appear on the top of grains which low height. These particles are well distributing on the surface. Some grains have higher height. These topography variations are shown in Figure 32b.

- At 700 °C, the surface presents formation of crystal with a medium height. There is an absence of grains on the surface. These variations are observed in Figure 32c.

- At 800 °C, the surface shown in Figure 32d is covered by crystals in pillar form of different heights.
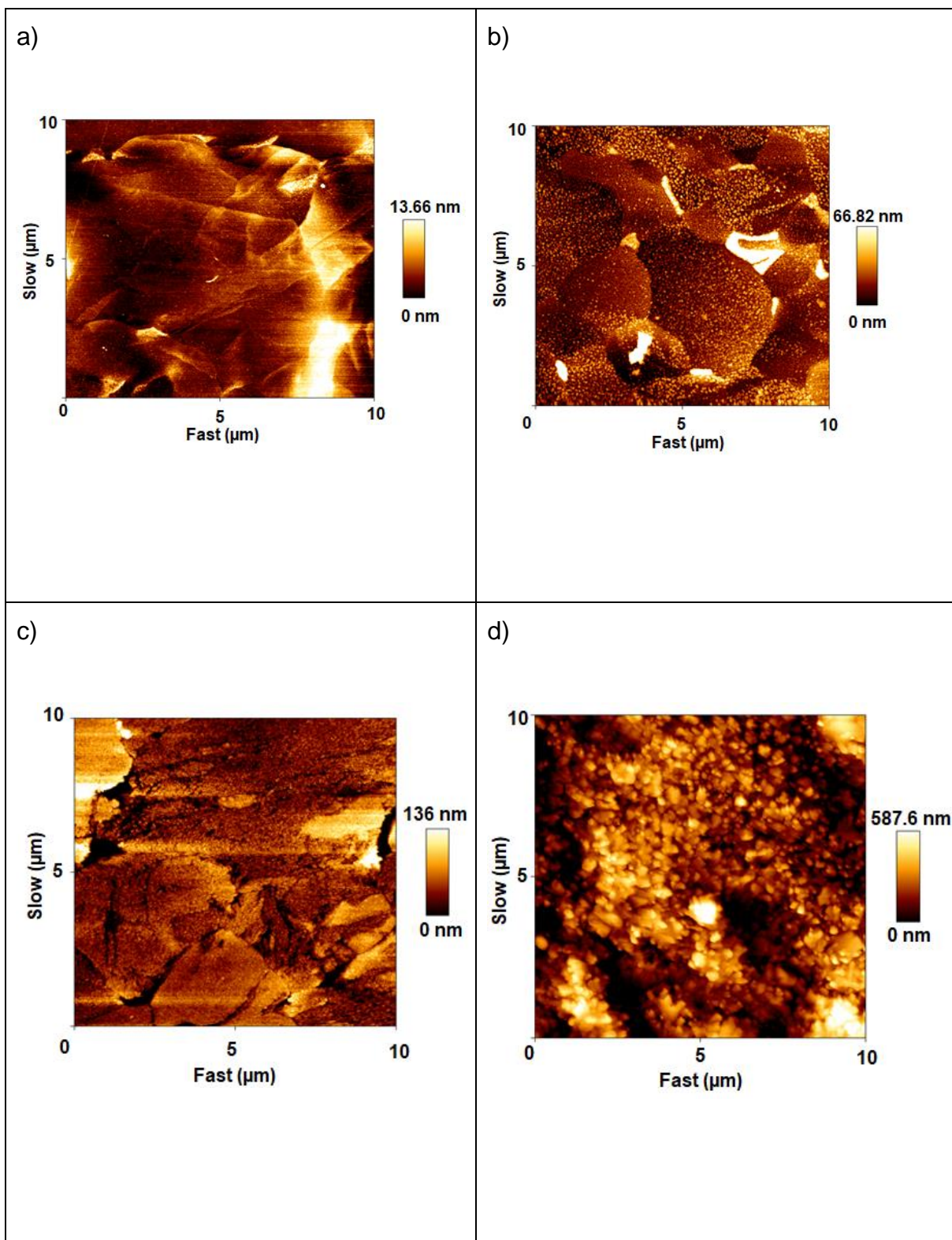
Figure 32: AFM image (10 μm x 10 μm) of a) $TO_{500\ °C}$, b) $TO_{600\ °C}$, c) $TO_{700\ °C}$, d) $TO_{800\ °C}$.

The AFM and interferometry roughness measurements of TO$_{500\text{-}800\ ^\circ C}$ surfaces are shown in Table 8. Both techniques indicate that the surface roughness increases with increasing the annealing temperature. Roughness measured by interferometry is almost the double the value compared to the roughness measured by AFM.

Table 8: Roughness measurements of TO$_{500\text{-}800\ ^\circ C}$ for by interferometry and AFM.

Annealing Temperature (°C)	Interferometry [+]		AFM [*]	
	S$_a$ (nm)	S$_y$ (nm)	R$_a$ (nm)	R$_q$ (nm)
500	-	-	2.3	3.1
600	24 ± 6	39 ± 8	10.2	15.2
700	35 ± 8	55 ± 10	20.6	30.9
800	230 ± 5	255 ± 97	106.9	133.5

[*] one measurement was performed in 512 x 512 pixels (10 x 10 µm); [+] 6 different areas were measured 432 µm x 321 µm

3.3.2.2.2. Surface crystal phase composition of polished Ti-6Al-4V surfaces thermally oxidised

XRD and Raman spectroscopy were used to analyse the surface crystal phases composition and vibrational states, respectively of TO$_{500\text{-}800\ ^\circ C}$.

The XRD diffractograms of TO$_{500\text{-}800\ ^\circ C}$ surfaces are shown in Figure 33 . The α Ti (JCPDS No. 44-1294), β Ti (JCPDS No. 44-1288), anatase (JCPDS No. 21-1272) and rutile (JCPDS No. 21-1276) patterns are also shown in Figure 33. The TO$_{500\text{-}800\ ^\circ C}$ diffractograms present different crystals:

- At 500 °C, α Ti is detected.
- At 600 °C, α Ti is present. A shoulder in 39.8 ° is detected.
- At 700 °C, α Ti is present. A peak around 39.8 ° is detected.

- At 800 °C, α Ti and rutile are detected.
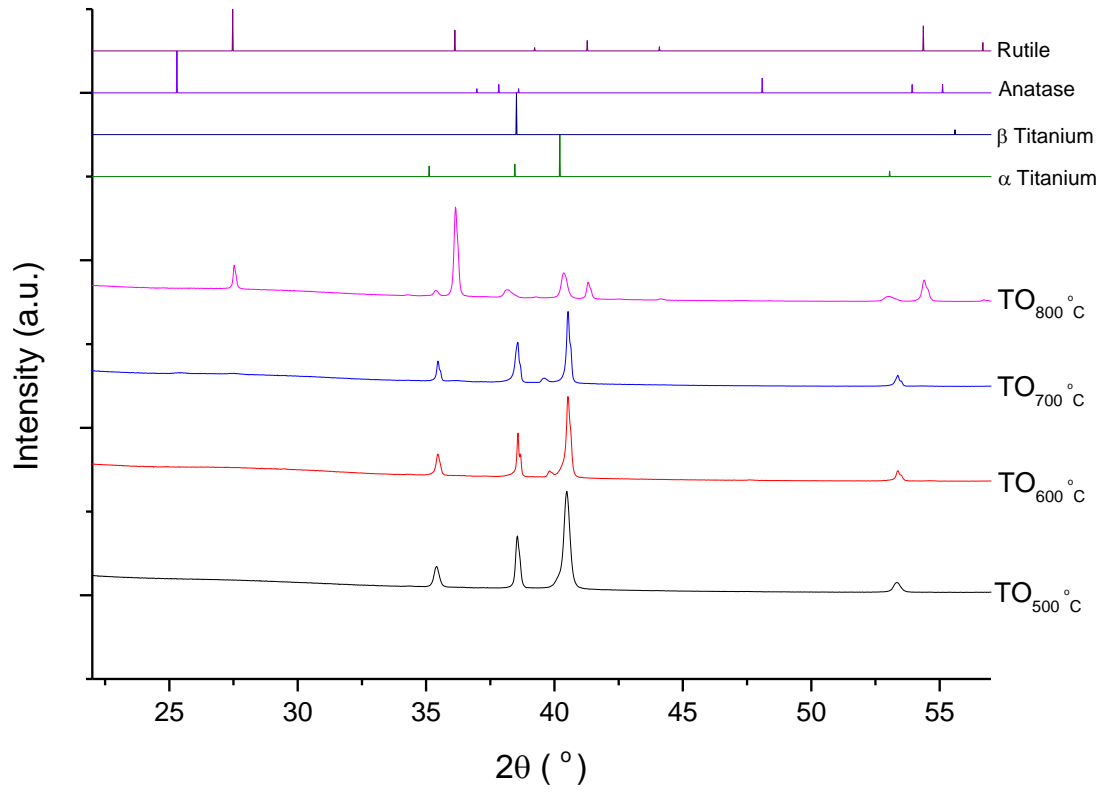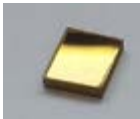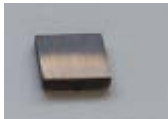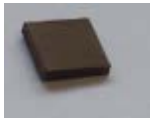
Figure 33: XRD diffractograms of TO$_{500\text{-}800\,°C}$, α Ti (JCPDS No. 44-1294), β Ti (JCPDS No. 44-1288), anatase (JCPDS No. 21-1272) and rutile (JCPDS No. 21-1276).

The differences of composition are perceived with the colour contrast between the four annealing temperatures shown in Table 9.

- At 500 °C, the surface has a metallic shin yellow colour.

- At 600 °C, the surface has a metallic shin blue colour.

- At 700 °C, the surface has a metallic shin brown colour.

- At 800 °C, the surface has an opaque brown colour.

Table 9: Pictures of $TO_{500-800 \, °C}$.

Sample	$TO_{500 \, °C}$	$TO_{600 \, °C}$	$TO_{700 \, °C}$	$TO_{800 \, °C}$

Raman spectra of $TO_{500-800 \, °C}$, anatase and rutile patterns are shown in Figure 34. Active vibrational modes of anatase in the spectrum are assigned to: E_g at 140 cm^{-1}, E_g at 196 cm^{-1}, B_{1g} at 395 cm^{-1} , A_{1g} at 515 cm^{-1} and E_g 639 cm^{-1} [133]. Active vibration modes of rutile are assigned to: B_{1g} at 142 cm^{-1}, E_g at 447 cm^{-1}, A_{1g} at 610 cm^{-1}, E_{2g} 812 cm^{-1} [134] and the peak around 240 cm^{-1} is associated with the multiple-Phonon scattering process [135].

Different vibration modes were detected in each treatment temperature:

- At 500 °C, the Raman spectrum displays broad and small peaks at 234 cm^{-1}, between 360 cm^{-1} – 480 cm^{-1}, around 515 cm^{-1} and around 560 cm^{-1} – 645 cm^{-1}. This means that anatase and rutile could both be present on the surface.

- At 600 °C, the Raman spectrum displays peaks at 155 cm^{-1}, 249 cm^{-1}, 414 cm^{-1}, 527 cm^{-1} and 610 cm^{-1}. This means that anatase and rutile could both be present on the surface.

- At 700 °C, the Raman spectrum displays peaks at 149 cm^{-1}, 242 cm^{-1}, 440 cm^{-1} and 612 cm^{-1}. This means that peaks fit with rutile presence on the surface.

- At 800 °C, the Raman spectrum displays peaks at 253 cm^{-1}, 432 cm^{-1}, 611 cm^{-1} and 812 cm^{-1}. This means that peaks fit with rutile presence on the surface.
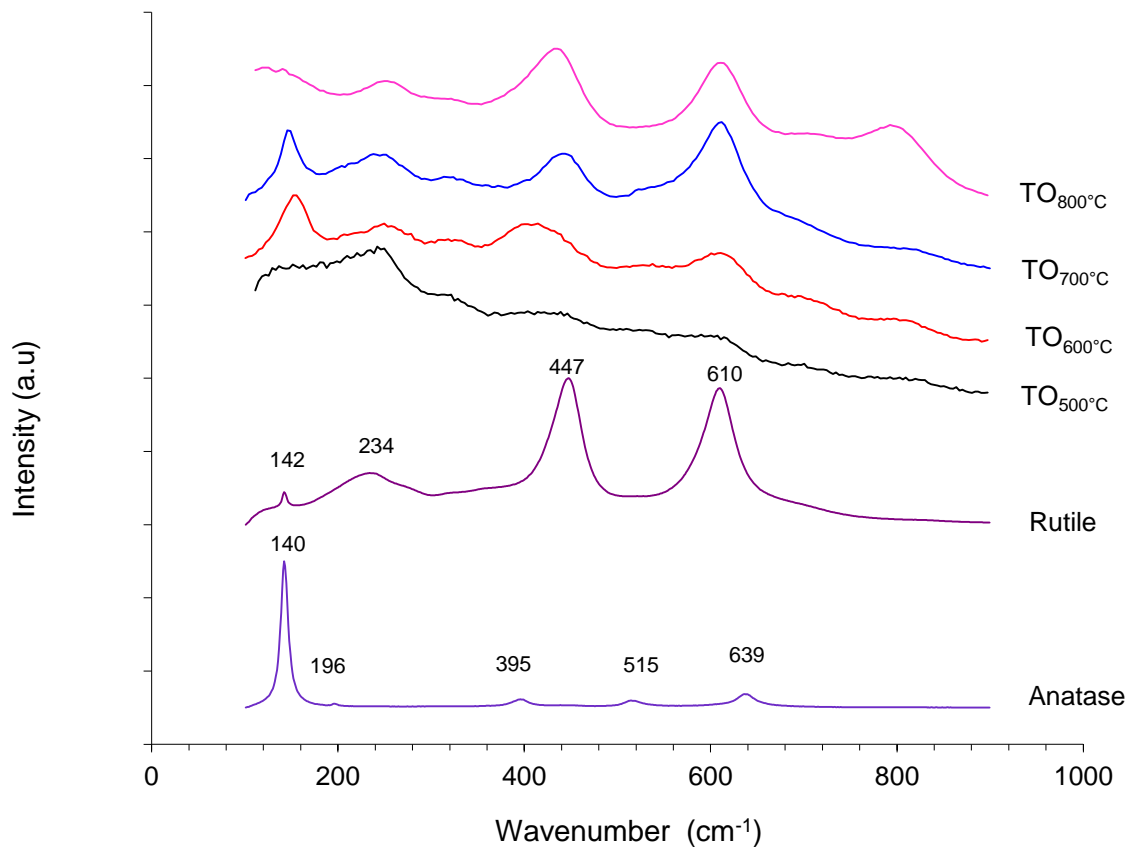
Figure 34: Raman spectrum of anatase and rutile and TO$_{500\text{-}800 \,°C}$.

3.3.2.2.3. Surface chemistry composition of polished Ti-6Al-4V thermally oxidised

XPS was used to study the chemical composition of $TO_{500-800\ °C}$.

The chemical composition is shown in Table 10. Ti percentage decreases when the annealing temperature increases specially between 700 °C and 800 °C. A different effect is shown by Al and V percentage which tend to increase with temperature increments. O percentage maintain around the same percentage. C, N and other impurities percentages decrease with temperature increases.

Table 10: Composition of $TO_{500-800\ °C}$ measured by XPS.

Annealing temperature (°C)	O%	V%	C%	Ti%	N%	Al%	*Other%
500	52.1	1.5	19.3	16.0	1.2	9.5	0.4
600	53.8	3.1	16.6	13.6	1.0	11.9	0.0
700	53.7	3.3	15.8	12.5	0.9	13.8	0.0
800	50.8	2.0	13.4	6.8	0.5	26.4	0.1

*Other includes P, Si Na and K

Figure 35 shows the changes in O/Ti ratio of $TO_{500-800\ °C}$. It is observed that increasing the temperature results in an increase of the O/Ti ratio which becomes sharper at temperatures higher than 700 °C.
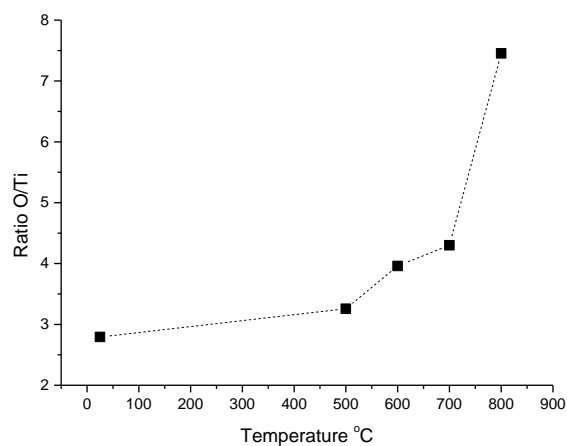
Figure 35: O/Ti ratio of $TO_{500\text{-}800\ ^\circ C}$ obtained by XPS.

Figure 36 displays the results of the XPS Ti 2p spectra of $TO_{500\text{-}800\ ^\circ C}$, showing three 2p doublets due to the oxidation states of Ti (II), Ti (III), Ti (IV). The metallic Ti (0) doublet previously observed in the MPT surface is not present in thermally treated samples. The dominant Ti oxidation state in the heat-treated samples is Ti (IV). The other 2 Ti oxidation states, Ti (II) and Ti (III), are present in small quantities.
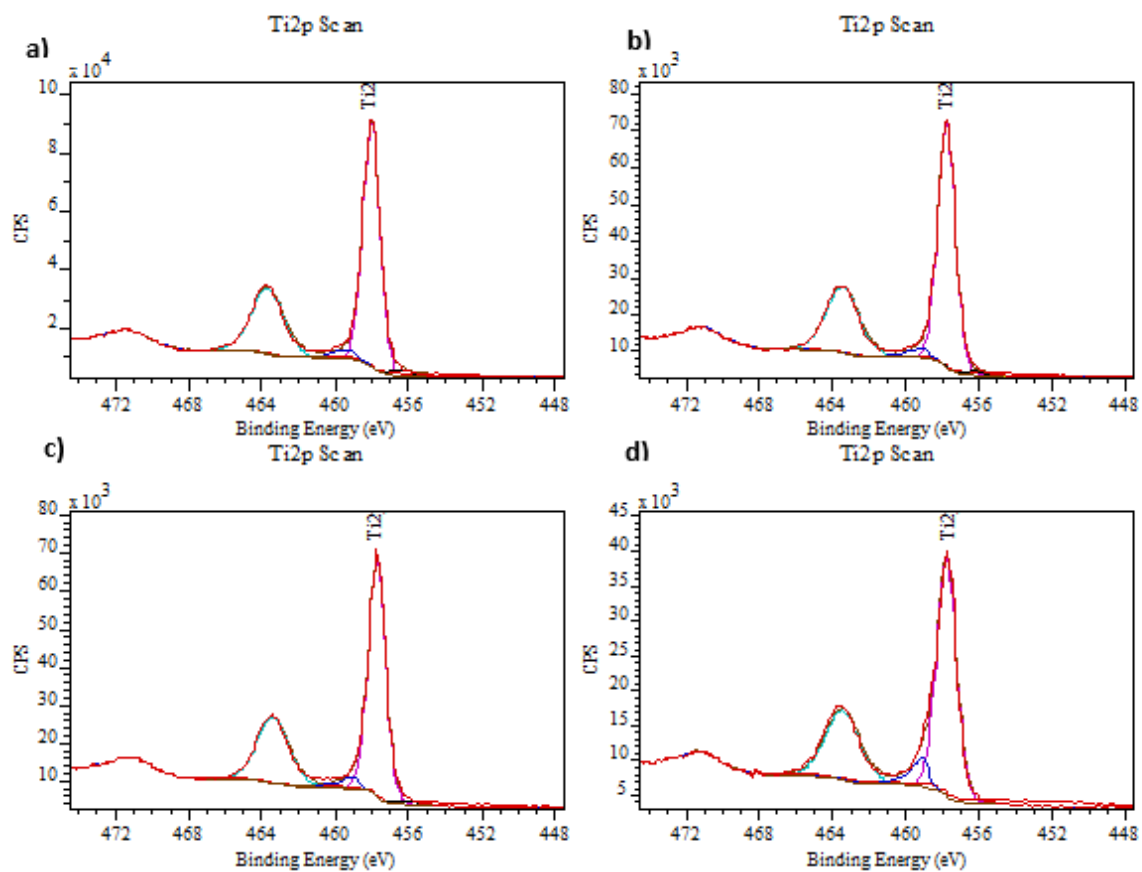
Figure 36: Ti 2p XPS spectrum of a) $TO_{500\,°C}$, b) $TO_{600\,°C}$, c) $TO_{700\,°C}$, d) $TO_{800\,°C}$.

3.3.2.2.4. Cellular adhesion on polished Ti-6Al-4V thermally oxidised

Figure 37 presents SEM micrographs of $TO_{500-800\ °C}$ surfaces seeded with HOS cells for 24 h. The following observations can be made:

- At 500 °C, cell adhered by lamellipodium attachment, observed in Figure 37a-b.

- At 600 °C, cell adhered by filopodia attachment, observed in Figure 37c-d.

- At 700 °C, cell adhered by lamellipodium attachment with dendritic projection, observed in Figure 37e-f.

- At 800 °C cell adhered by by filopodia attachment observed in Figure 37g-h.
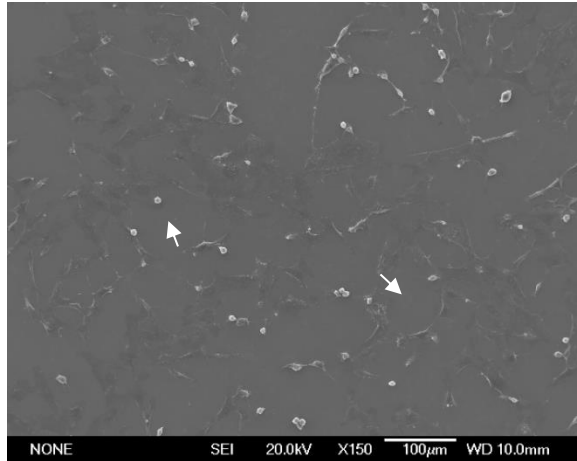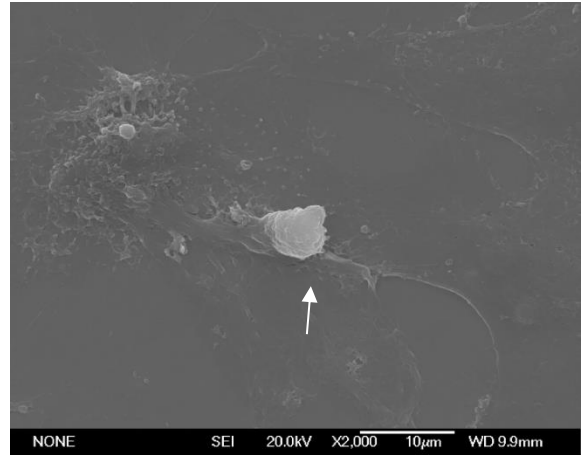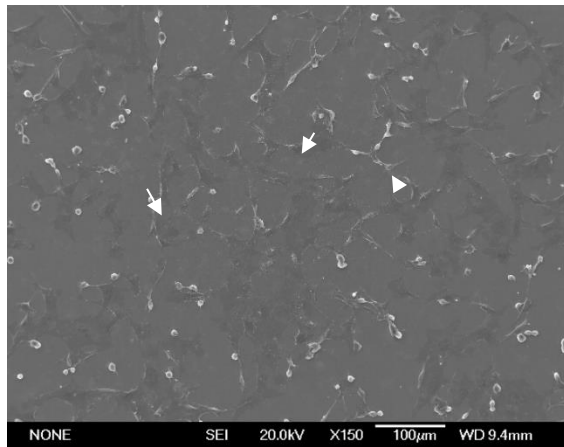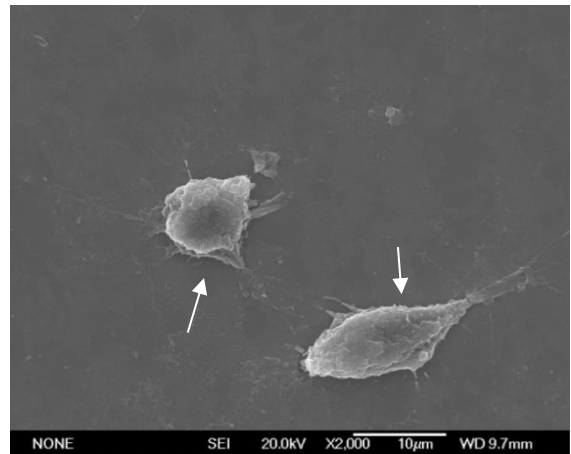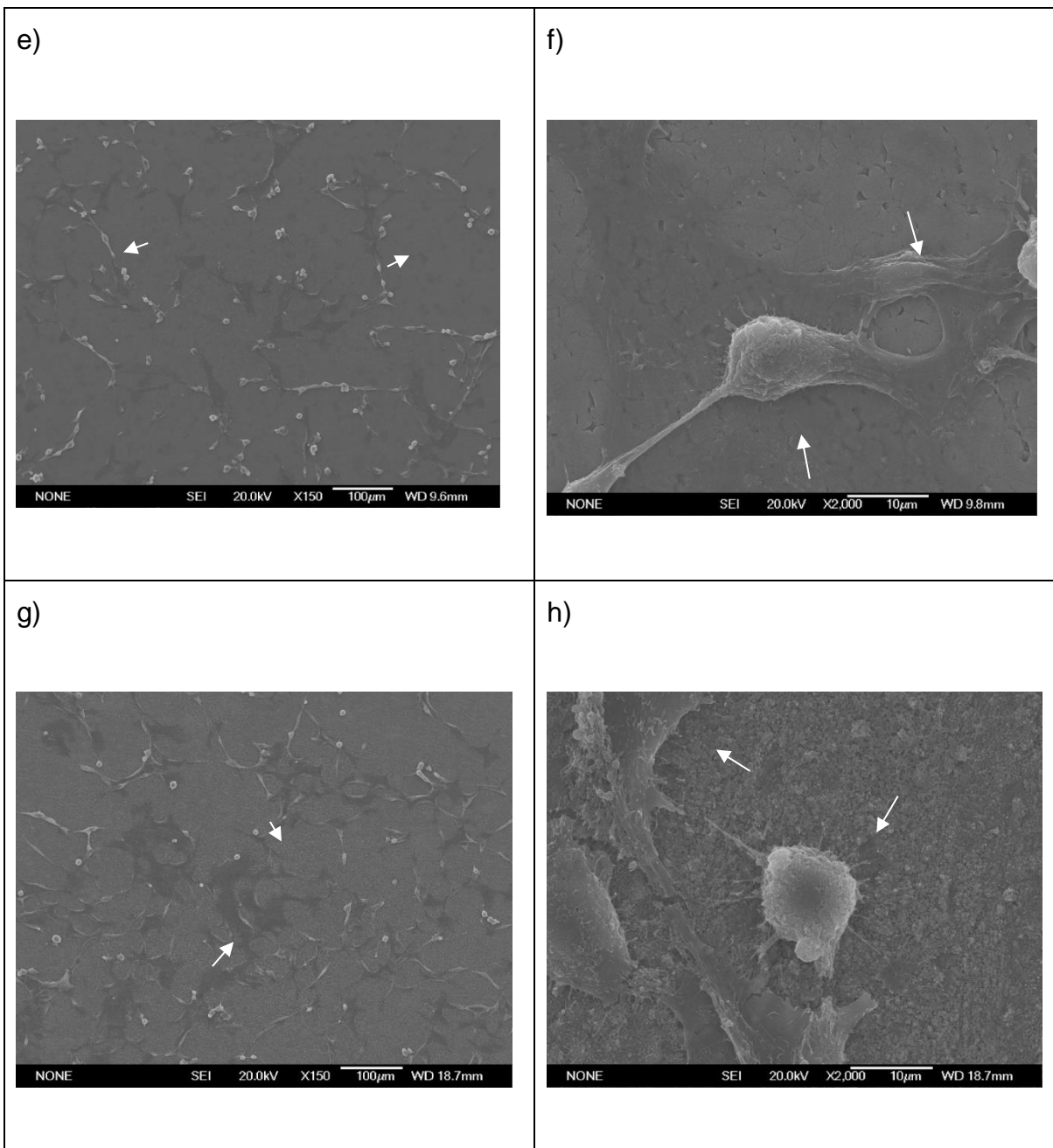
Figure 37: SEM micrographs at low and high magnification of HOS seeded for 24 h on a) and b) $TO_{500 °C}$, c) and d) $TO_{600 °C}$, e) and f) $TO_{700 °C}$, g) and h) $TO_{800 °C}$.

3.3.3. Discussion
3.3.3.1. Topography and composition of native titanium oxide from polished Ti-6Al-4V

Mechanical polishing helped to eliminate differences in topography and roughness on the MPT surfaces as well as removed any contamination from previous procedures. According with the literature mechanical polishing is a procedure where the surface material is subtracted obtaining rough or smooth surfaces according with the final polishing [1,136]. Small topography changes of MPT shown in Figure 26b with an R_a of 0.7 nm was desired to obtain in order to measure sensible changes for further surface modification. This was in accordance with a study performed by Jouanny *et al.* [136] who obtained smooth Ti-6Al-4V surfaces (R_a = 10 nm) for the nano characterisation of deposited TiO_x thin films on the surfaces.

The chemical element detection on MPT surfaces confirmed the presence of Al, Ti, O and C in the passive oxide layer. This was in accordance with the XPS study on Ti-6Al-4V performed by Roessler *et al.* [108] who showed the presence of Al in the passive oxide as well as C that was associated with adsorbed hydrocarbons. Other elements percentage shown in Table 6 such as Si and P were detected on the MPT surfaces and could be associated with the residual elements that were not specified in the manufacture's data certificate (Appendix 1).

In addition, Ti sub-oxides were analysed on MPT surface by XPS in Figure 29. The XPS spectrum of Ti 2p showed the metal / oxide system of Ti on MPT surfaces. Ti sub-oxides found on MPT surfaces were Ti (II), Ti (III) and Ti (IV) as well as metallic Ti (0). Table 7 shows that Ti (IV) sub-oxide presented a high percentage in the metal / oxide system compared with the other sub-oxides. This result was in accordance with the study performed by Lee and Chang [11] on Ti-6Al-4V native surfaces who detected the

same sub-oxides measured by XPS. Nevertheless, Roessler *et al.* [108] and Milošev et al. [12] who studied the Ti-6Al-4V surface by XPS also detected Al (III) in the outer oxide/solution interface.

Considering that 10 nm will typically be the maximum sub-surface depth that photoelectrons will escape from, during XPS measurements [137], the detection of Ti (0) in Ti 2p spectrum suggested the oxide thickness was below it. TiO_x thickness measured by Roessler *et al.* [108] on Ti-6Al-4V surfaces with variable angle spectroscopic ellipsometry showed an approximate value to 5 nm. This confirms that the presence of metallic Ti (0) in the XPS spectrum is because the thickness of the oxide layer is lower than 10 nm.

The MPT surface was demonstrated to be biocompatible by the HOS adhesion. However, heterogeneous cell adhesion type and cell morphology (round and flat) suggested the surface presents areas with greater biocompatibility than others that can be associated with the heterogenous composition of the surface. Cell morphology and attachment type indicated when surfaces are more adhesive than others [138]. Resende *et al.* [139] showed that round cells on the surface indicated poor cell extension whereas flatted cells showed good adhesion to the surface.

3.3.3.2. *Topography and composition of polished Ti-6Al-4V surfaces thermally oxidised*

Samples thermally treated present different topographies at each temperature. During TO above 600 °C, TiO_2 crystals were formed and O penetration in the substrate was detected [140]. Effects such as Al diffusion [141], O diffusion and TiO_2 crystals formation [50] changed the topography of Ti-6Al-4V surfaces, including the formation of nodules [141], small grains [50] and porosity [140] on the surfaces. These surface structure changes

became more pronounced with increasing the TO temperature, resulting in significant increase in surface roughness [50,51]. In Table 8 is possible to observe that roughness increased with temperature increases starting from R_a of 2.3 nm at 500 °C to around 100 nm at 800 °C. A similar trend in surface roughness with increasing temperature was also reported by Lee *et al.* [142] for commercially pure titanium (CpTi) surfaces thermally treated at 300, 500 and 750 °C for 30 min.

α Ti was present in all $TO_{500-800 \, °C}$ surfaces, shown in Figure 33. During the latter treatment ($TO_{800 \, °C}$), the XRD peak intensity of α Ti decreased considerably whereas the rutile XRD peak intensity increased suggesting that the thickness of the oxide after the treatment at 800 °C was greater than that of the treated samples at 500, 600 and 700 °C. Kumar *et al.* [51] showed that TiO_x thermally treated in air at 800 °C for 8 h was mainly consisted of rutile crystals and was thicker than the oxide layer formed after thermal treatment at 500 °C and 650 °C for 8 h which was composed of α, β Ti and TiO_x. This observation can be supported by the colour of the samples after the TO at 800 °C. The differences in the colour can be related to the thickness of the oxide layer [45] and /or the refraction index [143]. In this work, all the surfaces treated at 500, 600 and 700 °C were shiny characteristic of the smooth polishing, shown in Table 9, while the surface treated at 800 °C was opaque suggesting the presence of additional structures on the surface compared with the other samples.

TiO_2 crystals appeared on $TO_{600-800 \, °C}$ surfaces, shown in Figure 33. The presence of rutile on the surface $TO_{600 \, °C}$ was detected by XRD in a shoulder form around 39. 8°, and this shoulder transformed into an independent peak when the TO temperature increased to 700 °C. At 800 °C the XRD diffractogram showed a spectrum

characteristic of rutile. This is in accordance with a study reported by Krishna *et al.* [4] where CpTi was thermally oxidised at different temperatures for 5 h. They showed that the sample TO at 600 and 700 °C presented a similar trend of the XRD diffractogram around 40° as the one presented in this study on Ti-6Al-4V, whit the shoulder formation when the sample was treated at 600 °C and the peak formation when the sample was treated at 700 °C. Rutile was detected by them when the sample was treated at 800 °C.

Raman spectroscopy spectra of TO$_{500-600 \,°C}$ shown in Figure 34 presented vibrational mode of O and Ti for anatase and rutile and therefore both crystals could be present on these surfaces whereas TO$_{700-800 \,°C}$ exhibited the vibrational mode of rutile. These results were in agreement with Chang and Huang [112] who studied the TiO$_2$ crystals transformation by Thermo-Raman. They reported that amorphous TiO$_2$ and anatase were present in samples treated between 400 and 550 °C, that rutile was detected at 550 °C and that anatase phase was transformed completely to another phase at 700 °C, suggesting that rutile phase was formed at temperatures above 700 °C.

XPS studies have shown that the Al and V content of the oxide layer was increased with increasing the treatment temperature as is shown in Table 10. Du *et al.* [47] report that Al from the substrate can be diffused on the outer surface in Al$_2$O$_3$. Al diffusion is more pronounce with increasing the treatment temperature. A similar observation was also made by Kumar *et al.* [141] who reported that thermally treated Ti-6Al-4V surfaces were Al enriched compared with untreated Ti-6Al-4V. The V and Al enrichment were reported by Mac Donald *et al.* [47] in surfaces thermally treated at 600 °C. In addition, C and N were observed to be present on the surface of thermally oxidised Ti-6Al-4V

surfaces as shown in Table 10 but the levels were considerably decreased with increasing the temperature above 500 °C.

From the XPS spectrum of treated samples shown in Figure 36, it can be concluded that only TiO_x was present. The increase of O/Ti ratio in the thermally treated sample at 500 °C compared with that of the non-thermally treated sample was due to O diffusion on the substrate. The O/Ti ratio increased at treatment temperatures above 500 °C was mainly due to the formation of a dense oxide layer. Guleryuz and Cimenoglu [140] reported that dense oxide layers could be obtained at temperatures between 600 and 800 °C.

HOS Cells adhered on thermally treated samples shown in Figure 37. The cells were spread randomly on all surfaces but preferred the samples that exhibited low and compact texture such as the samples thermally treated at 500 and 700 °C as shown in Figure 31 and 32. A study performed by Saldaña *et al* [144]. evaluated the biocompatibility of human osteoblastic cells considering cell adhesion, proliferation and differentiation on Ti-6Al-4V surfaces TO at 500 and 700 °C for 1 h. They showed that the cell adhesion increased in both samples compared with the polished surface. The only difference was the increased secretion of osteoprotegerin protein in samples the surface of which was thermally treated at 700 °C. It was also shown by the literature that the cell adhesion differences can be largely attributed to the topography, roughness and composition of the surfaces [145,146].

3.4. Topography and composition of titania gel layer formed with H_2O_2/HCl on polished Ti-6Al-4V and titania gel layer thermally oxidised on polished Ti-6Al-4V

3.4.1. Specific objective

The objective of this section was to evaluate the surface's topography and composition of Ti-6Al-4V chemically treated and Ti-6Al-4V chemically treated and thermally oxidized at different temperatures to understand how the changes can influence the ionic peptide adsorption. In addition, the biocompatibility of the before mentioned surfaces was assessed to show how the modifications affect the cellular adhesion on the surfaces.

3.4.2. Results

In this section, modified Ti-6Al-4V surfaces were characterized to identify and, where possible, quantify surface topography, roughness, surface crystal phases composition and surface chemistry composition. The following surfaces were studied:

1) Titania gel layer (TGL) formed with 8.8 M H_2O_2 /0.1 M HCl at 80 °C for 30 min on MPT

2) TGL followed by TO for 1 h in air at 500, 600, 700 and 800 °C (TGL-TO$_{500-800 °C}$)

An adhesion cell test was performed for all surfaces using osteoblast-like cells, human osteosarcoma (HOS), to study the biocompatibility of the surfaces.

3.4.2.1. Topography and composition of titania gel layer formed with H_2O_2/HCl on polished Ti-6Al-4V

3.4.2.1.1. Surface topography of titania gel layer formed with H_2O_2/HCl on polished Ti-6Al-4V

SEM, AFM and interferometry analysis were used to characterised the surface topography of TGL.

The SEM micrograph shown in Figure 38 presents two defined grain topographies. Flat grains and rough grains with a porous structure. The surface also exhibits well defined grain boundary and grain absence due to the dissolution of grain during the reaction with H_2O_2/HCl.
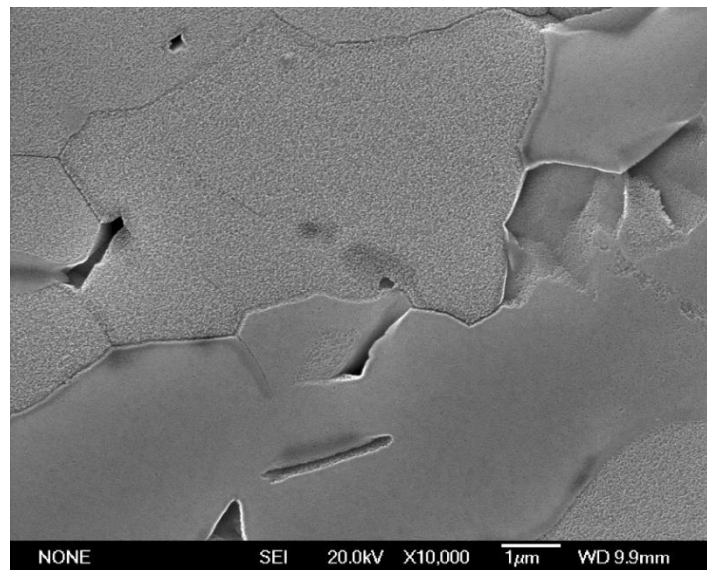
Figure 38: SEM micrograph of TGL surface formed by H_2O_2/HCl.

The sample shown in Figure 38 exhibits grains on the surface with different topographies but it is not clear what the difference is at micro scale, therefore higher magnification SEM was performed. Figure 39a shows a high magnitude SEM

micrograph of the grain surface identified with the low roughness in Figure 38 presenting porous structures. Figure 39b shows a high magnitude SEM micrograph of the grain surface identified with high roughness in Figure 38 with etched and porous structures.
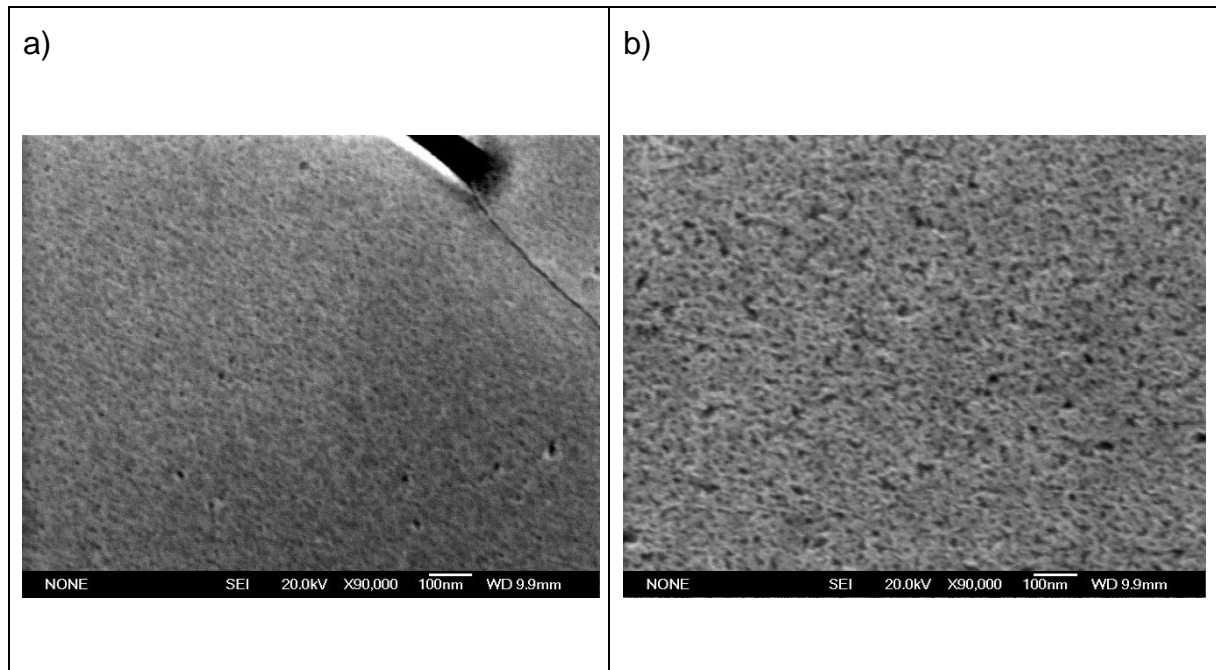
Figure 39: SEM micrograph of TGL surface in a) low roughness grains and b) high roughness grains.

The AFM analysis results shown in Figure 40 display 3 distinct heights according to the measurement of the scaling in the right-hand side. Dissolved grains are represented by low height areas, etched and porous grains by medium height areas, and plain grains by high height areas.
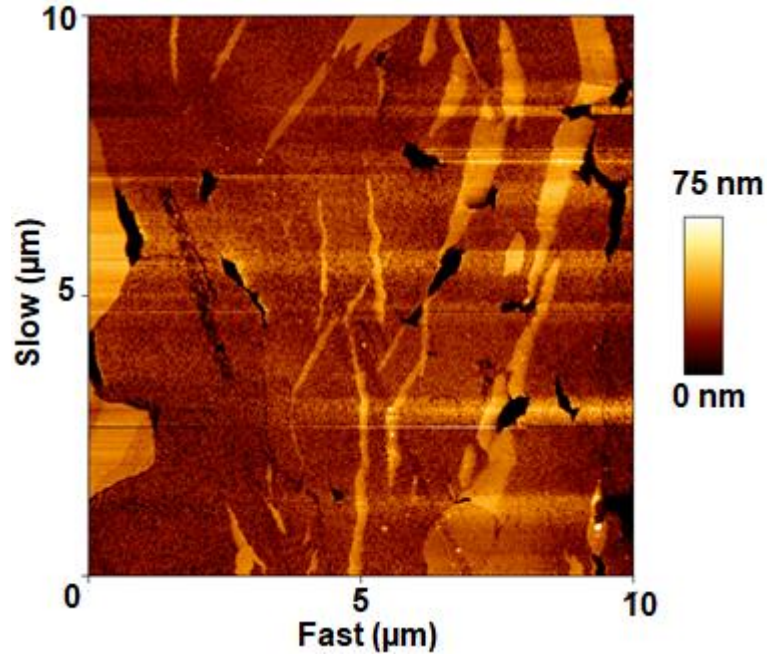
Figure 40: AFM image (10 μm x 10 μm) of TGL surface.

The average roughness (S_a) of TGL surface measured by interferometry was 26±1 nm and the root mean square roughness (S_q) was 40±3 nm. In contrast, the average roughness (R_a) of TGL surface measured by AFM is 8.5 nm and the root mean square roughness (R_q) was 17 nm.

3.4.2.1.2. Surfaces crystal phase and chemical composition of titania gel layer formed with H_2O_2/HCl on polished Ti-6Al-4V

XRD was used to analyse the surface crystal phase composition of TGL. The XRD diffractogram of TGL is shown in Figure 41 . The α (JCPDS No. 44-1294) and β Ti (JCPDS No. 44-1288) patterns are also shown in Figure 41. The crystal phases identified in the TGL diffractogram is α Ti, the same crystal observed in MPT.
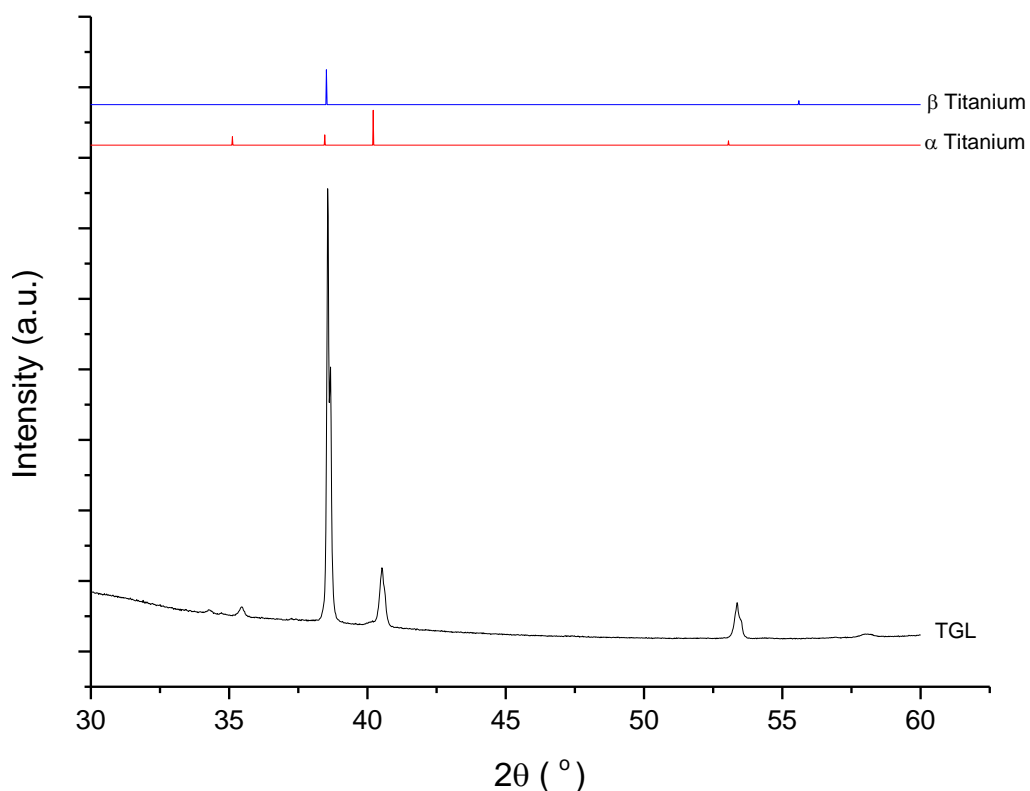
Figure 41: XRD diffractogram of TGL surface, α Ti (JCPDS No. 44-1294) and β Ti (JCPDS No. 44-1288).

Chemical element percentage of TGL samples measured by XPS are shown in Table 11. After the chemical treatment on MPT surfaces. C and N, increases from MPT samples whereas O and Al and other impurities decrease.

Table 11: Chemical elements percentage of TGL surface measured by XPS.

Element	O%	V%	C%	Ti%	N%	Al%	*Other %
	52	0.2	22.1	19.4	1.3	3.4	1.6

*Other includes P, Si Na and K

Ti 2p spectrum of TGL surface is shown in Figure 42. In the spectrum Ti (0) peak is not detected and Ti (IV) sub-oxide is the predominant oxidation state.
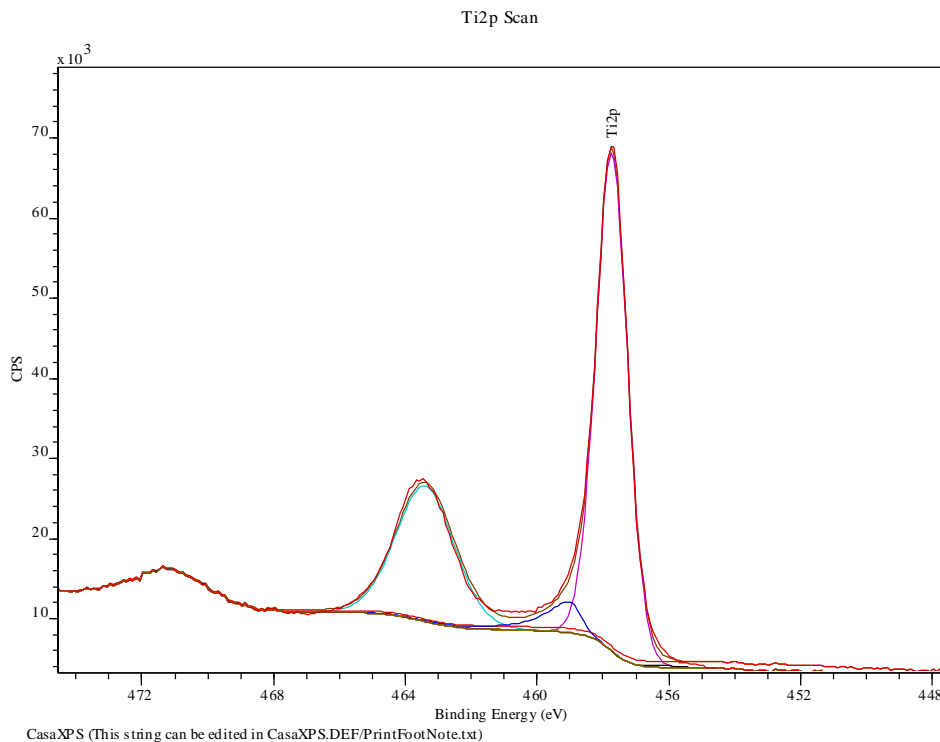
Figure 42: XPS spectrum of Ti 2p for TGL surface.

3.4.2.1.3. *Cellular adhesion on titania gel layer formed with H₂O₂/HCl on polished Ti-6Al-4V*

SEM micrograph of adhered HOS on TGL surface is shown in Figure 43a. High SEM magnitude micrograph is shown in Figure 43b. Cells indicated by arrows, exhibit round and flatted morphologies on TGL surface. It is possible to observed that some cells present filopodia attachment whereas others present lamellipodium attachment on TGL surface.
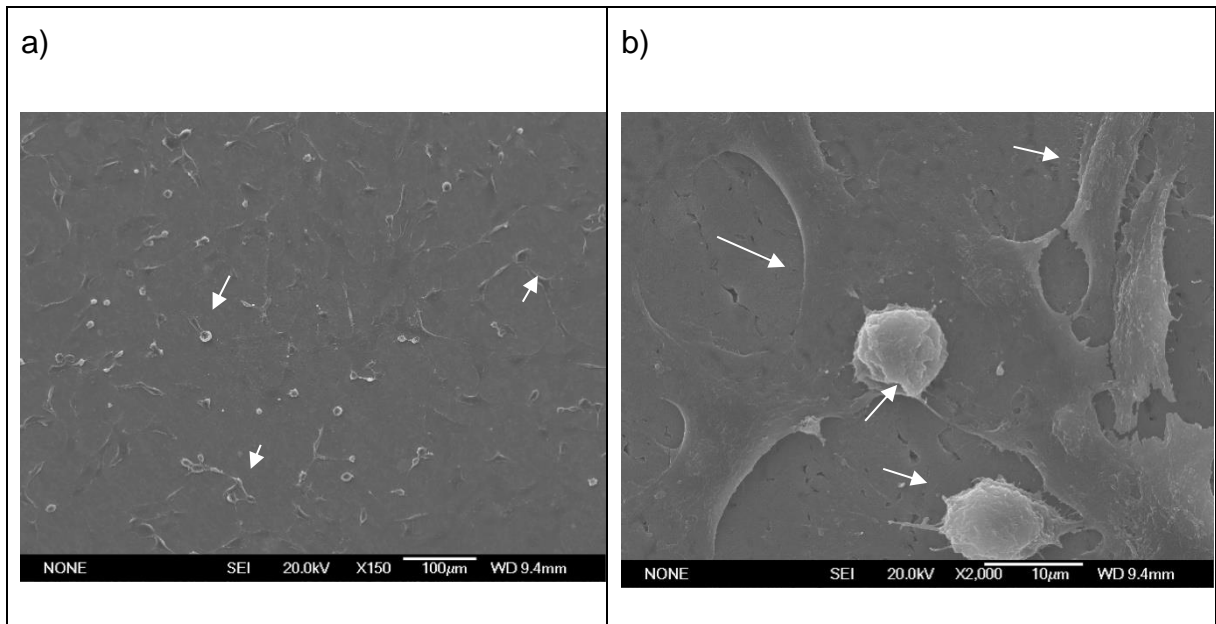
Figure 43: SEM micrograph of HOS on TGL surfaces a) low and b) high magnitude.

3.4.2.2. Topography and composition of titania gel layer formed with H_2O_2/HCl followed by thermal oxidation on polished Ti-6Al-4V

3.4.2.2.1. Surface topography of titania gel layer formed with H_2O_2/HCl followed by thermal oxidation on polished Ti-6Al-4V

SEM, AFM and interferometry were used to analyse the surface topography of TGL-$TO_{500-800\ °C}$.

SEM micrographs of TGL-$TO_{500-800\ °C}$ are shown in Figure 44 a-d. The following distinct morphological features can be observed in the SEM micrograph:

- At 500 °C, the grain boundaries and dissolved grains on the surface due to the chemical treatment is presented. Grains shown in Figure 44a exhibit different roughness.

- At 600 °C, grain boundaries and dissolved grains on the surface due to the chemical treatment, observed in Figure 44b.

77

- At 700 °C, grain boundaries and dissolved grains due to the chemical treatment and appearance of crystals on grain edges, observed in Figure 44c.

- At 800 °C, crystals are observed on the surface, observed in Figure 44d.
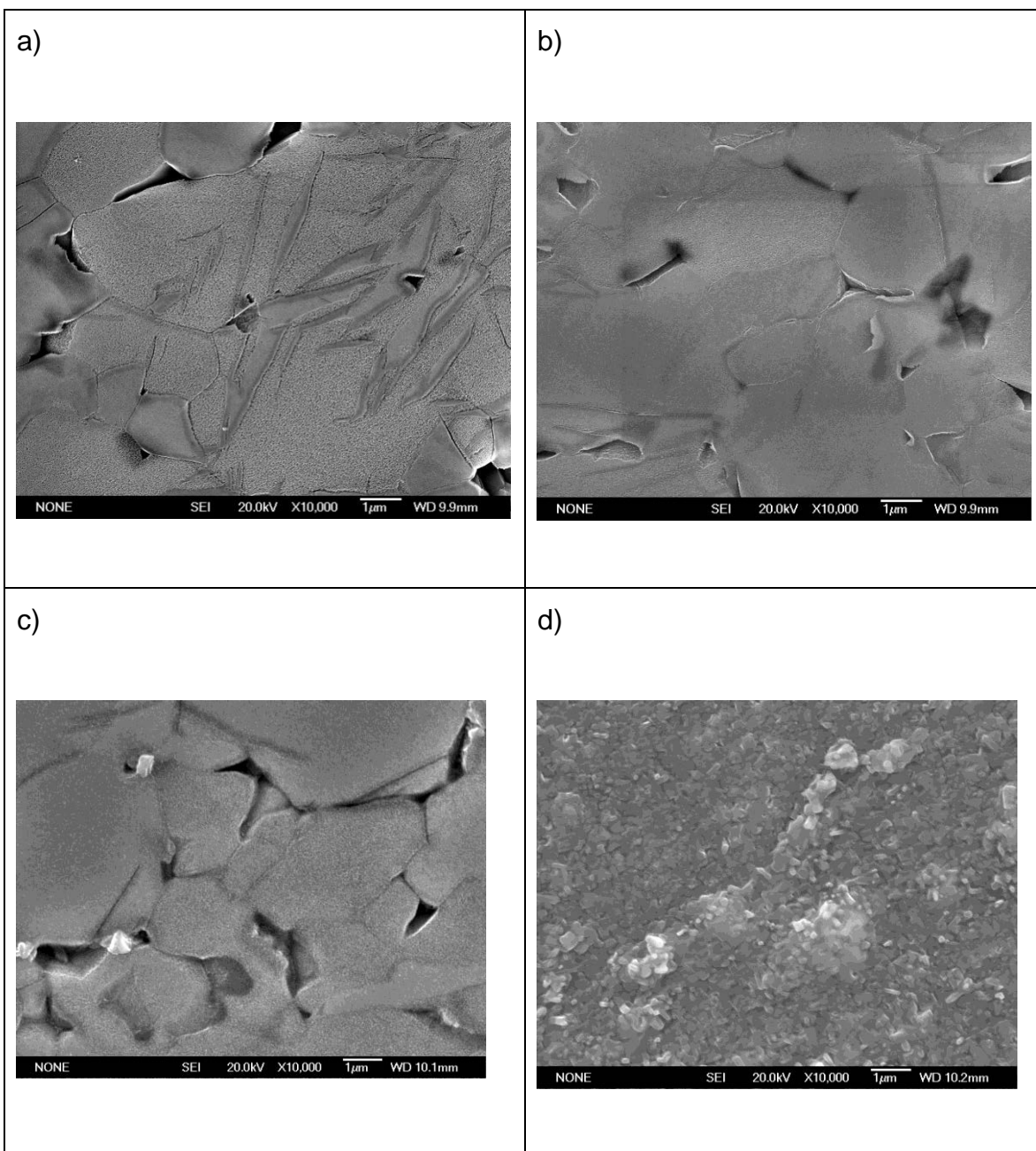
Figure 44: SEM micrograph of a) TGL-TO$_{500\,°C}$, b) TGL-TO$_{600\,°C}$, c) TGL-TO$_{700\,°C}$ and d) TGL-TO$_{800\,°C}$.

The topography changes on TGL-TO$_{500\text{-}800\,°C}$ studied by AFM are shown in Figure 45a-d. The following surface results are observed:

- At 500 °C, the surface presents craters and two heights. These variations are observed in Figure 45a.

- At 600 °C, the surface presents craters, granular and flat grains with different heights. These variations are observed in Figure 45b.

- At 700 °C, the surface is covered by thin crystals of different heights observed in Figure 45c.

- At 800 °C, the surface is covered by crystals of different heights observed in Figure 45d.
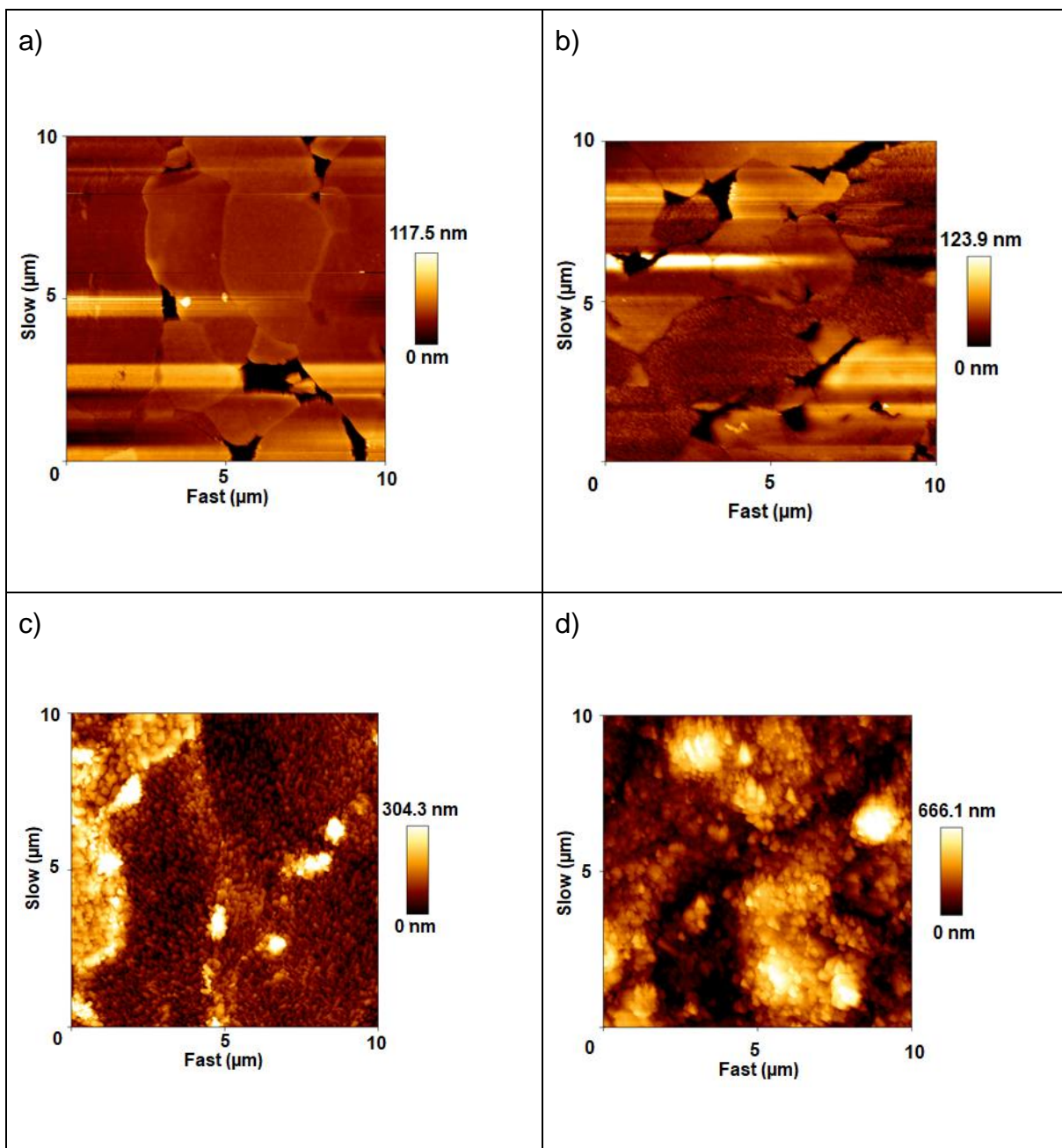
Figure 45: AFM images (10 µm x 10 µm) of a) TGL-TO$_{500\,°C}$, b) TGL-TO$_{600\,°C}$, c) TGL-TO$_{700\,°C}$ and d) TGL-TO$_{800\,°C}$.

The AFM and interferometry roughness measurements of TGL- TO$_{500-800\ °C}$ are shown in Table 12. The roughness increases when oxidation temperature increases. Both techniques show similar increasing trends.

Table 12: Roughness measurements TGL-TO$_{500-800\ °C}$ by interferometry and AFM.

Sample name	Interferometry [+]		AFM [*]	
	S$_a$ (nm)	S$_q$ (nm)	R$_a$ (nm)	R$_q$ (nm)
TGL-TO$_{500\ °C}$	13 ± 4	29 ± 13	12	26.7
TGL-TO$_{600\ °C}$	20 ± 2	32 ± 6	16.8	28.2
TGL-TO$_{700\ °C}$	92 ± 9	139 ± 10	49	69.2
TGL-TO$_{800\ °C}$	176 ± 8	244 ± 45	121	151.4

[*] one measurement was performed in 512 x 512 pixels (10 x 10 µm); [+] 6 different areas were measured 432 µm x 321 µm

3.4.2.2.2. Surface crystal composition of titania gel layer formed with H_2O_2/HCl followed by thermal oxidation on polished Ti-6Al-4V

XRD and Raman spectroscopy were used to analyse the surface crystal phase composition and vibrational states, respectively, of TGL-TO$_{500-800\ °C}$.

XRD diffractogram of TGL-TO$_{500-800\ °C}$ are shown in Figure 46. The α Ti (JCPDS No. 44-1294), β Ti (JCPDS No. 44-1288), anatase (JCPDS No. 21-1272) and rutile (JCPDS No. 21-1276) are also shown in Figure 46:

- At 500 °C, α Ti crystal is detected.

- At 600, α Ti is present. A shoulder around 2θ = 40° is detected.

- At 700 °C, α Ti is present. A peak around 2θ = 40° is detected.

- At 800 °C, α Ti and rutile are detected.
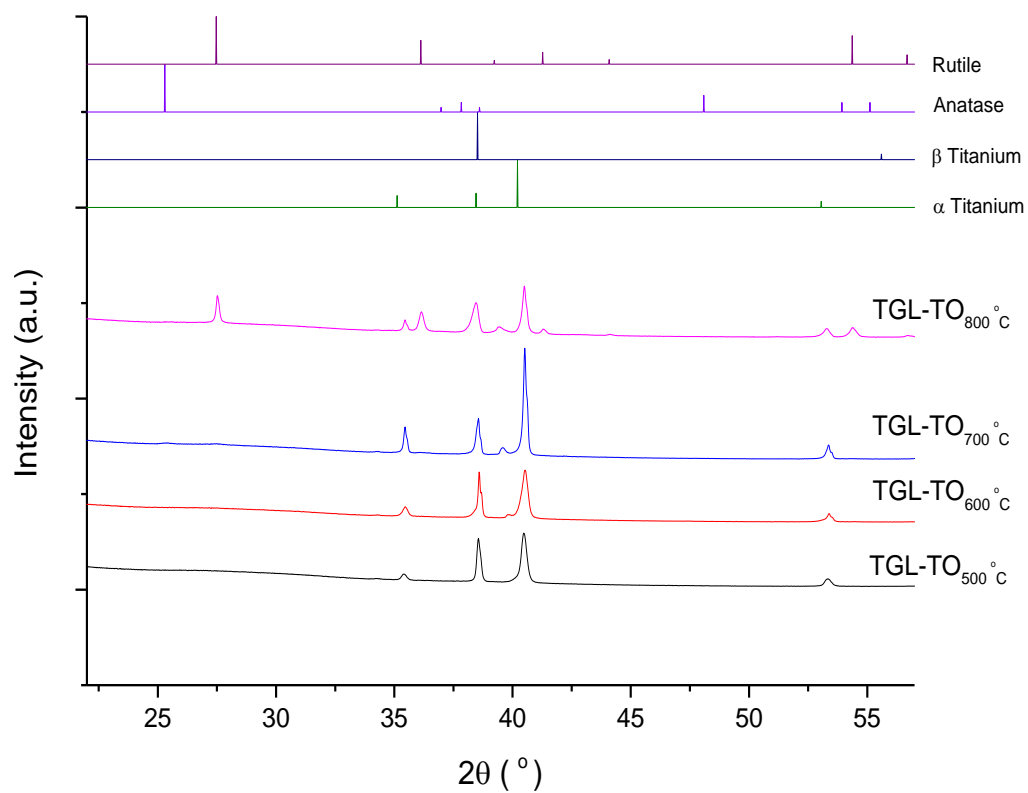
Figure 46: XRD diffractogram of TGL-TO$_{500-800\ °C}$, α Ti (JCPDS No. 44-1294), β Ti (JCPDS No. 44-1288), anatase (JCPDS No. 21-1272) and rutile (JCPDS No. 21-1276).

These composition differences are shown in Table 13. Each treatment temperature exhibits a distinct colour:

- At 500 °C, the surface has dark blue colour

- At 600°C, the surface has light blue colour

- At 700 °C, the surface has yellow colour

- At 800°C, the surface has brown colour

Table 13: Pictures of TGL-TO$_{500-800 \, °C}$.

Sample	TGL-TO$_{500 \, °C}$	TGL-TO$_{600 \, °C}$	TGL-TO$_{700 \, °C}$	TGL-TO$_{800 \, °C}$

Raman spectroscopy for TGL-TO$_{500-800 \, °C}$, anatase and rutile are shown in Figure 47. Anatase and rutile vibrational modes are labelled on the Raman spectrum. Different vibration modes were detected for each annealing temperature:

- At 500 °C, Raman spectrum displays broad peaks around 160 cm^{-1}, 240 cm^{-1}, 400 cm^{-1} and 612 cm^{-1}. This means that anatase and rutile could both be present on the surface

- At 600 °C, Raman spectrum display broad peaks around 160 cm^{-1}, 240 cm^{-1}, 448 cm^{-1}, 515 cm^{-1} and 612 cm^{-1}. This means that anatase and rutile could both be present on the surface.

- At 700 °C, Raman spectrum display peaks at 147 cm^{-1}, 240 cm^{-1}, 448 cm^{-1} and 612 cm^{-1}. These peaks fit with rutile vibration modes

84

- At 800 °C, Raman spectrum display peaks at 147 cm^{-1}, 240 cm^{-1}, 448 cm^{-1} and 612 cm^{-1}. These peaks fit with rutile vibration modes
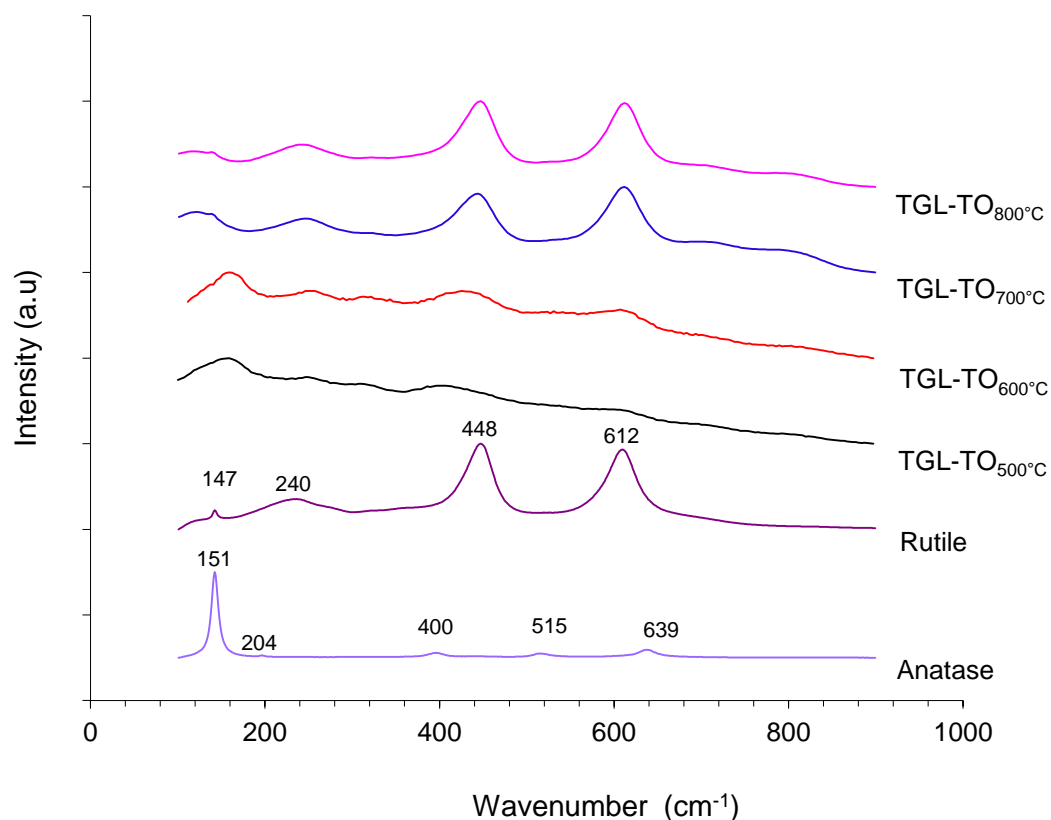
Figure 47: Raman spectrum of anatase, rutile and TGL-TO$_{500\text{-}800\ °C}$.

3.4.2.2.3. Surface chemical composition of titania gel layer formed with H_2O_2/HCl followed by thermal oxidation on polished Ti-6Al-4V

XPS was used to study the chemical composition of TGL-TO$_{500\text{-}800\ °C}$.

The chemical composition is shown in Table 14. O, V, C, Ti, N and Al were quantified. O percentage is maintained constant for all the samples, V and Al percentages increase when the temperature increases while Ti decreases. C, N and small impurities percentages decrease considerably when the sample is treated at 800 °C.

Table 14: Chemical percentage of TGL-TO$_{500-800\ °C}$ measured by XPS.

Annealing Temperature °C	O%	V%	C%	Ti%	N%	Al%	*Other %
500	52.7	0.4	19.9	20.6	1.0	3.8	1.6
600	53.3	0.9	19.4	19.4	1.0	4.4	1.6
700	53.0	2.3	18.1	15.6	1.0	9.5	0.5
800	52.5	2.3	14.5	11.4	0.6	18.7	0.0

*Other includes P, Si, Na and K

Ti 2p spectrum of TGL-TO$_{500-800\ °C}$ is shown in Figure 48. Ti (0) is non- detected and the dominant sub-oxide is Ti (IV).
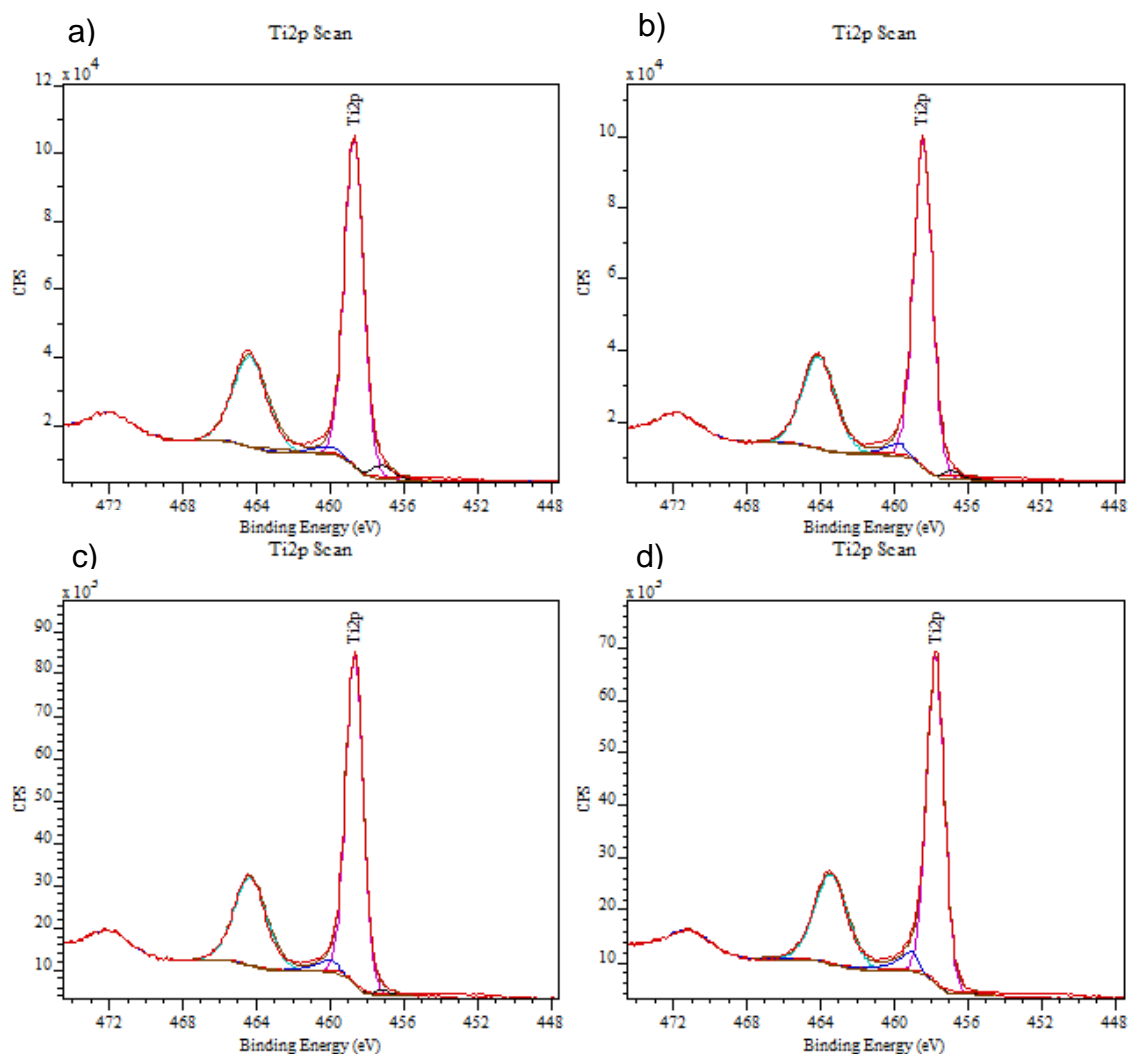
Figure 48: Ti 2p XPS spectrum of a) TGL-TO$_{500\,°C}$, b) TGL-TO$_{600\,°C}$, c) TGL-TO$_{700\,°C}$ and d) TGL-TO$_{800\,°C}$.

O/Ti ratio of TGL-TO$_{500\text{-}800\,°C}$ samples is shown in Figure 49. It is observed that increasing the temperature results in an increase of the O/Ti ratio above 500 °C which becomes sharper at temperatures higher than 700 °C.
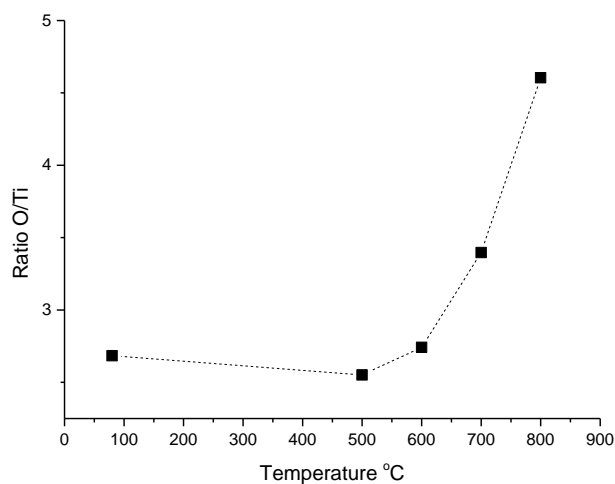
Figure 49: O/Ti ratio of TGL and TGL-TO$_{500-800 \ °C}$ obtained by XPS.

3.4.2.2.4. Cellular adhesion on titania gel layer formed with H$_2$O$_2$/HCl followed by thermal oxidation on polished Ti-6Al-4V

Figure 50 presents SEM micrographs of TGL-TO$_{500-800 \ °C}$ surfaces seeded with HOS cells (indicated by arrows) for 24 h. The following observations can be made:

- At 500 °C, cells present a round and flatted morphologies and the attachment is filopodia observed in Figure 50a-b.

- At 600 °C, cells present a round and flatted morphologies and the attachment is lamellipodium observed in Figure 50c-d.

- At 700 °C, cells present a round and flatted morphologies and the attachment is lamellipodium observed in Figure 50e-f.

- At 800 °C, cells present an elliptical and flatted morphologies the attachment is lamellipodium and filopodia observed in Figure 50g-h.
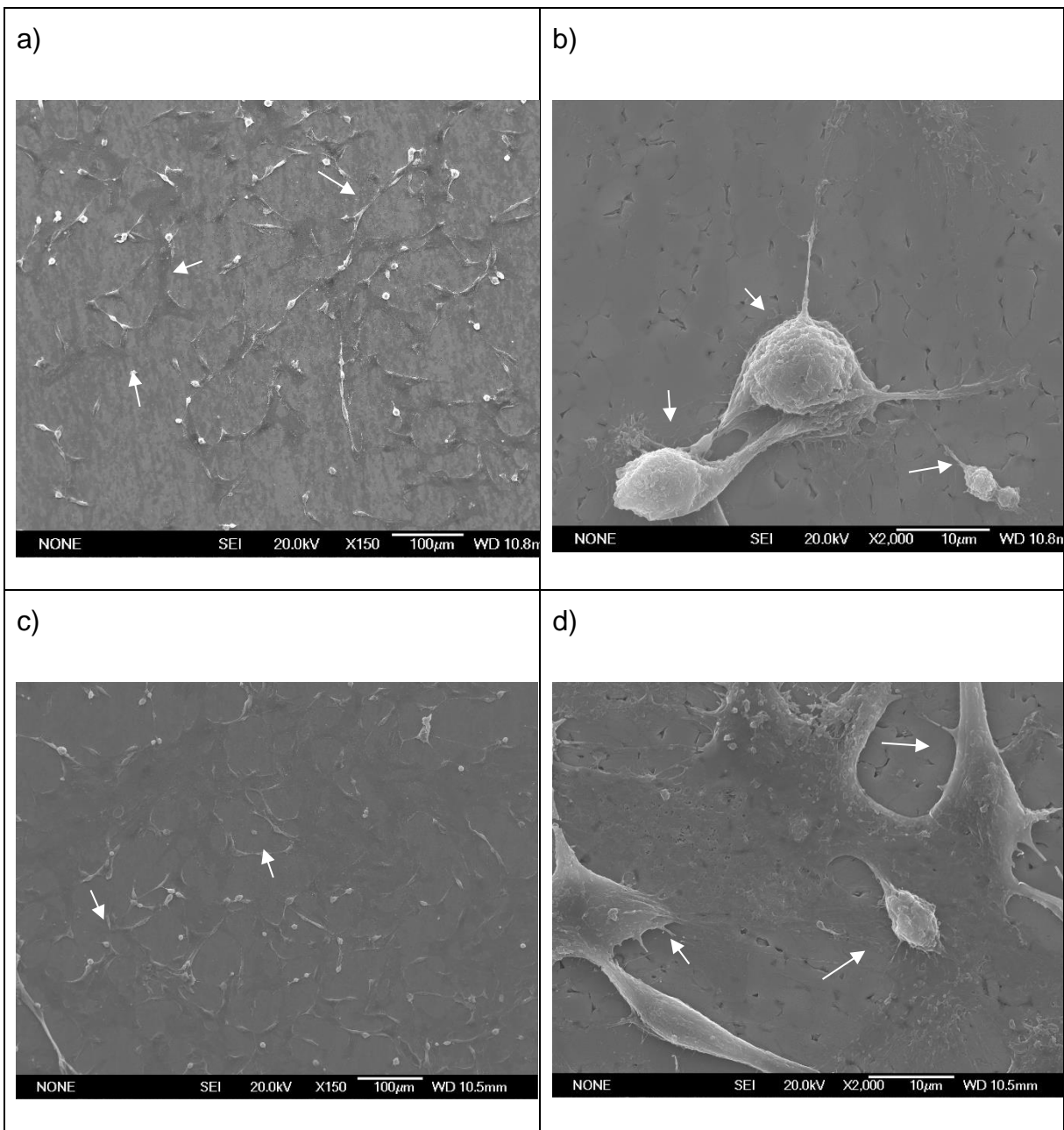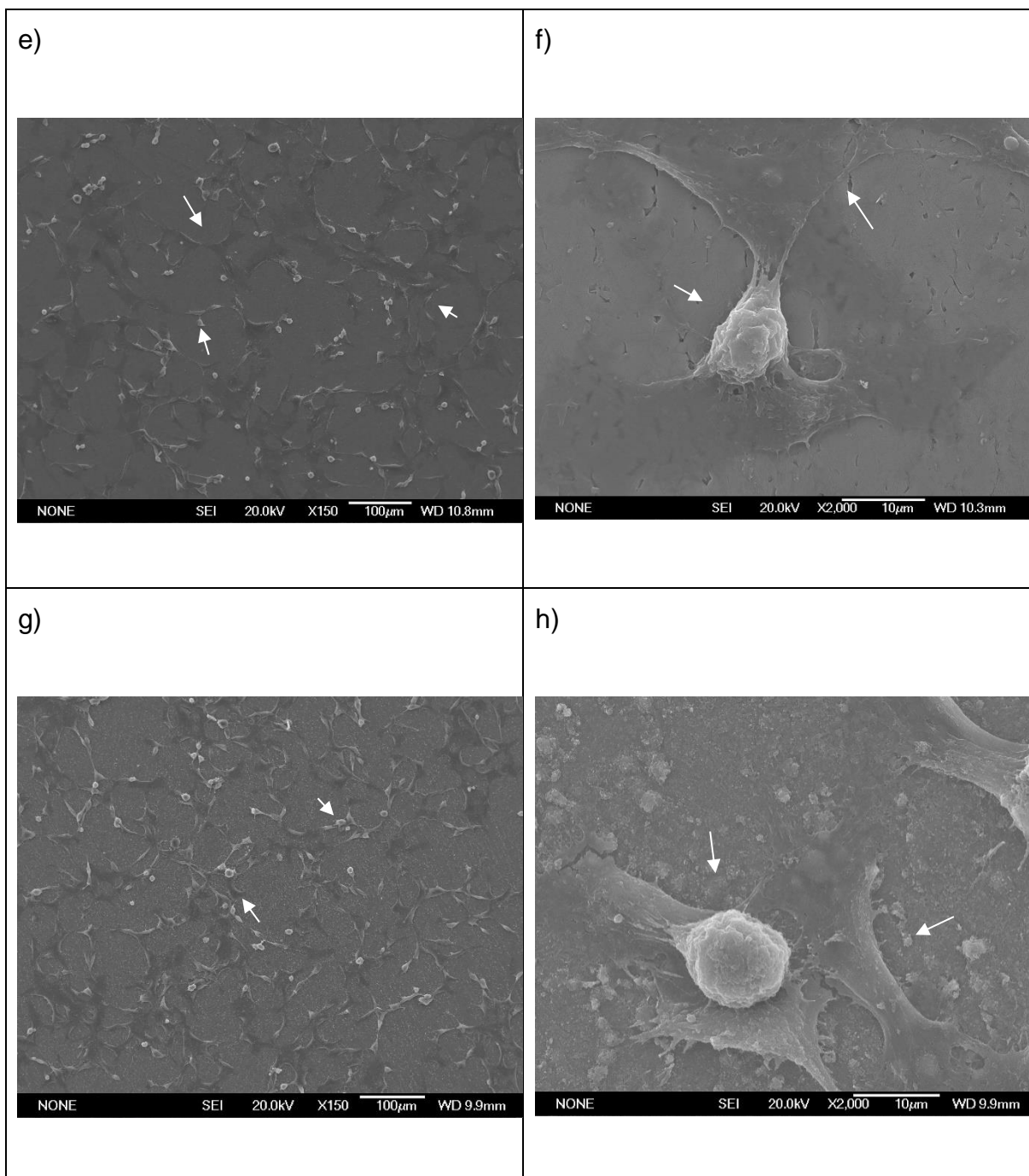
Figure 50 : SEM micrographs at low and high magnification of HOS seeded for 24 h on a) and b) TGL-TO$_{500\,°C}$, c) and d) TGL-TO$_{600\,°C}$, e) and f) TGL-TO$_{700\,°C}$, g) and h) TGL-TO$_{800\,°C}$.

3.4.3. Discussion

3.4.3.1. Topography and composition of titania gel layer formed with H_2O_2/HCl on polished Ti-6Al-4V

Pitting corrosion was obtained on Ti-6Al-4V surfaces after the treatment with H_2O_2 /HCl. This effect was described by Ferraris et al.[98] in Ti-6Al-4V surface exposed to H_2O_2 and explained that a local corrosion happened in the grain boundary between α and β Ti, inducing β surface grain disintegration and therefore pitting corrosion.

The TGL formed on the surface of Ti-6Al-4V when it was treated with H_2O_2 /HCl presented a porous structure on grains as shown in Figure 39a-b. According to previous researches, the TGL formed by H_2O_2 in acidic environments showed a porous surface in Ti and its alloys. Shi et al. [106] reported TGL porous structures on Ti-6Al-4V after the treatment with H_2O_2/HCl. Wang et al.[49] studied the formation of TGL on CpTi with different exposition times in 8.8 M H_2O_2 /0.1 M HCl at 80 °C. They showed that the TGL increased in thickness with a developed porosity when the exposure time in H_2O_2/HCl solution increased.

The X-ray diffractogram of TGL shown in Figure 41 exhibited α Ti phase on the surface but not the presence of TiO_2 crystals. Wu et al. [43] reported a broad peak between 22 and 28 ° using thin films XRD on CpTi after treated with H_2O_2 /Ta solution at 80 °C. They described that the peak was more likely to be an amorphous phase of TiO_2. In addition, it is shown in Figure 42 that the XPS spectrum of Ti 2p exhibited only TiO_x confirming the surface was oxidised.

HOS cells showed filopodia and lamellipodium attachment to TGL surfaces with round cell morphology. These variations on the cell adhesion could be attributed to the mixed

porous topography on the TGL surface. Zhu *et al.* [120] reported that porous Ti surfaces with micron and submicron sizes induced cells to anchor to the surfaces. They also presented a mechanism where both filopodium and lamellipodium structures were present on porous surfaces in different stages of the cell attachments. The filopodium was related to the sensing and adaptation of cell on the surfaces and the lamellipodium was related to the optimal and anchorable porous surface.

3.4.3.2. *Topography and composition of titania gel layer formed with H_2O_2/HCl followed by thermal oxidation on polished Ti-6Al-4V*

Pitting corrosion was observed in Figure 44 for TGL-TO$_{500-700 °C}$ whereas a layer of crystals was visualised on TGL-TO$_{800 °C}$. The structures of the chemically treated surface were lost with the increase of the TO temperature, and other structures due to the TO protruded on the surface as shown in Figure 44 and Figure 45. This similar effect was shown by Wang *et al.* [49] on the TGL formed with 8.8 M H_2O_2 /0.1 M HCl at 80 °C for 30 min and TO at 300, 400, 600, 700 and 800 °C on CpTi. They reported that the gel on the surfaces treated at high temperatures (700 and 800 °C) presented a densification.

TGL-TO$_{500-800 °C}$ surfaces exhibited an upward trend roughness with the increase of temperature as observed in Table 12 as well as the TiO$_x$ layer presented differences after the TO at each temperature as observed in Table 13. These effects on the surface were due to diffusion of Al, [141] diffusion of O and formation of crystals.[50]

Crystals detection on TGL-TO$_{500-800 °C}$ presented α Ti from the substrate and at higher temperatures exhibited rutile crystal phase. Similar observations were found by Wang

et al. [49] where Ti was detected in all the surfaces thermally treated and rutile in samples thermally treated at high temperature.

TGL-TO$_{500-600\ °C}$ did not show TiO$_2$ crystal phases. Kim *et al.* [147] reported that TGL obtained after treatment with NaOH and thermal treatment at 600 °C was amorphous. The broad lines in the XRD spectrum in Figure 46 around 24, 28 and 48° as well as the broad Raman peaks in Figure 47 at the vibrational modes of O and Ti shown that the oxide layer formed was amorphous.

Chemical elements analysed by XPS are shown in Table 14 .The Al % and V % only increased on TGL-TO$_{700\ °C}$ and TGL-TO$_{800\ °C}$ surfaces whereas the Al % and V % on TGL-TO$_{500\ °C}$ and TGL-TO$_{600\ °C}$ remained closer to the TGL sample as shown in Table 11. Sun and Wang [148] reported that the TGL formed with 30 w % H$_2$O$_2$ solution at 80 °C for 24 h on Ti-6Al-4V might act as a diffusion barrier from the substrate preventing Al and V ions release from there. After this observation and the results obtained in Table 14 it was possible to infer that the TGL in this thesis may also act as a barrier for the Al and V diffusion specially when the samples were TO at low temperatures.

Cell adhered on TGL-TO$_{500-800\ °C}$ showed round and flatted morphology and mainly lamellipodium attachment. Yang *et al.* [42] studied the adhesion of MC3T3-E1 osteoblast-like cells on CpTi surfaces with three different surface modifications. Cell adhesion suggested better spreading with more microvillus and better defined stress fibers in surfaces H$_2$O$_2$ /HCl and thermally treated than in surfaces with sandblasting and acid etching or simple polished. This spread cellular morphology is related with the strong interaction between cells and the surface implant.

3.5. Conclusions

Surfaces were modified in composition, topography and roughness by thermal oxidation and by H_2O_2/HCl treatment followed by thermal oxidation and it was observed that:

1) TO and TGL-TO presented an upward trend roughness with the increase of temperature. In addition, TGL-TO treated at low temperatures (500-600 °C) exhibited a porous surface due to the H_2O_2 treatment.

2) TiO_2 amorphous was predominant in passive TiO_x layers that became crystalline with the increase of temperature confirmed by XRD and Raman spectroscopy.

3) O diffusion increased with increasing treatment temperature.

4) Al and V diffusion occurred in all thermally treated samples excepted in TGL-$TO_{500 - 600 °C}$ suggesting the TGL is a barrier for Al and V diffusion from the substrate.

5) Adhesion of HOS was detected on all surfaces with some differences in the morphology and attachment depending on the surface structures and composition of the surface.

Chapter 4

Charge behaviour of titanium oxide surfaces, modified by thermal oxidation and chemically treated followed by thermal oxidation on polished Ti-6Al-4V, involving aqueous media

4.1. Introduction

Ti surfaces at physiological pH present a net negative charge [149] that can facilitate the adsorption of charged ions [150] and biomolecules on the oxide surface when in contact with aqueous solution [55]. The adsorption of ions, present in the physiological environment, onto the surface in many occasions induced to a hydroxyapatite layer formation that potentially attracted bone cells and contributed with bone formation.

There will usually exist a pH at which a metallic oxide surface in aqueous solution exhibits zero net charge; this pH is known as the isoelectric point (IEP). Below the IEP the metallic oxide has a positive charge ($-MH_2^+$) and above the IEP the metallic oxide has a negative charge ($-MO^-$). In the IEP all the OH^- moieties are un-dissociated [55]. The IEP of TiO_x is found between pH 4-6, and this range can be related with the OH^- density and impurities [108].

When an Ti implant is inserted in the body, the first interaction of its surface is with water due to the highly polar behaviour of TiO_2 [151]. Afterwards the surface interacts with other hydrated ions [54], such as Ca^{2+}, increasing the selective adsorption of proteins and in the best of the cases cell adsorption and maturation can take place to form [149]. TiO_2 chemically treated with H_2O_2 and thermally oxidised presents higher interaction with ions in aqueous solution than non-chemically treated surfaces [49].

In addition, the TiO_2 amphoteric behaviour can also induce the adsorption of other organic molecules such as charged amino acids (aspartic acid and lysine) [152,153],

peptides [123,154] and proteins [41,47,149]. Several studies found that the adsorption of these organic molecules on the surfaces is driven by electrostatic binding and therefore pH dependent [40,152,153].

4.2. Objective

The objective of this chapter was to study the behaviour of untreated and treated Ti surfaces involving aqueous environment and evaluated the changes in behaviour considering the composition of the oxide layer formed during treatments, the roughness and the pH of the environment.

4.3. Charge behaviour involving aqueous environment of native titanium oxide from polished Ti-6Al-4V and titanium oxides formed by thermal oxidation on polished Ti-6Al-4V

4.3.1. Specific objective

The objective of this section was to evaluate the charge behaviour of native TiO_x from polished Ti-6Al-4V and titanium oxides formed by thermal oxidation at 500, 600, 700 and 800 °C, in acidic, neutral and basic aqueous environment.

4.3.2. Results

Dynamic contact angle (DCA) titration and AFM force-distance measurements at pH 3, 5, 7 and 9 were performed on:

1) Native TiO_x ($nTiO_x$) on polished Ti-6Al-4V (MPT)

2) TiO_x form by thermal oxidation treated for 1h in air at 500, 600, 700 and 800 °C ($TO_{500-800\,°C}$)

AFM force-distance data was processed in order to determine the out-of-contact repulsion force (F_{rep}), jump-to force (F_{JT}), pull-off force (F_{PO}), and pull-off energy (W_{PO}),

4.3.2.1. Charge behaviour involving aqueous environment of native titanium oxide from polished Ti-6Al-4V

4.3.2.1.1. Contact angle titration measured on native titanium oxide from polished Ti-6Al-4V

DCA titration at pH 3, 5, 7 and 9 was measured MPT and the advancing contact angle

(θ_a) is shown in Figure 51. The MPT surface presents the highest contact angle at pH

5. At pH 3, pH 7 and pH 9, MPT surface presents a contact angle around 50 °.
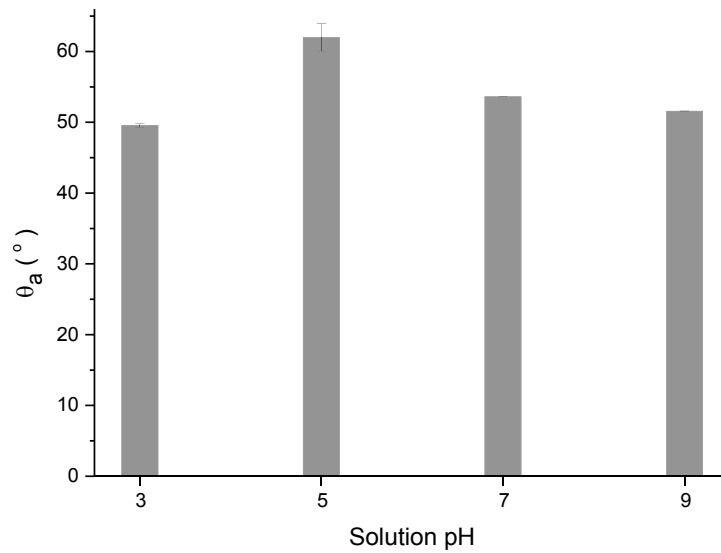
Figure 51: θ_a of MPT surfaces, measured at pH 3, 5, 7 and 9.

4.3.2.1.2. AFM force-distance curves measured on native titanium oxide from polished Ti-6Al-4V

4.3.2.1.2.1. Out-of-contact repulsion forces measured on native titanium oxide from polished Ti-6Al-4V

A Si cantilever was used to performed AFM force measurements. F_{rep} are measured

through the upwards deflection of the probe tip when is close to the surface of interest,

but not yet in contact.

F_{rep} measured at pH 3, 5, 7 and 9 on MPT surfaces are shown in Figure 52. F_{rep} increase with increasing solution pH. At pH 3, F_{rep} is close to 0 N/m with the minimum measured value. Between pH 3 and pH 9, repulsion forces increase gradually.
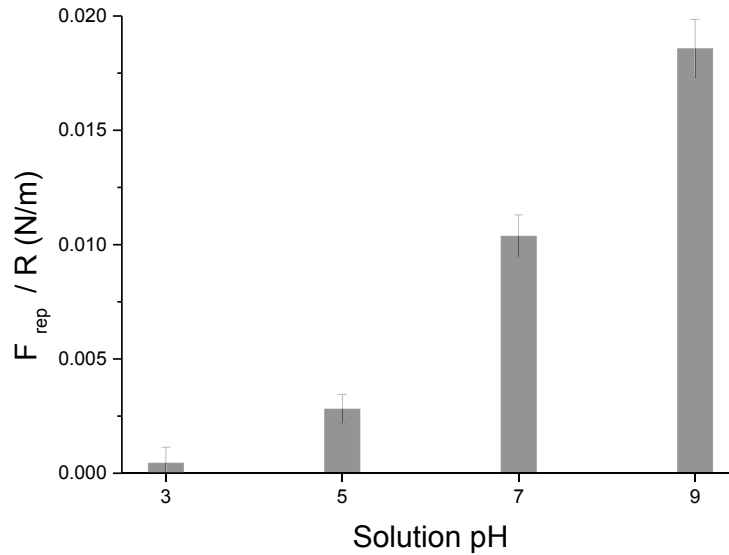
Figure 52: F_{rep} /R of MPT surface measured by AFM in aqueous solution at pH 3, 5, 7 and 9.

4.3.2.1.2.2. *Jump-to force measured on native titanium oxide from polished Ti-6Al-4V*

Attractive forces are measured as the cantilever jump-to occurs, and the cantilever tip has made contact with the surface of interest. The downwards deflection of the cantilever as contact is made is equivalent to the jump-to force (F_{JT}).

F_{JT} measured by AFM at pH 3, 5, 7 and 9 on MPT surface is shown in Figure 53. F_{JT} are higher when the pH is acid compared to the other pH solutions.
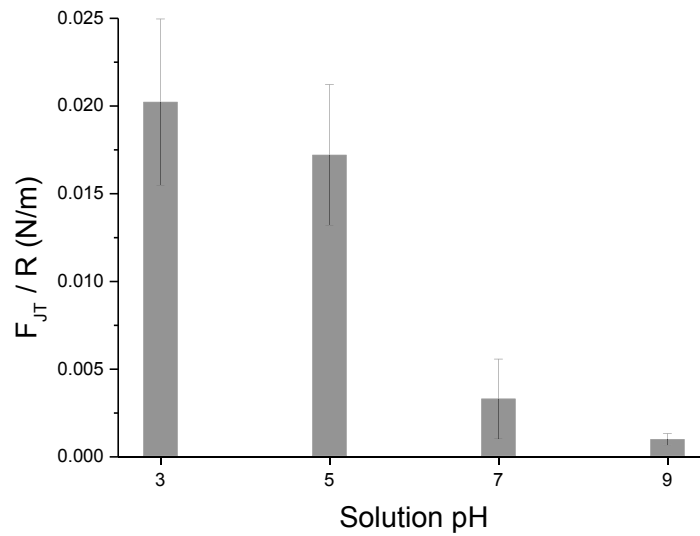
Figure 53: F_{JT}/ R of MPT surface measured by AFM in aqueous solution at pH 3, 5, 7 and 9.

4.3.2.1.2.3. *Pull-off force measured on native titanium oxide from polished Ti-6Al-4V*

Adhesion forces between the cantilever and the surface are measured when the cantilever is released from the surface of interest. This force is known as F_{PO}. The F_{PO} measured at pH 3, 5, 7 and 9 on MPT surface is shown in Figure 54 . In acid solution, F_{PO} or adhesion forces are higher compared to adhesion forces at pH 9. The F_{PO} slightly decreases between pH 7 and pH 3 compare with the decrease between pH 7 and pH 9.
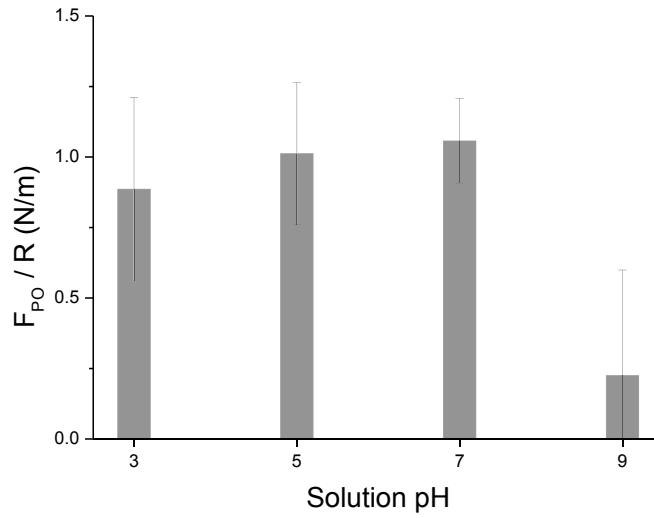
Figure 54: F_{PO} / R of MPT surface measured by AFM in aqueous solution at pH 3, 5, 7 and 9.

4.3.2.1.2.4. *Pull-off energy measured on native titanium oxide from polished Ti-6Al-4V*

The energy necessary to release the cantilever from the surface is known as W_{PO}.

W_{PO} measured at pH 3, 5, 7 and 9 on MPT surface is shown in Figure 55. The trend is similar to F_{PO}. At pH 3-7 W_{PO} is higher than at pH 9 solution. Slightly decrease is shown between pH 7 and pH 3 compared with the large decrease observed between pH 7 and pH 9.
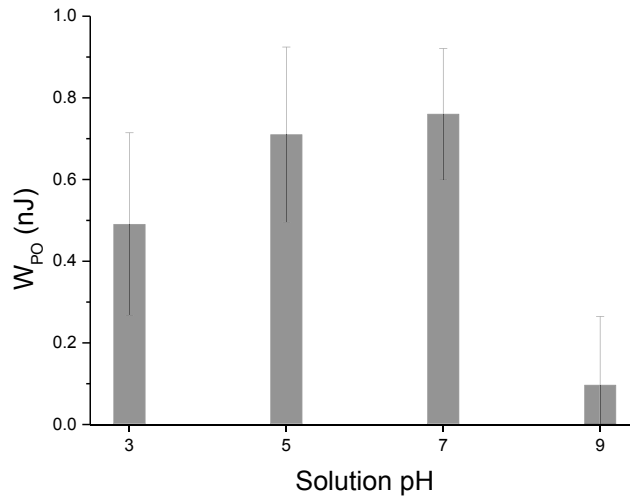
Figure 55: W_{PO} of MPT surface measured by AFM in aqueous solution at pH 3, 5, 7 and 9.

4.3.2.2. Charge behaviour involving aqueous environment of titanium oxides formed by thermal oxidation on polished Ti-6Al-4V

4.3.2.2.1. Contact angle titration measured on titanium oxides formed by thermal oxidation on polished Ti-6Al-4V

DCA titration at pH 3,5,7 and 9 was measured on $TO_{500\text{-}800\ °C}$ and the advancing contact angle (θ_a) is shown in Figure 56. Different trends are observed at each temperature:

- At 500 °C, the contact angle at pH 3 and 5 is around 46.5 °. At pH 7, slightly decreases and at pH 9 the contact angle is roughly 43.5 °. θ_a is shown in Figure 56a.

- At 600 °C, the contact angle at pH 3 and 5 is around 30 °. At pH 7, decreases around 23 ° and at pH 9 decreases around 19 °. θ_a is shown in Figure 56b.

- At 700 °C, the contact angle starts around 11 ° at pH 3 and remains below 10 ° for the other pH solutions. θ_a is shown in Figure 56c.

101

- At 800 °C, the contact angle maintains below 10 ° for all the pH scale. θ_a is shown in Figure 56d.
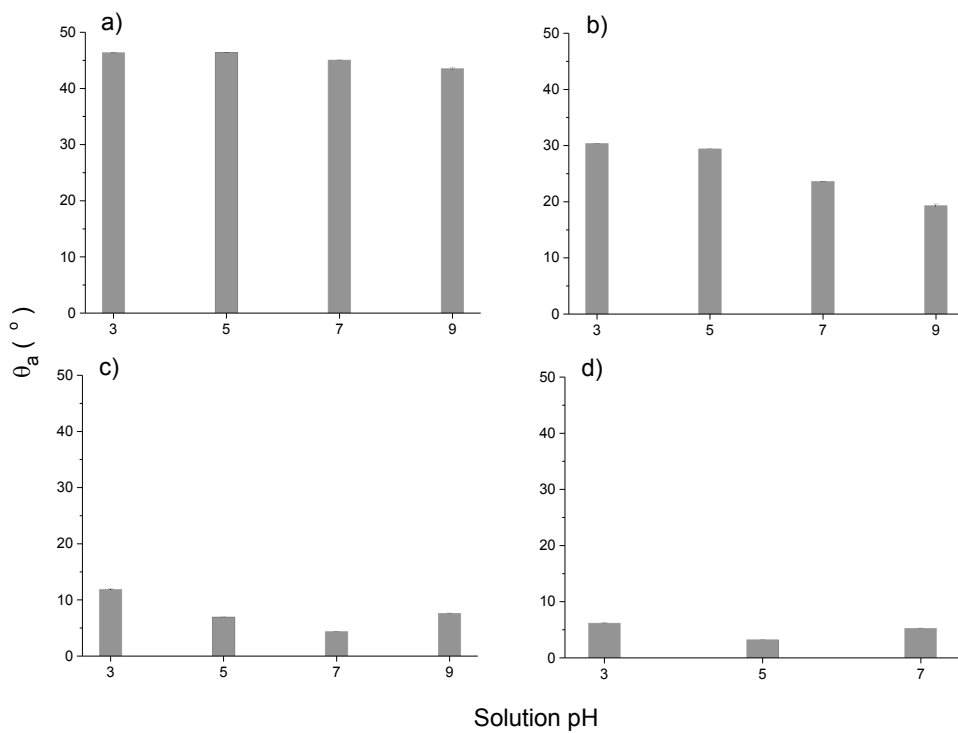
Figure 56: θ_a at pH 3, 5, 7, and 9 on a) $TO_{500\ °C}$, b) $TO_{600\ °C}$, c) $TO_{700\ °C}$ and d) $TO_{800\ °C}$.

4.3.2.2.2. AFM force-distance curve measured on titanium oxides formed by thermal oxidation on polished Ti-6Al-4V

4.3.2.2.2.1. Out-of-contact repulsion forces measured on titanium oxides formed by thermal oxidation on polished Ti-6Al-4V

F_{rep} measured on $TO_{500-800\ °C}$ are shown in Figure 57. F_{rep} change at each pH and are described for each temperature:

- At 500 °C, F_{rep} at pH 3 and 5 is close. At pH 7, the highest F_{rep} is present. At pH 9, F_{rep} slightly decreases from F_{rep} measured at pH 7. F_{rep} trend is shown in Figure 57a.

- At 600 °C, the highest F_{rep} is at pH 7. At pH 3 and 5, F_{rep} is close. At pH 9, F_{rep} slightly decreases from F_{rep} measured at pH 7. F_{rep} trend is shown in Figure 57b.

- At 700 °C, F_{rep} at pH 3, 5 and 7 are smaller than at pH 9. F_{rep} trend is shown in Figure 57c.

- At 800 °C, pH 3 and 7 present the lowest F_{rep}. At pH 5, the highest F_{rep} is present. F_{rep} trend is shown in Figure 57d.
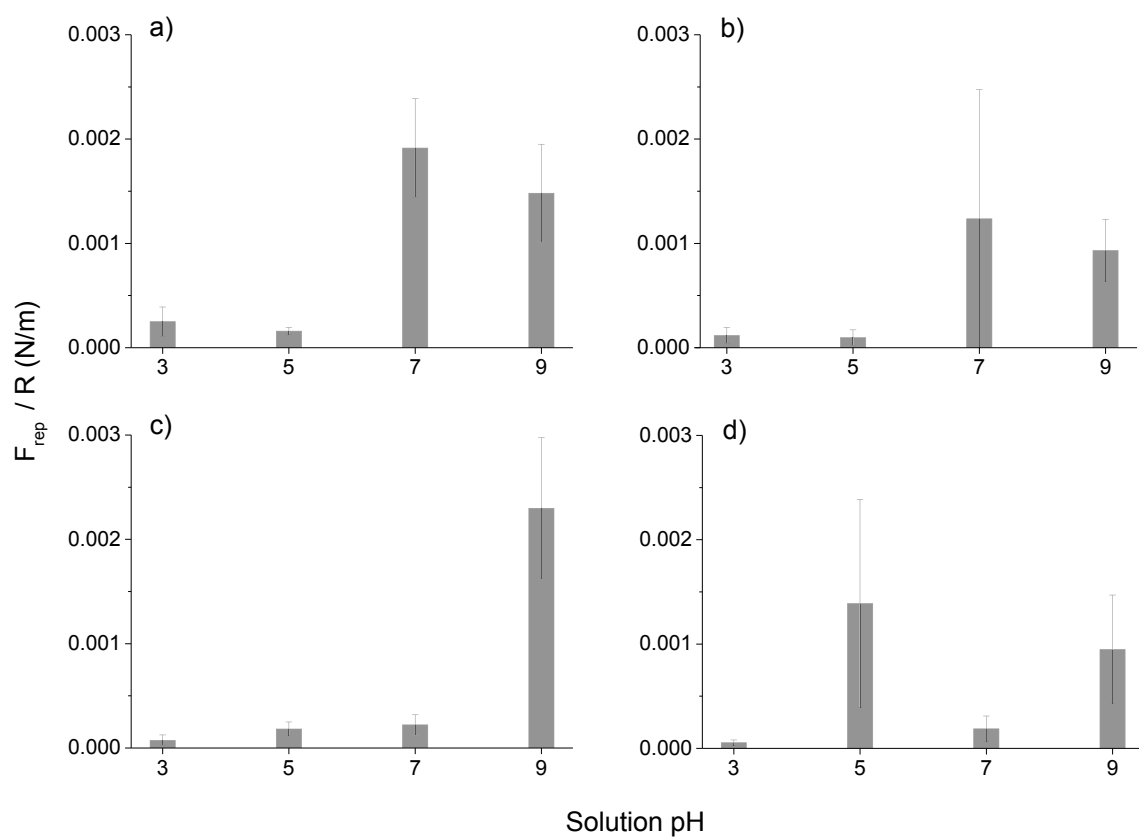
Figure 57: F_{rep} / R measured by AFM in aqueous solutions at pH 3, 5, 7 and 9 on a) $TO_{500\,°C}$, b) $TO_{600\,°C}$, c) $TO_{700\,°C}$ and d) $TO_{800\,°C}$.

4.3.2.2.2.2. Jump to force measured on titanium oxides formed by thermal oxidation on polished Ti-6Al-4V

F_{JT} measured by AFM on $TO_{500\text{-}800\ °C}$ are shown in Figure 58. All F_{JT} measured values are below 0.001 N/m. Each temperature shows a different trend:

- At 500 °C, the highest F_{JT} is at pH 3. The lowest value is at pH 5. At pH 7 and 9, F_{JT} is close. F_{JT} trend is shown in Figure 58a.

- At 600 °C, F_{JT} at pH 3 and 9 is close. At pH 5 and 7, F_{JT} is close. F_{JT} trend is shown in Figure 58b

- At 700 °C, F_{JT} at pH 3, 5, and 7 present smaller values than at pH 9. F_{JT} trend is shown in Figure 58c.

- At 800 °C, F_{JT} at pH 3, 5, and 7 present smaller values than at pH 9. F_{JT} trend is shown in Figure 58d.
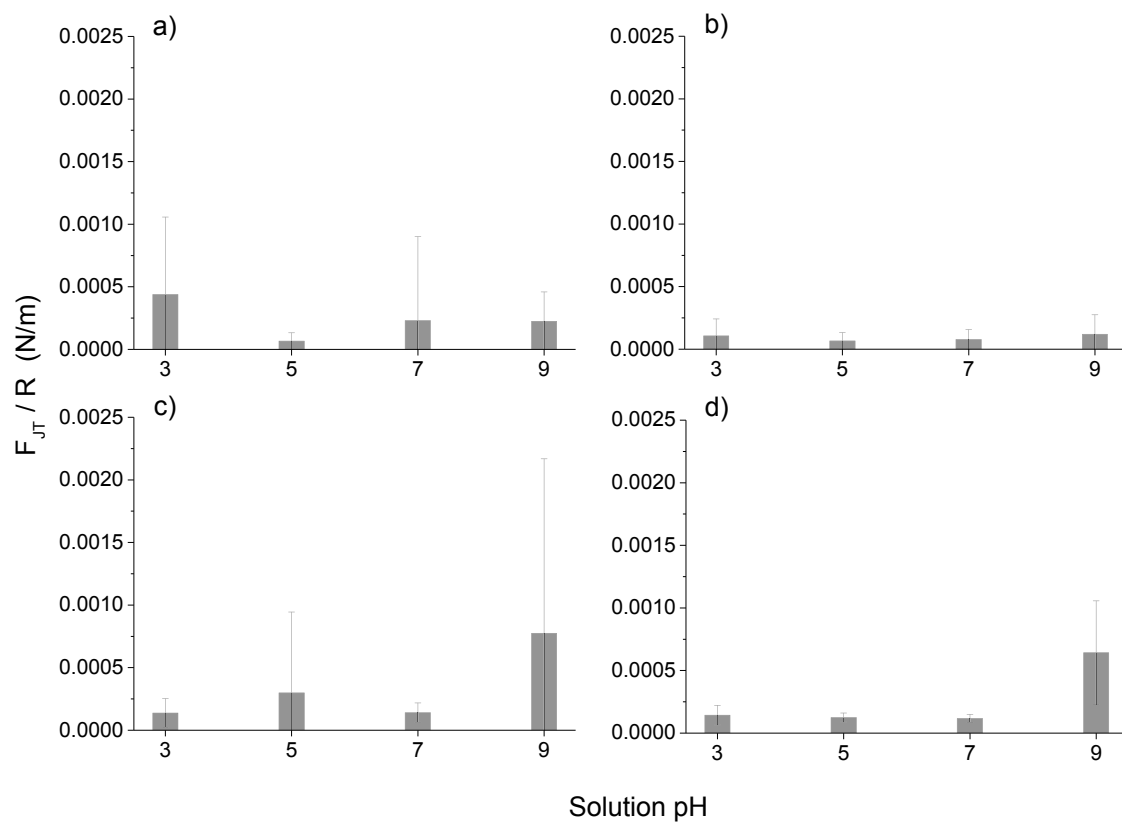
Figure 58: F_{JT} / R measurement by AFM in aqueous solution at pH 3, 5, 7 and 9 on a) $TO_{500\,°C}$, b) $TO_{600\,°C}$, c) $TO_{700\,°C}$ and d) $TO_{800\,°C}$.

4.3.2.2.2.3. Pull-off force measured on titanium oxides formed by thermal oxidation on polished Ti-6Al-4V

F_{PO} measured by AFM on $TO_{500-800\ °C}$ are shown in Figure 59. Different trends are detected at each temperature:

- At 500 °C, F_{PO} at pH 5 present the lowest valued. The highest F_{PO} is shown at pH 7. At pH 9, F_{PO} slightly decreases from the F_{PO} measured at pH 7. F_{PO} trend is shown in Figure 59a.

- At 600 °C, F_{PO} is the same at pH 3 and 5. At pH 9, the F_{PO} is the highest. F_{PO} trend is shown in Figure 59b.

- At 700 °C, F_{PO} at pH 3 and 7 is similar. At pH 5 and 9, F_{PO} value is close. F_{PO} trend is shown in Figure 59c.

- At 800 °C, the highest and lowest F_{PO} are measured at pH 3 and 5, respectively. F_{PO} trend is shown in Figure 59d.
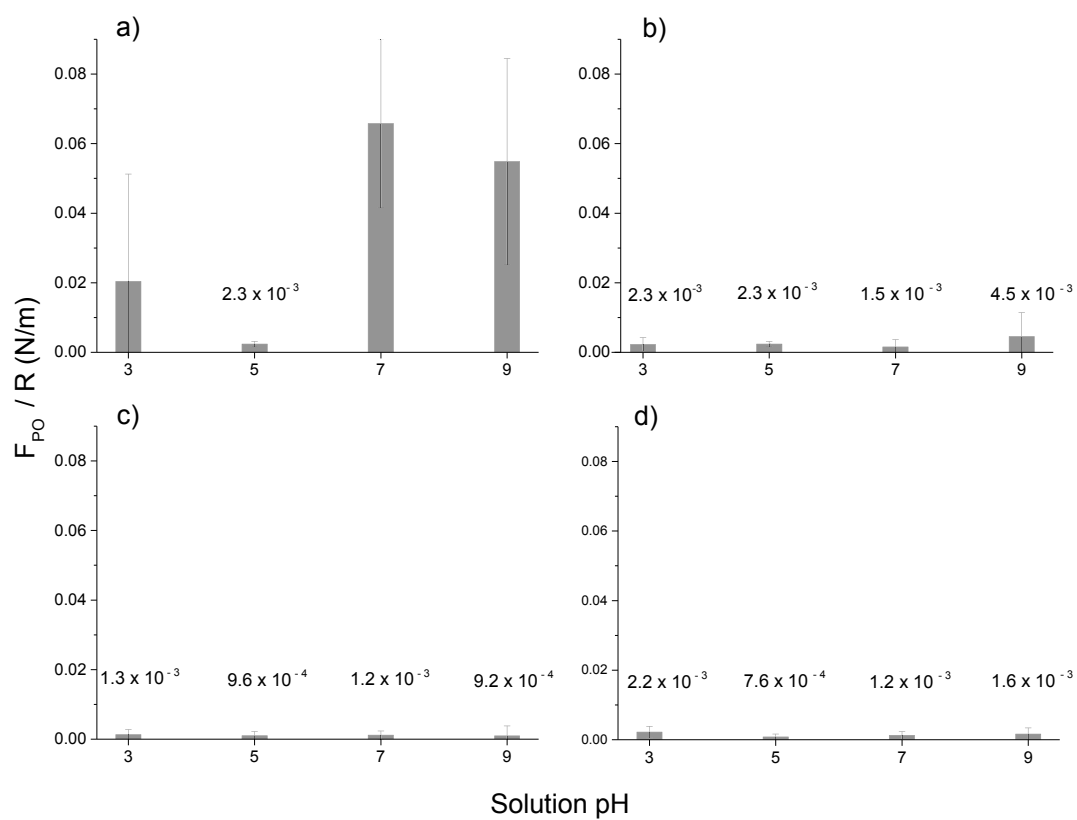
Figure 59: F_{PO} / R measured by AFM in aqueous solution at pH 3, 5, 7 and 9 on a) $TO_{500\,°C}$, b) $TO_{600\,°C}$, c) $TO_{700\,°C}$ and d) $TO_{800\,°C}$.

4.3.2.2.2.4. *Pull-off energy measured on titanium oxides formed by thermal oxidation on polished Ti-6Al-4V*

W_{PO} measured by AFM on TO $_{500\text{-}800\ °C}$ are shown in Figure 60. Different trends are observed at each temperature:

- At 500 °C, the highest W_{PO} is at pH 7. The lowest W_{PO} is at pH 5. W_{PO} trend is shown in Figure 60a.

- At 600 °C, W_{PO} at pH 3, 5, and 7 present similar values. At pH 9, W_{PO} present the highest value. W_{PO} trend is shown in Figure 60b.

- At 700 °C, the highest and lowest W_{PO} is at pH 5 and pH 9, respectively. At pH 3 and 7, W_{PO} present similar values. W_{PO} trend is shown Figure 60c.

- At 800 °C, W_{PO} values for all pH are below 0.15 fJ. W_{PO} trend is shown in Figure 60d.
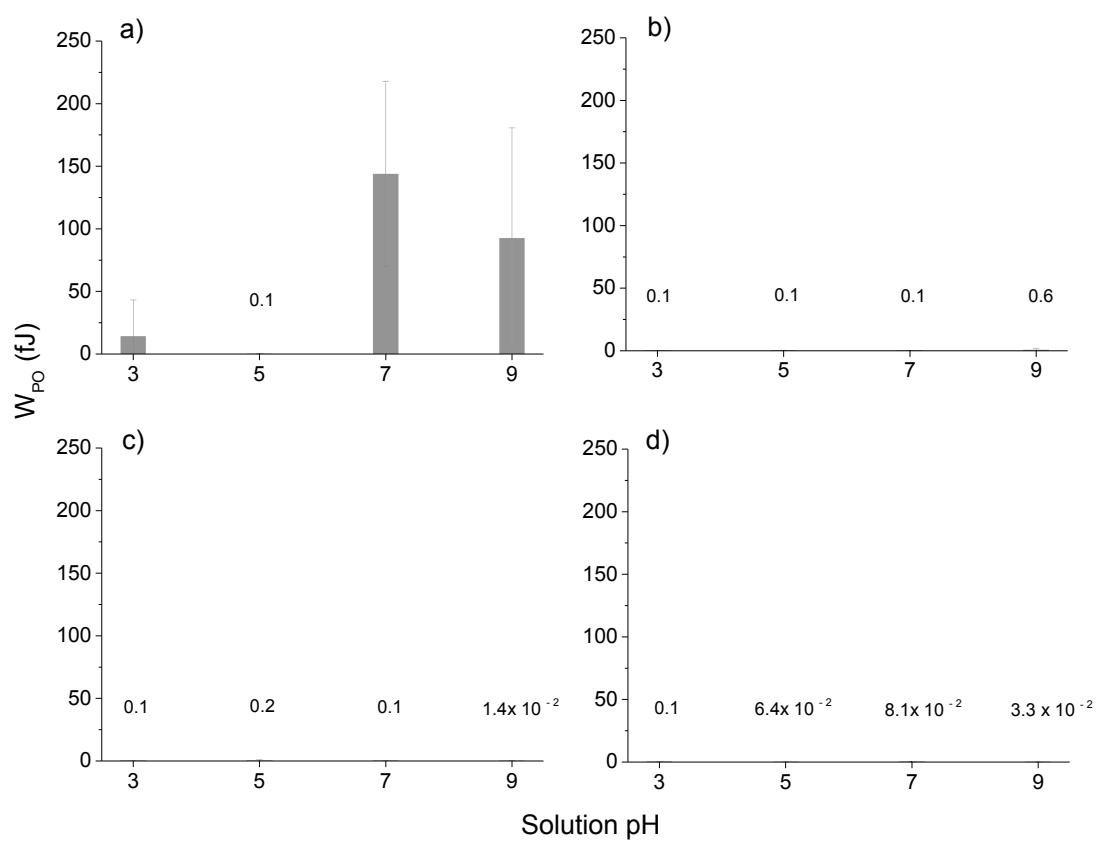
Figure 60: W_{PO} measured by AFM in aqueous solution at pH 3, 5, 7 and 9 on on a) $TO_{500\,°C}$, b) $TO_{600\,°C}$, c) $TO_{700\,°C}$ and d) $TO_{800\,°C}$.

4.3.3. Discussion

4.3.3.1. Charge behaviour involving aqueous environment of native titanium oxide from polished Ti-6Al-4V

The difference in contact angle obtained in surfaces at pH 3, 5, 7 and 9 was due to the change in the interfacial tension that was directly related with the intramolecular forces bounded by the solid and the contacting liquid [93]. The liquid surface tension of unbuffered water present insignificant changes for the addition of salt concentrations up to 1 M [155]. Consequently, changes in the contact angle titration behaviour could be attributed to the surface chemistry that interacts with the ionic content of the droplet [16,155].

In Figure 51, the θ_a of MPT surface shown higher contact angle at pH 5 than at other pH solutions. This maximum could be associated with the IEP of $nTiO_x$, as explained by Chau and Porter that in the absence of specific absorbed ions, the maximum angle in contact angle titration is related to the IEP [93]. This was also confirmed by McCafferty and Wightman that determined the IEP of Al_2O_3 and Cr_2O_3 as the maximum value obtained by contact angle titration [156]. According to the literature, the IEP of TiO_x could be found between pH 4–6 [157]. It has been also reported, that the IEP of TiO_x can be influenced by the hydroxyl groups density in the crystal phases, contamination and inclusion of ions [108]. For example the IEP of anatase powder can vary between pH 5.9 - 6.6 and for rutile powder between pH 4.7 – 6 [108]. Moreover, Roessler et al. [108] found that the surface IEP of native oxide on Ti-6Al-4V was around pH 4.4. Based on the information above, the use of contact angle titration could be a potential method to determine the IEP of MPT surfaces.

The AFM force-distance curves of MPT surfaces measured with a Si cantilever reinforce that the IEP point of the studied MPT surface can be around pH 5. The AFM adhesion analysis was performed with a Si cantilever that typically has a native SiO_2 with an IEP reported in some studies between pH 1 and 4 [158–160] and in some other studies at pH 3.9 [161,162]. For example, SiO_2 charge dependence of pH change and IEP reported by Raiteri *et al.* [159] is shown in Figure 61. The lowest F_{rep} of MPT surface shown in Figure 52 and the highest attraction force shown in Figure 53 is at pH 3, suggesting the cantilever was negatively charged and the MPT surface was positively charged. For solutions with higher pH than 5 it was expected that the negative charges of both SiO_2 and $nTiO_x$ of MPT surface increased in magnitude and this was verified with the measurement of the F_{rep} increasing with pH (from pH 5) and reaching the highest value at pH 9. The F_{rep} and attractive forces was also reported by Butt using an alumina probe and mica surface [163]. In this study the F_{rep} were detected when the pH was above 8.1 and the attraction forces occurred below pH 8.1. because the mica surface was negatively charged at the pH measured by Butt (between pH 3.1 and 10.4) and the alumina probe presented the IEP at pH 8.1 [163].
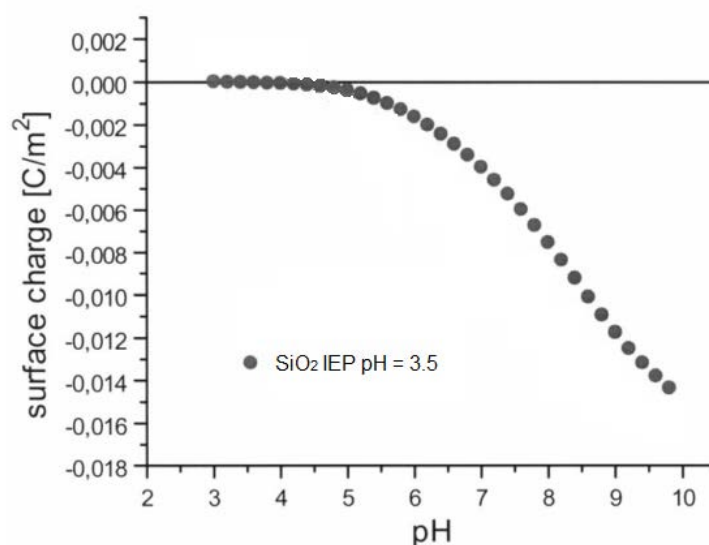
Figure 61: SiO$_2$ surface charge behaviour with the pH change and it IEP. In 1 mM KCl aqueous solution " adapted from reference [159]".

F$_{PO}$ on MPT surface, shown in Figure 54, presents the highest values at pH 5 and 7 but not at pH 9. These results can be explained with the fact that one of the surfaces are more negatively charged than the other suggesting that the effect of diffuse double-layer was involved in the interactions between the cantilever and the surface. Hence, the reduced negative charge surface (nTiO$_x$ of the MPT) present less attraction of water molecules than the large negative charge surface (SiO$_2$). This allows the forces in the aqueous interface interact generating larger adhesion forces at pH 5 and 7 compared with those at pH 9 where both surfaces were negatively charged. The reduction of the magnitude of the surface potential when the pH was closer to the IEP was reported by Walsh *et al.* [164] that experimented on surfaces and cantilever of the same TiO$_2$ coated material (IEP at pH 5.1) and observed that the surfaces at pH 6.5

113

present negatively charged but not as large as at pH 10 where the diffuse double-layer was large enough to repulse both surfaces.

4.3.3.2. *Charge behaviour involving aqueous environment of titanium oxides formed by thermal oxidation on polished Ti-6Al-4V*

Measurements of DCA and AFM force–distance curves are normally performed on smooth surfaces [164,165]. In this study the roughness RMS of surfaces treated above 600 °C, measured by AFM and discussed in the previous chapter for the accuracy of AFM in xyz directions, present values higher than 15 nm. These surfaces roughness together with the composition variation when the temperature of oxidation increases bring difficulties to measure the forces and surface tension using DCA and AFM force–distance curves techniques. Regardless of these surface properties, a general qualitative behaviour of TiO_x surfaces at pH 3, 5, 7, and 9 is presented below.

θ_a results of thermally oxidised samples present a decrease in contact angle when the temperature of oxidation increases and this trend occurs for all pHs. The decrease in contact angle can be attributed to 2 main phenomena associated to the oxidation temperature: the increment of Al and V on the surface by the diffusion of them from the substrate [47], and the increment of the contact area on the surface caused by the increased roughness [8].

θ_a of $TO_{500\ °C}$, shown in Figure 56a, presents high contact angle at pH 5 suggesting this is the IEP, whereas the literature for TiO_2 expects IEP to be between 5.4 and 6 [166]. The reason for the difference in IEP can be attributed to the fact that the $TO_{500\ °C}$ sample has a mixture of amorphous and crystal TiO_2 that can shift the IEP above pH 5.

F_{rep} of $TO_{500\,°C}$ and $TO_{600\,°C}$, shown in Figure 57a and b, are low at pH 3 and 5, and high at pH 7 and 9. This suggests both surfaces are positively charged below pH 5 and negatively charged above pH 5. The above results were in agreement with previous work done by MacDonald *et al.* [8] who reported that Ti-6Al-4V thermally treated at 600 °C showed F_{rep} (negatively charged surface) between pH 6 and 8.4.

F_{rep} of $TO_{700\,°C}$, shown in Figure 57c, exhibits low F_{rep} at pH 3, 5, and 7 and high F_{rep} at pH 9. The possible explanation for these results is that the surface is slightly positively charged below pH 7 due to the presence of Al_2O_3. At pH 9, the TiO_2 surface with Al enrichment tends to be negatively charged, and this could be associated with the fact that both IEPs of TiO_2 and Al_2O_3 are below pH 9 [167].

The attraction force or F_{JT} of $TO_{500\,°C}$ is the highest at pH 3 and the lowest at pH 5, and at pH 7 and 9 the values are intermediate as shown in Figure 58a. The trend of the measurements could have been expected to be similar to those in the MPT surface, however the presence of Al_2O_3 [168] in the surface alters the results. The IEP of Al_2O_3 is around pH 9 while the TiO_2 is around pH 5 reducing the overall surface positive charge with the increase of pH, but still maintaining a slight positive charge at pH 9 [108]. At the same time the cantilever negative charges increase with the increment of pH and generate an attraction force.

F_{PO} and W_{PO} of $TO_{500\,°C}$, show in Figure 59a and Figure 60a, exhibit large values at pH 7 and 9, suggesting the cantilever and the surface charge have a large diffuse double-layer effect. At pH 5, F_{PO} is the lowest and W_{PO} is not detected. These results can be associated with slight negatively and positively charged TiO_2-Al_2O_3-V_2O_5 (IEP V_2O_5 =

1.4 [169]) surface close to pH 5 interacting with a negatively charged SiO_2 cantilever but with a reduced potential magnitude [8].

F_{PO} and W_{PO} of $TO_{600\,°C}$, shown in Figure 59b and Figure 60b, display similar values at pH 3, 5, and 7 suggesting the IEP of the sample shift from around pH 5 towards pH 7 due to the change on the sample composition. At pH 9, F_{PO} and W_{PO} are the highest, suggesting the TiO_2- Al_2O_3- V_2O_5 surface is negatively charged and therefore the diffuse double-layer is having effect on the surface and cantilever [164].

The effect of the roughness in AFM force-distance measurements can affect the result because of 2 reasons: on the one hand, the cantilever probe size can be smaller than the asperities conducting an increment or decrement in the contact area, on the other hand, the cantilever probe size could be larger than the asperities thus some areas on the surface could be not in contact with the tip [170,171], schema shown in Figure 62. For example, this effect is observed in the study of surfaces treated at 700 °C where the F_{PO} is similar at all pHs and at 800 °C where the F_{PO} is highest at pH 3, shown in Figure 59c and d. The detected variations of F_{PO} suggest the results are not replicable when surfaces are rough.
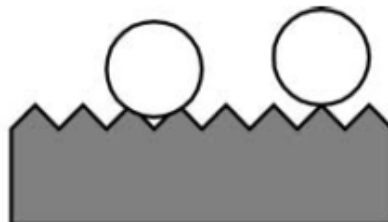
Figure 62: Schema of cantilever tip larger in size than the asperities on the surface, and the interaction possibilities [170].

4.4. Charge behaviour involving aqueous environment of titania gel layer formed with H_2O_2/HCl on polished Ti-6Al-4V and titania gel layer followed by thermal oxidation on polished Ti-6Al-4V

4.4.1. Specific objective

The objective of this section was to evaluate the charge behaviour of titanium oxides chemically treated on polished Ti-6Al-4V and chemically treated on polished Ti-6Al-4V followed by thermal oxidation at 500, 600, 700 and 800 °C, in acidic, neutral and basic aqueous environment.

4.4.2. Results

Aqueous DCA titration and AFM force-distance curves, out-of-contact F_{rep}, F_{JT}, F_{PO} and W_{PO} measured at pH 3, 5, 7 and 9 were performed on:

1) Titania gel layer prepared via 8.8 M H_2O_2 /0.1 M HCl at 80 °C for 30 min (TGL)

2) Titania gel layer followed by thermal oxidation at 500, 600, 700 and 800 °C

   (TGL-TO$_{500\text{-}800\,°C}$)

4.4.2.1. Charge behaviour involving aqueous environment of titania gel layer formed with H_2O_2/HCl on polished Ti-6Al-4V

4.4.2.1.1. Contact angle titration measured on titania gel layer formed with H_2O_2/HCl on polished Ti-6Al-4V

DCA titration at pH 3, 5, 7 and 9 on TGL was measured and the advancing contact angle (θ_a) is shown in Figure 63. At pH 3, the highest contact angle is measured on TGL surfaces around 21 °. Contact angle decreases between pH 3 and 7 and then slightly increases at pH 9.
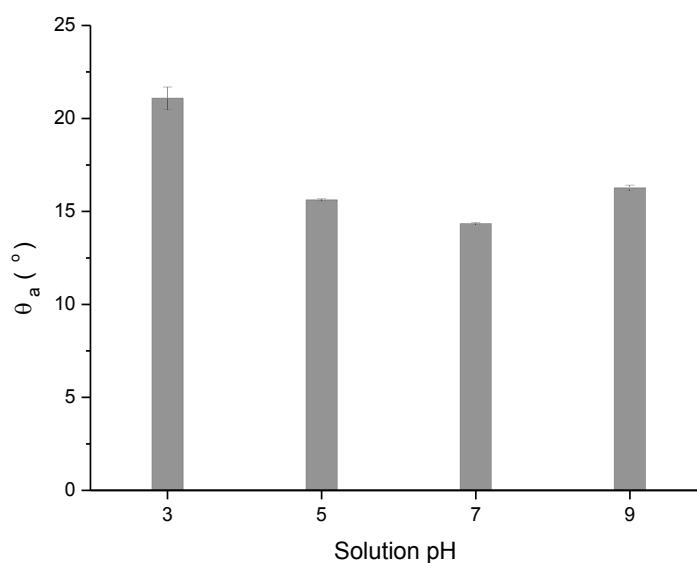
Figure 63: θ_a measured at pH 3, 5, 7 and 9 on TGL surfaces.

4.4.2.1.2. AFM force-distance curves measured on titania gel layer formed with H₂O₂/HCl on polished Ti-6Al-4V

4.4.2.1.2.1. Out-of-contact repulsion forces measured on titania gel layer formed with H₂O₂/HCl on polished Ti-6Al-4V

F_{rep} measured at pH 3, 5, 7 and 9 by AFM on TGL surfaces are shown in Figure 64.

The tendency of F_{rep} is to increase when the pH become alkaline.
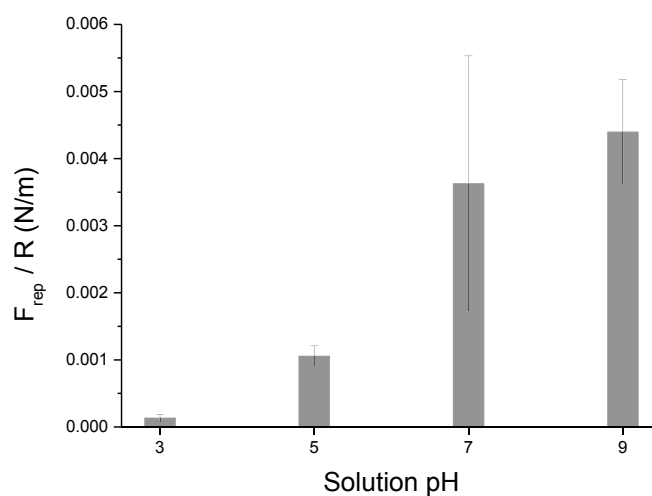
Figure 64: F_{rep} / R measured by AFM in aqueous solution at pH 3, 5, 7 and 9 on TGL surfaces.

4.4.2.1.2.2. *Jump to force measured on titania gel layer fromed with H_2O_2/HCl on polished Ti-6Al-4V*

F_{JT} or attraction force measured at pH 3, 5, 7, and 9 by AFM on TGL surfaces is shown in Figure 65. The highest F_{JT} is observed at pH 9 and the lowest F_{JT} is measured at pH 5.
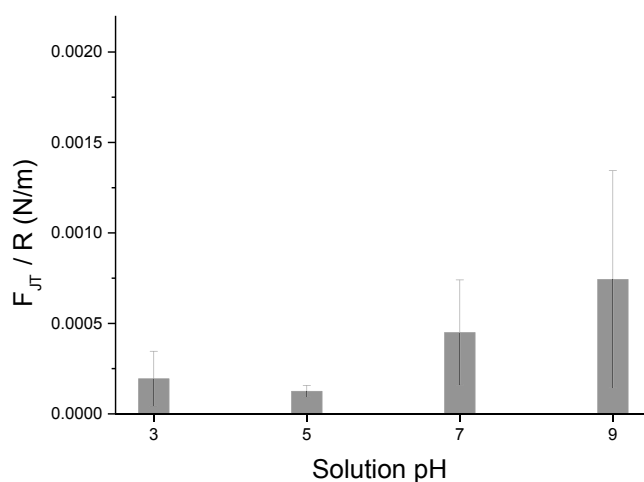
Figure 65: F_{JT} / R measured by AFM in aqueous solution at pH 3, 5, 7 and 9 on TGL surfaces.

4.4.2.1.2.3. Pull-off force measured on titania gel layer fromed with H_2O_2/HCl on polished Ti-6Al-4V

F_{PO} measured at pH 3, 5, 7 and 9 by AFM on TGL surfaces are shown in Figure 66.

Higher values of F_{PO} are present at pH 3 and 9 compared to the measured F_{PO} at pH

5 and 7.
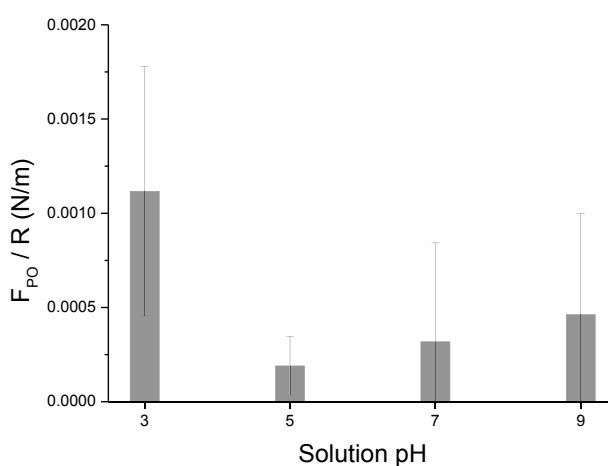
Figure 66: F_{PO} / R measured by AFM in aqueous solution at pH 3, 5, 7 and 9 on TGL surfaces.

4.4.2.1.2.4. Pull-off energy measured on titania gel layer fromed with H_2O_2/HCl on polished Ti-6Al-4V

W_{PO} measured at pH 3, 5, 7, and 9 By AFM on TGL surfaces are shown in Figure 67.

W_{PO} maintains low values in acid and neutral pH, and slightly increases its value at pH

9.
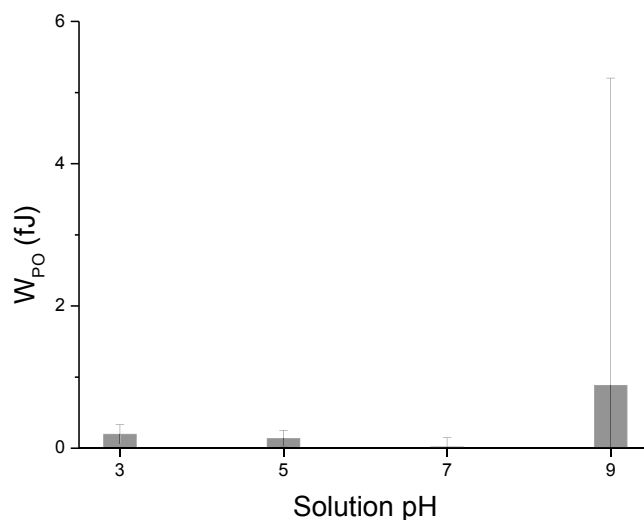
Figure 67: W_{PO} measured by AFM in aqueous solution at pH 3, 5, 7 and 9 on TGL surfaces.

4.4.2.2. Charge behaviour involving aqueous environment of titania gel layer formed with H_2O_2/HCl followed by thermal oxidation on polished Ti-6Al-4V

4.4.2.2.1. Contact angle titration measured on titania gel layer formed with H_2O_2/HCl followed by thermal oxidation on polished Ti-6Al-4V

DCA titration at pH 3,5, 7 and 9 was measured on TGL-TO$_{500\text{-}800\ °C}$ and advancing contact angle (θ_a) is shown in Figure 68. Different trends are observed at each temperature:

- At 500 °C, the highest contact angle is found at pH 7 with a measured value of 38 °. Contact angle increases between pH 3 and pH 7. At pH 9, the contact angle slightly decreases. θ_a is shown in Figure 68a.

- At 600 °C, the contact angle increases between pH 3 and 5 and maintains similar values between pH 5 and pH 9. Contact angle is between 16 and 20 °. θ_a is shown in Figure 68b.

121

- At 700 °C, the highest contact angle is at pH 5 with a measured value of 16 °. On the other hand, the lowest contact angle is at pH 7 with a measured value of 9 °. At pH 3 and 9, contact angle measured values are close to the highest measured value. θ_a is shown in Figure 68c.

- At 800 °C, contact angle behaves in a similar way across the pH scale, from acid to alkaline. At pH 3, 5 and 9, measured contact angle is between 3.4° and 3.8 °. Except at pH 7 where the contact angle decreases in 1 °. θ_a is shown in Figure 68d.
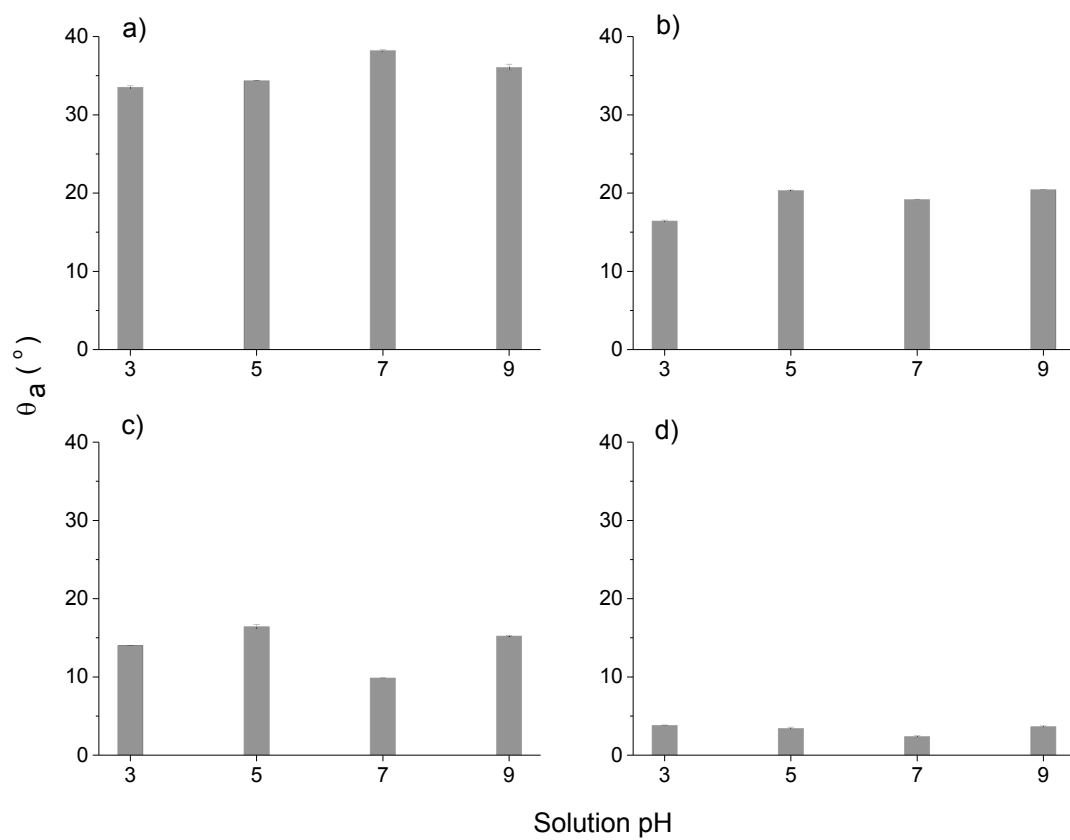
Figure 68: θ_a at pH 3, 5, 7, and 9 on a) TGL-TO$_{500\,°C}$, b) TGL-TO$_{600\,°C}$, c) TGL-TO$_{700\,°C}$ and d) TGL-TO$_{800\,°C}$.

4.4.2.2.2. AFM force – distance curves measured on titania gel layer formed with H_2O_2/HCl followed by thermal oxidation on polished Ti-6Al-4V

4.4.2.2.2.1. Out-of-contact repulsion force measured on titania gel layer formed with H_2O_2/HCl followed by thermal oxidation on polished Ti-6Al-4V

F_{rep} measured by AFM on TGL-TO$_{500\text{-}800\ °C}$ are shown in Figure 69. Similar F_{rep} trends are observed after thermally treated at 500 °C and 600 °C. Samples are described at each temperature:

- At 500 °C, F_{rep} at pH 3, 5 and 7 is smaller than at pH 9. F_{rep} trend is shown in Figure 69a.

- At 600 °C, F_{rep} at pH 3, 5 and 7 is smaller than at pH 9. F_{rep} trend is shown in Figure 69b.

- At 700 °C, the highest F_{rep} is at pH 9. On the other hand, the lowest F_{rep} is at pH 3. F_{rep} at pH 5 is higher than F_{rep} at pH 7. F_{rep} trend is shown in Figure 69c.

- At 800 °C, F_{rep} increases when pH becomes alkaline. F_{rep} trend is shown in Figure 69d.
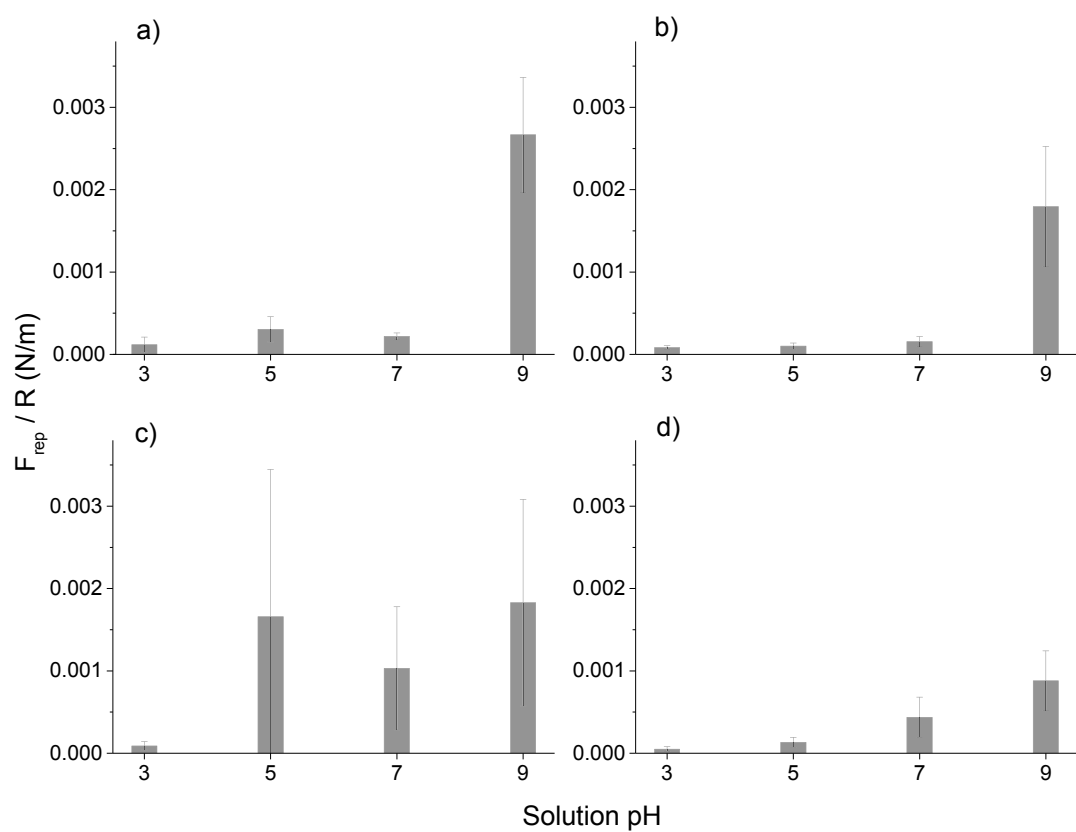
Figure 69: F_{rep} /R measured by AFM in aqueous solution pH at 3, 5, 7 and 9 on a) TGL-TO$_{500\ °C}$, b) TGL-TO$_{600\ °C}$, c) TGL-TO$_{700\ °C}$ and d) TGL-TO$_{800\ °C}$.

4.4.2.2.2.2. Jump to force measured on titania gel layer formed with H_2O_2/HCl followed by thermal oxidation on polished Ti-6Al-4V

F_{JT} samples measured by AFM on TGL-TO$_{500\text{-}800\,°C}$ are shown in Figure 70. It is possible to observe similar trends in one side at 500 and 600 °C and in the other side at 700 °C and 800 °C. Samples are described at each temperature:

- At 500 °C, the highest F_{JT} is at pH 5. F_{JT} at pH 3, 7 and 9 is similar. F_{JT} trend is shown in Figure 70a.

- At 600 °C, the highest F_{JT} is at pH 5. The lowest F_{JT} is at pH 3. F_{JT} trend is shown in Figure 70b.

- At 700 °C, F_{JT} is higher above neutral pH than acid pH. F_{JT} trend is shown in Figure 70c.

- At 800 °C, F_{JT} is similar at pH 3 and 5. At pH 7 and 9, F_{JT} is higher than mentioned pH and similar in value. F_{JT} trend is shown in Figure 70d.
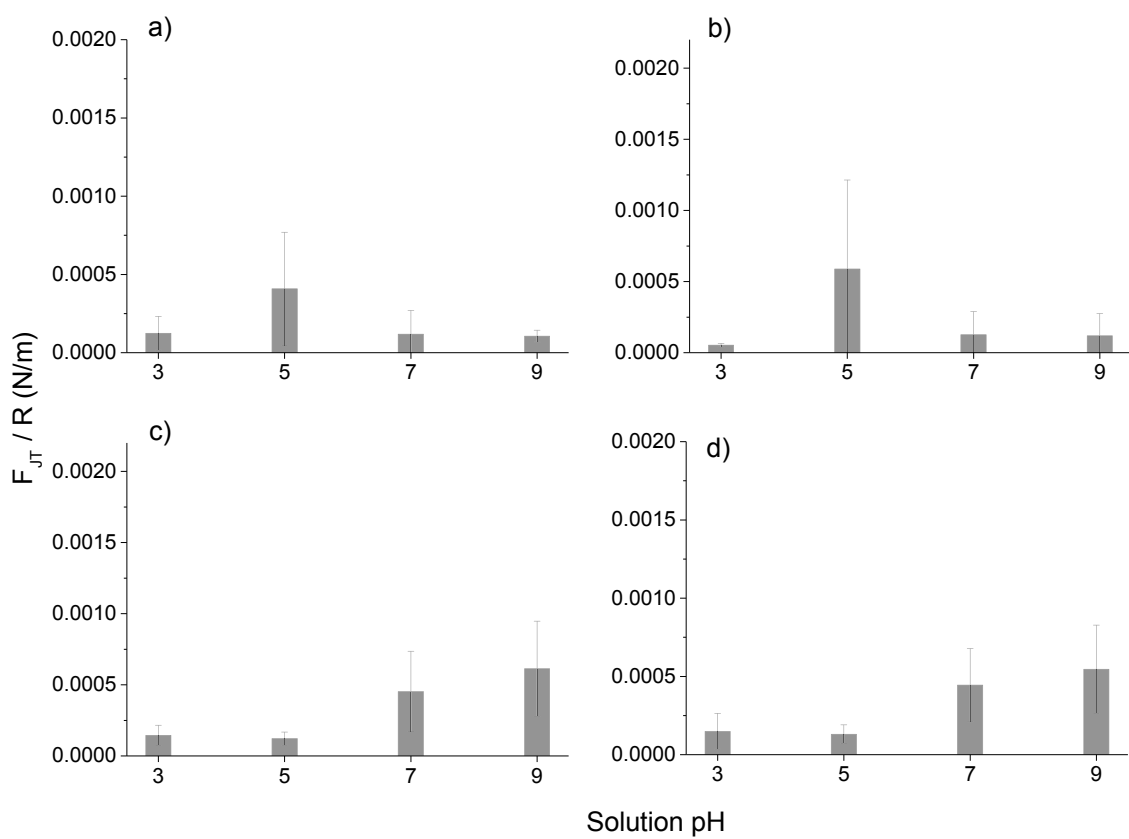
Figure 70: F_{JT} / R measured by AFM in aqueous solution pH at 3, 5, 7 and 9 on a) TGL-TO$_{500\ °C}$, b) TGL-TO$_{600\ °C}$, c) TGL-TO$_{700\ °C}$ and d) TGL-TO$_{800\ °C}$.

4.4.2.2.2.3. Pull-off force measured on titania gel layer formed with H_2O_2/HCl followed by thermal oxidation on polished Ti-6Al-4V

F_{PO} measured by AFM on TGL-TO$_{500\text{-}800\,°C}$ are shown in Figure 71. Samples are described at each temperature:

- At 500 °C, the highest F_{PO} is at pH 5. At pH 9, the lowest F_{PO} is detected. F_{PO} trend is shown in Figure 71a.

- At 600 °C, the highest F_{PO} is at pH 5. At pH 7, the lowest F_{PO} is detected. F_{PO} trend is shown in Figure 71b.

- At 700 °C, the highest F_{PO} is at pH 3. At pH 5 and 7, F_{PO} decreases. At pH 9, F_{PO} increases. F_{PO} trend is shown in Figure 71c.

- At 800 °C, the highest F_{PO} is at pH 3. At pH 5 and 7, F_{PO} slightly decreases. At pH 9, F_{PO} remains equal to the one measured in neutral pH. F_{PO} trend is shown in Figure 71d.
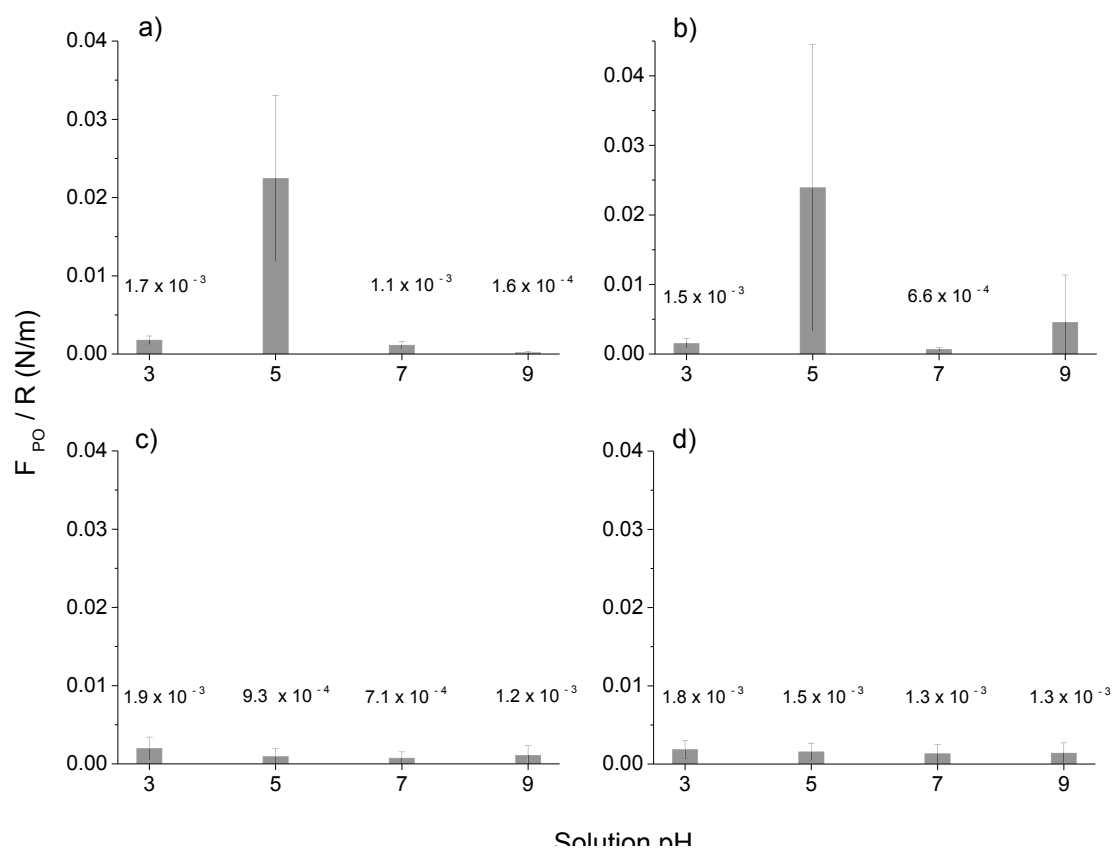
Figure 71: F_{PO} / R measured by AFM in aqueous solution pH at 3, 5, 7 and 9 on a) TGL-TO$_{500\,°C}$, b) TGL-TO$_{600\,°C}$, c) TGL-TO$_{700\,°C}$ and d) TGL-TO$_{800\,°C}$.

4.4.2.2.2.4. *Pull-off energy measured on titania gel layer formed with H_2O_2/HCl followed by thermal oxidation on polished Ti-6Al-4V*

W_{PO} measured by AFM on TGL-TO$_{500-800 \text{ °C}}$ are shown in Figure 72. Different trends are observed at each temperature:

- At 500 °C, the highest W_{PO} is at pH 5. W_{PO} trend is shown in Figure 72a.

- At 600 °C, the highest W_{PO} is at pH 5. W_{PO} trend is shown in Figure 72b

- At 700 °C, the highest W_{PO} is at pH 3. At pH 5, 7 and 9, W_{PO} slightly decreases. W_{PO} trend is shown in Figure 72c.

- At 800 °C, W_{PO} at pH 7, present the lowest value. W_{PO} trend is shown in Figure 72d.
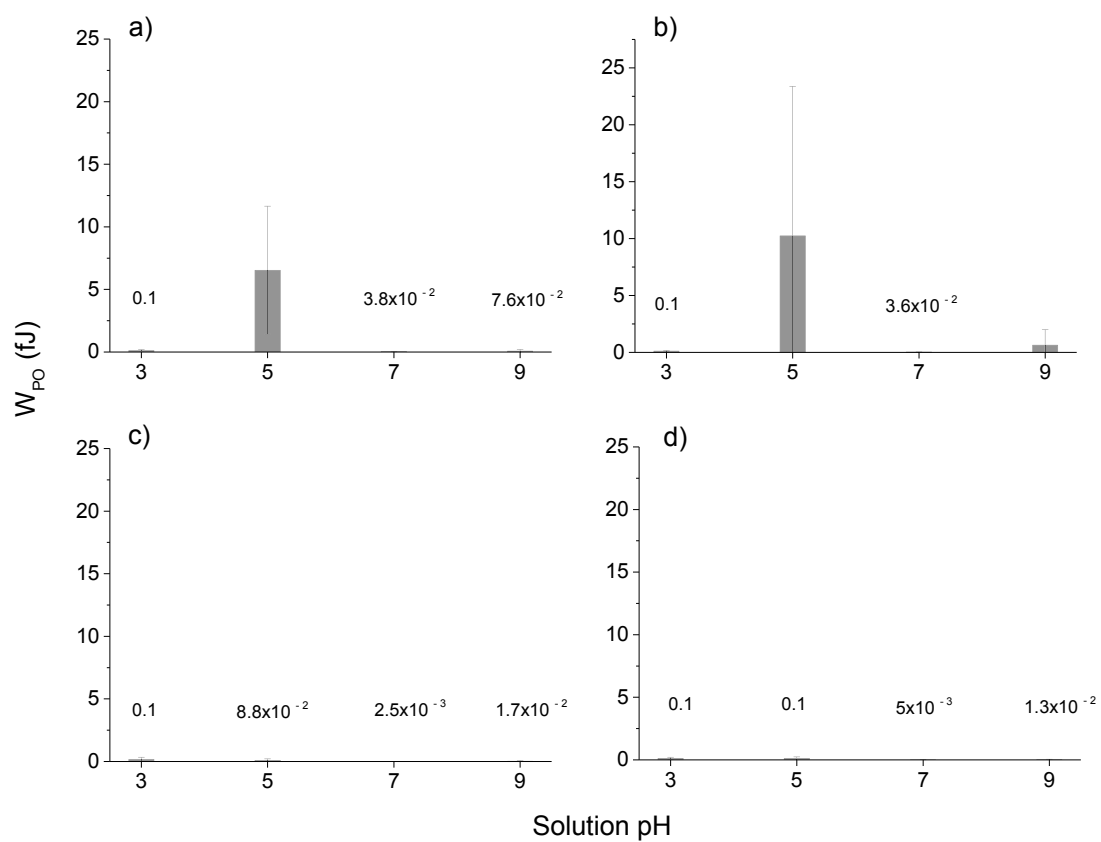
Figure 72: W_{PO} measured by AFM in aqueous solution pH at 3, 5, 7 and 9 on a) TGL-$TO_{500\,°C}$, b) TGL-$TO_{600\,°C}$, c) TGL-$TO_{700\,°C}$ and d) TGL-$TO_{800\,°C}$.

4.4.3. Discussion
4.4.3.1. Charge behaviour involving aqueous environment of titania gel layer formed with H_2O_2/HCl on polished Ti-6Al-4V

θ_a of TGL, shown in Figure 63, exhibited a range of contact angle for all pH between 14 -21 ° compared to the measured range of MPT surface of 49-61 °. These results were also observed by McDonald *et al.* [47] and Takemoto *et al.* [172] where they confirmed that samples treated with H_2O_2 presented lower contact angle than the sample before exposure to H_2O_2. This difference in θ_a between TGL and MPT surfaces could be attributed to the titania gel composition and topography that includes pitting corrosion, porosity [49], and etched structures.

4.4.3.2. Charge behaviour involving aqueous environment of titania gel layer formed by H_2O_2/HCl followed by thermal oxidation on polished Ti-6Al-4V

TGL-TO$_{500-800 °C}$ present different topography and in some cases combination of pitting corrosion, porous surfaces and crystal type structures. When MPT surfaces are H_2O_2 and thermally treated, the surface presented an increased roughness [47,48]. At the same time, the composition of the surface varied with the temperature presenting in proportions Ti-peroxide complexes [47,52,110], TiO_2 phases [49], and Al_2O_3 [173]. These changes of composition and topography on the surfaces increased the difficulty to analyse them at atomic level caused by the heterogeneity of the sample and the high asperity. Despite of this difficulty, the surfaces treated with H_2O_2 and thermally oxidised were widely studied because of their bioactivity [43,49,174,175]. The bioactivity of these surfaces was linked to their behaviour in aqueous solution at physiological pH because the surface negative charges favour the interaction with proteins [110]. In addition, the TiOH groups on the surfaces increase the adsorption of Ca and P for further nucleation of apatite [175].

132

The contact angle of TGL-TO$_{500\ °C}$ surfaces were higher than the measured for TGL samples in all the measured pHs, even when the thermally treated surface presented a higher average roughness (R$_a$) than TGL samples (shown in Chapter 3). To explain this behaviour, it is necessary first to understand the formation and composition of the TGL surface and its surface composition changes with thermal treatment. The surface composition has Ti-H$_2$O$_2$ complexes such as Ti-superoxide, TiO$_2^-$, Ti-peroxide, TiO$_2$ [172,176,177]. The chemical treatment of the surface with H$_2$O$_2$ leads to the formation of titania gel layer with components such as TiOOH $_{(aq)}$, TiO$_3$ $_{(aq)}$ and TiO$_2$ $_{(aq)}$ [175]. The chemical reactions and final components on Ti surfaces after the reaction with H$_2$O$_2$ are described by Osaka *et al.* [175] and Tengvall and Lundström [110] as follows:

$$Ti_{(s)} + 2H_2O_2 \rightarrow TiOOH_{(aq)} + \frac{1}{2} O_{2\ (g)} + H_3O^+$$

$$TiOOH + \frac{1}{2} O_{2\ (g)} + H_3O^+ \rightarrow Ti(OH)_4$$

$$Ti(OH)_4 \rightarrow TiO_{2\ (aq)} + 2\ H_2O$$

$$Ti(OH)_4 \rightarrow Ti\ (OH)_{4-n}^{4+} + n\ OH^-$$

$$TiO_{2\ (aq)} + 4H^+ \rightarrow Ti(IV)_{(aq)} + 2H_2O$$

$$Ti(IV)_{(aq)} + H_2O_2 \rightarrow Ti(IV)O_2(OH)_{n-2}^{(4-n)+} + nH^+$$
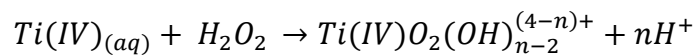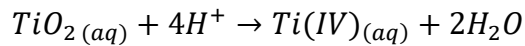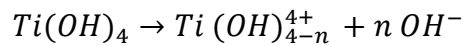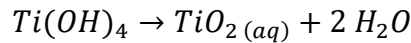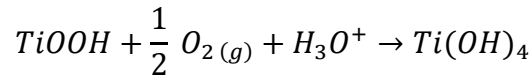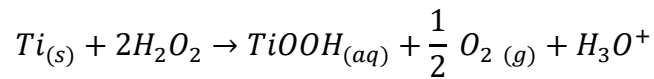
The Ti-complexes slowly form polynuclear cations and anions obtaining a final precipitation of peroxotitanium hydrate ($Ti(IV)O_3(H_2O)_x$ with x = 1, 2 or TiO$_3$ $_{(aq)}$. The peroxotitanium hydrate is suggested to form a µ-bridge (Ti-O-Ti) and consist of Ti$_2$O$_5$

[110,175]. Osaka *et al.* [175] detected the presence of -O-O- (related with the peroxotitanium hydrate species) on Ti treated with H_2O_2 samples by FT-IR at 890 cm^{-1}. These samples were thermally treated at 400 °C afterwards and the absence of the previously measured peak at 890 cm^{-1} suggested the -O-O- groups were eliminated by the thermal treatment. The elimination of the Ti-complexes together with the surface composition after thermal treatment could be the explanation of the differences in the contact angle between TGL and TGL-TO$_{500 °C}$ observed in Figure 63 and Figure 68a, respectively.

4.5. Conclusions

MPT, TO$_{500- 800 °C}$, TGL, TGL- TO$_{500- 800 °C}$ surfaces present different behaviour with the pH change and are described as follows:

1) The IEP of MPT surface was estimated around pH 5 by contact angle titration.

2) F$_{rep}$ and F$_{JT}$ results suggested that MPT surface was positively charged in aqueous solution below pH 5 and negatively charged above pH 5.

3) The differences on F$_{PO}$ result measured on MPT surfaces shown, that the reduction in magnitude when the pH was close to the IEP of the study surface increase the adhesion forces with the strong negatively charged cantilever.

4) The IEP of TO$_{500 °C}$ could be around pH 5.

5) TO$_{500 °C}$ was observed to be positively charged below pH 5 and negatively charged above pH 5.

6) Surface hydrophilicity increased with the increment of the thermal oxidation temperature suggesting roughness, topography and composition modifications are associated with changes on the contact angle.

7) Al_2O_3 presence on $TO_{500\,°C}$ could explain the behaviour of F_{PO} and W_{PO} at pH 5, 7 and 9.

8) It was observed that the IEP of the $TO_{600\,°C}$ was shift towards pH 7 for results obtained in the F_{PO} curve.

9) Heterogenous samples that present RMS roughness higher than 15 nm showed not clear trends or measurements by DCA and AFM force distance curves.

10) TGL-$TO_{500\,°C}$ presented higher contact angle than TGL samples. This difference can be attributed the Ti- H_2O_2 complexes elimination with the thermal treatment.

Chapter 5

Adsorption of peptides in aqueous environment on titanium oxides surfaces obtained by thermal oxidation and chemical treatment followed by thermal oxidation on polished Ti-6Al-4V

5.1.   Introduction

TiO_x presents a negatively net charged surface at physiological pH that induces adsorption of ions and/or of biomolecules that present positive charges in the physiological environment [149]. In particular, the existence of amine and carboxyl available functional groups, present in amino acids (aa) and peptides are associated to the electrostatic interaction with TiO_2 [123]. Two studies have been shown the adsorption of aa with available amine moieties in lysine (K) and available carboxyl moieties in aspartic acid (D) on TiO_2.   Gertler *et al.* [123] studied the presence of electrostatic behaviour that led to the adsorption of the peptide sequence K-G_5-K, where G is glycine, on anatase and rutile (10 µm particles) at pH 7.4. Roddick-Lanzilotta and McQuillan studied the adsorption increase of aspartic acid (D), that contains carboxyl groups, on TiO_2 particle films when the pH favours the electrostatic interaction [152].

Peptide with anionionic and cationic charge presents also an electrostatic adsorption on TiO_2 [40]. RKLPDA (minTBP-1) peptide presents proline (P) that is a structural aa that confers a trans-cis isomerization behaviour to the peptide and as result both terminals of the peptide can interact with the target material [40]. The peptide exhibit charged aa in arginine (R), K and D combining positive and negative charges but with an overall positive charge at pH 7.4. It was shown by Sano and Shiba that the minTBP-1 interacts electrostatically strongly with TiO_2. The suggested mechanism of minTBP-1 adsorption on TiO_2 by Sano and Shiba is shown in Figure 73. The positively charged R in the first

position of the peptide sequence is a Lewis base that absorbed on the -Ti-O$^-$ and the negatively charged D in the fifth position of the peptide sequence is a Lewis acid that absorbed on the Ti-OH$_2$$^+$ [40].

Figure 73: Interaction model of minTBP-1 with TiO$_2$ suggested by Sano and Shiba [40].

This peptide aptamer (minTBP-1) that binds to TiO$_2$ inorganic material is of general use to link biomolecules on Ti surfaces because this biding mechanism does not seem to functionally affect biomolecules. Some examples of biomolecules adsorbed on TiO$_2$ using minTBP-1 as the binding interface are ferritin [125], bone morphogenetic protein-2 (BMP-2) [178] and RGD [39]. It has been shown in these studies that after the adsorption on TiO$_2$ surfaces the biomolecules maintain their activity unaffected [39,125,178].

The peptide aptamer used in our study is the minTBP-1 modified in the first aa. As result KKLPDA peptide aptamer was obtained and was linked to a polyglutamic motif E$_8$ that works as a nucleating agent of apatite [38,179]. Both the organic peptide aptamer and TiO$_2$ surface are pH responsive and an electrostatic adsorption of the peptides onto the surface is expected.

5.2. Objectives

The objectives of this chapter were first to evaluate the adsorption of 5-FAM-KKLPDAKKLPDAEEEEEEEE peptide on modified titanium oxides surfaces by polished and thermal oxidation of Ti-6Al-4V, and titania gel layers formed by H_2O_2/HCl and H_2O_2/HCl followed by thermal oxidation. The second objective was to identify the surface that presented the optimal peptide adsorption for further experiments. And the third objective was to identify the coating time at which the peptide adsorbed optimally on the surface.

5.3. Adsorption of peptides on native titanium oxide from polished Ti-6Al-4V and titanium oxides formed by thermal oxidation on polished Ti-6Al-4V

5.3.1. Specific objective

In this section, the objective was to evaluate the adsorption of the peptide sequence 5-FAM- KKLPDAKKLPDAEEEEEEEE on titanium oxide surfaces obtained by polished and thermal oxidation of Ti-6Al-4V.

5.3.2. Results

Titanium samples were immersed in phosphate buffered saline (PBS) at pH 4 (close to the IEP of the peptide sequence) with 10 µM of 5-FAM-KKLPDAKKLPDAEEEEEEEE (Ti-HA-pep) for 3 hours. Fluorescence dye (5-FAM) added to the peptide sequence as another aa was used to track and quantify the intensity of the absorbed peptide Ti-HA-pep on surfaces by fluorescence microscopy. Intensities were measured from fluorescence micrographs which were taken before and after the dip coating on the interested surfaces.

Intensity results for native TiO_x polished Ti-6Al-4V (MPT) and thermally oxidised polished Ti-6Al-4V at 500, 600, 700 and 800 °C ($TO_{500-800 °C}$), uncoated ($I_{uncoated}$) and peptide coated (I_{coated}), are shown in Table 15.

Table 15: Intensity measured on fluorescence micrographs of uncoated and peptide coated on MPT and $TO_{500-800 °C}$ surfaces.

	MTP	**TO$_{500 °C}$**	**TO$_{600 °C}$**	**TO$_{700 °C}$**	**TO$_{800 °C}$**
$I_{uncoated}$ (a.u.)	15±1	16±1	15±1	15±1	15±1
I_{coated} (a.u.)	23±1	33±1	28±1	23±2	32±2

The fluorescence intensity of the uncoated surface is subtracted from the intensity emitted by the peptide coated surface resulting in the final intensity (I_{final}), shown in Eq. 6.

$$I_{final} = I_{coated} - I_{uncoated} \qquad \text{Eq. 6}$$

Where: I_{final} = Final fluorescence intensity (a.u.)

I_{coated} = Fluorescence intensity of peptide coated surfaces

$I_{uncoated}$ = Fluorescence intensity of uncoated peptides surfaces

I_{final} calculated from data in Table 15 and Eq. 6 are shown in Figure 74. The MPT surface presents the lowest intensity emitted by the peptide coating. $TO_{500-800 °C}$ and samples present higher intensity compared with MPT surfaces. Between 500 °C and 700 °C, peptide intensity decreases followed by an increase in the intensity measured on samples treated at 800 °C.
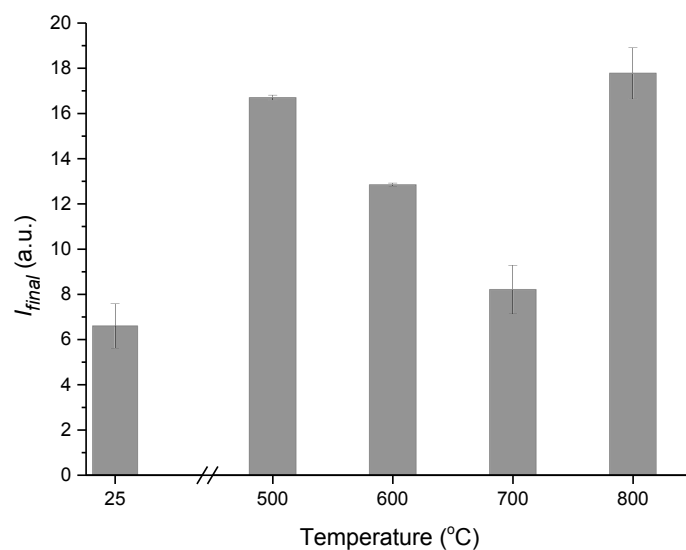
Figure 74: I_{final} values from $I_{uncoated}$ and I_{coated} fluorescence intensity data of MPT and TO$_{500-800\ °C}$ surfaces.

The MPT and TO$_{500-800\ °C}$ surfaces were not covered totally by peptides and therefore measured intensities present low values. A fluorescence micrograph of TO$_{800\ °C}$ surface that present the surfaces with highest intensity is shown in Figure 75. Emitted fluorescence is observed in the circled areas.
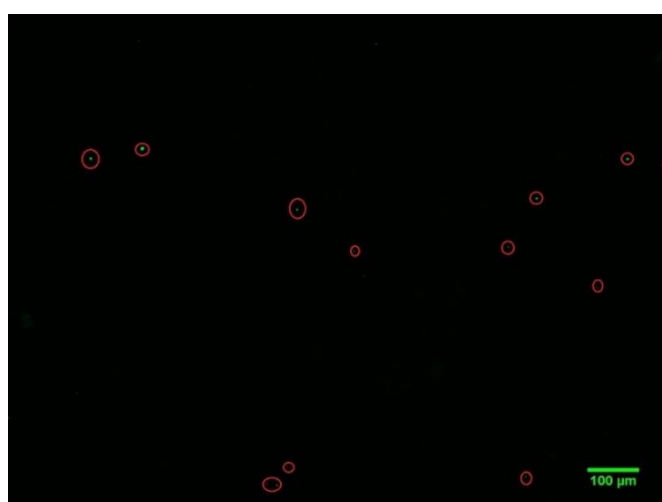
Figure 75: Fluorescence micrograph of TO$_{800\ °C}$ peptide coated.

5.3.3. Discussion

In Chapter 4 it was shown that the TiO_2 surfaces exposed to a cantilever of SiO_2 presented a large attraction force where both materials presented an opposite charge which was above the isoelectric point IEP of SiO_2 (pH < 3) and below the IEP of TiO_2 (pH ≥ 5). This observation was in agreement with the zeta potential measurements exhibited by Attard *et al.* [56] shown in Figure 76.
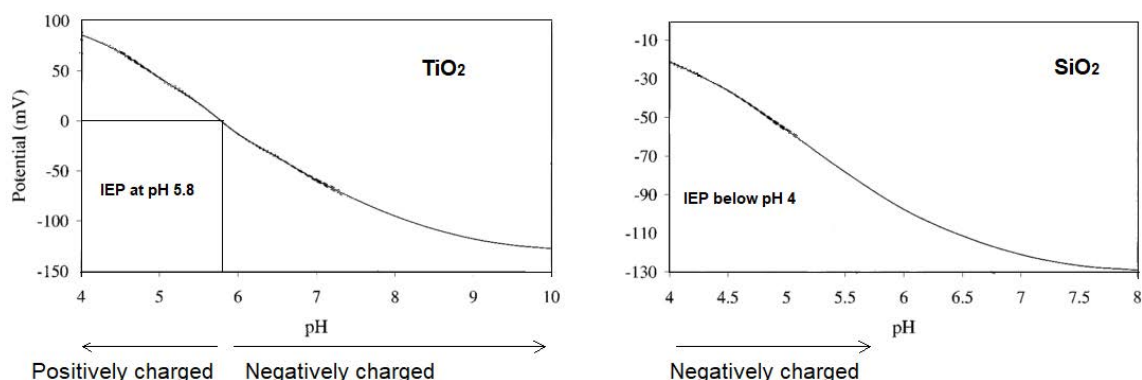
Figure 76: Zeta potential in 10 mM monovalent electrolyte solution of TiO_2 and SiO_2, "Schema modified from reference [56]".

The peptide/surface interaction can present a similar behaviour as the SiO_2 / TiO_2 (cantilever/surface) and therefore it was expected that the attraction interaction of Ti-HA-pep on the TiO_2 was large in a pH where both (surface and peptide) presented an opposite charge. To achieve such an opposite charge, a pH between the IEP of TiO_2 surface and the IEP of Ti-HA-pep was selected. The charge of Ti-HA-pep with the change of the pH and IEP is shown in Figure 77 [180].
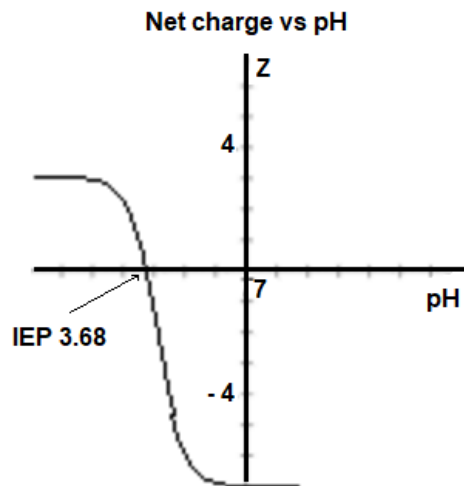
Figure 77: Net charge of Ti-HA-pep with the pH change [180].

In Figure 74, the MPT surface had the lowest I_{final} indicating the lowest adsorption of Ti-HA-pep on the surface. The difference in intensities associated with the adsorption of Ti-HA-pep between the MPT and the thermally treated samples could be attributed to the change in composition and topography of the surface (discussed in Chapter 3) and the possible slight increase of their IEPs (discussed in Chapter 4). Table 16 shows how the observations of the surface in Chapters 3 and 4 could affect the adsorption of the peptides.

Table 16: Observation methods used in Chapter 3 and Chapter 4 and how each method can support the assessment of the adsorption of the peptide on TiO_x surfaces

Observation method	Observation	Interpretation and assessment
XPS	Increase of Al_2O_3 and V_2O_5 on the surfaces thermally treated.	Changes on the surface composition increase surface heterogeneity and influence IEP
XRD	Combination of amorphous and TiO_2 crystals	Changes on the surface phases affect the IEP
AFM, interferometry and contact angle	Rough surfaces and surface tension	Changes on the topography affect the anchoring points of the surface
AFM distance force curves	Areas of the studied surfaces present higher attraction forces than other areas of the same surface	Surface charges in aqueous environment shows heterogeneity that affects the IEP

5.4.   Adsorption of peptides on titania gel layer formed by H$_2$O$_2$/HCl and titania gel layer thermally oxidised on polished Ti-6Al-4V

5.4.1. Specific objectives

The objectives of this section were:

1) Evaluated   the   adsorption   of   the   peptide   sequence   5-FAM-KKLPDAKKLPDAEEEEEEEE on titania gel layer surfaces formed by H$_2$O$_2$/HCl and titania gel layer thermally oxidised on polished Ti-6Al-4V.

2) Identified the surface with higher peptide adsorption

3) Assessed optimal coating time to obtain a higher adsorption of the peptides on TiO$_x$ surfaces

5.4.2. Results

5.4.2.1. Adsorption of peptides on titania gel layer formed by H$_2$O$_2$/HCl and titania gel layer thermally oxidised on polished Ti-6Al-4V

Titania gel layer (TGL) and TGL followed by thermal oxidation at 500, 600, 700 and 800 °C (TGL-TO$_{500\text{-}800\ °C}$) samples were immersed in PBS at pH 4 with 10 µM of Ti-HA-pep for 3 h. Intensities were measured from fluorescence micrographs which were taken before and after the dip coating on the interested surfaces. The surface that presented the highest intensity was then exposed at different coating times to assess later on which sample presented the highest peptide adsorption. Fluorescence intensity of TGL and TGL-TO$_{500\text{-}800\ °C}$ uncoated and peptide coated are shown in Table 17.

Table 17: Intensity measured on fluorescence micrographs of uncoated and peptide coated on TGL and TGL-TO$_{500-800\,°C}$.

	TGL	TGL-TO$_{500\,°C}$	TGL-TO$_{600\,°C}$	TGL-TO$_{700\,°C}$	TGL-TO$_{800\,°C}$
$I_{uncoated}$ (a.u.)	14±1	14±1	14±1	16±1	16±1
I_{coated} (a.u.)	281±14	625±30	583±5	73±9	30±1

I_{final} calculated from data in Table 17 and Eq. 6 are shown in Figure 78. Intensity measured on TGL surface presents higher intensity than TGL-TO$_{700-800\,°C}$. The highest intensity is presented on TGL-TO$_{500\,°C}$ followed by the intensity measured on TGL-TO$_{600\,°C}$.
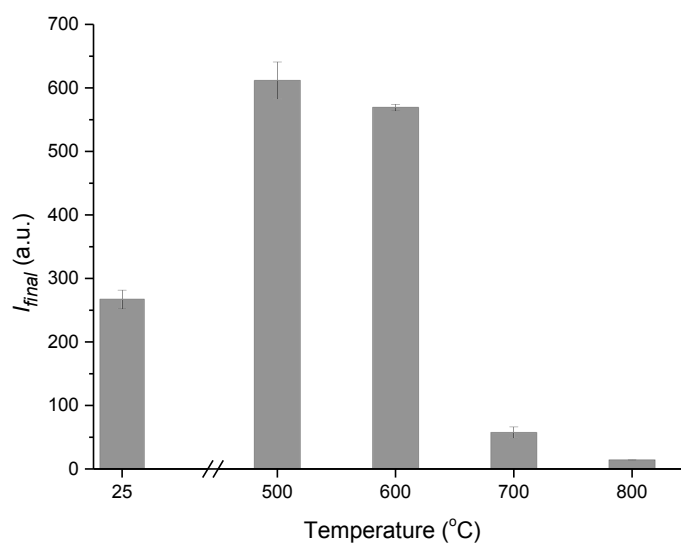
Figure 78: I_{final} values from $I_{uncoated}$ and I_{coated} fluorescence intensity data of TGL and TGL-TO$_{500-800\,°C}$ surfaces.

TGL, TGL-TO$_{500\,°C}$ and TGL-TO$_{600\,°C}$ surfaces present a peptide coating that covers the entire area of the surface. A fluorescence micrograph of TGL-TO$_{500\,°C}$ presents the surfaces with highest intensity and it is shown in Figure 79.
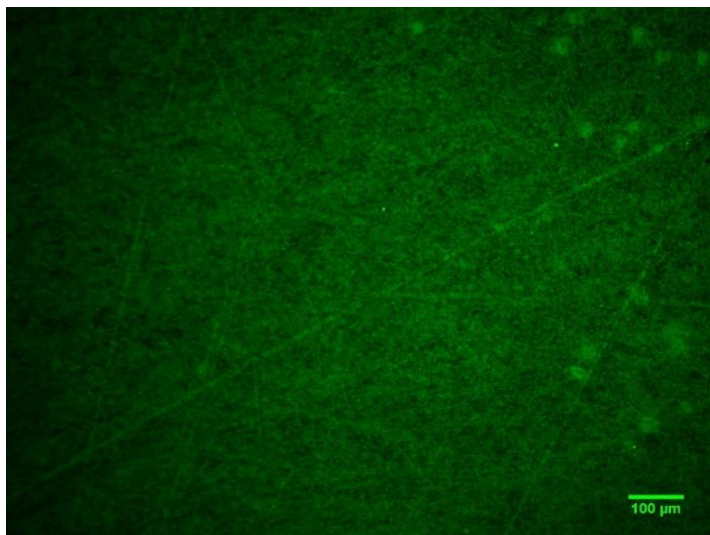
Figure 79: Fluorescence micrograph of TGL-TO$_{500\,°C}$ peptide coated.

5.4.2.2. Adsorption of peptides at different coating times on titania gel layer formed by H$_2$O$_2$/HCl followed by thermal oxidation at 500 °C

TGL-TO$_{500\,°C}$ was dip coated in PBS with 10 µM Ti-HA-pep at pH 4 for 1, 3, 6, 9 and 12 hours. Uncoated and peptide coated intensities are shown in Table 18.

Table 18: Intensity measured on fluorescence micrographs of uncoated and peptide coated for 1, 3, 6, 9, 12 h on TGL-TO$_{500\,°C}$.

	$I_{uncoated}$ (a.u.)	I_{coated} (a.u.)				
Coating time	0 h	1 h	3 h	6 h	9 h	12 h
	14±1	635±10	552±17	564±6	598±4	216±12

I_{final} calculated from data in Table 18 and Eq. 6 are shown in Figure 80. Intensities between 1 h and 9 h present higher values than those at 12 h. The highest intensity is observed when the sample was immersed in the solution for 1 h.
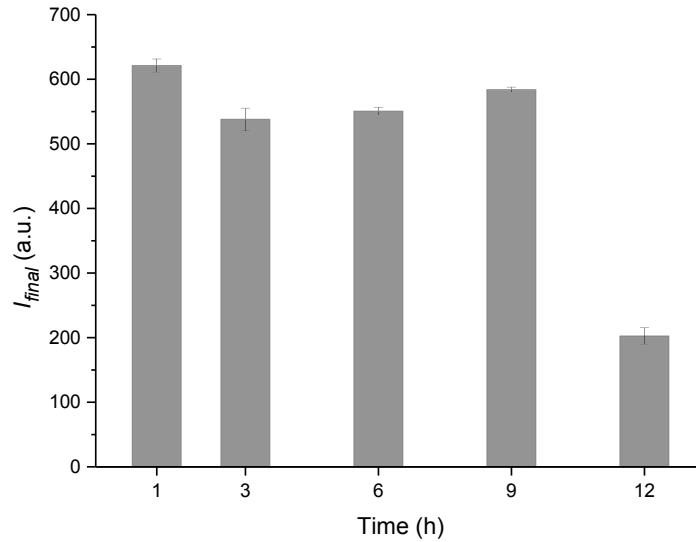
Figure 80 : I_{final} values from $I_{uncoated}$ and I_{coated} fluorescence intensity data of TGL-$TO_{500°C}$ for 1, 3, 6, 9 and 12 h.

5.4.3. Discussion

In Figure 78 it is possible to visualise how the fluorescence intensity increased between TGL and TGL-$TO_{500 °C}$ surfaces. This increment could be related with the composition of the TGL after the thermal treatment (already discussed in previous Chapter 4) and could indicate that TGL thermally treated surfaces interacted with greater affinity for ions or charged molecules in solution than non-thermally treated TGL. Similar results were obtained by studies that form apatite on treated titanium surfaces from simulated body fluid (SBF) [44,181] strongly related with the adsorption of Ca^{2+} and PO_4^{3-} ions on TiO_2. In the study performed by Ohtsuki *et al.* [182], TGL surfaces were immersed in SBF for 14 days and did not detect any apatite formation. However, in the studies

147

performed by Osaka *et al.* [175] and Wang *et al.* [68], the TGL treated surface following by thermal treatment induced apatite formation after 1 day in SBF.

In the same Figure 78, TGL-TO$_{700\,°C}$ and TGL-TO$_{800\,°C}$ presented a decrease in the fluorescence intensity. This decrease could be associated with two possibilities that are linked with the increase of the oxidation temperature: the first one is the increase of Al$_2$O$_3$ on surfaces (already discussed in Chapter 3 and Chapter 4) that can interfere in the changes of the electrostatic behaviour of the surface and the second one is the possible reduction in number of the Ti-OH groups on the surface [43]. The reduction of the negative charges was exhibited in Chapter 4 where the pull of force (F$_{PO}$) of TGL-TO$_{500\text{-}800\,°C}$ measured at pH 5 presented a decrease with the thermal oxidation temperature increase, shown in Figure 81.This indicates that the F$_{PO}$ necessary to pull the cantilever out of the surface is larger when the surface was treated at 500 and 600 °C that could be attributed to the large density of the negative charges at pH 5 than at 700 and 800 °C.
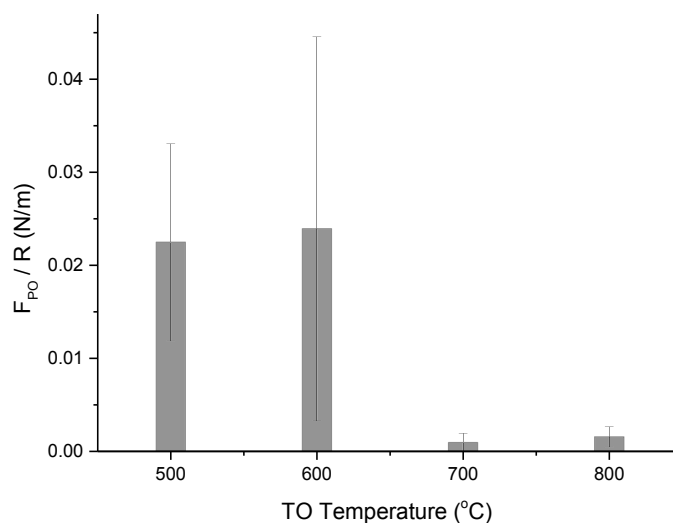
Figure 81: F_{PO}/R of TGL-TO$_{500\text{-}800\,°C}$ measured at pH 5.

The surface with the highest fluorescence intensity was TGL-TO$_{500\,°C}$ and therefore was the surface selected for further experiment. The TGL-TO$_{500\,°C}$ was exposed to the Ti-HA-pep at different times of immersion, shown in Figure 80. It was observed that 1 h of immersion was enough to have a maximum fluorescence intensity (high Ti-HA-pep adsorption) and it was also observed that after 12 h of immersion the fluorescence intensity decreased. It could be expected that once the peptide or adsorbed molecule (protein) reaches the maximum adsorption level on TiO$_2$, then this level was maintained with the increase of immersion time. However, the results showed a decrease in fluorescence intensity after 12 h of immersion. This effect can be attributed to the adsorption of peptides between them due to the charges interactions creating a multilayer coating on the surface. The decrease of intensity can also be attributed to the orientation of the adsorbed peptides on the surface because the orientation of the adsorbed peptides after certain time can change between the "end-on" to the "side-on"

149

as is shown in Figure 82 [53]. It has been reported that the orientation of adsorbed

proteins on solid surface can change from "end-on" to "side-on" [53,183,184]. For example

Daly *et al.* [183] reported that the configuration "side-on" of the absorbed proteins can be

due to the attraction of the fluorophore to a negative side of the surface, leading to a

protonation of the fluorophore (pH-dependent) resulting in a reduction of the

fluorescence emission intensity. Another example of the protein orientation change on

solid surfaces between the "end-on" to "side-on" is the reported by Wertz *et al.* [184] who

suggest that the proteins adsorbed on the "end-on" can be lost and the "side-on"

configuration can take place because of their stronger binging to the surface than the

"end-on". In addition, the "end-on" configuration was suggested to require 1.5 times

more space than the "end-on" and therefore expected a reduction in the amount of

proteins on the surface. The combination of orientation change and reduction in the

amount of proteins (behaviour that could be extrapolated to peptides) with time could

explain the measured decrease in the fluorescence intensity after 12 hours.
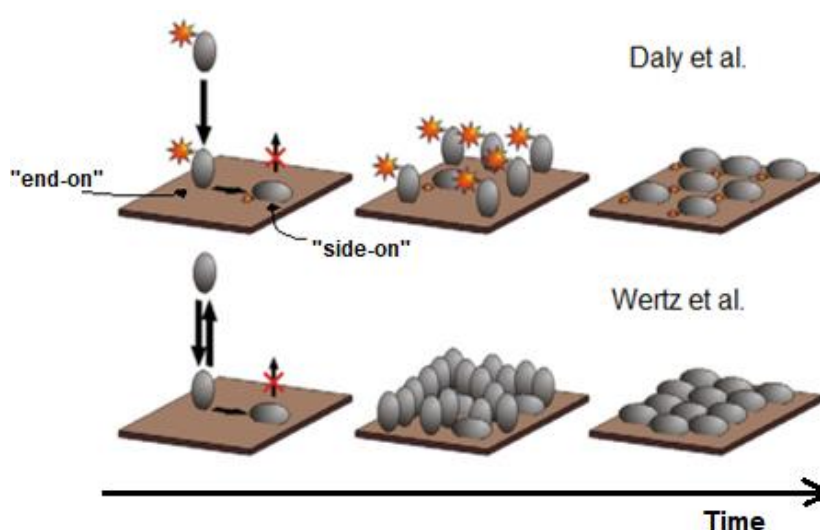
Figure 82: Protein adsorption in solid surfaces and possible configuration change of the adsorbed protein with time, explained by Daly et al.[183] and Wertz et al. [184] "adapted from reference [53] ".

5.5. Conclusions

Surface peptide coating was fluorescence tracked after dip coating in PBS at pH 4 procedure that contain the Ti-HA-pep labelled with the fluorophore (5-FAM) and it was found that:

1) Native TiOx present the lowest fluorescence intensity for all treated samples that can be linked to the composition of the surface and the close IEP to pH 4.

2) TGL-TO$_{500\ °C}$ present the highest fluorescence intensity for 1 hour that can be associated to the titania gel composition.

3) The increment of oxidation temperature decreased the fluorescence intensity of the peptides on the surfaces that can be related to the Al$_2$O$_3$ presence and Ti-OH reduction.

Chapter 6

Presence of peptides on titania gel layer formed by H_2O_2/HCl followed by thermal oxidation at 500 °C on polished Ti-6Al-4V

6.1. Introduction

The peptide used for this coating has two specific motifs, the first one binds to TiO_2 surface (peptide sequence / Ti-pep), and the second one nucleates hydroxyapatite (HA) [38,179] (functional peptide / HA-pep), shown in Figure 83. In addition, the peptide sequence includes a fluorophore (5-FAM) used for monitoring the peptide.

| 5-FAM | K | K | L | P | D | A | K | K | L | P | D | A | E | E | E | E | E | E | E | E |

Fluorophore dye TiO_2 motif   HA motif
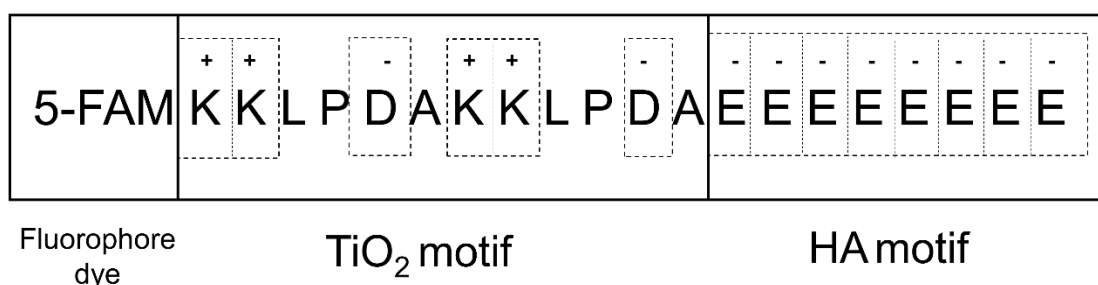
Figure 83: Ti-HA-pep with motif targets materials.

The Ti-pep motif binds to TiO_2 surface electrostatically between the charged aa and the charged surface in aqueous environment (discussed in Chapter 5). The HA-pep motif, functional peptide, plays a role in the formation of HA due to the presence of E aa [185] suggesting that the carboxyl groups (COOH) present on E lead to the adsorption of Ca^{2+} at physiological pH as the moieties are deprotonated presenting COO^- [59]. This is in agreement with the study reported by Tanahashi and Matsuda [60] who showed that the self-assembled monolayers (SAMs) of alkanethiols with COOH moieties (COOH SAM) surfaces when exposed to SBF at pH 7.4 presented negatively charged surfaces that induced the adsorption of Ca^{2+} and PO_4^{3-}, and the formation of HA.

The presence of the coating on the surface could be identified via the analysis of chemical differences in the surface by XPS, and via the changes of charge density due to acid and basic aa on the sequence (K, D and E) by DCA titration and AFM force-distance curves. The charge density changes were also studied by Gao *et al.* [186] in hydrophilic polymer brushes conjugated with antimicrobial peptides (AMPs), which presented different ionic aa in the peptide sequence. They reported that the contact angle and adhesion forces changed with the aa ionic sequence composition (chemical properties) of the AMPs.

6.2. Objective

The objective of this chapter was to evaluate the peptide coating presence in titania gel layer formed by H_2O_2/HCl and thermally oxidised at 500 °C surfaces by measuring the difference in chemical composition and surface charge against the uncoated surfaces.

6.3. Results

Titania gel layer followed by thermal oxidation at 500 °C (TGL-TO$_{500\,°C}$) and dip coated TGL-TO$_{500\,°C}$ in PBS at pH 4 with 10 µM of Ti-HA-pep for 1 hour (TGL-TO$_{500\,°C}$-pep) were analysed and compared by XPS, contact angle and AFM to assess the changes or differences between the peptide uncoated and coated surfaces.

6.3.1. *Chemical composition of titania gel surfaces treated at 500 °C coated and uncoated with titanium- hydroxyapatite peptide sequence*

Chemical composition of TGL-TO$_{500\,°C}$ and TGL-TO$_{500\,°C}$-pep measured by XPS is shown in Table 19. C and N are elements found in the chemical structure of peptides and both chemical elements are present on peptide coated samples. Content of C and N are observed in TGL-TO$_{500\,°C}$ surfaces but in less percentage compared to TGL-

TO$_{500 °C}$-pep surfaces. On other hand, the percentage of O, V, Ti and Al decreases on

TGL-TO$_{500 °C}$-pep.

Table 19: Chemical composition of TGL-TO$_{500 °C}$ and TGL-TO$_{500 °C}$-pep surfaces measured by XPS.

Sample	O%	V%	C%	Ti%	N%	Al%	*Other%
TGL-TO$_{500 °C}$	52.7	0.4	19.9	20.6	1.0	3.8	1.6
TGL-TO$_{500 °C}$-pep	46.0	0.3	29.2	16.1	3.8	2.9	1.7

*Other includes P, Si, Na and K

6.3.2. Contact angle titration of titania gel surfaces treated at 500 °C coated and uncoated with titanium- hydroxyapatite peptide sequence

Advancing contact angle (θ_a) using unbuffered aqueous solution at pH 3, 5, 7 and 9

measured on TGL-TO$_{500 °C}$ and TGL-TO$_{500 °C}$-pep is shown in Figure 84. TGL-TO$_{500 °C}$-

pep samples present lower advancing contact angle than TGL-TO$_{500 °C}$ samples.

Contact angle measured values for TGL-TO$_{500 °C}$ and TGL-TO$_{500 °C}$-pep are around 30

and 38 °. At pH 3, θ_a difference between TGL-TO$_{500 °C}$ and TGL-TO$_{500 °C}$-pep is around

2.5 °. At pH 5, θ_a difference between TGL-TO$_{500 °C}$ and TGL-TO$_{500 °C}$-pep is the lowest

from all the analysed pH and is around 0.3 °. At pH 7, θ_a difference between TGL-TO$_{500}$

$_{°C}$ and TGL-TO$_{500 °C}$-pep is the largest one from all the analysed pH with around 4 °. At

pH 9, θ_a difference between TGL-TO$_{500 °C}$ and TGL-TO$_{500 °C}$-pep is around 1 °.
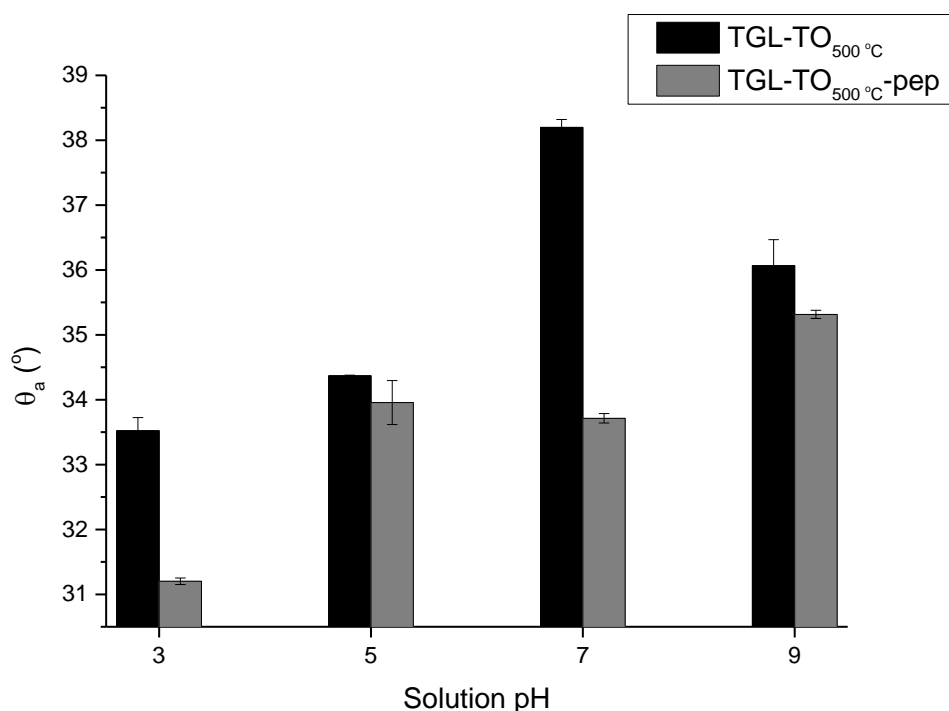
Figure 84: θ_a measured at pH 3,5, 7 and 9 on TGL-TO$_{500\,°C}$ and TGL-TO$_{500\,°C}$ - pep surfaces.

Receding contact angle (θ_r) at pH 3, 5, 7 and 9 measured on TGL-TO$_{500\,°C}$ and TGL-TO$_{500\,°C}$-pep is shown in Figure 85. θ_r measured values are around 9 and 22.5 °. θ_r for TGL-TO$_{500\,°C}$-pep are in general higher than TGL-TO$_{500\,°C}$ with an exception at pH 7. The largest difference in θ_r between TGL-TO$_{500\,°C}$-pep and TGL-TO$_{500\,°C}$ is exhibited at pH 3 with around 10 °. At pH 5 and 9, θ_r differences between TGL-TO$_{500\,°C}$ and TGL-TO$_{500\,°C}$-pep are around 6 and 1.5 °, respectively. At pH 7, measured values of θ_r for TGL-TO$_{500\,°C}$ and TGL-TO$_{500\,°C}$-pep are very close.
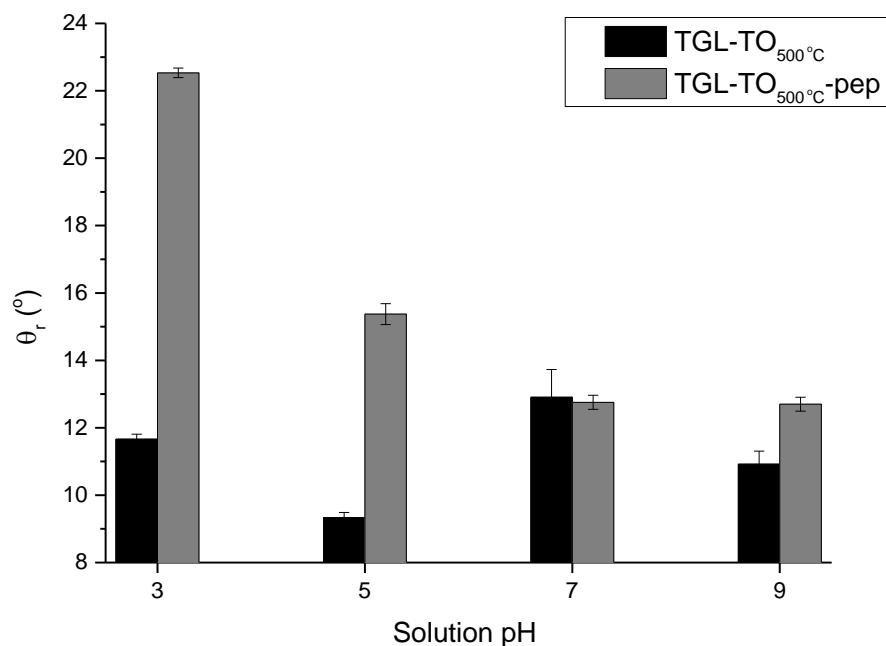
Figure 85: θ_r measured at pH 3,5, 7 and 9 of TGL-TO$_{500\,°C}$ and TGL-TO$_{500\,°C}$-pep surfaces.

The contact angle hysteresis ($\Delta\theta$) for TGL-TO$_{500\,°C}$ and TGL-TO$_{500\,°C}$-pep surfaces are shown in Figure 86. TGL-TO$_{500\,°C}$ surfaces exhibit larger hysteresis than TGL-TO$_{500\,°C}$-pep surfaces at all other pH solutions. TGL-TO$_{500\,°C}$-pep hysteresis trend increases when pH becomes neutral. Between pH 3 and pH 5, the TGL-TO$_{500\,°C}$-pep hysteresis presents the largest increment compared to the increments between the other pH. On the other hand, TGL-TO$_{500\,°C}$ hysteresis increases between pH 3 and 5, and when the pH increases between pH 5 and 9 the hysteresis remains constant.
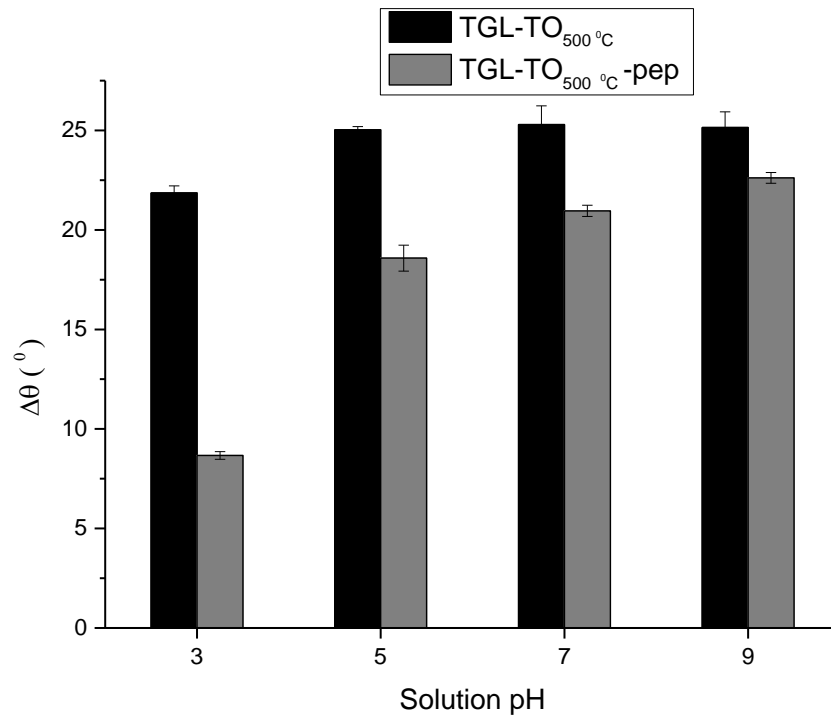
Figure 86: Δθ measured at pH 3, 5, 7, and 9 of TGL-TO$_{500\,°C}$ and TGL-TO$_{500\,°C}$-pep surfaces.

6.3.3. *AFM force-distance curves of titania gel surfaces treated at 500 °C coated and uncoated with titanium- hydroxyapatite peptide sequence*

AFM force-distance curves in unbuffered solution at pH solution at 3, 5, 7 and 9 were performed on TGL-TO$_{500\,°C}$ and TGL-TO$_{500\,°C}$ -pep surfaces to quantify the differences in F_{rep}, F_{JT}, F_{PO} and W_{PO} due to the peptide coating.

6.3.3.1. *Out-of-contact repulsion force of titania gel surfaces treated at 500 °C coated and uncoated with titanium- hydroxyapatite peptide sequence*

F_{rep} of TGL-TO$_{500\,°C}$ and TGL-TO$_{500\,°C}$-pep surfaces are shown in Figure 87 TGL-TO$_{500}$ $_{°C}$ surfaces present lower F_{rep} than TGL-TO$_{500\,°C}$-pep surfaces at each pH. The highest F_{rep} for both surfaces is exhibited at pH 9.

TGL-TO$_{500\,°C}$-pep F$_{rep}$ trend increases when the pH increases with an exception at pH 5 where the F$_{rep}$ value decrease from the F$_{rep}$ measured at pH 3.
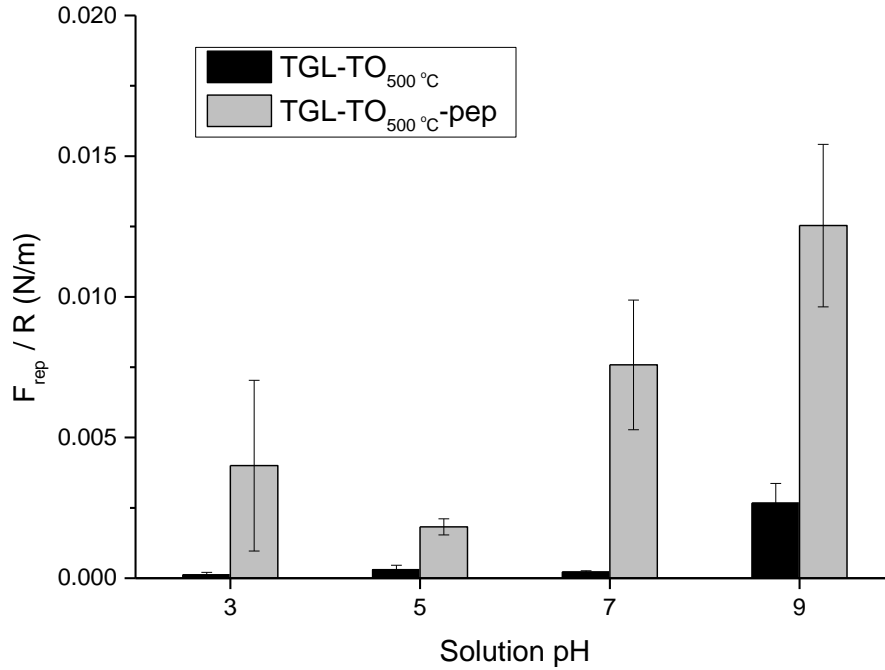
Figure 87: F$_{rep}$/ R measured by AFM at pH solution 3, 5, 7 and 9 of TGL-TO$_{500\,°C}$ and TGL-TO$_{500\,°C}$-pep surfaces.

6.3.3.2. *Jump to force of titania gel surfaces treated at 500 °C coated and uncoated with titanium- hydroxyapatite peptide sequence*

F$_{JT}$ of TGL-TO$_{500\,°C}$ and TGL-TO$_{500\,°C}$-pep surfaces is shown in Figure 88. TGL-TO$_{500}$ $_{°C}$-pep surfaces exhibit higher F$_{JT}$ than TGL-TO$_{500\,°C}$ surfaces at each pH. The highest force value for both surfaces is detected at pH 5.

TGL-TO$_{500\,°C}$-pep F$_{JT}$ presents similar values between pH 3 and 5, and between pH 7 and 9 solution.
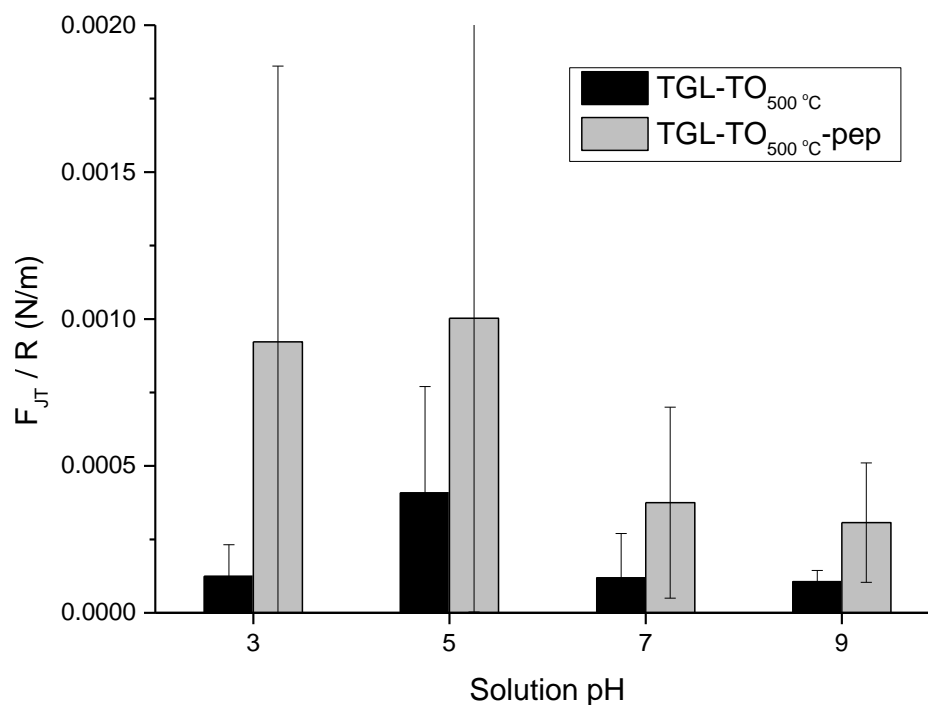
Figure 88: F_{JT} / R measured by AFM at pH solution 3, 5, 7 and 9 of TGL-TO$_{500}$ $_{°C}$ and TGL-TO$_{500 °C}$-pep surfaces.

6.3.3.3. *Pull-off force of titania gel surfaces treated at 500 °C coated and uncoated with titanium- hydroxyapatite peptide sequence*

F_{PO} of TGL-TO$_{500 °C}$ and TGL-TO$_{500 °C}$-pep surfaces is shown in Figure 89. TGL-TO$_{500}$ $_{°C}$-pep presents higher F_{PO} than TGL-TO$_{500 °C}$ surface at pH 3, 7 and 9. At pH 5, the case is the opposite as the TGL-TO$_{500 °C}$ surface presents higher F_{PO} than TGL-TO$_{500}$ $_{°C}$-pep surface.

TGL-TO$_{500 °C}$-pep F_{PO} exhibits a higher value at pH 5. At pH 3 and 7, F_{PO} is similar. At pH 9, the lowest value of pull-off force occurs.
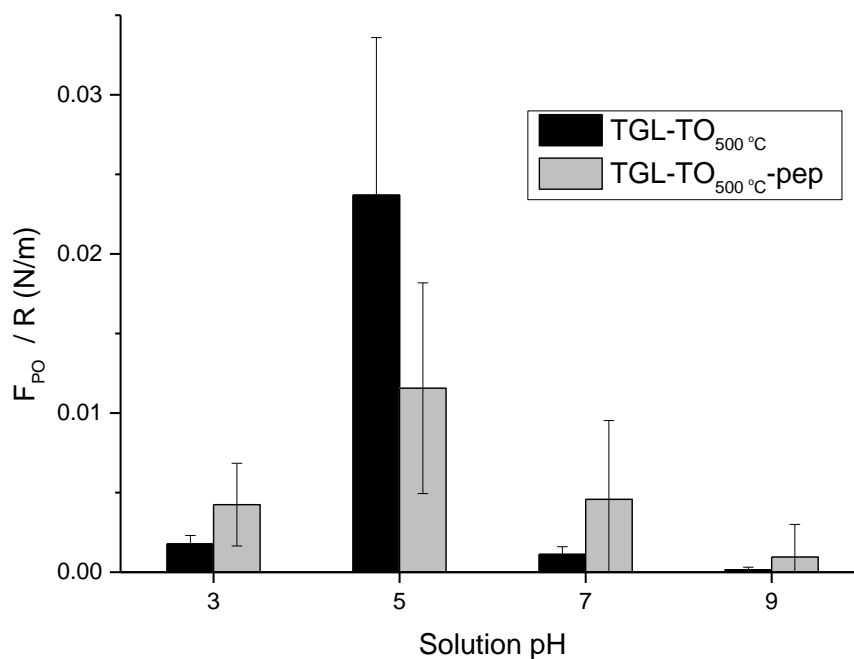
Figure 89: F_{PO} / R measured by AFM at pH solution 3, 5, 7 and 9 of TGL-TO$_{500}$ $_{°C}$ and TGL-TO$_{500 °C}$-pep surfaces.

6.3.3.4. *Pull-off energy* of *titania gel surfaces treated at 500 °C coated and uncoated with titanium- hydroxyapatite peptide sequence*

W_{PO} of TGL-TO$_{500 °C}$ and TGL-TO$_{500 °C}$-pep surfaces are shown in Figure 90. W_{PO} is

small for both surfaces at pH 3, 7 and 9. The highest W_{PO} value is present at pH 5.
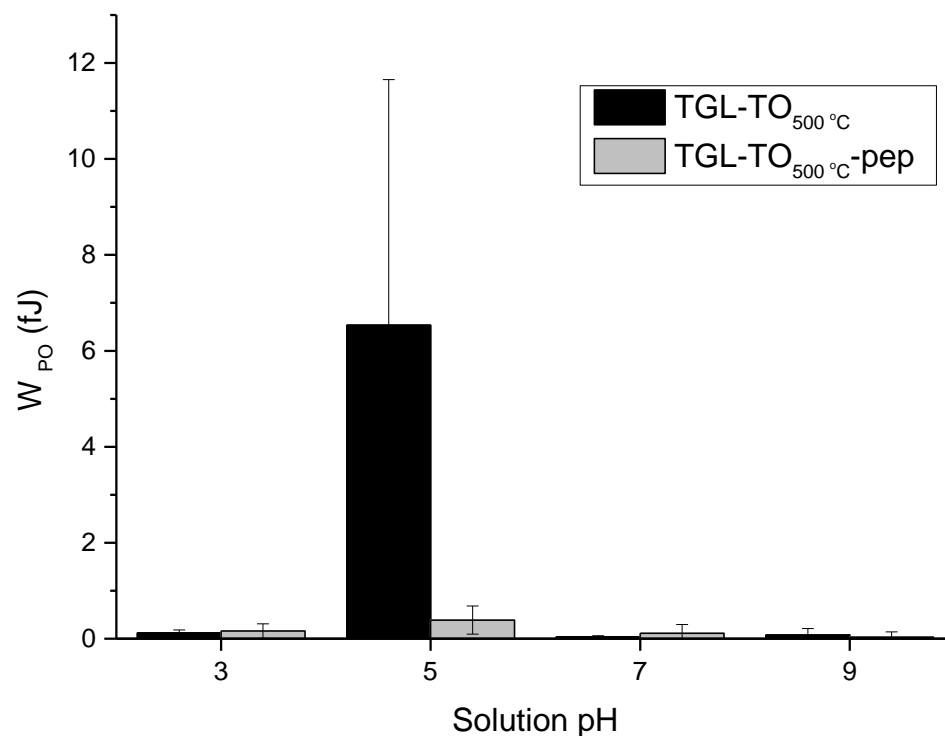
Figure 90: W_{PO} measured by AFM at pH solution 3, 5, 7 and 9 of TGL-TO$_{500\ °C}$ and TGL-TO$_{500\ °C}$-pep surfaces.

6.4. Discussion

The chemical composition of the peptide coated surfaces, shown in Table 19, presents an increase in C and N content and a decrease in Ti, O, V and Al content suggesting the existence of an organic coating on the surfaces. The content of metallic Ti, V, and Al elements decreased in the same percentage whereas the content of O presented a smaller decrease than the other elements that could be associated with the content of O in the peptide coating. Similar behaviour in the increase of the organic content and the decrease of the metallic content was found by Baber *et al.* [187] in RGD coated Ti surfaces, and Fraioli *et al.* [188] in integrin-bindings coated Ti surfaces.

161

TGL-TO$_{500 \, °C}$-pep surfaces presented less θ_a than TGL-TO$_{500 \, °C}$ surfaces, shown in Figure 84, and a similar behaviour was present in a study performed by Yang *et al.* [189] where the contact angle of highly ordered pyrolytic graphite (HOPG) surface (contact angle between 60 – 82 °) decreased when it was functionalized with the peptide sequences EAK16-II that contain, E aa (contact angle =39 °). In addition, the differences in θ_a of TGL-TO$_{500 \, °C}$-pep surfaces can be attributed to the net charge of the surface along the pH, where the COOH residue from E aa is protonated at pH 3 and deprotonated at pH ≥ 7. A similar behaviour was studied by Werener *et al.* [190] who showed that grafted polyglutamic acid surfaces were highly dependent of the pH solution.

The $\Delta\theta$ of TGL-TO$_{500 \, °C}$ and TGL-TO$_{500 \, °C}$-pep surfaces, shown in Figure 86, can occur because of the different roughness and chemical changes of the surface. The increment of hysteresis on TGL-TO$_{500 \, °C}$-pep surface compared to the TGL-TO$_{500 \, °C}$ surface when the pH increases can be associated with the protonation and deprotonation of the HA-pep motif (E$_8$). The ionization of polyglutamic acid at high pH (>4.25) and protonation at low pH (<4.25) allows to have pH dependent systems such as the swelling/ deswelling hydrogels [191], and the opening and closing of the pores of permeable water membranes [192]. These examples show how the charges of the E residues change with the pH and therefore different effects, such as change of the surface hysteresis due to the charge density, can happen above and below the E pK_a (≈ 4.25)

The F$_{rep}$ of TGL-TO$_{500 \, °C}$-pep surfaces, shown in Figure 87, is larger for all pH compared with TGL-TO$_{500 \, °C}$ surface suggesting that both surfaces presented

differences on the surface charge. It was shown by Hu *et al.* [193] how the F_{rep} was higher in samples coated with a polymeric anion hexametophosphate (negatively charged) than in uncoated TiO_2 samples, concluding that the F_{rep} change could be due to the additional charge of the coating.

The trend of the F_{rep} measured in TGL-TO$_{500\ °C}$-pep surfaces increased when the pH becomes alkaline with an exception at pH 5, as shown in Figure 87 . The F_{rep} increase could be explained by the COOH deprotonation of the HA-pep motif at pH 7 and 9. The outlier result at pH 5 can be attributed to the protonation of the COOH of the HA-pep motif leading to a positively charged surface that decreased the F_{rep} when interacted with the negatively charged SiO_2 cantilever. This last result suggests the pK_a could be more than 4.25 (COOH) and this was in line with a study performed by Vezenov *et al.* [63] where it was shown how immobilized SAM with COOH terminals present a pK_a of 5.5 ± 0.5, demonstrating how the pK_a of the COOH immobilised on the surface can be different from 4.25. At pH 3 the $F_{rep,}$ shown in Figure 87 is higher than at pH 5 probably because the COOH and NH_3^+ of the charged aa were protonated.

The F_{JT}, shown in Figure 88, is higher for TGL-TO$_{500\ °C}$-pep samples that TGL-TO$_{500\ °C}$ possibly due to the coating in the same way as the F_{rep}. The difference in the measured forces for TGL-TO$_{500\ °C}$-pep surfaces can be due to the protonation/ deprotonation of the E aa and protonation of K (2nd and 8th position of the Ti-HA-pep sequence). The studies carried on TGL-TO$_{500\ °C}$-pep at different pH solutions allowed to have positive charge on the coated surface from the NH_2 (K) at all pH, and variations between negative charges (at pH 7 and 9 where the E is ionised) and neutral charges (at pH 3 and 5 where the E motif is possibly neutral). The negatively charged surfaces that

interact with a negatively charged cantilever showed lower F_{JT} than the surfaces where the negative charges were not present.

The F_{PO}, shown in Figure 89, is higher in almost all pH for TGL-TO$_{500 °C}$-pep surfaces than TGL-TO$_{500 °C}$ surfaces that could be associated with the positive charge of the protonated K residue (NH$_3^+$) interacting with the cantilever and therefore increased of the F_{PO}. In the only case where the F_{PO} was higher for TGL-TO$_{500 °C}$ than for TGL-TO$_{500 °C}$-pep was at pH 5 and this could be attributed to the charge of the materials that are interacting (TiO$_2$, SiO$_2$ and Ti-HA-pep). According with the literature TiO$_2$ and SiO$_2$ can attract the peptide sequence minTBP-1 [122] making possible that the modified Ti-pep with similar behaviour to minTBP-1 (electrostatic adsorbed) can be attracted for both materials. For that reason, it is possible that at pH 5 the cantilever tip (negatively charged) that is in contact with the surface presents a greater interaction with the peptide sequence (positively and possibly negatively charged) than the metallic surface (IEP ≈ pH 5).

6.5. Conclusion

TGL-TO$_{500 °C}$-pep presents a Ti-HA-pep coating, and the presence of the coating on the surface can be measured by difference in chemistry, contact angle hysteresis, and AFM force- distance curves as shown below:

1) C and N content, measured by XPS, increases in the TGL-TO$_{500 °C}$-pep and the measured metallic content decreases.

2) The θ_a is smaller for all measured pH in TGL-TO$_{500 °C}$-pep than in TGL-TO$_{500 °C}$ surfaces, suggesting a difference in net surface charge.

3) The contact angle hysteresis of TGL-TO$_{500\,°C}$ -pep increment with the pH suggests the coating chemistry change with the pH, protonation/ deprotonation of COOH contained in the E$_8$ motif.

4) F$_{rep}$ and F$_{JT}$ increase between TGL-TO$_{500\,°C}$ and TGL-TO$_{500\,°C}$-pep surfaces can be related with a coating that contain acidic and basic aa (E and K).

5) F$_{rep}$ increases in TGL-TO$_{500\,°C}$-pep at pH 7 and 9 suggests the surface is negatively charged possibly for the ionised HA-pep motif.

6) High F$_{po}$ at pH 5 from the TGL-TO$_{500\,°C}$-pep can be associated with the adsorption and desorption of the Ti-HA-pep sequence on TiO$_2$ (analysed surface) and SiO$_2$ (cantilever).

Chapter 7

Peptide coating stability and functionality on titania gel surfaces treated at 500 °C on polished Ti-6Al-4V surfaces

7.1.   Introduction

Already existing research has shown that Ti-6Al-4V surface modification via H_2O_2/HCl with thermal treatment improved the bioactivity of the Ti-6Al-4V. Shi *et al.* [106] showed that when the surface was treated with H_2O_2/HCl and then thermally oxidised, the *in vitro* cells increased their proliferation. An alternate study performed *in vivo* by He *et al.* [107] it was shown that when a sandblast Ti-6Al-4V surface was treated with H_2O_2/HCl, and then thermally oxidised at 400 °C, the bone to implant contact percentage at 2 and 4 weeks increased around 5 % more than the control (without chemical and thermal treatment).

The bioactivity mechanism of the TiO_x surfaces is commonly attributed to the formation of apatite on the surface. Most authors suggest that the adsorption of Ca^{2+} on the negative charged surface together with PO_4^{3-} ions in the physiological media form an apatite layer of deficient hydroxyapatite (HA) similar to the mineral phase of bone [58–61]. Wang *et al*. [49] showed that TiO_x surfaces treated with H_2O_2/HCl and thermally oxidised at 500 °C formed a layer of HA with low crystallinity when immersed in SBF.

The additional use of peptide binder 5-FAM-KKLPDAKKLPDAEEEEEEEE (Ti-HA-pep) coating on the chemically and then thermally treated surfaces could increase the rate of formation of apatite crystals on the surface due to the increment of Ca^{+2} adsorption as a result of the higher negative charges generated by peptide presence (glutamic acid motif E_8 / HA-pep discussed in previous chapter) at physiological pH (deprotonation of COOH moieties, showed in previous chapter).

7.2. Objectives

The objective of this chapter was to assess the stability of the interaction between the peptide coating and the titania gel layer treated at 500 °C on polished Ti-6Al-4V under different conditions of pH, temperature and ionic strength, as well as evaluated the formation of apatite in uncoated and coated titania gel layer treated at 500 °C surfaces.

7.3. Stability of the peptide coating in titania gel treated at 500 °C on polished Ti-6Al-4V at different conditions of pH, temperature and ionic strength

7.3.1. Specific objective

The objective in this section was to evaluate the change of the peptide coating in a sample emulating some of the conditions present in the human body such as temperature, pH and ionic strength against samples that could potentially be found in external conditions in a pre-implantation moment. To simulate the conditions, the study was performed using combinations of the environmental conditions for different periods of time: unbuffered aqueous solution and buffer (SBF and PBS) aqueous solutions, pH (pH 5 and 7.4) and temperature (37 °C and 21±2 °C).

7.3.2. Results

Ti-HA-pep coated titania gel layer followed by thermal oxidation at 500 °C (TGL-TO$_{500}$ $_{°C}$ -pep) samples were exposure to unbuffered aqueous solution (aq), saturated simulated body fluid (SBF X 1.5) and phosphate buffer saline (PBS). Each solution was calibrated at pH 5 and 7.4. and exposed at room temperature (21 ± 2°C) and corporeal temperature (37 °C). TGL-TO$_{500}$ $_{°C}$-pep surfaces were measured by fluorescence microscopy before and after each immersion time. Each TGL-TO$_{500}$ $_{°C}$ -

pep sample was exposed to one solution, one pH, one temperature, and one immersion time. Immersions were performed for 1, 3, 6, 24, 48 and 72 h.

7.3.2.1. *Fluorescence intensity measured after immersion in aqueous solutions at pH 5 and 21±2 °C of peptide coated titania gel treated at 500 °C on polished Ti-6Al-4V*

Fluorescence intensity data measured on TGL-TO$_{500\,°C}$-pep surfaces before and after immersion in unbuffered (aq), SBF X 1.5 and PBS at pH 5 and 21±2 °C for 1, 3, 6, 24, 48 and 72 h is shown in Table 20. This data is used below to calculate ΔI.

Table 20: Fluorescence intensity before (I_0) and after (I_1) the immersion of TGL-TO$_{500\,°C}$-pep surfaces in unbuffered (aq), SBF X 1.5, PBS at pH 5 and 21±2 °C for 1, 3, 6, 24, 48 and 72 h.

Immersion time (h)	Unbuffered (aq)		SBF X 1.5		PBS	
	I_0 (a.u.)	I_1 (a.u.)	I_0 (a.u.)	I_1 (a.u.)	I_0 (a.u.)	I_1 (a.u.)
1	407±8	421±23	709±9	851±7	588±7	439±11
3	373±18	467±17	626±6	582±15	462±11	353±26
6	453±1	468±22	530±8	433±13	644±12	434±19
24	664±12	726±10	425±11	338±8	613±8	249±11
48	606±9	552±27	444±5	76±5	540±12	124±7
72	490±2	414±5	639±11	336±14	742±2	130±18

ΔI is calculated using Eq. 7 and data from Table 20

$$\Delta I = I_1 - I_0 \qquad \text{Eq. 7}$$

Where I_0 is the intensity before exposure and I_1 is the intensity after exposure to each ionic solution. The calculated ΔI at each exposure time in unbuffered (aq), SBF X 1.5 and PBS is shown in Figure 91.
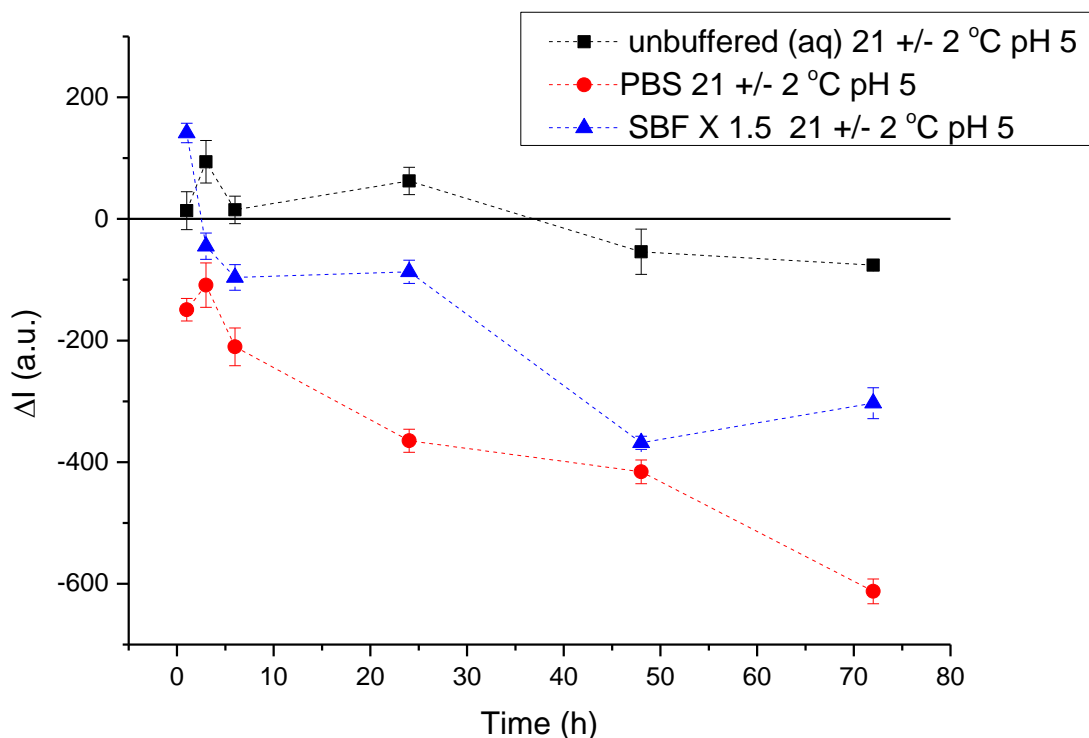
Figure 91: ΔI of TGL-TO$_{500\,°C}$ -pep surfaces when exposure to unbuffered (aq), PBS, SBF X 1.5 at pH 5 and 21±2 °C for 1, 3, 6, 24, 48 and 72 h.

For unbuffered (aq), at 1, 3, 6 and 24 h the ΔI of TGL-TO$_{500\,°C}$ -pep present positive values. At 48 and 72 h of exposure to unbuffered (aq), a drop in the ΔI that present negative values is observed in Figure 91. For SBF X 1.5, the ΔI decreases with the increase of time. At 1 h of exposure, ΔI is positive. At 3, 6, 24 48 and 72 h of exposure the ΔI present negative values attributed to the loss of the fluorescence, the lowest ΔI is detected at 48 h. For PBS, the ΔI decreases with the increase of time. In PBS all

the ΔI values are negative from the 1st hour of exposure and lower ΔI compared to the

other buffers.

7.3.2.2. *Fluorescence intensity measured after immersion in aqueous solutions at pH 7.4 and 21±2 °C of titania gel treated at 500 °C and peptide coated*

Fluorescence intensity data measured on TGL-TO$_{500 °C}$ -pep surfaces before and after

immersion in unbuffered (aq), SBF X 1.5 and PBS at pH 7.4 and 21±2 °C for 1, 3, 6,

24, 48 and 72 h are shown in Table 21. This data is used below to calculate ΔI.

Table 21: Fluorescence intensity before (I_0) and after (I_1) the immersion of TGL-TO$_{500 °C}$ -pep surfaces in unbuffered (aq), SBF X 1.5, PBS at pH 7.4 and 21±2 °C for 1, 3, 6, 24, 48 and 72 h.

Immersion time (h)	Unbuffered (aq)		SBF X 1.5		PBS	
	I_0 (a.u.)	I_1 (a.u.)	I_0 (a.u.)	I_1 (a.u.)	I_0 (a.u.)	I_1 (a.u.)
1	470±25	700±14	397±3	341±5	428±17	186±2
3	429±13	653±11	452±8	385±37	349±12	106±4
6	396±7	544±33	360±17	234±20	395±19	110±22
24	354±12	439±34	401±11	161±21	386±2	43±0.5
48	395±12	659±19	541±3	166±3	430±10	37±1
72	367±1	411±12	454±2	118±12	418±18	48±1

ΔI is calculated using Eq. 7 and data from Table 21. The calculated ΔI at each exposure

time in unbuffered (aq), SBF X 1.5 and PBS is shown in Figure 92.
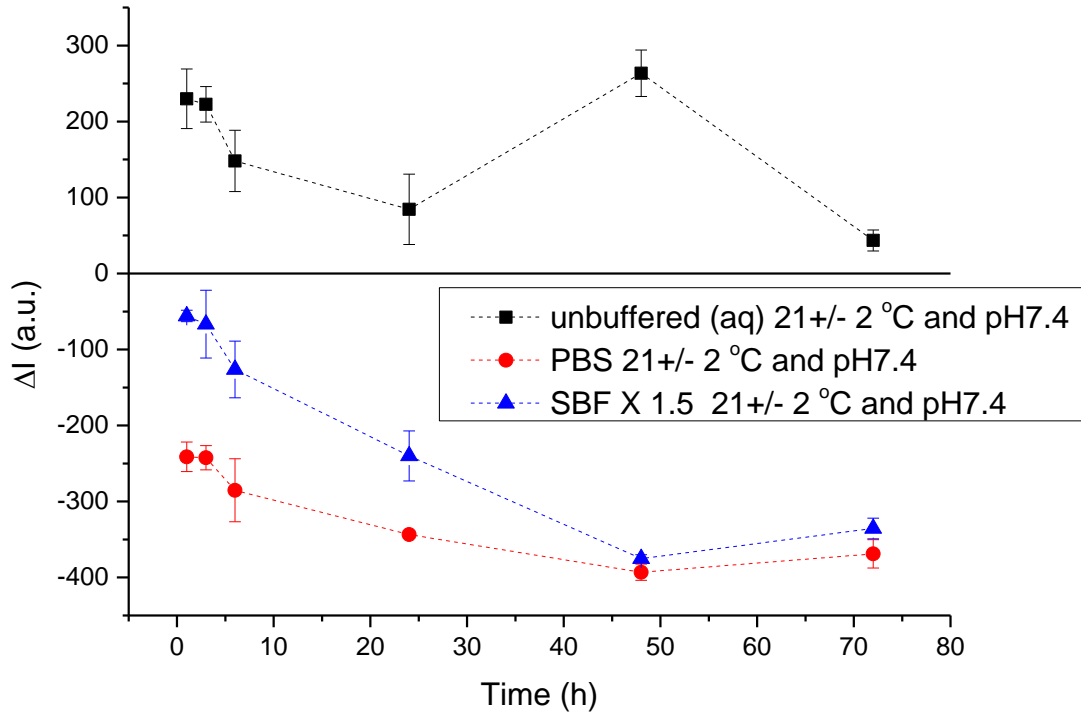
Figure 92: ΔI of TGL-TO$_{500\,°C}$ -pep surfaces when exposure to unbuffered (aq), PBS, SBF X 1.5 at pH 7.4 and 21±2 °C for 1, 3, 6, 24, 48 and 72 h.

For unbuffered (aq), all the immersion times present positive ΔI. For SBF X 1.5, the ΔI trend decrease between 1 and 72 h. At 72 h of immersion in SBF X1.5, 73 % of the I$_0$ is lost from TGL-TO$_{500\,°C}$ -pep surface. For PBS, ΔI present low values from the 1st hour. At 1 h of immersion in PBS, half of the I$_0$ is lost from TGL-TO$_{500\,°C}$ -pep surface. Between 3 and 6 h of immersion in PBS, around 72 % of I$_0$ is reduced from the surface. Between 24, and 72 h of immersion in PBS, ΔI remains constant.

171

7.3.2.3. Fluorescence intensity measured after immersion in aqueous solutions at pH 5 and 37 of titania gel treated at 500 °C and peptide coated

Fluorescence intensity data measured on TGL-TO$_{500\,°C}$-pep surfaces before and after immersion in unbuffered (aq), SBF X 1.5 and PBS at pH 5 and 37 °C for 1, 3, 6, 24, 48 and 72 h are shown in Table 22. This data is used below to calculate ΔI.

Table 22: Fluorescence intensity before (I_0) and after (I_1) the immersion of TGL-TO$_{500\,°C}$-pep surfaces in unbuffered (aq), SBF X 1.5, PBS at pH 5 and 37 °C for 1, 3, 6, 24, 48 and 72 h.

Immersion time (h)	Unbuffered (aq)		SBF X 1.5		PBS	
	I_0 (a.u.)	I_1 (a.u.)	I_0 (a.u.)	I_1 (a.u.)	I_0 (a.u.)	I_1 (a.u.)
1	421±12	560±13	638±16	604±33	545±4	325±10
3	514±2	566±5	666±46	590±80	600±12	293±3
6	483± 6	534±10	555±9	390±57	639±1	269±7
24	463±3	480±7	436±4	285±54	498±2	135±2
48	670± 5	539±15	624±15	270±9	625± 5	58±1
72	724±40	419±24	633±20	276±7	592±12	31±13

ΔI is calculated using Eq. 7 and data from Table 22. The calculated ΔI at each exposure time in unbuffered (aq), SBF X 1.5 and PBS is shown in Figure 93.
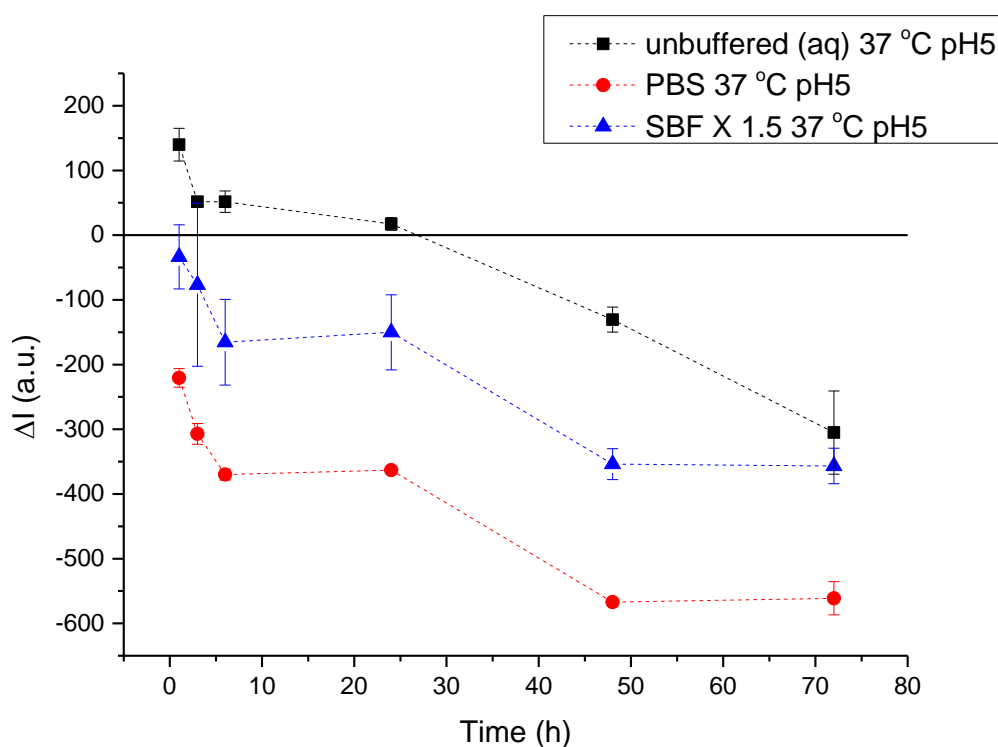
Figure 93: ΔI of TGL-TO$_{500\,°C}$ -pep surfaces when exposure to unbuffered (aq), PBS, SBF X1.5 at pH 5 and 37 °C for 1, 3, 6, 24, 48 and 72 h.

For unbuffered (aq), the trend within the first 24 h of immersion is constant and non-release is quantified until 48 and 72 h of immersion in unbuffered (aq). For SBF X 1.5, the ΔI decreases between 1 and 48 h of immersion in SBF X1.5, and then remains constant between 48 and 72 h. For PBS, ΔI presents a similar trend to SBF X1.5 but with low ΔI values.

7.3.2.4. *Fluorescence intensity measured after immersion in aqueous solutions at pH 7.4 and 37 °C of titania gel treated at 500 °C and peptide coated*

Fluorescence intensity data measured on TGL-TO$_{500\,°C}$-pep surfaces before and after immersion in unbuffered (aq), SBF X1.5 and PBS at pH 7.4 and 37 °C for 1, 3, 6, 24, 48 and 72 h are shown in Table 23. This data is used below to calculate ΔI.

Table 23: Fluorescence intensity before (I_0) and after (I_1) the immersion of TGL-TO$_{500\,°C}$-pep surfaces in unbuffered (aq), SBF X 1.5, PBS at pH 7.4 and 37 °C for 1, 3, 6, 24, 48 and 72 h.

Immersion time (h)	Unbuffered (aq)		SBF X 1.5		PBS	
	I_0 (a.u.)	I_1 (a.u.)	I_0 (a.u.)	I_1 (a.u.)	I_0 (a.u.)	I_1 (a.u.)
1	557±6	718±53	241±7	65±5	395±12	65±5
3	396±8	498±1	139±11	44±1	458±19	44±1
6	474±9	739±34	147±1	43±5	489±15	43±5
24	509±8	638±18	88±2	24±1	414±19	24±1
48	414±11	407±3	75±2	23±1	504±5	23±1
72	391±12	433±5	70±1	22±1	472±2	22±1

ΔI is calculated using Eq. 7 and data from Table 23. The calculated ΔI at each exposure time in unbuffered (aq), SBF X 1.5 and PBS is shown in Figure 94.
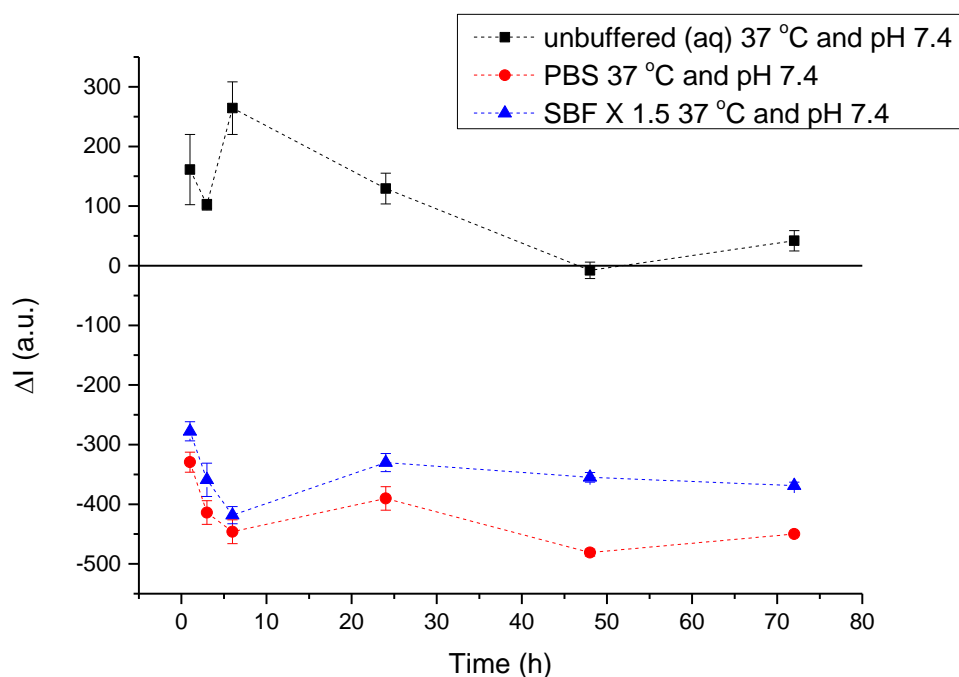
Figure 94: ΔI of TGL-TO$_{500\,°C}$ -pep surfaces when exposure to unbuffered (aq), PBS, SBF X 1.5 at pH 7.4 and 37 °C for 1, 3, 6, 24, 48 and 72 h.

For unbuffered (aq), ΔI present positive values for all immersion times. For SBF X 1.5, half of I_0 is reduced in the 1st h. At 1, 3 and 6 h of immersion in SBF X 1.5, ΔI decreases. At 24, 48 and 72 h of immersion in SBF X 1.5, ΔI slightly decreases. For PBS, ΔI presents a similar trend to SBF X 1.5 but with low ΔI values.

7.3.3. Discussion

The positive values on the ΔI, associated to an increase in fluorescence intensity and shown in Figure 91-94, of all TGL-TO$_{500\,°C}$-pep surfaces soaked in unbuffered (aq) could be explained by the configuration of the biomolecules on the surface [194] and/or the reorganisation of the peptide layer on the surface. The alteration in the configuration of the peptides on the surface could be associated to the change of the

ionic charges of the coating (discussed in Chapter 6) when pH increases above 4 (from the coated pH). The negative ΔI values after the exposure for 48 and 72 h at 21±2 and 37 °C in unbuffered (aq) at pH 5 could be due to the desorption of the peptide from the surface indicating that at low pH the release rate increases. This is in accordance with a multilayer system of poly-acrylic acid/ poly- allylamine hydrochloride studied by Chung and Rubner [195] where the release mechanism response to the change of pH that increased at low pH (pH 5).

TGL-TO$_{500\ °C}$-pep surfaces immersed in PBS, shown in Figure 91-94, present a decrease of the ΔI from the 1st hour of exposure to the solution that can be explained due to the presence of phosphate ions in the solution. This decrease could be related to the simultaneous desorption of the Ti-HA-pep from the TiO$_2$ surface and the chemisorption of phosphate ions into the TiO$_x$ surfaces. The strong interaction of the phosphates with TiO$_2$ in aqueous solution was studied by Connor and McQuillan [196] via *in situ* internal reflection infrared spectroscopy, showing that in the desorption curves the phosphate ions were still presented.

The decrease of ΔI on TGL-TO$_{500\ °C}$-pep samples that were immersed in SBF X 1.5, shown in Figure 91-94, could be associated with the presence of apatite layer on the surfaces that can decrease the emission of the fluorophore and therefore decrease the fluorescence intensity of the surface. The fluorescence intensity decreases more in the sample exposed at pH 7.4, where the formation of apatite according with the literature is favourable [197], than at pH 5. In addition, the surface at pH 7.4 presents a negative charge due to the ionised coating on the surface because of the presence of

Ti-HA-pep (discussed in Chapter 6) that can further increase the Ca-P nucleation on the surface.

7.4. Calcium phosphate biomimetic coating on peptide coated and uncoated titania gel treated at 500 °C on polished Ti-6Al-4V

7.4.1. Specific objective

The objective of this section was to evaluate the formation of apatite on peptide coated and uncoated titania gel layer treated at 500 °C on polished Ti-6Al-4V after the immersion in saturated simulated body fluid.

7.4.2. Results

Titania gel layer followed by thermal oxidation at 500 °C (TGL-TO$_{500\,°C}$) and Ti-HA-pep coated titania gel layer followed by thermal oxidation at 500 °C (TGL-TO$_{500\,°C}$-pep) samples were immersed in saturated body fluid (SBF X 1.5) for 1, 2, 3, 4, 5, 8, and 15 days. The surfaces were analysed by XRD, Raman spectroscopy, XPS, and visualised by SEM to evaluate the apatite formation on the surface.

7.4.2.1. Characterization of biomimetic apatite on peptide uncoated titania gel treated at 500 °C on polished Ti-6Al-4V

7.4.2.1.1. Crystal surface composition of biomimetic apatite on peptide uncoated titania gel treated at 500 °C on polished Ti-6Al-4V

XRD diffractograms of TGL-TO$_{500\,°C}$ surfaces immersed in SBF X 1.5 for 1, 4, 8 and 15 days and calcium phosphate hydroxide (JCPDS No. 9-0432) pattern are shown in Figure 95. All diffractograms contain α Ti crystals represented by peaks in 2θ: 35.42°, 38.54°, 40.44° and 53.26°. Non-apatite crystals are detected the first day, but the 4th, 8th and 15th days calcium phosphate hydroxides are presented with low crystallinity represented by the peaks around 2θ: 25.8 and 32°.
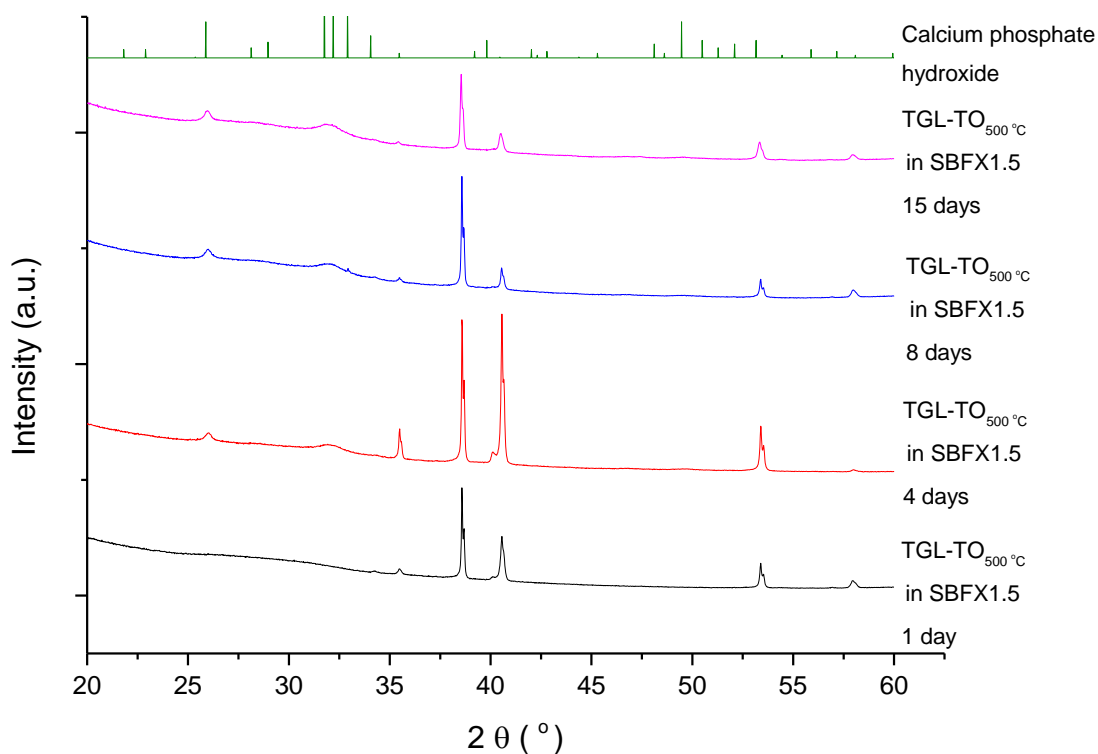
Figure 95: XRD diffractogram of TGL-TO$_{500\ °C}$ after been immersed in SBF X 1.5 for 1, 4, 8, 15 days and calcium phosphate hydroxide (JCPDS No. 9-0432) pattern.

Raman spectroscopy of TGL-TO$_{500\ °C}$ surfaces immersed in SBF X 1.5 for 1, 4, 8 and 15 days are shown in Figure 96. The highest band for all the samples immersed in SBF X 1.5 is at 960 cm^{-1} that band corresponds to the υ1 mode of PO$_4$ [198–200]. Raman spectrum of the sample immersed for 1 day shows two additional broad bands at 430 and 590 cm^{-1} that corresponds to the vibrational modes υ2 and υ4 of PO$_4$ [198,200], respectively. For 4, 8 and 15 days of immersion in SBF X 1.5 the bands mentioned before are present as well as an extra peak at 1070 cm^{-1} due to the vibrational mode υ3 of PO$_4$ [198,200].
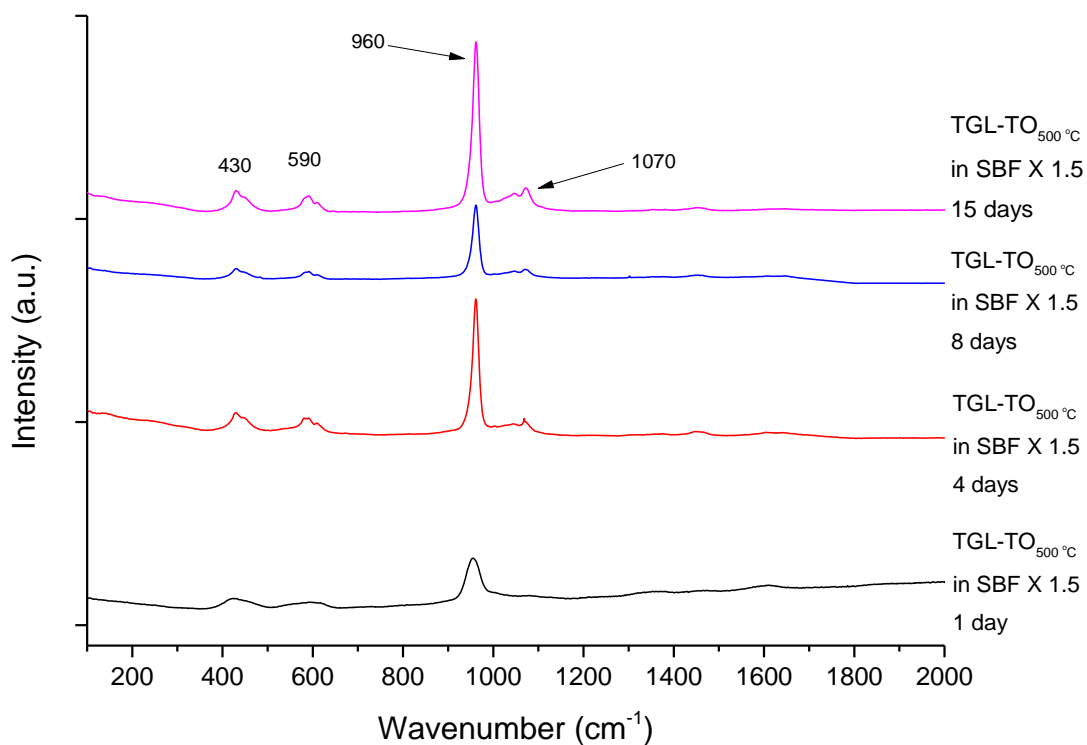
Figure 96: Raman spectrum of TGL-TO$_{500\,°C}$ immersed in SBF X 1.5 for 1, 4, 8 and 15 days.

7.4.2.1.2. *Chemical surface composition of biomimetic apatite on peptide uncoated titania gel treated at 500 °C on polished Ti-6Al-4V*

The XPS spectrum of TGL-TO$_{500\,°C}$ surfaces immersed in SBF X 1.5 show peaks in the binding energies of O 1s (531.1 eV), Ti 2p (448.1eV), Ca 2p (347.1 eV), C 1s (285.1 eV) and P 2p (133.1 eV). Figure 97 shows the spectrum of TGL-TO$_{500\,°C}$ immersed in SBF X 1.5 for 5 days. For all spectra, the same elements were analysed.
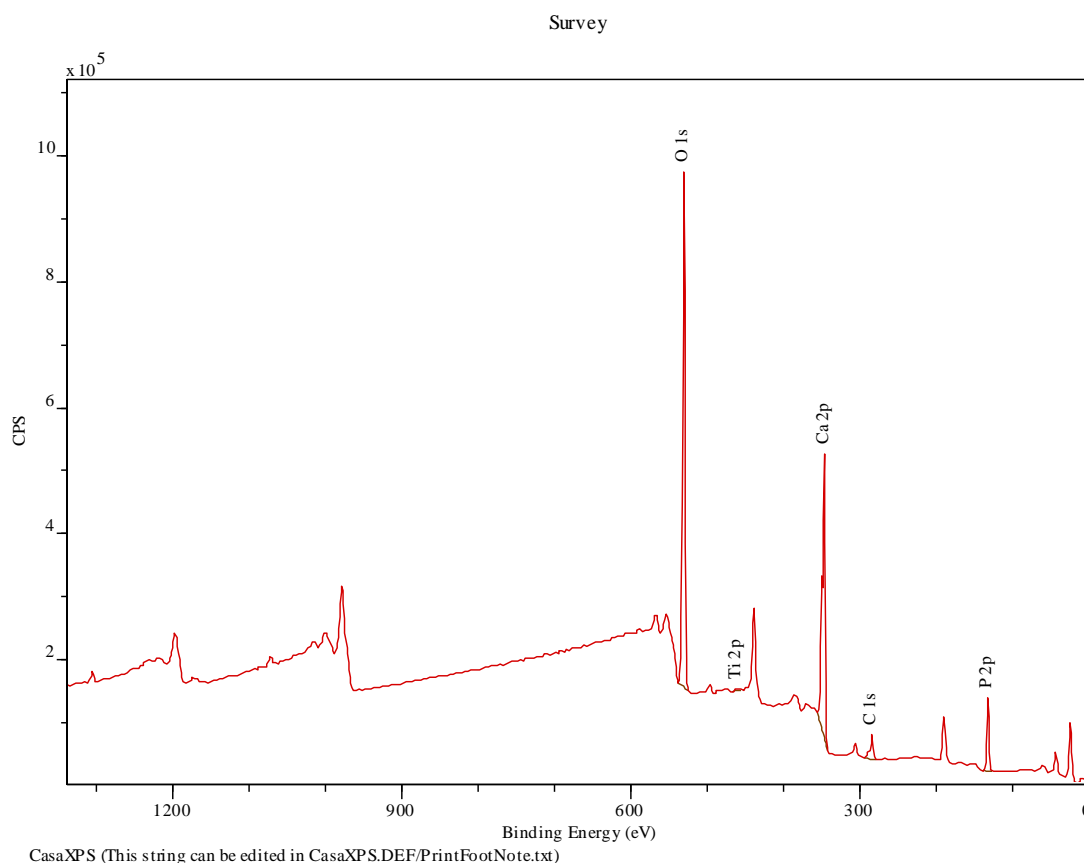
Figure 97: XPS spectrum survey of TGL-TO$_{500\,°C}$ immerse in SBF X 1.5 for 5 days.

The chemical composition of TGL-TO$_{500\,°C}$ immersed in SBF X 1.5 for 1, 2, 3, 4, 5, 8 and 15 days is shown in Table 24. O and Ca increase between the first and second day of immersion in SBF X 1.5 and maintain constant until the 8th day of immersion in SBF X 1.5. Both elements decrease by the 15th day of immersion in SBF X 1.5. Ti vanishes in the second day of immersion in SBF X 1.5. P maintains between 14.2 – 14.9 % for all the immersion times in SBF X 1.5. C contamination is present for all the samples.

Table 24: Chemical composition of TGL-TO$_{500\ °C}$ immersed in SBF X 1.5 for 0, 1, 2, 3, 4, 5, 8 and 15 days.

TGL-TO$_{500}$ °C immersed time in SBF X 1.5 (days)	O %	Ti %	Ca %	C %	P %	*Other %
0	52.7	20.6	0	19.9	1.4	5.4
1	46.8	0.8	17.7	20.4	14.3	0
2	49.1	0.2	20.0	15.8	14.9	0
3	50.2	0.1	20.3	14.6	14.8	0
4	49.6	0.1	20.0	15.6	14.7	0
5	49.5	0.1	20.1	15.5	14.8	0
8	49.9	0.1	20.6	14.8	14.6	0
15	48.3	0.1	19.6	17.8	14.2	0

*Other: V, N, Al, Si, Na and K

Ratio of Ca/P was calculated from XPS and is shown in Figure 98. Ca/P ratio has a significant increase from 1.24 to 1.37 between the 1st and the 3rd day. Between the 4th and 5th day, Ca/P ratio slightly decreases around 1.35. At the 8th day, the highest ratio is observed at around 1.40 and maintains closer in the 15th day.
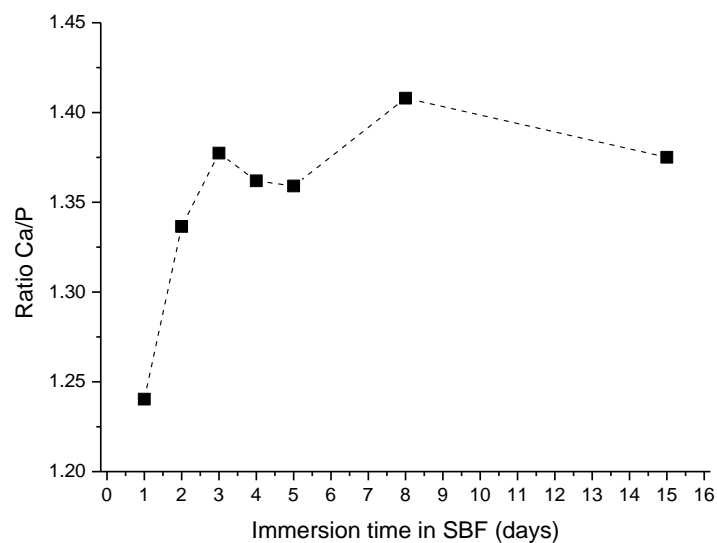
Figure 98: Ca/P ratio from XPS of TGL-TO$_{500\,°C}$ immersed in SBF X 1.5 for 1, 2, 3, 4, 5, 8 and 15 days.

7.4.2.1.3. Scanning electron microscopy of biomimetic apatite on peptide uncoated titania gel treated at 500 °C on polished Ti-6Al-4V

The morphology of the Ca-P on MPTG surfaces after being soaked in SBF X1.5 for 5 days is shown in Figure 99. Ca-P globular particles deposited on the surface of the already formed Ca-P layer that cover completely the metal surface are shown in Figure 99a. The layer formed underneath the particles of Ca- P shows in Figure 99b a homogenous layer of flake crystals.
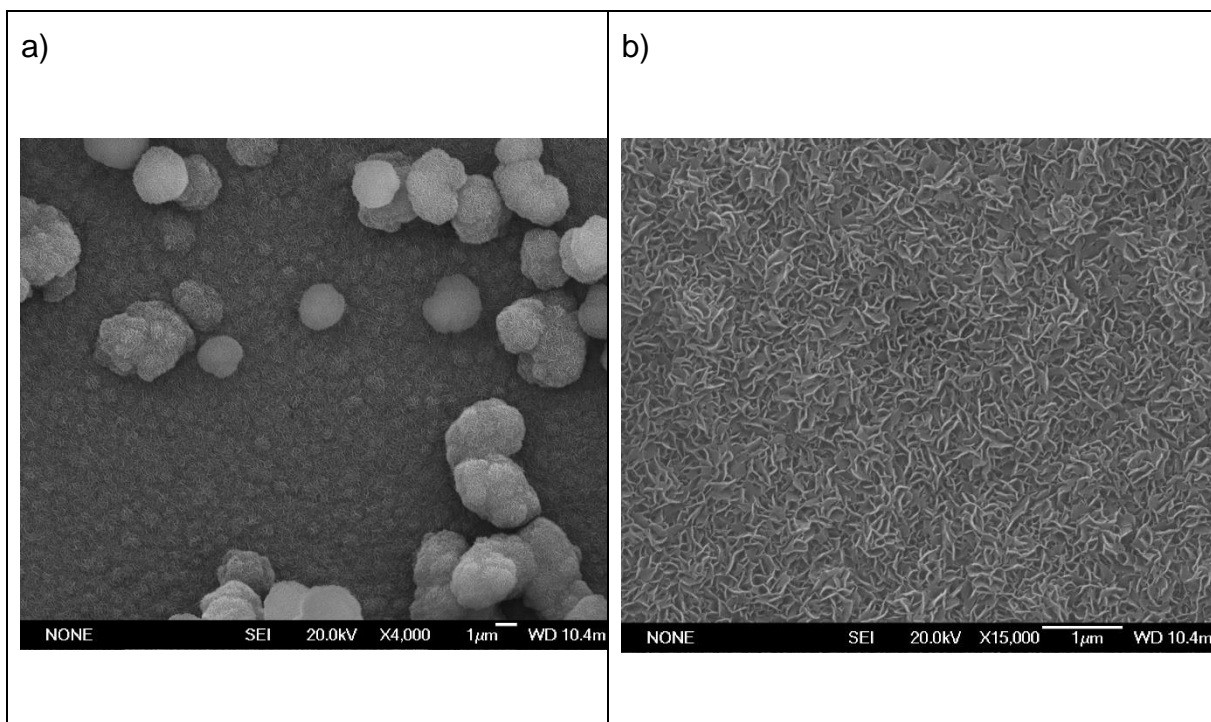
Figure 99: SEM picture of TGL-TO$_{500\,°C}$ after 5 days of immersion in SBF X 1.5 of a) Ca-P particles at low and b) Ca-P layer at high magnification.

7.4.2.2. Characterization of biomimetic apatite on peptide coated titania gel treated at 500 °C on polished Ti-6Al-4V

7.4.2.2.1. Crystal surface composition of biomimetic apatite on peptide coated titania gel treated at 500 °C on polished Ti-6Al-4V

XRD diffractogram of TGL-TO$_{500\,°C}$-pep surfaces immersed in SBF X 1.5 for 1, 4, 8,15 days and calcium phosphate hydroxide (JCPDS No. 9-0432) pattern are shown in Figure 100. α Ti is present for all the analysed samples. Apatite crystals are not present in the first day of immersion in SBF X 1.5 but in the 4th, 8th and 15th day of immersion in SBF X 1.5 low crystallinity of calcium phosphate hydroxide is observed around 2θ: 25.8 and 32°.
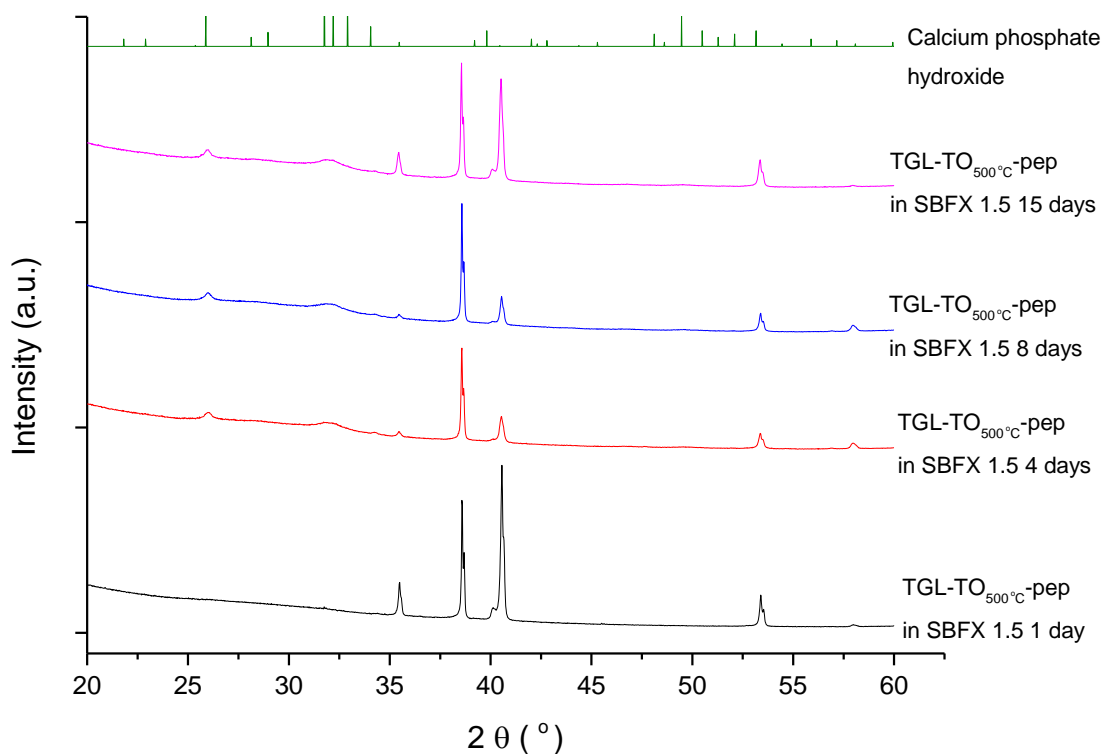
Figure 100: XRD diffractogram of TGL-TO$_{500\,°C}$-pep immersed in SBF X 1.5 for 1, 4, 8,15 days and calcium phosphate hydroxide (JCPDS No. 9-0432) pattern.

Raman spectrum of TGL-TO$_{500\,°C}$-pep immersed in SBF X 1.5 for 1, 4, 8 and 15 days are shown in Figure 101. The highest band for all the samples measured by Raman is at 960 cm^{-1} that corresponds to υ1 vibration mode of PO$_4$ [198–200]. The sample immersed for 1 day in SBF X 1.5 presents broad bands in 430 and 590 cm^{-1} that correspond to the vibrational modes υ2 and υ4 of PO$_4$ [198,200]. In addition, a small shoulder at around 1070 cm^{-1} due to υ3 vibrational mode of PO$_4$ [198,200] can be observed. At 4 days of immersion in SBF X 1.5, TGL-TO$_{500\,°C}$-pep surface presents similar Raman spectrum as the surface immersed during 1 day in SBF X 1.5. At 8 and 15 days of immersion in

184

SBF X 1.5, Raman spectrum presents intense peaks in υ2 and υ4 vibrational modes of PO$_4$.
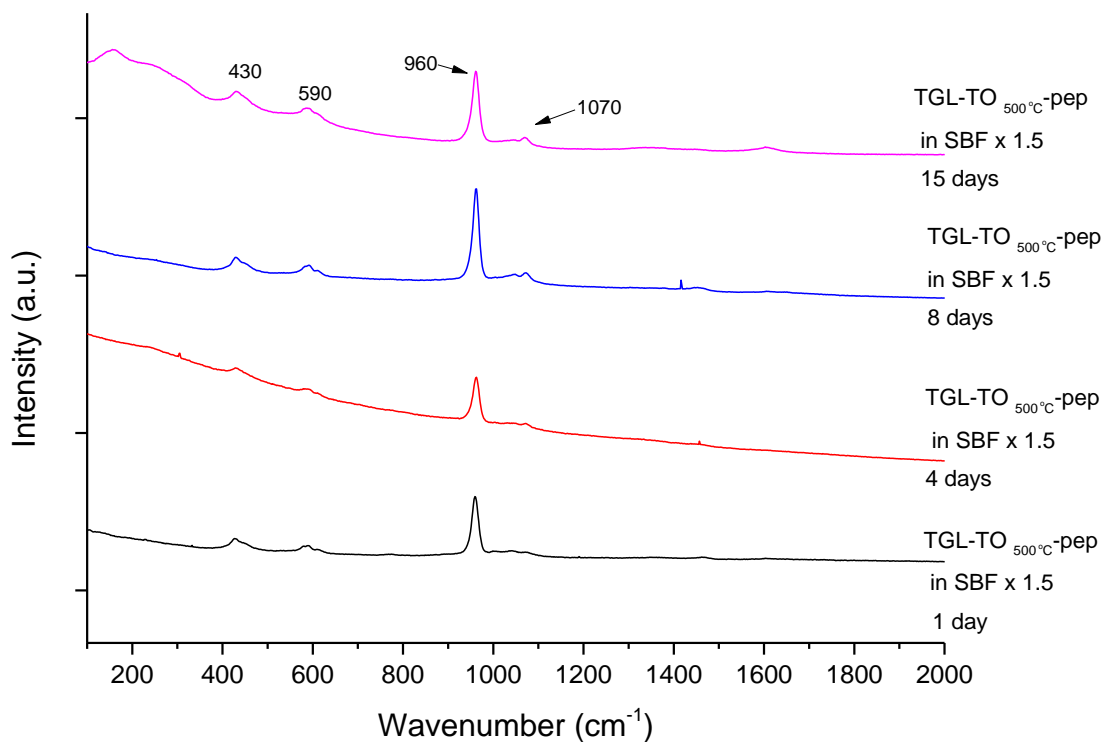
Figure 101: Raman spectrum of TGL-TO$_{500\,°C}$-pep immersed in SBF X 1.5 for 1, 4, 8 and 15 days.

7.4.2.2.2. Chemical surface composition of biomimetic apatite on peptide coated titania gel treated at 500 °C on polished Ti-6Al-4V

The chemical composition measured by XPS of TGL-TO$_{500\,°C}$-pep immersed in SBF X 1.5 for 1, 2, 3, 4, 5, 8 and 15 days is shown in Table 25. O percentage is around 51 % the first day of immersion SBF X 1.5 and increases the second day of immersion in SBF X 1.5 to 53 %. This last percentage remains constant for longer periods of immersion in SBF X 1.5. Ti highest percentage on TGL-TO$_{500\,°C}$-pep surfaces

immersed in SBF X 1.5 is 0.1 %. Ca percentage increases between the 1st and 2nd and maintains constant. C percentage decreases after the 2nd day of immersion in SBF X 1.5 between 12 % to 9.8 %. C percentages slightly decrease for the other immersion times. P percentage is maintained constant at around 15.8 % for all immersion times.

Table 25: Chemical composition of TGL-TO$_{500\,°C}$-pep immersed in SBF X 1.5 for 0, 1, 2, 3, 4, 5, 8 and 15 days.

TGL-TO$_{500\,°C}$-pep immersed time in SBF X 1.5 (days)	O %	Ti %	Ca %	C %	P %	*Other %
0	46	16.1	0	29.2	1.4	7.3
1	51.3	0.1	19.8	12.9	15.9	0
2	53.1	0.1	21.3	9.8	15.7	0
3	53.1	0.1	21.4	9.7	15.7	0
4	52.8	0.0	21.6	9.6	16.0	0
5	53.5	0.0	21.6	9.1	15.8	0
8	53.6	0.1	21.6	9.0	15.7	0
15	53.3	0.1	21.6	9.4	15.6	0

*Other includes V, N, Al, Si, Na and K

Ca/P ratio of TGL-TO$_{500\,°C}$-pep is shown in Figure 102. Ca/P ratio largest variation occurs between the 1st and 2nd day compared to the samples immerse for 3, 4, 5, 8 and 15 days in SBF X 1.5. Ca/P ratio trend slightly increases until 1.39 for the 15th day of immersion in SBF X 1.5.
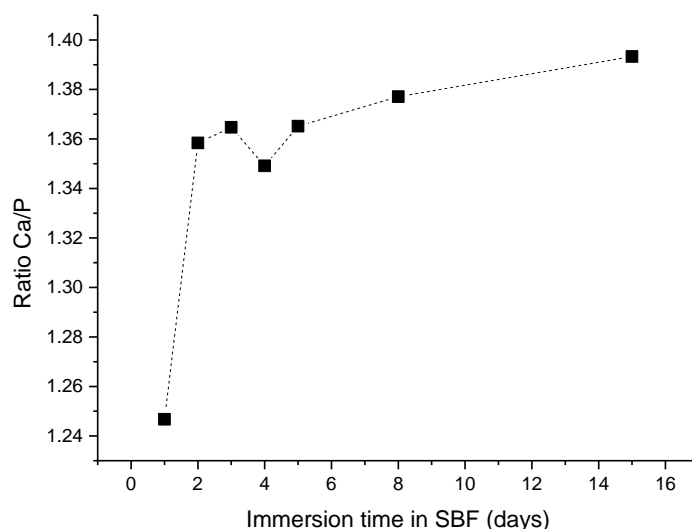
Figure 102: Ca/P ratio from XPS of TGL-TO$_{500\,°C}$-pep immersed in SBF X 1.5 for 1, 2, 3, 4, 5, 8, 15 days.

7.4.2.2.3. Scanning electron microscopy of biomimetic apatite on peptide coated titania gel treated at 500 °C on polished Ti-6Al-4V

TGL-TO$_{500\,°C}$-pep surface immersed in SBF X1.5 for 5 days is shown in Figure 103. A layer that covers the surfaces and round particles dispersed on the surface are observed on the SEM micrographs. Ca-P globular particles are shown in Figure 103a and the Ca-P layer morphology with flake like crystals is shown in Figure 103b.
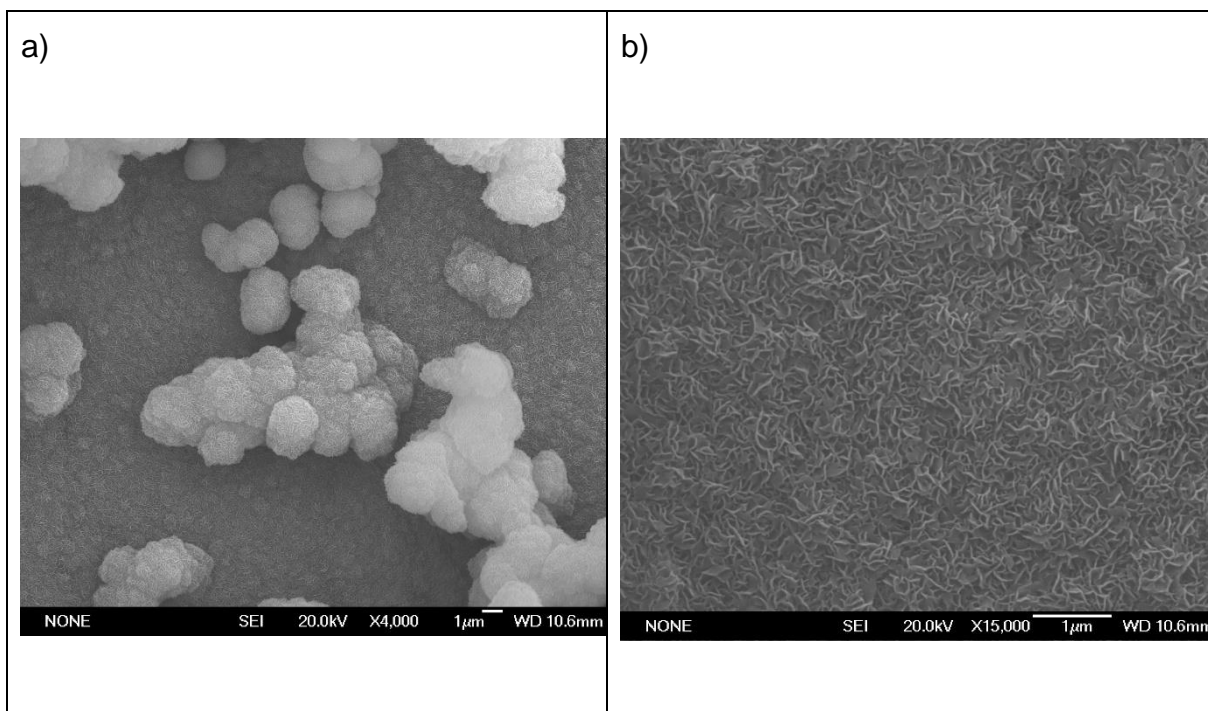
Figure 103: SEM micrograph of TGL-TO$_{500\,°C}$-pep surfaces after immersion in SBF X 1.5 for 5 days of a) Ca-P particles at low and b) Ca-P layer at high magnification.

7.4.2.3. Cellular adhesion on peptide coated titania gel layer treated at 500 °C on polished Ti-6Al-4V with and without biomimetic Ca-P apatite coating

SEM micrographs of human osteosarcoma (HOS) cells adhered on TGL-TO$_{500\,°C}$-pep are shown in Figure 104a and b at low and high magnification, respectively. Cells indicated by arrows present round and flatted morphologies. Some cells present filopodia attachment whereas some others present lamellipodium attachment on the TGL-TO$_{500\,°C}$-pep surface. These cells are adhered to the surface in larger areas than the TGL-TO$_{500\,°C}$ surfaces (presented in Figure 50 a and b from Chapter 3).

188
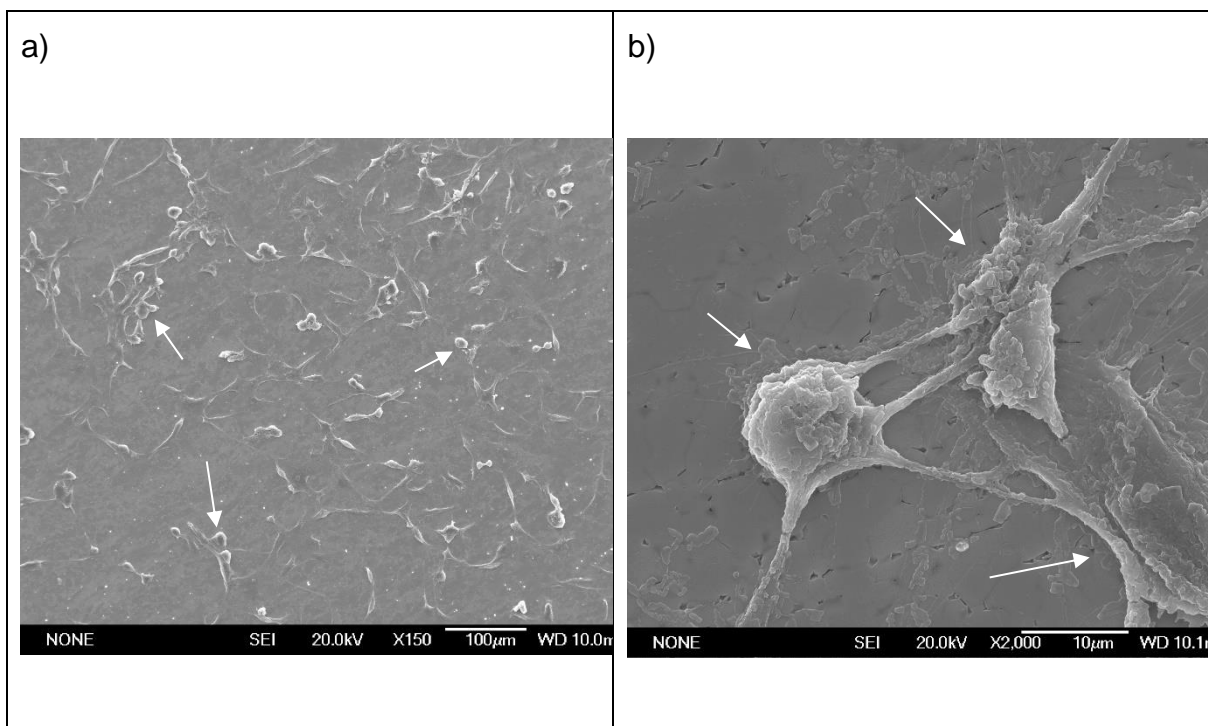
Figure 104: SEM micrograph of HOS on TGL-TO$_{500\,°C}$-pep surfaces a) low and b) high magnification.

SEM micrograph of TGL-TO$_{500\,°C}$-pep + apatite (form after 5 immersion days in SBF X 1.5) with cells is shown in Figure 105. Low magnitude SEM micrograph shows in Figure 105a areas cover by cells on the surface, indicating by arrows. High magnitude SEM micrograph shows in Figure 105b a well spread monolayer of cells on the surface.
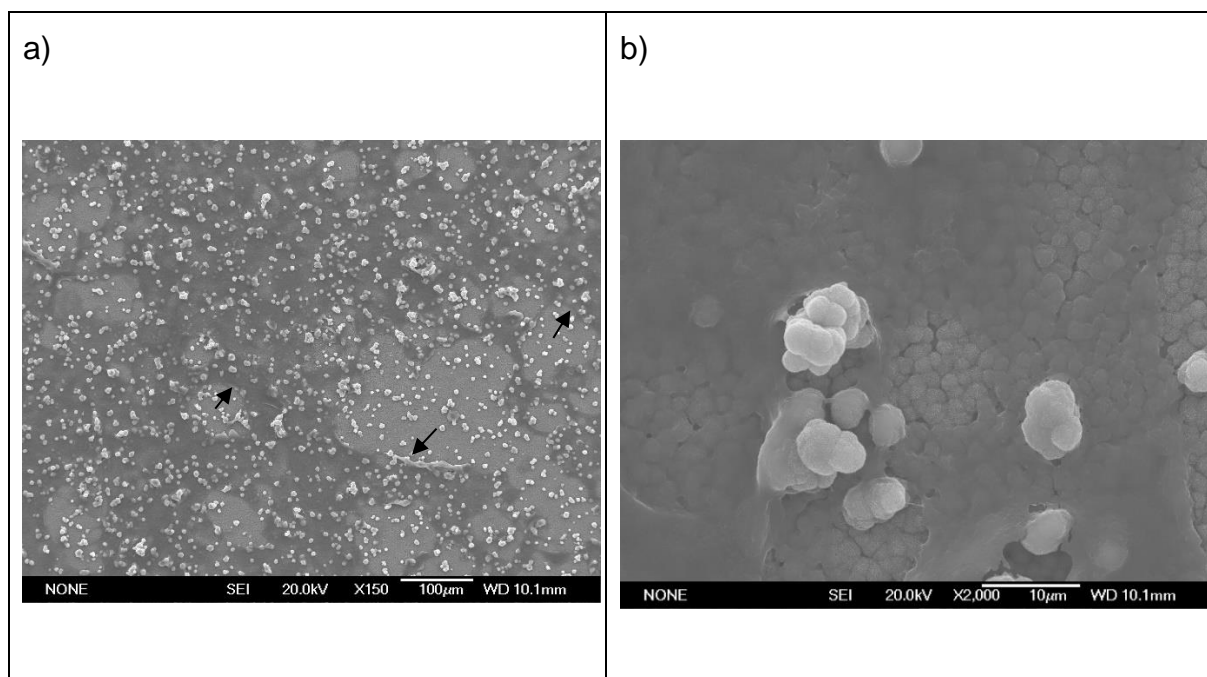
Figure 105 : SEM micrograph of HOS on TGL-TO$_{500\,°C}$-pep and apatite surfaces form after 8 days immersed in SBF X 1.5 a) low and b) high magnification.

7.4.3. Discussion

Low Ca-P crystallinity was detected on the apatite layer formed on TGL-TO$_{500\,°C}$ and TGL-TO$_{500\,°C}$-pep during the first days when samples were immersed in SBF X 1.5, shown in Figure 95 and 100. This result is in accordance with the studies performed by Habibovic *et al.* [27] and Barrere *et al.* [201] where poor crystallinity of Ca-P on the apatite layer was shown in the first 24 h of exposure in supersaturated SBF.

The Ca-P crystals measured by Raman spectrum, shown in Figure 96 and 101, could be associated with HA due to the single band at 960 cm^{-1}. According with the study

190

performed by Pecheva et al. [200] the strongest peak of the Raman spectrum on surfaces immersed in SBF for 6 days was at 952 cm^{-1} and this peak was associated with HA. A different study from Cuscó et al. [198] suggested as well that a single peak in μ-Raman at 960 cm^{-1} was related to HA.

The Ca/P ratio of the apatite layer for TGL-TO$_{500\,°C}$ and TGL-TO$_{500\,°C}$-pep, shown in Figure 98 and 102, present low Ca/P ratio in the first hours (Ca-poor apatite) but increases with the SBF X 1.5 immersion time. In addition, the Ca/P ratio of TGL-TO$_{500\,°C}$-pep is greater than TGL-TO$_{500\,°C}$ suggesting a large Ca enrichment on the apatite layer when E$_8$ motif is present. The increment of the Ca/P ratio are in accordance with the study performed by Kim et al. [28] where it was shown that crystal formation starts in the first hours with the enrichment of Ca, followed by the formation of a Ca-poor layer of amorphous Ca-P (due to the adsorption of PO$_4^{3-}$) that results in apatite layer that later incorporates Ca^{2+}, PO$_4^{3-}$, Mg^{+2}, Na$^+$, K$^+$, Cl$^-$, HCO$_3^-$ ions in around 12 h and finally achieving deficient HA similar to bone.

The Ca/P ratios measured by XPS, shown in Figure 98 and 102, present values between 1.2 and 1.4 that can be attributed to the formation of HA precursors that can be found when saturated SBF is used [202–204]. Octa-calcium phosphate (OCP) could be found on the apatite layer in the 1st and 2nd days, followed by β-tricalcium phosphate (β-TCP) in the 3rd, 4th and 5th days, and finally HA in the 8th and 15th days. These Ca/P ratios are in accordance with the measured Ca/P ratios using XPS by Lu et al. [205] where HA was 1.47 ± 0.09, OCP was1.24 ± 0.09 and for β-TCP was 1.35 ± 0.04.

The cell adhesion in TGL-TO$_{500\,°C}$-pep + apatite increased compared to the other surfaces previously shown in Chapter 3 and to TGL500- pep surfaces shown in Figure

104. The increase in cell adhesion can be observed in Figure 105 with cells well spread on the surface.

7.5.   Conclusions

1) A different configuration of peptides on TGL-TO$_{500\ °C}$ surfaces can take place when the samples are immersed in unbuffered (aq) at pH 7.4.

2) Reduction of the fluorescence intensity in TGL-TO$_{500\ °C}$-pep samples when exposed to PBS suggested the peptide coating was desorbed from the surface and it was replaced by phosphate ions that can chemisorbed on TiO$_2$.

3) Reduction of the fluorescence intensity in TGL-TO$_{500\ °C}$-pep samples when exposed to SBF X 1.5 showed that the apatite layer formed on the surface could potentially reduce the emission of the fluorophore.

4) Formation of low crystallinity Ca-P on TGL-TO$_{500\ °C}$ and TGL-TO$_{500\ °C}$-pep was detected during short immersion times.

5) HA layer was formed on TGL-TO$_{500\ °C}$ and TGL-TO$_{500\ °C}$-pep when surfaces were immersed in SBF X 1.5 after the 8th days.

6) A Ca-P layer rich in Ca was measured on TGL-TO$_{500\ °C}$-pep surfaces during the first days of immersion in saturated SBF X1.5.

Chapter 8

Summary and future work

8.1. Summary

Bioactive surfaces were obtained using a peptide interface capable of interacting electrostatically with titanium oxide (TiO_x) surfaces at one end and nucleating hydroxyapatite (HA) precipitation at the other end.

The electrostatic interaction between the peptide sequence 5FAM-KKLPDAKKLPDAEEEEEEEE (Ti-HA-pep) and TiO_x surface were studied on polished Ti-6Al-4V modified by three procedures, the first one was thermal oxidation (TO) at 500, 600, 700 and 800 °C, the second one was the chemical treatment with H_2O_2 8.8 M / HCl 0.1 M that after the reaction formed a titania gel layer (TGL) and the third one was the TGL followed by thermal oxidation (TGL-TO) at 500, 600, 700 and 800 °C. It was identified that TGL-TO$_{500\ °C}$ surface presented the highest adsorption with the Ti-HA-pep. Ti-HA-pep coated surface on TGL-TO$_{500\ °C}$ shown *in vitro* bioactivity with the formation of HA measured after 8 days of immersion in simulated body fluid (SBF). In addition, human osteosarcoma cells (HOS) adhered to the surface and spread with a flatter morphology on the biomimetic HA layer, showing that this surface presented a higher biocompatibility than the other modified surfaces (TO, TGL, TGL-TO) which presented round morphology. Figure 106 shows the process and modified surfaces to obtain a bioactive surface using a metal-peptide system.
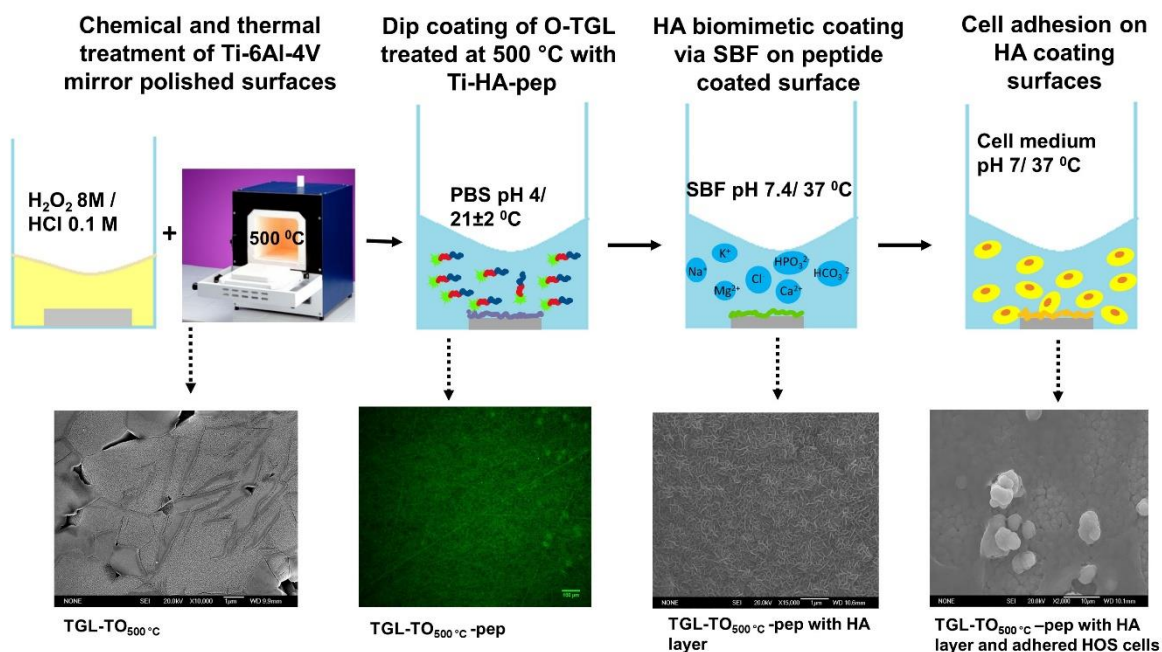
Figure 106: Process to obtain a bioactive surface using metal-peptide interface on TGL-TO$_{500\ ^\circ C}$.

The modified surface by TO and TGL-TO treated 600, 700 and 800 °C showed TiO$_2$ crystal formation. On top of this, it was observed that with the increase of TO temperature the O reacted from the air, the Al and V diffused from the substrate, and the average roughness (R$_a$) presented an upward tendency (R$_{a\ 500\ ^\circ C}$ < R$_{a\ 600\ ^\circ C}$ < R$_{a\ 700\ ^\circ C}$ < R$_{a\ 800\ ^\circ C}$). Samples chemically treated presented an additional topography for the previous reaction with H$_2$O$_2$ forming a titania gel layer (TGL) that presented porous structure on the Ti alloy grains and some pitting corrosion on the grain boundary possibly from the disintegration of the β grains on the surface. In addition, the TGL was suggested to be a barrier against the Al and V diffusion from the substrate as exhibited

in the TGL-TO $_{500\ °C}$ and TGL-TO $_{600\ °C}$ with Al and V % similar to the polished surfaces (MPT).

The behaviour of the modified surfaces TO and TGL-TO treated at 500, 600, 700 and 800 °C and its controls (MPT and TGL) in aqueous acidic and alkaline solution showed that the MPT surface presented a clear trend on the analysis (describe below) while the other surfaces presented difficulties to be analysed because of their heterogeneous surface chemistry and roughness. The MPT with an average roughness (R_a) of ≈ 0.7 nm showed that at pH 3 the surface presented a positive charge, between pH 7 and 9 the surface presented a negative charge and an isoelectric point (IEP) around pH 5. The accuracy of the measurement of other modified surfaces (TGL, TGL-TO and TO) was affected by the roughness ($R_a > 15$ nm), amorphous and crystal TiO_2 phase variation, and diverse composition of TiO_2, Al_2O_3 and possibly V_2O_5 (not detected). However, the charge of modified surfaces was predicted to be similar to the MPT surface (positively charged at pH 3, negatively charged at pH 7 and 9).

The adsorption of the Ti-HA-pep was present on surfaces chemically treated and showed higher fluorescence intensity on TGL, TGL-TO $_{500\ °C}$ and TGL-TO $_{600\ °C}$ than on the other modified surfaces. This result can be attributed to the chemistry of the surface after the reaction with H_2O_2/HCl mixture. The highest adsorption was presented by the TGL-TO $_{500\ °C}$ surface. This can be explained by the change in the surface chemistry and charge after the TO that conducted to a better electrostatic interaction with the Ti-HA-pep.

The coated Ti-HA-pep surface (TGL-TO $_{500\ °C}$-pep) presented chemical and charge surface differences from the uncoated surface (TGL-TO $_{500\ °C}$) due to the presence of

195

the peptide coating. The coated sample present an increase of atomic C % and N % and different contact angle hysteresis from the uncoated samples that could be attributed to the change in the chemistry. The difference response of coated and uncoated surfaces under the pH changes suggests that the HA motif (EEEEEEEE) of the Ti-HA-pep is facing outward, away from the surface, because of the charge changes due to the protonation and deprotonation of the COOH moieties which are contained in the HA motif.

The stability of the Ti-HA-pep coating on the TGL-TO$_{500\ °C}$ surfaces was evaluated under the permutation of pH (7.4 and 5) and temperatures (21 and 37 °C) showing that the coating could be desorbed in presence of phosphate buffered saline (PBS), maintained similar in presence of unbuffered solution and formed HA in presence of SBF optimal at pH 7.4 and 37 °C.

Both uncoated (TGL-TO$_{500\ °C}$) and coated (TGL-TO$_{500\ °C}$-pep) surfaces induced the formation of Ca/P layers and therefore could be considered bioactive. According to the Ca/P ratio, some precursors of the HA were obtained as follows: In the first 2 days of immersion in SBF the Ca/P ratio was associated with octa-calcium phosphate (OCP), followed in the next 3 days by a Ca/P ratio associated with β-tricalcium phosphate (β-TCP), and on the 8th day the Ca/P ratio was associated with HA. The Ti-HA-pep coated surface presented a richer Ca apatite layer in the first day compared to the uncoated sample and this difference can be attributed to the multiple COO$^-$ present in the Ti-HA-pep. Finally, cells that were adhered on the biomimetic HA layer surfaces were flat and spread on the surface indicating a higher cell adhesion compared to the other modified surfaces.

8.2. Future work

The objective of this section is to provide an indication of additional works for the improvement of the Ti-HA-pep interaction with the surface. The first identified works are related to surface improvements to achieve homogeneity and subsequent characterization. A second aspect is the additional need to prove the adsorption and desorption at molecular level to assess the mechanisms of electrostatic interaction. In addition, it is recommended to conduct further experiments to assess how the HA motif (EEEEEEE) impacts the nucleation of HA. Finally, the works carried out and current literature research indicate the possibilities of the peptide to perform additional functionalities such as drug delivery.

8.2.1. Surface chemistry and topography

Modified surfaces by chemical H_2O_2 and TO resulted in heterogenous roughness and chemistry surfaces, and this impacted the results of the characterization used to determine the charge changes because of the accuracy of the measurement magnitude and the surface chemistry and topography, therefore any alteration on the surface can lead to a different result. To understand how the charge can influence on the adsorption of the peptides it is recommended to work with surfaces that present homogenous chemistry and roughness. It is proposed to develop surfaces with a single TiO_2 crystal phase ,rutile or anatase, and smoother topography that can be produced by reactive magnetron sputtering [206], radio frequency magnetron sputtering [207] or atomic layer deposition [164] .

8.2.2. Characterizations for charged surfaces

The characterization of modified surfaces (TO, TGL and TGL-TO) to assess the surface charge at different pH presented a data with large standard deviation that was

attributed to the heterogeneity of the surface as mentioned before. To improve the measurements, it is recommended to work with a homogenous surface before implementing the following procedures:

- The contact angle titration could be performed in with small intervals (e.g. 0.5) to identify the IEP of the modified surface.
- The cantilever use for the AFM distance-force curves could be coated with the same material as the coated surfaces, to standardise and understand better the interaction forces when the ionic strength of the solution changes.
- The use of streaming potential measurements [108,160,190] to verify the IEP.

8.2.3. Peptide adsorption and desorption

The results obtained in Chapter 6 suggest that the peptide sequence 5-FAM-KKLPDAKKLPDAEEEEEEEE (Ti-HA-pep) binds electrostatically between the Ti motif (KKLPDAKKLPDA) and the TiO$_x$ surfaces. There is however no previous scientific evidence of the nature for the binding interaction and therefore the fully binding mechanisms cannot be fully confirmed. To address this, it is recommended to perform a phage display measurements between the Ti-HA-pep sequence and the TiO$_x$ surface, similar to the study performed by Sano and Shiba [40] with the peptide sequences minTBP-1 on TiO$_2$ surfaces.

Another issue was the quantification of the desorption of the peptides from the surface. The evidence of desorption showed in this thesis was measured through the decrease of the fluorescence intensity on the surfaces. Using this experiment as the evidence of desorption presents some drawbacks because the decrease in the intensity produced by the fluorophore is impacted by possibility of protonation and deprotonation

(pK_a =6.5) of the fluorophore, and the possible decay of the fluorophore. To mitigate this interference, it is recommended to use an experiment that allows to measure the surface desorption of the peptides with methods such as QCM in real time. Another alternative is to use AFM distance-force to measure the surfaces under the same conditions after each desorption and compared the results with the coated and uncoated samples.

8.2.4. HA formation peptide presence on peptide coated surfaces

The formation of HA in presence of the Ti-HA-pep was evaluated and compared against another surface previously studied that was shown to present HA formation, and the results did not provide full evidence that the peptide coating had the expected relevant role in the HA nucleation. To evaluate how the HA motif (EEEEEEEE) interferes in the nucleation of the HA two approaches are recommended: firstly, to adsorb Ti-HA-pep on smooth surfaces, secondly, to immobilize the HA motif on the surface via a self-assembled monolayer [208].

Once the HA is adsorbed or immobilized on the surface, it will be possible to evaluate the properties of the surface such as IEP and pK_a with the peptides, as well as how the peptide interferes in the nucleation of HA. Some techniques that could be used to determine how the crystals of HA change in the presence of the peptides are real time in situ QCM for the variation of kinetics [209] , Raman spectroscopy in real time and TEM in real time [210].

8.2.5. Other functionalities of adsorbed peptides

There are functionalities of great importance for the orthopaedics and dental fields that can be explored using the Ti binder (KKLPDAKKLPDA) and replacing the HA motif for

other peptide sequences or drug delivery systems. Some examples of the replacement molecules can be antimicrobial peptides [211], integrin sequences [127] or coordination spheres (molecules carriers) [124], that can help with the problems that are presenting nowadays the implants such as biofilm formation and failure of bone regeneration.

Appendix 1

Appendix 2
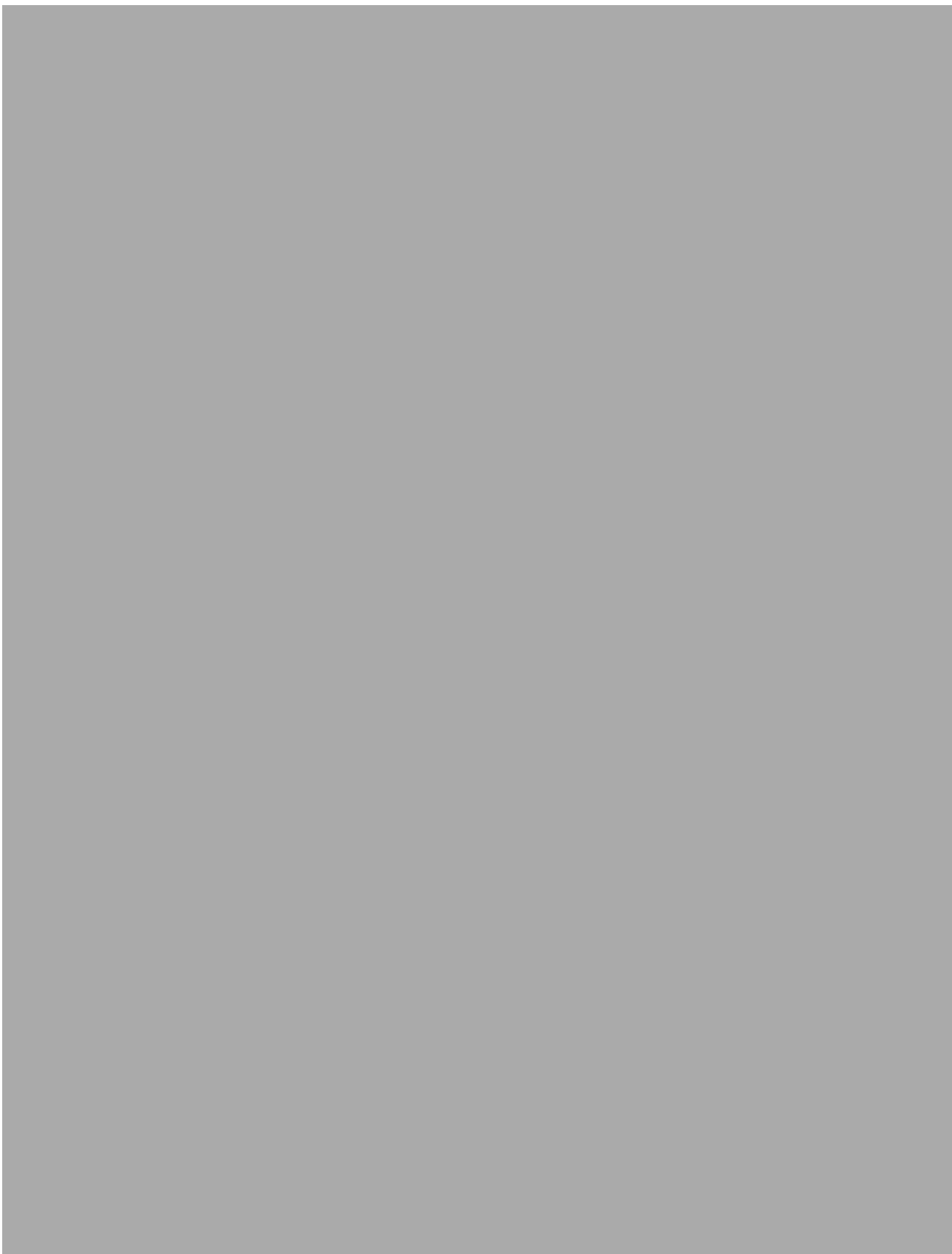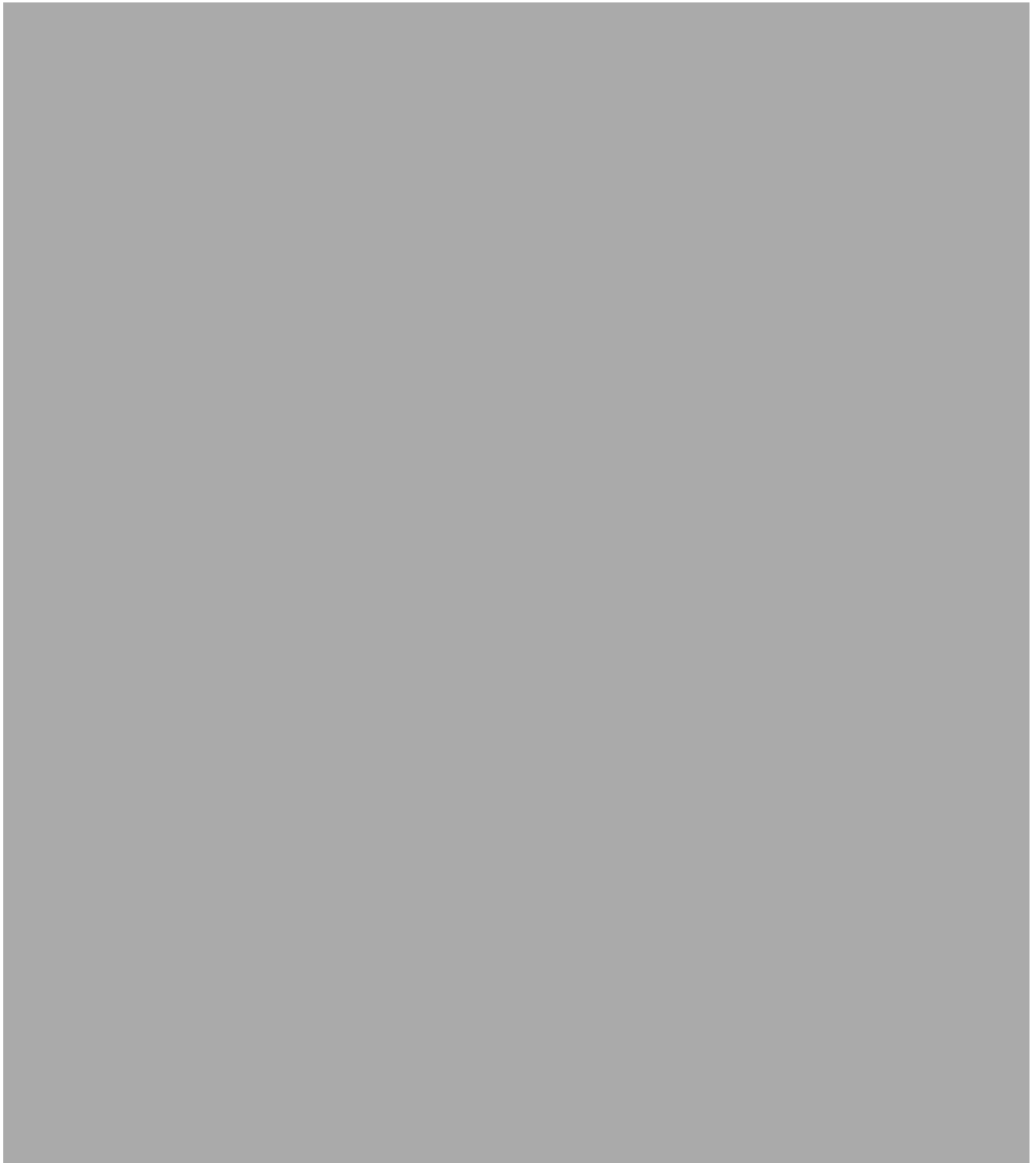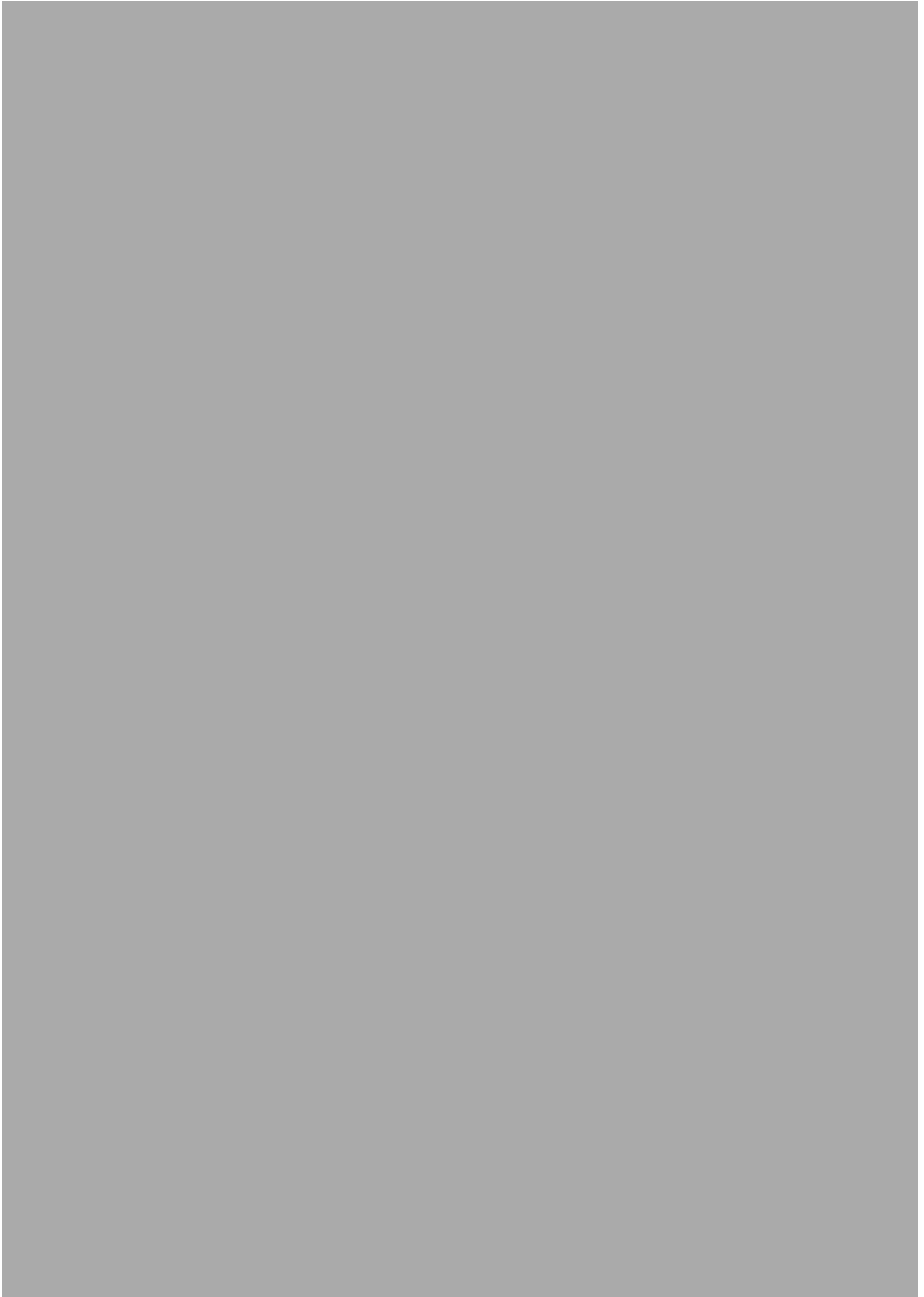
Appendix 3

The next paper (title and abstract) is pending for publication in the journal: Colloids and Surfaces B: Biointerfaces. It has undergone peer-review, and revisions have been submitted.

Functionalisation of Ti6Al4V and Hydroxyapatite surfaces with combined peptides based on KKLPDA and EEEEEEEE peptide aptamers.

Gabriela Melo Rodriguez[1], James Bowen[2,3], David Grossin[4], Besim Ben-Nissan[5] and Artemis Stamboulis[1]*

[1]School of Metallurgy and Materials, University of Birmingham, Edgbaston, Birmingham, B15 2TT, UK [2]School of Chemical Engineering, University of Birmingham, Edgbaston, Birmingham, B15 2TT, UK

[3]Faculty of Mathematics, Computing and Technology, Department of Engineering and Innovation, The Open University, Walton Hall, Milton Keynes, MK7 6AA, UK

[4]CIRIMAT Université de Toulouse, CNRS, INPT, UPS, ENSIACET, 4 allée Emile Monso, BP 44362, 31030 Toulouse cedex 4, France.

[5]Advanced Tissue Regeneration & Drug Delivery Group, School of Life Sciences, University of Technology Sydney, P.O. Box 123, Broadway, NSW 2007, Australia.

Abstract

The functionalisation of Ti6Al4V and hydroxyapatite surfaces using the (5-FAM) KKLPDAKKLPDAEEEEEEEE titanium-hydroxyapatite (Ti-Hap) peptide aptamers was achieved. Homogeneous peptide coatings in phosphate buffer solution (PBS) at pH

7.4 were obtained on the Ti6Al4V surface after treatment for 24 and 48 hours with a 30 wt % aqueous solution of H_2O_2. The titanium surfaces were oxidised for 24 and 48 hours and presented an average roughness (S_a) of 197 nm and 128 nm respectively; whereas an untreated polished sample exhibited an average roughness of 13 nm. The contact angle of the titanium oxide layer after 1 hour of exposition at 30 wt % aqueous solution of H_2O_2 was around 65 degrees, decreasing gradually with time until it reached 35 degrees at 48 hours, suggesting the hydrophilicity increased over the etching time. The peptide coating on the titanium surface using the KKLPDA peptide aptamer showed similar adsorption on the titanium oxide surface compared with the RKLPDA sequence. This result confirmed that both arginine and lysine can be used in the sequences of the peptide aptamer. For this particular work the lysine dimer KKLPDA was chosen. The Ti-Hap aptamer (5-FAM)-KKLPDAEEEEEEEE (Ti-Hap1) was not adsorbed by the treated Ti6Al4V surfaces and therefore was modified. The modifications involved the inclusion of a glycine spacer between the binding terminals (Ti-Hap2) and the addition of a second titanium binder (KKLPDA) (Ti-Hap3 and Ti-Hap4). The Ti-Hap peptide aptamer which exhibited the strongest intensity after the titanium dip coating was (5-FAM)-KKLPDAKKLPDAEEEEEEEE (Ti-HAp4). On the other hand, hydroxyapatite surfaces after polishing with an average roughness (S_a) of 1.42 µm had a higher adsorption of all peptide aptamers compared with titanium surfaces. This electrostatic organic coating can be suitable for adding functionality to medical titanium and hydroxyapatite surfaces, such as the attachment of antimicrobial peptides and specialised drugs for drug delivery.

References

1.	Liu X, Chu PK, Ding C. Surface modification of titanium, titanium alloys, and related materials for biomedical applications. *Mater Sci Eng R Reports*. 2004;47(3-4):49-121. doi:10.1016/j.mser.2004.11.001.

2.	Niinomi M. Mechanical biocompatibilities of titanium alloys for biomedical applications. *J Mech Behav Biomed Mater*. 2008;1(1):30-42. doi:10.1016/j.jmbbm.2007.07.001.

3.	Niinomi M. Recent metallic materials for biomedical applications. *Metall Mater Trans A*. 2002;33(3):477-486. doi:10.1007/s11661-002-0109-2.

4.	Siva Rama Krishna D, Brama YL, Sun Y. Thick rutile layer on titanium for tribological applications. *Tribol Int*. 2007;40(2 SPEC. ISS.):329-334. doi:10.1016/j.triboint.2005.08.004.

5.	Chen Q, Thouas GA. Metallic implant biomaterials. *Mater Sci Eng R Reports*. 2015;87:1-57. doi:10.1016/j.mser.2014.10.001.

6.	Mahyudin F, Widhiyanto L, Hermawan H. Biomaterials in orthopaedics. *Adv Struct Mater*. 2016;58(July):161-181. doi:10.1007/978-3-319-14845-8_7.

7.	Dong H, Bloyce A, Morton PH, Bell T. Surface engineering to improve tribological performance of Ti–6Al–4V. *Surf Eng*. 1997;13(5):402-406. doi:10.1179/sur.1997.13.5.402.

8.	MacDonald DE, Rapuano BE, Schniepp HC. Surface oxide net charge of a titanium alloy: Comparison between effects of treatment with heat or

radiofrequency plasma glow discharge. *Colloids Surfaces B Biointerfaces*. 2011;82(1):173-181. doi:10.1016/j.colsurfb.2010.08.031.

9. Kasemo B, Gold J. Implant surfaces and interface processes. *Adv Dent Res*. 1999;13(v):8-20. doi:10.1177/08959374990130011901.

10. Sidambe AT. Biocompatibility of advanced manufactured titanium implants-A review. *Materials (Basel)*. 2014;7(12):8168-8188. doi:10.3390/ma7128168.

11. Lee TM, Chang E, Yang CY. Surface characteristics of Ti6Al4V alloy: effect of materials, passivation and autoclaving. *J Mater Sci Mater Med*. 1998;9:439-448. doi:10.1023/A:1008815316564.

12. Milošev I, Metikoš-Huković M, Strehblow HH. Passive film on orthopaedic TiAlV alloy formed in physiological solution investigated by X-ray photoelectron spectroscopy. *Biomaterials*. 2000;21(20):2103-2113. doi:10.1016/S0142-9612(00)00145-9.

13. Yerokhin AL, Nie X, Leyland A, Matthews A. Characterisation of oxide films produced by plasma electrolytic oxidation of a Ti–6Al–4V alloy. *Surf Coatings Technol*. 2000;130:195-206. doi:10.1016/S0257-8972(00)00719-2.

14. Le Guéhennec L, Soueidan A, Layrolle P, Amouriq Y. Surface treatments of titanium dental implants for rapid osseointegration. *Dent Mater*. 2007;23(7):844-854. doi:10.1016/j.dental.2006.06.025.

15. Narayanan R, Seshadri SK, Kwon TY, Kim KH. Calcium phosphate-based coatings on titanium and its alloys. *J Biomed Mater Res - Part B Appl Biomater*.

2008;85(1):279-299. doi:10.1002/jbm.b.30932.

16. Hurwitz G, Guillen GR, Hoek EMV. Probing polyamide membrane surface charge, zeta potential, wettability, and hydrophilicity with contact angle measurements. *J Memb Sci*. 2010;349(1):349-357. doi:10.1016/j.memsci.2009.11.063.

17. Wennerberg A, Albrektsson T, Andersson B. Bone tissue response to commercially pure titanium implants blasted with fine and coarse particles of aluminum oxide. *Int J Oral Maxillofac Implants*. 1996;11(1).

18. Cooper LF, Masuda T, Whitson SW, Yliheikkilä P, Felton DA. Formation of mineralizing osteoblast cultures on machined, titanium oxide grit-blasted, and plasma-sprayed titanium surfaces. *Int J Oral Maxillofac Implants*. 1999;14(1).

19. Cao W, Hench LL. Bioactive materials. *Ceram Int*. 1996;22(6):493-507. doi:10.1016/0272-8842(95)00126-3.

20. Khoo X, Hamilton P, Toole GAO, et al. Directed assembly of PEGylated-peptide coatings for infection-resistant titanium metal. 2009:10992-10997.

21. Sun L, Berndt CC, Gross K a, Kucuk A. Material fundamentals and clinical performance of plasma-sprayed hydroxyapatite coatings : a review. *J Biomed Mater Res*. 2001;58(5):570-592. doi:10.1002/jbm.xxxx.

22. Yang Y, Kim K-H, Ong JL. A review on calcium phosphate coatings produced using a sputtering process--an alternative to plasma spraying. *Biomaterials*. 2005;26(3):327-337. doi:10.1016/j.biomaterials.2004.02.029.

23. de Groot K, Wolke JG, Jansen J a. Calcium phosphate coatings for medical implants. *J Eng Med*. 1998;212(2):137-147. doi:10.1243/0954411981533917.

24. Suchanek W, Yoshimura M. Processing and properties of hydroxyapatite-based biomaterials for use as hard tissue replacement implants. *J Mater Res*. 1998;13(1):94-117. doi:10.1557/JMR.1998.0015.

25. Ellies LG, Nelson DGA, Featherstone JDB. Crystallographic changes in calcium phosphates during plasma-spraying. *Biomaterials*. 1992;13(5):313-316. doi:10.1016/0142-9612(92)90055-S.

26. Filiaggi MJ, Coombs N a, Pilliar RM. Characterization of the interface in the plasma-sprayed HA coating/Ti-6Al-4V implant system. *J Biomed Mater Res*. 1991;25:1211-1229. doi:10.1002/jbm.820251004.

27. Habibovic P, Barrere F. Biomimetic hydroxyapatite coating on metal implants. *J Am Ceram Soc*. 2002;85(3):517-522. doi:10.1111/j.1151-2916.2002.tb00126.x.

28. Kim H-M, Himeno T, Kawashita M, Kokubo T, Nakamura T. The mechanism of biomineralization of bone-like apatite on synthetic hydroxyapatite: an in vitro assessment. *J R Soc Interface*. 2004;1(1):17-22. doi:10.1098/rsif.2004.0003.

29. Kokubo T, Kim HM, Kawashita M. Novel bioactive materials with different mechanical properties. *Biomaterials*. 2003;24(13):2161-2175. doi:10.1016/S0142-9612(03)00044-9.

30. Yan WQ, Nakamura T, Kawanabe K, Nishigochi S, Oka M, Kokubo T. Apatite layer-coated titanium for use as bone bonding implants. *Biomaterials*.

1997;18(17):1185-1190. doi:10.1016/S0142-9612(97)00057-4.

31. Bagno A, Piovan A, Dettin M, et al. Human osteoblast-like cell adhesion on titanium substrates covalently functionalized with synthetic peptides. *Bone*. 2007;40(3):693-699. doi:10.1016/j.bone.2006.10.007.

32. Xiao SJ, Textor M, Spencer ND, Wieland M, Keller B, Sigrist H. Immobilization of the cell-adhesive peptide Arg-Gly-Asp-Cys (RGDC) on titanium surfaces by covalent chemical attachment. *J Mater Sci Mater Med*. 1997;8(12):867-872. doi:10.1023/A:1018501804943.

33. Rezania A, Johnson R, Lefkow AR, Healy KE. Bioactivation of metal oxide surfaces. 1. Surface characterization and cell response. *Langmuir*. 1999;15(20):6931-6939. doi:10.1021/la990024n.

34. Rezania A, Healy KE. The effect of peptide surface density on mineralization of a matrix deposited by osteogenic cells. *J Biomed Mater Res*. 2000;52(4):595-600. doi:10.1002/1097-4636(20001215)52:4<595::AID-JBM3>3.0.CO;2-3.

35. Hubbel JA, Massia SP, Drumheller PD. Surface-grafted cell-binding peptides in tissue engineering of the vascular graft. *Ann N Y Acad Sci*. 1992;665(1 Biochemical E):253-258. doi:10.1111/j.1749-6632.1992.tb42589.x.

36. Massia SP, Hubbell JA. Covalent surface immobilization of Arg-Gly-Asp- and Tyr-Ile-Gly-Ser-Arg-containing peptides to obtain well-defined cell-adhesive substrates. *Anal Biochem*. 1990;187(2):292-301. http://www.ncbi.nlm.nih.gov/pubmed/2382830. Accessed November 30, 2017.

37. Joshi S, Ghosh I, Pokhrel S, Mädler L, Nau WM. Interactions of amino acids and polypeptides with metal oxide nanoparticles probed by fluorescent indicator adsorption and displacement. *ACS Nano.* 2012;6(6):5668-5679. doi:10.1021/nn301669t.

38. Fujisawa R, Wada Y, Nodasaka Y, Kuboki Y. Acidic amino acid-rich sequences as binding sites of osteonectin to hydroxyapatite crystals. *Biochim Biophys Acta - Protein Struct Mol Enzymol.* 1996;1292(1):53-60. doi:10.1016/0167-4838(95)00190-5.

39. Wang D, Mao J, Zhou B, et al. A chimeric peptide that binds to titanium and mediates MC3T3-E1 cell adhesion. *Biotechnol Lett.* 2011;33(1):191-197. doi:10.1007/s10529-010-0411-9.

40. Sano KI, Shiba K. A hexapeptide motif that electrostatically binds to the surface of titanium. *J Am Chem Soc.* 2003;125(47):14234-14235. doi:10.1021/ja038414q.

41. Wälivaara B, Aronsson BO, Rodahl M, Lausmaa J, Tengvall P. Titanium with different oxides: in vitro studies of protein adsorption and contact activation. *Biomaterials.* 1994;15(10):827-834. doi:10.1016/0142-9612(94)90038-8.

42. Yang X feng, Chen Y, Yang F, He FM, Zhao S fang. Enhanced initial adhesion of osteoblast-like cells on an anatase-structured titania surface formed by H_2O_2/HCl solution and heat treatment. *Dent Mater.* 2009;25(4):473-480. doi:10.1016/j.dental.2008.09.007.

212

43. Wu J, Hayakawa S, Tsuru K, Osaka A. Low-temperature preparation of anatase and rutile layers on titanium substrates and their ability to induce in vitro apatite deposition. *J Am Ceram Soc*. 2004;87(9):1635-1642. doi:10.1111/j.1551-2916.2004.01635.x.

44. Amin MS, Randeniya LK, Bendavid A, Martin PJ, Preston EW. Apatite formation from simulated body fluid on various phases of TiO_2 thin films prepared by filtered cathodic vacuum arc deposition. *Thin Solid Films*. 2010;519(4):1300-1306. doi:10.1016/j.tsf.2010.09.029.

45. Velten D, Biehl V, Aubertin F, Valeske B, Possart W, Breme J. Preparation of TiO_2 layers on cp-Ti and Ti6Al4V by thermal and anodic oxidation and by sol-gel coating techniques and their characterization. *J Biomed Mater Res*. 2002;59(1):18-28. doi:10.1002/jbm.1212.

46. Black J. Biological performance of materials: fundamentals of biocompatibility. In: CRC Press; 2005.

47. MacDonald DE, Rapuano BE, Deo N, Stranick M, Somasundaran P, Boskey AL. Thermal and chemical modification of titanium-aluminum-vanadium implant materials: Effects on surface properties, glycoprotein adsorption, and MG63 cell attachment. *Biomaterials*. 2004;25(16):3135-3146. doi:10.1016/j.biomaterials.2003.10.029.

48. Pan J, Liao H, Leygraf C, Thierry D, Li J. Variation of oxide films on titanium induced by osteoblast-like cell culture and the influence of an H_2O_2 pretreatment. *J Biomed Mater Res*. 1998;40:244-256. doi:10.1002/(SICI)1097-

4636(199805)40:2<244::AID-JBM9>3.0.CO;2-L.

49.   Wang XX, Hayakawa S, Tsuru K, Osaka A. Bioactive titania gel layers formed
       by chemical treatment of Ti substrate with a H_2O_2/HCl solution. *Biomaterials*.
       2002;23(5):1353-1357. doi:10.1016/S0142-9612(01)00254-X.

50.   Guleryuz H, Cimenoglu H. Surface modification of a Ti-6Al-4V alloy by thermal
       oxidation.   *Surf   Coatings   Technol.*   2005;192(2-3):164-170.
       doi:10.1016/j.surfcoat.2004.05.018.

51.   Kumar S, Sankara Narayanan TSN, Ganesh Sundara Raman S, Seshadri SK.
       Thermal oxidation of Ti6Al4V alloy: Microstructural and electrochemical
       characterization.   *Mater   Chem   Phys.*   2010;119(1-2):337-346.
       doi:10.1016/j.matchemphys.2009.09.007.

52.   MacDonald D., Deo N, Markovic B, Stranick M, Somasundaran P. Adsorption
       and dissolution behavior of human plasma fibronectin on thermally and
       chemically modified titanium dioxide particles. *Biomaterials*. 2002;23(4):1269-
       1279. doi:10.1016/S0142-9612(01)00317-9.

53.   Rabe M, Verdes D, Seeger S. Understanding protein adsorption phenomena at
       solid   surfaces.   *Adv   Colloid   Interface   Sci.*   2011;162(1-2):87-106.
       doi:10.1016/j.cis.2010.12.007.

54.   De Jonge LT, Leeuwenburgh SCG, Wolke JGC, Jansen JA. Organic-inorganic
       surface   modifications   for   titanium   implant   surfaces.   *Pharm   Res.*
       2008;25(10):2357-2369. doi:10.1007/s11095-008-9617-0.

55.   McCafferty E. *Surface Chemistry of Aqueous Corrosion Processes.*; 2015.

56.   Attard P, Antelmi D, Larson I. Comparison of the zeta potential with the diffuse layer potential from charge titration. *Langmuir*. 2000;16(4):1542-1552. doi:10.1021/la990487t.

57.   Jayaweera P, Hettiarachchi S, Ocken H. Determination of the high temperature zeta potential and pH of zero charge of some transition metal oxides. *Colloids Surfaces A Physicochem Eng Asp*. 1994;85(1):19-27. doi:10.1016/0927-7757(93)02737-Y.

58.   Li P, Ohtsuki C, Kokubo T, et al. Apatite formation induced by silica gel in a simulated body fluid. *J Am Ceram Soc*. 1992;75(8):2094-2097. doi:10.1111/j.1151-2916.1992.tb04470.x.

59.   Sugino A, Miyazaki T, Ohtsuki C. Apatite-forming ability of polyglutamic acid hydrogels in a body-simulating environment. *J Mater Sci Mater Med*. 2008;19(6):2269-2274. doi:10.1007/s10856-007-3327-8.

60.   Tanahashi M, Matsuda T. Surface functional group dependence on apatite formation on self-assembled monolayers in a simulated body fluid. *J Biomed Mater Res*. 1997;34(3):305-315. doi:10.1002/(SICI)1097-4636(19970305)34:3<305::AID-JBM5>3.0.CO;2-O [pii].

61.   Kokubo T. Apatite formation on surfaces of ceramics, metals and polymers in body environment. *Acta Mater*. 1998;46(7):2519-2527. doi:10.1016/S1359-6454(98)80036-0.

62. Farbod K, Nejadnik MR, Jansen J a, Leeuwenburgh SCG. Interactions between inorganic and organic phases in bone tissue as a source of inspiration for design of novel nanocomposites. *Tissue Eng Part B Rev.* 2014;20(2):173-188. doi:10.1089/ten.TEB.2013.0221.

63. Vezenov D V., Noy A, Rozsnyai LF, Lieber CM. Force titrations and ionization state sensitive imaging of functional groups in aqueous solutions by chemical force microscopy. *J Am Chem Soc.* 1997;119(8):2006-2015. doi:10.1021/ja963375m.

64. Cole MA, Voelcker NH, Thissen H, Griesser HJ. Stimuli-responsive interfaces and systems for the control of protein-surface and cell-surface interactions. *Biomaterials.* 2009;30(9):1827-1850. doi:10.1016/j.biomaterials.2008.12.026.

65. Kokubo T, Takadama H. How useful is SBF in predicting in vivo bone bioactivity? *Biomaterials.* 2006;27(15):2907-2915. doi:10.1016/j.biomaterials.2006.01.017.

66. Faeda RS, Tavares HS, Sartori R, Guastaldi AC, Marcantonio E. Biological performance of chemical hydroxyapatite coating associated with implant surface modification by laser beam: biomechanical study in rabbit tibias. *J Oral Maxillofac Surg.* 2009;67(8):1706-1715. doi:10.1016/j.joms.2009.03.046.

67. Luz GM, Mano JF. Mineralized structures in nature: Examples and inspirations for the design of new composite materials and biomaterials. *Compos Sci Technol.* 2010;70(13):1777-1788. doi:10.1016/j.compscitech.2010.05.013.

68. Wang X-X, Hayakawa S. Improvement of bioactivity of H_2O_2/$TaCl_5$-treated

titanium after subsequent heat treatments. 2000;196(7):3-12.

69. Anselme K. Osteoblast adhesion on biomaterials. *Biomaterials*. 2000;21(7):667-681. doi:10.1016/S0142-9612(99)00242-2.

70. C. Giordano, E. Sandrini, B. Del Curto, E. Signorelli, G. Rondelli, L. Di Silvio. Titanium for osteointegration: Comparison between a novel biomimetic treatment and commercially exploited surfaces. *J Appl Biomater Biomech*. 2004;2:35-44.

71. Boyan BD, Hummert TW, Dean DD, Schwartz Z. Role of material surfaces in regulating bone and cartilage cell response. *Biomaterials*. 1996;17(2):137-146. doi:10.1016/0142-9612(96)85758-9.

72. Le Guehennec L, Lopez-Heredia M-A, Enkel B, Weiss P, Amouriq Y, Layrolle P. Osteoblastic cell behaviour on different titanium implant surfaces. *Acta Biomater*. 2008;4(3):535-543. doi:10.1016/j.actbio.2007.12.002.

73. Kroese-Deutman HC, van den Dolder J, Spauwen PHM, Jansen J a. Influence of RGD-loaded titanium implants on bone formation in vivo. *Tissue Eng*. 2015;11(11-12):1867-1875. doi:10.1089/ten.2005.11.1867.

74. Demnati I, Grossin D, Combes C, Parco M, Braceras I, Rey C. A comparative physico-chemical study of chlorapatite and hydroxyapatite: from powders to plasma sprayed thin coatings. *Biomed Mater*. 2012;7(5):54101. doi:10.1088/1748-6041/7/5/054101.

75. TECHNOORG - LINDA. http://www.technoorg.hu/news-and-

events/articles/high-resolution-scanning-electron-microscopy-1/. Accessed July 5, 2017.

76. 1. Introduction | Development of X-ray crystallography - University of Illinois at Urbana-Champaign. https://publish.illinois.edu/x-raycrystallography/2014/12/18/introduction/. Accessed July 5, 2017.

77. Speakman SA. Basics of X-Ray Powder Diffraction. http://prism.mit.edu/xray.

78. Raman Spectroscopy | Science Facts. http://www.sciencefacts.net/raman-spectroscopy.html. Accessed July 5, 2017.

79. JPK Instruments AG - What is Atomic Force Microscopy? http://www.jpk.com/what-is-atomic-force-microscopy.432.en.html. Accessed July 5, 2017.

80. 2- Stretching | IGCSE Physics. https://hgphysics.com/gph/c-forces/2-force-effects/2-stretching/. Accessed July 5, 2017.

81. JPK Instruments AG - Imaging mode practicalities. http://www.jpk.com/imaging-mode-practicalities.434.en.html. Accessed July 5, 2017.

82. Jandt KD. Atomic force microscopy of biomaterials surfaces and interfaces. 2001;491.

83. Bowen J, Cheneler D, Walliman D, et al. On the calibration of rectangular atomic force microscope cantilevers modified by particle attachment and lamination. *Meas Sci Technol.* 2010;21(11):115106.

84. Young's Double Slit Experiment : What would happen if the "first slit " was too wide? - Physics Stack Exchange. https://physics.stackexchange.com/questions/114926/youngs-double-slit-experiment-what-would-happen-if-the-first-slit-was-too-w. Accessed July 5, 2017.

85. Soap-Film Painting: Color, Light Waves Science Activity Exploratorium Teacher Institute Project. https://www.exploratorium.edu/snacks/soap-film-painting. Accessed July 5, 2017.

86. Interferometry: Measuring with Light , Photonics Handbook® , EDU.Photonics.com. https://www.photonics.com/EDU/Handbook.aspx?AID=25128. Accessed July 5, 2017.

87. Photoelectron Spectrometer XPS and UPS - CleanEnergyWIKI. http://photonicswiki.org/index.php?title=Photoelectron_Spectrometer_XPS_and _UPS. Accessed July 5, 2017.

88. Ultra High Vacuum Lab. http://jacobs.physik.uni-saarland.de/english/instrumentation/uhvl.htm. Accessed July 5, 2017.

89. 5(6)-FAM-RISPC BioVinc LLC. https://www.biovinc.com/product/56-fam-rispc/. Accessed July 5, 2017.

90. FluorescenceFilters 2008-09-28.svg - Wikimedia Commons. https://commons.wikimedia.org/wiki/File:FluorescenceFilters_2008-09-28.svg.

Accessed July 5, 2017.

91. Contact angle.svg - Wikimedia Commons. https://commons.wikimedia.org/wiki/File:Contact_angle.svg. Accessed July 5, 2017.

92. Contact Angle Meter - WEISTRON. http://www.weistron.com/products/contact-angle-meter/. Accessed July 5, 2017.

93. Chau LK, Porter MD. Surface isoelectric point of evaporated silver films: Determination by contact angle titration. *J Colloid Interface Sci.* 1991;145(1):283-286. doi:10.1016/0021-9797(91)90121-N.

94. Boyer R, Welsch G, Collings EW. Materials properties handbook : titanium alloys. In: ASM International; 1994:1176.

95. Geetha M, Singh AK, Asokamani R, Gogia AK. Ti based biomaterials, the ultimate choice for orthopaedic implants - A review. *Prog Mater Sci.* 2009;54(3):397-425. doi:10.1016/j.pmatsci.2008.06.004.

96. Donachie MJ. Titanium : a technical guide. In: ASM International; 2000:381.

97. Browne M, Gregson PJ. Surface modification of titanium alloy implants. *Biomaterials.* 1994;15(11):894-898. doi:10.1016/0142-9612(94)90113-9.

98. Ferraris S, Spriano S, Pan G, et al. Surface modification of Ti-6Al-4V alloy for biomineralization and specific biological response: Part I, inorganic modification. *J Mater Sci Mater Med.* 2011;22(3):533-545. doi:10.1007/s10856-011-4246-2.

220

99. Bjursten LM, Rasmusson L, Oh S, Smith GC, Brammer KS, Jin S. Titanium dioxide nanotubes enhance bone bonding in vivo. *J Biomed Mater Res - Part A*. 2010;92(3):1218-1224. doi:10.1002/jbm.a.32463.

100. Sundgren J-E, Bodö P, Lundström I. Auger electron spectroscopic studies of the interface between human tissue and implants of titanium and stainless steel. *J Colloid Interface Sci*. 1986;110(1):9-20. doi:10.1016/0021-9797(86)90348-6.

101. Lowenberg B, Chernecky R, Shiga A, Davies JE. Mineralized Matrix Production by Osteoblasts on Solid Titanium In Vitro. *Cells Mater CELLS Mater*. 1991;1(2):177-187.

102. Kokubo T. Bioactive glass ceramics: properties and applications. *Biomaterials*. 1991;12(2):155-163. doi:10.1016/0142-9612(91)90194-F.

103. Advincula MC, Rahemtulla FG, Advincula RC, Ada ET, Lemons JE, Bellis SL. Osteoblast adhesion and matrix mineralization on sol-gel-derived titanium oxide. *Biomaterials*. 2006;27(10):2201-2212. doi:10.1016/j.biomaterials.2005.11.014.

104. Zreiqat H, Valenzuela SM, Nissan B Ben, et al. The effect of surface chemistry modification of titanium alloy on signalling pathways in human osteoblasts. *Biomaterials*. 2005;26(36):7579-7586. doi:10.1016/j.biomaterials.2005.05.024.

105. Ku CH, Pioletti DP, Browne M, Gregson PJ. Effect of different Ti-6Al-4V surface treatments on osteoblasts behaviour. *Biomaterials*. 2002;23(6):1447-1454. doi:10.1016/S0142-9612(01)00266-6.

106. Shi G, Ren L, Wang L, Lin H, Wang S, Tong Y. H_2O_2/HCl and heat-treated Ti-

6Al-4V stimulates pre-osteoblast proliferation and differentiation. *Oral Surgery, Oral Med Oral Pathol Oral Radiol Endodontology*. 2009;108(3):368-375. doi:10.1016/j.tripleo.2009.05.033.

107. He FM, Yang GL, Li YN, Wang XX, Zhao SF. Early bone response to sandblasted, dual acid-etched and H_2O_2/HCl treated titanium implants: an experimental study in the rabbit. *Int J Oral Maxillofac Surg*. 2009;38(6):677-681. doi:10.1016/j.ijom.2009.03.716.

108. Roessler S, Zimmermann R, Scharnweber D, Werner C, Worch H. Characterization of oxide layers on Ti6Al4V and titanium by streaming potential and streaming current measurements. *Colloids Surfaces B Biointerfaces*. 2002;26(4):387-395. doi:10.1016/S0927-7765(02)00025-5.

109. Karthega M, Rajendran N. Hydrogen peroxide treatment on Ti-6Al-4V alloy: A promising surface modification technique for orthopaedic application. *Appl Surf Sci*. 2010;256(7):2176-2183. doi:10.1016/j.apsusc.2009.09.069.

110. Tengvall P, Lundström I. Physico-chemical considerations of titanium as a biomaterial. *Clin Mater*. 1992;9(2):115-134. doi:10.1016/0267-6605(92)90056-Y.

111. Hanaor DAH, Sorrell CC. Review of the anatase to rutile phase transformation. doi:10.1007/s10853-010-5113-0.

112. Chang H, Huang PJ. Thermo-Raman studies on anatase and rutile. *J Raman Spectrosc*. 1998;29(2):97-102. doi:10.1002/(SICI)1097-

4555(199802)29:2<97::AID-JRS198>3.0.CO;2-E.

113. Biswas A, Dutta Majumdar J. Surface characterization and mechanical property evaluation of thermally oxidized Ti-6Al-4V. *Mater Charact*. 2009;60(6):513-518. doi:10.1016/j.matchar.2008.12.014.

114. Rinner M, Gerlach J, Ensinger W. Formation of titanium oxide films on titanium and Ti6Al4V by O_2-plasma immersion ion implantation. *Surf Coatings Technol*. 2000;132(2-3):111-116. doi:10.1016/S0257-8972(00)00712-X.

115. Oh SM, Ishigaki T. Preparation of pure rutile and anatase TiO_2 nanopowders using RF thermal plasma. *Thin Solid Films*. 2004;457(1):186-191. doi:10.1016/j.tsf.2003.12.043.

116. Vallee A, Humblot V, Pradier C-M. Peptide interactions with metal and oxide surfaces. *Acc Chem Res*. 2010;43(10):1297-1306. doi:10.1021/ar100017n.

117. Lee MH, Park IS, Min KS, et al. Evaluation of in vitro and in vivo tests for surface-modified titanium by H_2SO_4 and H_2O_2 treatment. *Met Mater Int*. 2007;13(2):109-115. http://www.scopus.com/inward/record.url?eid=2-s2.0-34249323040&partnerID=tZOtx3y1.

118. Zhao L, Mei S, Chu PK, Zhang Y, Wu Z. The influence of hierarchical hybrid micro/nano-textured titanium surface with titania nanotubes on osteoblast functions. *Biomaterials*. 2010;31(19):5072-5082. doi:10.1016/j.biomaterials.2010.03.014.

119. Jayaraman M, Meyer U, Bühner M, Joos U, Wiesmann HP. Influence of titanium

surfaces on attachment of osteoblast-like cells in vitro. *Biomaterials*. 2004;25(4):625-631. doi:10.1016/S0142-9612(03)00571-4.

120. Zhu X, Chen J, Scheideler L, Altebaeumer T, Geis-Gerstorfer J, Kern D. Cellular reactions of osteoblasts to micron- and submicron-scale porous structures of titanium surfaces. *Cells Tissues Organs*. 2004;178(1):13-22. doi:10.1159/000081089.

121. Deligianni D, Katsala N, Ladas S, Sotiropoulou D, Amedee J, Missirlis Y. Effect of surface roughness of the titanium alloy Ti-6Al-4V on human bone marrow cell response and on protein adsorption. *Biomaterials*. 2001;22(11):1241-1251. doi:10.1016/S0142-9612(00)00274-X.

122. Mirau PA, Naik RR, Gehring P. Structure of peptides on metal oxide surfaces probed by NMR. *J Am Chem Soc*. 2011;133(45):18243-18248. doi:10.1021/ja205454t.

123. Gertler G, Fleminger G, Rapaport H. Characterizing the adsorption of peptides to TiO_2 in aqueous solutions by liquid chromatography. *Langmuir*. 2010;26(9):6457-6463. doi:10.1021/la903490v.

124. Khatayevich D, Gungormus M, Yazici H, et al. Biofunctionalization of materials for implants using engineered peptides. *Acta Biomater*. 2010;6(12):4634-4641. doi:10.1016/j.actbio.2010.06.004.

125. Sano KI, Ajima K, Iwahori K, et al. Endowing a ferritin-like cage protein with high affinity and selectivity for certain inorganic materials. *Small*. 2005;1(8-9):826-

832. doi:10.1002/smll.200500010.

126. Sano KI, Sasaki H, Shiba K. Specificity and biomineralization activities of Ti-binding peptide-1 (TBP-1). *Langmuir*. 2005;21(7):3090-3095. doi:10.1021/la047428m.

127. Ikemi M, Kikuchi T, Matsumura S, Shiba K, Sato S, Fujita M. Peptide-coated, self-assembled M12L24 coordination spheres and their immobilization onto an inorganic surface. *Chem Sci*. 2010;1(1):68. doi:10.1039/c0sc00198h.

128. Shiba K. Exploitation of peptide motif sequences and their use in nanobiotechnology. *Curr Opin Biotechnol*. 2010;21(4):412-425. doi:10.1016/j.copbio.2010.07.008.

129. Patwardhan S V, Patwardhan G, Perry CC. Interactions of biomolecules with inorganic materials: principles, applications and future prospects. *J Mater Chem*. 2007;17(28):2875-2884. doi:10.1039/b704075j.

130. Mann S, Archibald DD, Didymus JM, et al. Crystallization at inorganic-organic interfaces : biominerals and biomimetic synthesis. *Science (80-)*. 1993;261(5126):1286-1292. http://www.jstor.org/stable/2882151.

131. Hunter GK, Kyle CL, Goldberg HA. Modulation of crystal formation by bone phosphoproteins: role of glutamic acid-rich sequences in the nucleation of hydroxyapatite by bone sialoprotein. *Biochem J*. 1994;300 (Pt 3:723-728. doi:10.1042/bj3020175.

132. Biesinger MC, Lau LWM, Gerson AR, Smart RSC. Resolving surface chemical

states in XPS analysis of first row transition metals, oxides and hydroxides: Sc, Ti, V, Cu and Zn. *Appl Surf Sci*. 2010;257(3):887-898. doi:10.1016/j.apsusc.2010.07.086.

133. Wang X, Shen J, Pan Q. Raman spectroscopy of sol-gel derived titanium oxide thin films. *J Raman Spectrosc*. 2011;42(7):1578-1582. doi:10.1002/jrs.2899.

134. Frank O, Zukalova M, Laskova B, Kürti J, Koltai J, Kavan L. Raman spectra of titanium dioxide (anatase, rutile) with identified oxygen isotopes (16, 17, 18). *Phys Chem Chem Phys*. 2012;14(42):14567-14572. doi:10.1039/c2cp42763j.

135. Xing-Yuan G, Da-Peng X, Zhan-Hui D, Wen-Hui S. Preparation and Raman spectrum of rutile single crystals using floating zone method. *Chinese Phys Lett*. 2006;23(6):1645-1647.

136. Jouanny I, Labdi S, Aubert P, et al. Structural and mechanical properties of titanium oxide thin films for biomedical application. *Thin Solid Films*. 2010;518(12):3212-3217. doi:10.1016/j.tsf.2009.09.046.

137. Takadama H, Kim HM, Kokubo T, Nakamura T. An X-ray photoelectron spectroscopy study of the process of apatite formation on bioactive titanium metal. *J Biomed Mater Res*. 2001;55(2):185-193. doi:10.1002/1097-4636(200105)55:2<185::AID-JBM1005>3.0.CO;2-P [pii].

138. Al-Hiyasat AS, Al-Sa'Eed OR, Darmani H. Quality of cellular attachment to various root-end filling materials. *J Appl Oral Sci*. 2012;20(1):82-88.

139. Resende CX, Lima IR, Gemelli E, Granjeiro JM, Soares G de A. Cell adhesion

on different titanium-coated surfaces. *Matéria (Rio Janeiro)*. 2010;15(2):386-391.

140. Guleryuz H, Cimenoglu H. Oxidation of Ti-6Al-4V alloy. *J Alloys Compd*. 2009;472(1-2):241-246. doi:10.1016/j.jallcom.2008.04.024.

141. Du HL, Datta PK, Lewis DB, Burnell-Gray JS. Air oxidation behavior of Ti-6Al-4V alloy between 650 and 850 °C. *Corros Sci*. 1994;36(4):631-642. doi:http://dx.doi.org/10.1016/0010-938X(94)90069-8.

142. Lee Y-J, Cui D-Z, Jeon H-R, et al. Surface characteristics of thermally treated titanium surfaces. *J Periodontal Implant Sci*. 2012;42(3):81. doi:10.5051/jpis.2012.42.3.81.

143. Fitzgibbons ET, Sladek KJ, Hartwig WH. TiO$_2$ film properties as a function of processing temperature. *J Electrochem Soc*. 1972;119(6):735. doi:10.1149/1.2404316.

144. Saldaña L, Vilaboa N, Vallés G, González-Cabrero J, Munuera L. Osteoblast response to thermally oxidized Ti6Al4V alloy. *J Biomed Mater Res - Part A*. 2005;73(1):97-107. doi:10.1002/jbm.a.30264.

145. Anselme K, Linez P, Bigerelle M, et al. The relative influence of the topography and chemistry of TiAl6V4 surfaces on osteoblastic cell behaviour. *Biomaterials*. 2000;21(15):1567-1577. doi:10.1016/S0142-9612(00)00042-9.

146. Roach P, Eglin D, Rohde K, Perry CC. Modern biomaterials: A review - Bulk properties and implications of surface modifications. *J Mater Sci Mater Med*.

2007;18(7):1263-1277. doi:10.1007/s10856-006-0064-3.

147. Kim HM, Miyaji F, Kokubo T, Nishiguchi S, Nakamura T. Graded surface structure of bioactive titanium prepared by chemical treatment. *J Biomed Mater Res.* 1999;45(2):100-107. doi:10.1002/(SICI)1097-4636(199905)45:2<100::AID-JBM4>3.0.CO;2-0.

148. Sun T, Wang M. A comparative study on titania layers formed on Ti, Ti-6Al-4V and NiTi shape memory alloy through a low temperature oxidation process. *Surf Coatings Technol.* 2010;205(1):92-101. doi:10.1016/j.surfcoat.2010.06.019.

149. Ellingsen JE. A study on the mechanism of protein adsorption to TiO_2. *Biomaterials.* 1991;12(6):593-596. doi:10.1016/0142-9612(91)90057-H.

150. Hanawa T, Ota M. Characterization of surface film formed on titanium in electrolyte using XPS. *Appl Surf Sci.* 1992;55(4):269-276. doi:10.1016/0169-4332(92)90178-Z.

151. Parsegian VA. Molecular forces governing tight contact between cellular surfaces and substrates. *J Prosthet Dent.* 1983;49(6):838-842. doi:10.1016/0022-3913(83)90360-8.

152. Roddick-Lanzilotta A, McQuillan A. An in situ infrared spectroscopic study of glutamic acid and of aspartic acid adsorbed on TiO_2: implications for the biocompatibility of titanium. *J Colloid Interface Sci.* 2000;227(1):48-54. doi:10.1006/jcis.2000.6864.

153. Roddick-lanzilotta AD, Connor PA, Mcquillan AJ. An in situ infrared

spectroscopic study of the adsorption of lysine to TiO_2 from an aqueous solution. *Langmuir*. 1998;(17):6479-6484. doi:10.1021/la980425n.

154. Chen H, Su X, Neoh KG, Choe WS. QCM-D analysis of binding mechanism of phage particles displaying a constrained heptapeptide with specific affinity to SiO_2 and TiO_2. *Anal Chem*. 2006;78(14):4872-4879. doi:10.1021/ac0603025.

155. Van Oss CJ, Giese RF. Influence of the pH of Water on its Electron-Accepticity and Donicity. *J Adhes*. 2005;81(3-4):237-244. doi:10.1080/00218460590944530.

156. McCafferty E, Wightman J. Determination of the Surface Isoelectric Point of Oxide Films on Metals by Contact Angle Titration. *J Colloid Interface Sci*. 1997;194(2):344-355. doi:DOI: 10.1006/jcis.1997.5138.

157. Wang XJ, Li YC, Lin JG, Hodgson PD, Wen CE. Apatite-inducing ability of titanium oxide layer on titanium surface : the effect of surface energy. *J Mater Res*. 2008;23(6):1682-1688. doi:10.1557/jmr.2008.0195.

158. Fung CD, Cheung PW, Ko WH. A generalized theory of an electrolyte-insulator-semiconductor field-effect transistor. *IEEE Trans Electron Devices*. 1986;33(1):8-18.

159. Raiteri R, Margesin B, Grattarola M. An atomic force microscope estimation of the point of zero charge of silicon insulators. *Sensors and Actuators B-Chemical*. 1998;46(2):126-132. doi:10.1016/s0925-4005(98)00098-7.

160. Bousse L, Mostarshed S, Van der Shoot B, De Rooij NF, Gopel W. Zeta Potential

Measurements of Ta_2O_5 and SiO_2 Thin Films. *J Colloid Interface Sci.* 1991;147(1):22-32. doi:10.1016/0021-9797(91)90130-Z.

161. Trevino KJ, Shearer JC, Tompkins BD, Fisher ER. Comparing Isoelectric Point and Surface Composition of Plasma Modified Native and Deposited SiO_2 Films Using Contact Angle Titrations and X-ray Photoelectron Spectroscopy. *Plasma Process Polym.* 2011;8(10):951-964. doi:10.1002/ppap.201100010.

162. Cuddy MF, Poda AR, Brantley LN. Determination of isoelectric points and the role of pH for common quartz crystal microbalance sensors. *ACS Appl Mater Interfaces.* 2013;5(9):3514-3518. doi:10.1021/am400909g.

163. Butt HJ. Measuring electrostatic, van der Waals, and hydration forces in electrolyte solutions with an atomic force microscope. *Biophys J.* 1991;60(December):1438-1444. doi:10.1016/S0006-3495(91)82180-4.

164. Walsh RB, Nelson A, Skinner WM, Parsons D, Craig VSJ. Direct measurement of Van der Waals and diffuse double-layer forces between titanium dioxide surfaces produced by atomic layer deposition. *J Phys Chem C.* 2012;116(14):7838-7847. doi:10.1021/jp300533m.

165. Bullard JW, Cima MJ. Orientation dependence of the isoelectric point of TiO_2 (rutile) surfaces. *Langmuir.* 2006;22(24):10264-10271. doi:10.1021/la061900h.

166. Kosmulski M. The significance of the difference in the point of zero charge between rutile and anatase. *Adv Colloid Interface Sci.* 2002;99(3):255-264. doi:10.1016/S0001-8686(02)00080-5.

167. Tamura H, Katayama N, Furuichi R. Modeling of ion-exchange reactions on metal oxides with the Frumkin isotherm. 1. acid−base and charge characteristics of MnO_2 , TiO_2 , Fe_3O_4 , and Al_2O_3 surfaces and adsorption affinity of . *Environ Sci Technol*. 1996;30(4):1198-1204. doi:10.1021/es9504404.

168. Hazan R, Brener R, Oron U. Bone growth to metal implants is regulated by their surface chemical properties. *Biomaterials*. 1993;14(8):570-574. doi:10.1016/0142-9612(93)90172-X.

169. Blasco T, Lopez-Nieto JM. Oxidative dyhydrogenation of short chain alkanes on supported vanadium oxide catalysts. *Appl Catal A Gen*. 1997;157(1-2):117-142. doi:10.1016/S0926-860X(97)00029-X.

170. Beach ER, Tormoen GW, Drelich J, Han R. Pull-off force measurements between rough surfaces by atomic force microscopy. *J Colloid Interface Sci*. 2002;247(1):84-99. doi:10.1006/jcis.2001.8126.

171. Drelich J, Tormoen GW, Beach ER. Determination of solid surface tension from particle-substrate pull-off forces measured with the atomic force microscope. *J Colloid Interface Sci*. 2004;280(2):484-497. doi:10.1016/j.jcis.2004.08.002.

172. Takemoto S, Yamamoto T, Tsuru K, Hayakawa S, Osaka A, Takashima S. Platelet adhesion on titanium oxide gels: effect of surface oxidation. *Biomaterials*. 2004;25(17):3485-3492. doi:10.1016/j.biomaterials.2003.10.070.

173. Yu C, Zhu S, Wei D, Wang F. Amorphous sol-gel SiO_2 film for protection of Ti6Al4V alloy against high temperature oxidation. *Surf Coatings Technol*.

2007;201(12):5967-5972. doi:10.1016/j.surfcoat.2006.11.004.

174. Wang X-X, Hayakawa S, Tsuru K, Osaka A. A comparative study of in vitro apatite deposition on heat-, H_2O_2-, and NaOH-treated titanium surfaces. *J Biomed Mater Res*. 2001;54(2):172-178.

175. Osaka A, Tsuru K, Hayakawa S. Titania derived from combined chemical and thermal treatments of titanium : In vitro apatite forming ability. *Phosphorous Res Bull*. 2004;17:130-141.

176. Tengvall P, Elwing H, Lundström I. Titanium gel made from metallic titanium and hydrogen peroxide. *J Colloid Interface Sci*. 1989;130(2):405-413. doi:10.1016/0021-9797(89)90117-3.

177. Tengvall P, Bertilsson L, Liedberg B, Elwing H, Lundström I. Degradation of dried Ti-peroxy gels made from metallic titanium and hydrogen peroxide. *J Colloid Interface Sci*. 1990;139(2):575-580. doi:10.1016/0021-9797(90)90131-7.

178. Kashiwagi K, Tsuji T, Shiba K. Directional BMP-2 for functionalization of titanium surfaces. *Biomaterials*. 2009;30(6):1166-1175. doi:10.1016/j.biomaterials.2008.10.040.

179. Hunter GK, Goldberg HA. Modulation of crystal formation by bone phosphoproteins: role of glutamic acid-rich sequences in the nucleation of hydroxyapatite by bone sialoprotein. *Biochem J*. 1994;302(1):175 LP-179. http://www.biochemj.org/content/302/1/175.abstract.

180. PepCalc.com - Peptide calculator. http://pepcalc.com/.

181. Kim H-M, Miyaji F, Kokubo T, Nakamura T. Preparation of bioactive Ti and its alloys via simple chemical surface treatment. *J Biomed Mater Res.* 1996;32(3):409-417. doi:10.1002/(SICI)1097-4636(199611)32:3<409::AID-JBM14>3.0.CO;2-B.

182. Ohtsuki C, Iida H, Hayakawa S, Osaka A. Bioactivity of titanium treated with hydrogen peroxide solutions containing metal chlorides. *J Biomed Mater Res.* 1997;35(1):39-47. doi:10.1002/(SICI)1097-4636(199704)35:1<39::AID-JBM5>3.0.CO;2-N.

183. Daly SM, Przybycien TM, Tilton RD. Adsorption of poly(ethylene glycol)-modified lysozyme to silica. *Langmuir.* 2005;21(4):1328-1337. doi:10.1021/la048316y.

184. Santore MM, Wertz CF. Protein spreading kinetics at liquid-solid interfaces via an adsorption probe method. *Langmuir.* 2005;21(22):10172-10178. doi:10.1021/la051059s.

185. George A, Veis A. Phosphorylated proteins and control over apatite nucleation, crystal growth, and inhibition. *Chem Rev.* 2008;108(11):4670-4693. doi:10.1021/cr0782729.

186. Gao G, Lange D, Hilpert K, et al. The biocompatibility and biofilm resistance of implant coatings based on hydrophilic polymer brushes conjugated with antimicrobial peptides. *Biomaterials.* 2011;32(16):3899-3909. doi:10.1016/j.biomaterials.2011.02.013.

187. Barber T a, Golledge SL, Castner DG, Healy KE. Peptide-modified p(AAm-co-

233

EG/AAc) IPNs grafted to bulk titanium modulate osteoblast behavior in vitro. *J Biomed Mater Res A*. 2003;64:38-47. doi:10.1002/jbm.a.10321.

188. Fraioli R, Rechenmacher F, Neubauer S, et al. Mimicking bone extracellular matrix: integrin-binding peptidomimetics enhance osteoblast-like cells adhesion, proliferation, and differentiation on titanium. *Colloids Surfaces B Biointerfaces*. 2015;128:191-200. doi:10.1016/j.colsurfb.2014.12.057.

189. Yang H, Fung SY, Pritzker M, Chen P. Modification of hydrophilic and hydrophobic surfaced using an ionic-complementary peptide. *PLoS One*. 2007;2(12). doi:10.1371/journal.pone.0001325.

190. Werner C, Zimmermann R, Kratzmüller T. Streaming potential and streaming current measurements at planar solid/liquid interfaces for simultaneous determination of zeta potential and surface conductivity. *Colloids Surfaces A Physicochem Eng Asp*. 2001;192(1-3):205-213. doi:10.1016/S0927-7757(01)00725-7.

191. Markland P, Zhang Y, Amidon GL, Yang VC. A pH- and ionic strength-responsive polypeptide hydrogel: synthesis, characterization, and preliminary protein release studies. *J Biomed Mater Res*. 1999;47(4):595-602. doi:10.1002/(SICI)1097-4636(19991215)47:4<595::AID-JBM17>3.0.CO;2-I.

192. Ito Y, Ochiai Y, Park YS, Imanishi Y. pH-sensitive gating by conformational change of a polypeptide brush grafted onto a porous polymer membrane. *J Am Chem Soc*. 1997;119(7):1619-1623. doi:10.1021/ja963418z.

193. Hu K, Fan F-RF, Bard AJ, Hillier AC. Direct measurement of diffuse double-layer forces at the semiconductor/electrolyte interface using an atomic force microscope. *J Phys Chem B*. 1997;101(Scheme 1):8298-8303. doi:10.1021/jp971887x.

194. Robeson JL, Tilton RD. Spontaneous reconfiguration of adsorbed lysozyme layers observed by total internal reflection fluorescence with a pH-sensitive fluorophore. *Langmuir*. 1996;12(25):6104-6113. doi:10.1021/la960476p.

195. Chung AJ, Rubner MF. Methods of loading and releasing low molecular weight cationic molecules in weak polyelectrolyte multilayer films. *Langmuir*. 2002;18(4):1176-1183. doi:10.1021/la010873m.

196. Connor PA, McQuillan AJ. Phosphate adsorption onto TiO_2 from aqueous solutions: an in situ internal reflection infrared spectroscopic study. *Langmuir*. 1999;15(8):2916-2921. doi:10.1021/la980894p.

197. Lu X, Leng Y. Theoretical analysis of calcium phosphate precipitation in simulated body fluid. *Biomaterials*. 2005;26(10):1097-1108. doi:10.1016/j.biomaterials.2004.05.034.

198. Cuscó R, Guitián F, de Aza S, Artús L. Differentiation between hydroxyapatite and β-tricalcium phosphate by means of μ-Raman spectroscopy. *J Eur Ceram Soc*. 1998;18(9):1301-1305. doi:10.1016/S0955-2219(98)00057-0.

199. Gu YW, Tay BY, Lim CS, Yong MS. Biomimetic deposition of apatite coating on surface-modified NiTi alloy. *Biomaterials*. 2005;26(34):6916-6923.

doi:10.1016/j.biomaterials.2005.04.051.

200. Pecheva E V., Pramatarova LD, Maitz MF, Pham MT, Kondyuirin A V. Kinetics of hydroxyapatite deposition on solid substrates modified by sequential implantation of Ca and P ions: Part II: morphological, composition and structure study. *Appl Surf Sci.* 2004;235(1-2):170-175. doi:10.1016/j.apsusc.2004.05.178.

201. Barrere F, Van Blitterswijk CA, De Groot K, Layrolle P. Influence of ionic strength and carbonate on the Ca-P coating formation from SBF×5 solution. *Biomaterials.* 2002;23(9):1921-1930. doi:10.1016/S0142-9612(01)00318-0.

202. Brown WE, Chow LC, Siew C, Gruninger S. Acidic calcium phosphate precursors in formation of enamel mineral. *Tooth Enamel IV.* 1984;8.

203. Nancollas GH. Phase tranformation during precipitation of calcium salts. In: *Biological Mineralization and Demineralization.* Springer; 1982:79-99.

204. Kim JH, Kim SH, Kim HK, Akaike T, Kim SC. Synthesis and characterization of hydroxyapatite crystals: a review study on the analytical methods. *J Biomed Mater Res.* 2002;62(4):600-612. doi:10.1002/jbm.10280.

205. Lu HB, Campbell CT, Graham DJ, Ratner BD. Surface characterization of hydroxyapatite and related calcium phosphates by XPS and TOF-SIMS. *Anal Chem.* 2000;72(13):2886-2894. doi:10.1021/ac990812h.

206. Wang B, Wei S, Guo L, et al. Effect of deposition parameters on properties of TiO_2 films deposited by reactive magnetron sputtering. *Ceram Int.* 2017;43(14):10991-10998. doi:10.1016/j.ceramint.2017.05.139.

207. Martin N, Rousselot C, Savall C, Palmino F. Characterizations of titanium oxide films prepared by radio frequency magnetron sputtering. *Thin Solid Films*. 1996;287(1-2):154-163. doi:10.1016/S0040-6090(96)08782-2.

208. Tack L, Schickle K, B?ke F, Fischer H. Immobilization of specific proteins to titanium surface using self-assembled monolayer technique. *Dent Mater*. 2015;31(10):1169-1179. doi:10.1016/j.dental.2015.06.019.

209. Eliaz N, Kopelovitch W, Burstein L, Kobayashi E, Hanawa T. Electrochemical processes of nucleation and growth of calcium phosphate on titanium supported by real-time quartz crystal microbalance measurements and X-ray photoelectron spectroscopy analysis. *J Biomed Mater Res - Part A*. 2009;89(1):270-280. doi:10.1002/jbm.a.32129.

210. Yang X, Xie B, Wang L, Qin Y, Henneman ZJ, Nancollas GH. Influence of magnesium ions and amino acids on the nucleation and growth of hydroxyapatite. *CrystEngComm*. 2011;13:1153. doi:10.1039/c0ce00470g.

211. Yoshinari M, Kato T, Matsuzaka K, Hayakawa T, Shiba K. Prevention of biofilm formation on titanium surfaces modified with conjugated molecules comprised of antimicrobial and titanium-binding peptides. *Biofouling*. 2010;26(1):103-110. doi:10.1080/08927010903216572.